First spectroscopy of ^{11} Zr with MINOS

Nancy Paul

université PARIS-SACLAY

NNT : 2018SACLS547

Thèse de doctorat

CEA – Saclay

UNIVERSITÉ PARIS SUD

Comprendre le monde, construire l'avenir

First Spectroscopy of ^{110}Zr with MINOS

Thèse de doctorat de l'Université Paris-Saclay
préparée à l'Université Paris-Sud
au sein de l'Irfu/DPhN du CEA Saclay

École doctorale n°576
Particules, Hadrons, Énergie, Noyau,
Instrumentation, Imagerie, Cosmos et Simulation (PHENIICS)

Spécialité de doctorat : Structure et réactions nucléaires

Thèse présentée et soutenue à Saclay, le 12 décembre 2018, par

Nancy PAUL

Composition du Jury :

Denis Lacroix	Directeur de Recherche IPN-Orsay, France	Président du jury
Navin Alahari	Directeur de Recherche GANIL, France	Rapporteur
Stéphane Grévy	Directeur de Recherche CENBG, France	Examinateur
Elias Khan	Professeur Université Paris Sud, France	Examinateur
Gerda Neyens	Professeur KU Leuven, Belgique	Rapporteur
Alexandre Obertelli	Professeur TU Darmstadt, Allemagne	Directeur de thèse
Anna Corsi	Ingénieure de Recherche CEA Saclay	Invitée

for Paul and Marie-Hélène

Acknowledgements

First I would like to thank Navin Alahari, Stéphane Grévy, Elias Khan, Denis Lacroix, and Gerda Neyens for accepting to participate as jury members for my PhD. The finalization of this manuscript and the defense were moments of stimulating academic exchange and I greatly appreciate the time and attention that they consecrated to this work.

Then of course I owe the success and joy of these last three years to Alexandre Obertelli and Anna Corsi, my thesis director and co-supervisor, respectively. They provided a working environment that was rigorous and intellectually stimulating on a daily basis, while simultaneously full of laughter and joy. They accompanied with grace and kindness my family that blossomed at the same time as the results presented here, leaving me space when I needed it, but always gently leading me towards better, more rigorous, deeper scientific output. I could not have imagined a more wonderful duo to learn from, and I sincerely hope that we will continue to work together in the future.

My PhD dream team was rounded out by Alain Gillibert, Valérie Lapoux, and Lolly Pollacco who provided continuous support for everything from data analysis and paper writing, to helping me navigate the perils of french grammar and administration. Notably Lolly supervised the last part of this thesis work, introducing me to the fascinating world of electronics and detector development while providing a much appreciated space for good 'ol anglophone chit-chats.

Next I would like to thank the IRFU technicians, engineers, and scientific staff, Gilles Authelet, Denis Calvet, Alain Delbart, Jean-Marc Gheller, Arnaud Giganon, and Ioannis Katsioulas. Jean-Marc and Gilles taught me French and Toulousain during my first trip to Japan, Denis Calvet made everything work and helped me find Japanese food that I could eat during pregnancy, Arnaud was my MINOS setup buddy, and Alain and Ioannis helped me with many interesting discussions during the last phase of my PhD working on the PUMA TPC. I am very humbled by intense technical know-how that was concentrated in this team, and the great kindness and patience of all who took time to help me understand TPCs, cryogenics, and the hardware and software that all together make possible exceptional physics.

The DPHN family made coming into the office every day a great joy. A big thank you to Danielle Coret who helped me with all the very important details related to both immigration and family leave, and to Franck Sabatié, Jacques Ball, and Christophe Theisen who provided continuous support to me professionally and personally. There are too many people and anecdotes to list, but I have been truly touched by the many incredible people that make up this department. From buying Christmas gifts for my children, to sharing coffee or offering meals when I was clearly overwhelmed, to bringing clothes or sending funny parenting comics, you all helped make everything a bit lighter and easier for me and my family. And to the Precaires of DPHN, I have never been part of a more welcoming, intelligent, crazy wonderful group of students in my life. You guys are the best.

I am forever indebted to Ani Aprahamian who met me at a jazz bar in downtown South Bend, introduced me to the wonderful world of nuclear physics, and sent me to France where this adventure began. Ani gave me an incredible start in this field, taught me much about science and the life that surrounds it, and I only hope that I can continue to make her proud. Then of course I would like to thank Piet van Isacker who welcomed me for a theory internship at GANIL in 2011, despite the fact that I knew essentially nothing about nuclear theory, and our "wacky" IBM calculations mark the beginning of my French scientific career.

They say that development includes components of both nature and nurture, and I had a double dose of both from Mom and Dad. Mom, an analytical water chemist, had my brother and I in the lab before we were old enough to go to school, and we grew up with the experience that science was both

normal and cool. Dad, a salesman, would let me skip school to travel with him to electrical utility tradeshows all around the USA and taught me to love talking to people and seeing new places. I know that the distance is difficult now, but hard core science + a love of exotic places...I am pretty sure this is all your fault.

Finally, all of this is really made possible by my most wonderful husband and perfect partner in physics and parenting, Guillaume. He both corrected and contributed to my grasp of the concepts discussed in this work, while in the next moment doing the laundry and keeping the kids quiet so that I could analyse data. And Paul and Marie-Hélène, if you read this someday, know that your presence during this work made it all the sweeter.

Contents

Introduction

The atomic nucleus is an exquisitely complex object. Held together by the strong force, its constituent fermions are concurrently subject to the Coulomb and weak forces, as well as many-body correlations. At low energies ($\leq$ 1 GeV) the theory of quantum chromodynamics (QCD) that governs the strong force is non-perturbative. While extracting a nucleon-nucleon interaction directly from lattice QCD shows promise, it can only currently be done for $A = 2$ systems with unphysical pion masses, see for example [1]. One can take advantage of the separation of scales made possible by chiral symmetry breaking, meaning that at the energies typical of nuclear physics only nucleons and pions are necessary explicit degrees of freedom while internal nucleonic degrees of freedom can be taken into account effectively through contact terms. However even using an effective interaction derived from chiral effective field theory[1], the overwhelmingly large number of degrees of freedom makes exact calculations quickly intractable. Brute-force resolution of the Schrodinger equation for a five nucleon system takes tens of millions of CPU hours on the world's largest supercomputers, and implementing such approaches for masses larger than A$\sim$10 is not possible with current technology.

As both the interaction and many body problem cannot be resolved microscopically for all but the simplest systems, modern efforts seek not to derive all physics from a grand unifying theory, but rather to construct a series of effective theories, each adapted for a given domain of observation [2]. The success of such effective theories is determined by their ability to identify and describe the relevant degrees of freedom that drive the observables of a given energy scale.

The domain explored in this work is medium-mass nuclear structure, where the advent of radioactive beams has changed our understanding of the determinant physics ingredients. While the structure of stable nuclei can be described with central and spin-orbit forces, measurements away from stability reveal a rearrangement of level structure that seems to originate in a complicated interplay between deformation, nucleon-nucleon interactions, and myriad fine details of the nuclear interaction. The tensor interaction, three-body forces, and continuum-coupling are all known to play a role, but the relative contributions of each of these mechanisms as a function of proton and neutron number are largely unconstrained. As one example out of many, Figure 0.1 shows the predicted neutron skin thicknesses as calculated with different effective interactions in mean field models for isotopes from mass 40 to 208 as a function of proton-neutron asymmetry $I = (N - Z)/A$. The predictions diverge by as much as a factor 15 for the most neutron-rich species.

This is where we, experimentalists, enter the picture. Measurements of fundamental observables in regions where theoretical predictions diverge can help pin down the relevant physics driving exotic structure evolution. The most neutron rich nuclei are often studied at fragmentation facilities, such as the RIBF in Japan where the data presented in this work was obtained. The RIBF is the only new generation fragmentation facility currently operational, though others will follow soon such as GSI in Germany, or FRIB in the USA. Relativistic beams with thick targets provide the highest luminosity of rare nuclei, but historically these gains were limited by poor spectroscopic resolution due to imprecise doppler correction. A breakthrough was achieved with the MINOS system, which combines a thick liquid hydrogen target with a proton tracker allowing simultaneously high luminosity and resolution via reaction vertex reconstruction [4, 5]. This work uses proton removal reactions with the MINOS system to study the structure of the key benchmark nucleus ^{110}Zr, participating in the global effort to make targeted measurements of the most exotic species in contested regions of structure evolution (Part I, Chapters 1-4).

The nucleon removal reactions used to populate exotic species with MINOS, and similar systems,

[1] a controlled low energy expansion based on power counting and fit to low energy properties

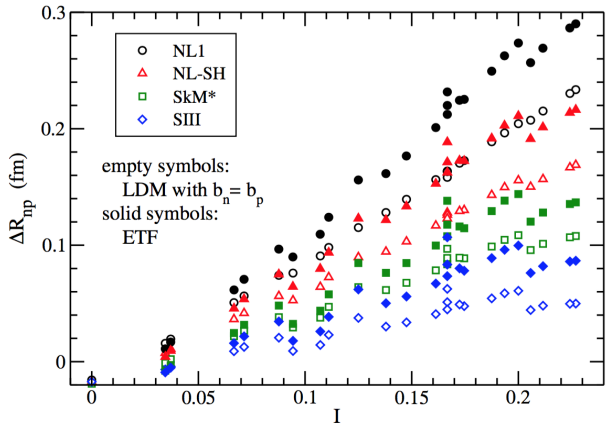

Figure 0.1. Predicted neutron skin thickness as a function of proton-neutron asymmetry, $I = (N - Z)/A$, for isotopes from mass 40 to 208 as calculated with different effective interactions in mean field models. Figure from [3].

are themselves poorly understood. Nucleon removal in classical kinematics has been studied with stable targets and medium energy proton beams, where the incident proton energy is much larger than the separation energy of the nucleon to be removed. This work conducted largely from the 60s-80s, suggests that the reactions can be well described within the quasi-free scattering paradigm. In this picture, the target may be considered as a mostly inert core and a valence nucleon and the reaction proceeds principally via a single scattering event. Single nucleon removal reaction systematics for *exotic* nuclei are however poorly benchmarked, and the governing quantities that drive the reaction systematics unknown. Divergences have been seen using composite targets, attributed to missing correlations in the underlying structure models or a more complicated reaction mechanism. There is a need thus for a cleaner probe of nucleon removal from exotic systems, similar to the work done with stable beams. To date, however, little data of this kind exists. Thus here a complementary study has been undertaken to understand nucleon removal reactions from exotic nuclei with proton targets in hopes of shedding light on the physics that drive these reactions in exotic nuclei (Part II, Chapters 5-7).

Both these measurements–spectroscopy and cross sections with proton targets–are embedded in the larger goal of measuring structure and reaction observables in regions where nuclear structure is contested, and with the cleanest probes possible for optimal exchange with theory. The new PUMA project at CERN was born of this same philosophy [6]. PUMA aims at measuring neutron skins in exotic nuclei on the fringes of the nuclear surface, where theories diverge the most. This feat is accomplished through low-energy antiproton-nucleus collisions, providing a new sensitivity and still-to-be-proven competitive rates for the most exotic species. At the heart of PUMA is a time projection chamber, very similar to the one used in MINOS. This work concludes with electric field simulations for the PUMA pion tracker, a contribution towards to next generation of exotic structure studies (Part III, Chapter 8).

Part I.

Spectroscopy of ^{110}Zr

The important thing is not to stop questioning. Curiosity has its own reason for existence. One cannot help but be in awe when he contemplates the mysteries of eternity, of life, of the marvelous structure of reality. It is enough if one tries merely to comprehend a little of this mystery each day.

Albert Einstein

1 Introduction

1.1. Mayer and the Shell Model

The nuclear shell model was arguably born at Argonne National Laboratory in 1946, as Maria Goeppert-Mayer and Edward Teller were trying to make sense of the relative abundances of the elements. Mayer assembled data from abundances, decay probabilities, binding energy discontinuities, fission distributions, and neutron absorption cross sections, and observed that the most abundant and stable isotopes had proton/neutron numbers of 2, 8, 20, 28, 50, 82, 126 [7]. Some of these observations had already been made by Elasser and Guggenheimer [8, 9], who attributed such phenomena to closed shells of nucleons due to fully occupied quantized energy levels, analogous to shells in atomic systems. Elasser and Guggenheimer's results were not taken seriously however, partly due to the fact that their calculations diverged for masses larger than 8, and partly due to fierce opposition from Niels Bohr who thought that the high density in the nucleus would prevent nucleons from following well defined orbits. Nevertheless, Mayer noted in her 1948 paper that the experimental observations were consistent with calculations by Wigner and Barkas [10, 11] that pointed to some of these configurations emerging from shell closures in a model where nucleons moved independently under a common potential. The breakthrough arrived when Fermi, also at Argonne, asked Mayer if there was any indication in the data of spin-orbit coupling. Mayer realised immediately that this was the missing piece of the puzzle, and one year later published a theory describing the observed "magic numbers"[1] by combining a rounded square-well potential, angular momentum coupling, and a one-body spin-orbit term, leading to the shell structure shown in Fig 1.1 [13]. An independent identical formulation was submitted to Physical Review by Hans Jensen and colleagues at the same time [14], and Mayer and Jensen shared one half of the Nobel Prize in 1963 for their Shell Model. The model enjoyed instant success as it was able to explain not just the available experimental systematics of isotopic abundances, but also spins, magnetic moments, isomeric states, and beta-decay, at the time limited at or near the valley of stability.

Today, nearly 70 years later, the theoretical constructs and vernacular of Mayer and Jensen's Shell Model still serve as the principal scaffolding for our discussions of nuclear structure. The fundamental premise is that nucleons behave in first approximation as independent particles in a common potential generated by the net effect of all the other particles. Nucleons fill up the first A orbitals of this potential, identified by index i aggregating the $n\ell_j$ quantum numbers, according to the Pauli principle, e.g.

[1] Supposedly this term was dubiously coined by Wigner [12].

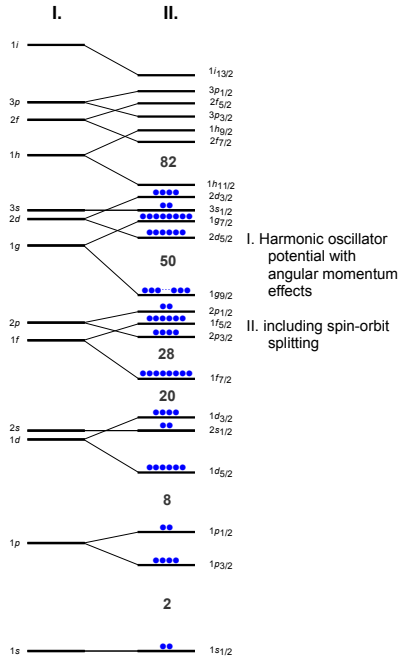

Figure 1.1. Schematic of the classical Shell-Model. Nucleon magic numbers are shown in bold in the shell gaps. The shell model levels are shown filled with 70 nucleons.

$$H \equiv H_0 = \sum_i \epsilon_i n_i \tag{1.1}$$

where ϵ_i are the single particle energies, and n_i are occupation probabilities which can take values of 0 or 1. The nucleus is however a many-body quantum system where correlations play an important role, pairing being the most prominent example. The independent particle picture is thus too strong of an assumption and many-body correlations must be included, i.e. anything in the wavefunction that cannot be described by a single product of single-particle states. The general expression of a two-body hamiltonian is

$$H = T + V = \sum_{i=1}^{A} \frac{\mathbf{p}_i^2}{2\mu} + \sum_{i>k=1}^{A} V_{ik}(|\mathbf{r}_i - \mathbf{r}_k|) \tag{1.2}$$

where $\mathbf{p}_i$ is the momentum of the nucleon, μ is the nucleon reduced mass, and V_{ik} is a nucleon-nucleon interaction. Following the paradigm established by Mayer, a mean-field contribution can be singled out by adding and subtracting a one-body potential $U_i(r_i)$ to yield

$$H = \sum_{i=1}^{A} \left[\frac{\mathbf{p}_i^2}{2m_i} + U_i(r_i) \right] + \sum_{i>k=1}^{A} \left[V_{ik}(|\mathbf{r}_i - \mathbf{r}_k|) - \delta_{i,k} U_i(r_i) \right] = H_0 + H_{residual} \tag{1.3}$$

In this expression, $H_{residual}$ is believed to be a small perturbation however it breaks the simple idea of independent particles moving in a mean-field. The goal of all many-body methods is to treat the correlations generated by the residual interaction. A concrete example is the Configuration Interaction Method (or No-Core Shell Model in nuclear physics). It seeks to solve the Schrödinger equation in a model space. The ansatz wavefunction is

$$\left|\Psi^A\right\rangle = \sum_i c_i \left|\phi_i^A\right\rangle \tag{1.4}$$

where ϕ_i^A are A-body slater determinants, and c_i are the variational coefficients corresponding to the weight of each configuration. This method has the potential to offer a complete microscopic accounting for the collective and single particle properties of nuclei, unfortunately realistic calculations become quickly computationally intractable and are currently only possible up to mass ∼10 [15]. Shell model calculations may be simplified by treating the nucleus as an inert core and valence nucleons, i.e. a subset of states ϕ_i^A spanned by Equation 1.4, under the hypothesis that strictly the latter define the resulting physics [16]. This however means that an effective interaction must be used in Equation 1.3, generally fit on nearby nuclei leading to limited predictive capabilities [17, 18]. Current efforts seek to renormalize interactions fit on light nuclei into these reduced valence spaces, which will significantly improve the predictive capabilities of these approaches [19].

Mean field methods offer a more computationally tractable solution by focusing exclusively on H_0 with a schematic potential representing the effect of all other nucleons. This reduces the A-body problem to an effective one-body problem. The ground state properties of the chart of the nuclides can thus be easily calculated. Specific contributions in terms of position, spin and isospin operators known to drive the low-energy properties of nuclei are included, e.g. central and spin-orbit terms. Mean field approaches attempt to phenomenologically incorporate the effect of correlations into the one-body potential with a density dependent term that may include effective two and three nucleon forces. A modern mean-field hamiltonian takes the general form shown in Equation 1.5, where A is the total number of nucleons, T_i is the kinetic energy term, V_{ij} is an effective interaction, and ρ is the nuclear density. The V_{ij} term contains the Coulomb interaction and the effective nuclear interaction, the latter of which principally governs the resulting physics and the average potential created by the other nucleons. Particularly for Hartree Fock method, the average single particle or mean field potential may be written as in Equation 1.6, where $|\phi\rangle$ is a Slater determinant corresponding to the one body density ρ, and $\frac{\delta V}{\delta \rho}$ is the functional derivative of the effective interaction [20].

$$H_{MF} = \sum_i^A h_i(\rho) = \sum_i^A T_i + 1/2 \sum_{i \neq j}^A V_{ij}(\rho) \tag{1.5}$$

$$h_i(\rho) = T_i + \sum_j V_{ij}\rho_j + \langle\phi| \frac{\delta V}{\delta \rho} |\phi\rangle \tag{1.6}$$

The most widely used modern effective interactions are the Skyrme [21, 22] and Gogny [23] forces, known for their ability to reproduce experimental observables across the chart of nuclides. Consider briefly the structure of the Gogny D1S interaction, shown in Equation 1.7. The first line describes the central part of the nuclear force, two gaussians that try to capture the attractive and repulsive components of the NN interaction, together forming a shallow well and including all possible spin-isospin exchange operators. The second line accounts for density dependence, changing the relative strength of the interaction if the particle is deep inside the nucleus or at the surface. The third line introduces a zero-range spin orbit force, and the last line is the Coulomb force. The parameters $u_j, W_j, B_j, H_j, M_j, t_3, x_0, \alpha$, and W_{LS} are global variables fit to data. We see that this interaction accounts for both microscopic (central+spin-orbit) effects similar to the potential used by Mayer and Jensen, but also includes in-medium correlation (density dependent) terms to mimic the effect of

multi-nucleon correlations.

$$
\begin{aligned}
V(|\mathbf{r}_1-\mathbf{r}_2|) = \sum_{j=1}^{2} e^{(|\mathbf{r}_1-\mathbf{r}_2|)^2/u_j^2} \left(W_j + B_j P_\sigma - H_j P_\tau - M_j P_\sigma P_\tau\right) \\
+t_3 \left(1 + x_0 P_\sigma\right) \delta\left(\mathbf{r}_1 - \mathbf{r}_2\right) \left[\rho \frac{\mathbf{r}_1 + \mathbf{r}_2}{2}\right]^\alpha \\
+iW_{LS} \overleftarrow{\bigtriangledown}_{12} \delta\left(\mathbf{r}_1 - \mathbf{r}_2\right) \times \overrightarrow{\bigtriangledown}_{12} \cdot \left(\sigma_1 + \sigma_2\right) \\
+ \left(1 + 2\tau_{1z}\right)\left(1 + 2\tau_{2z}\right) \frac{e^2}{|\mathbf{r}_1 - \mathbf{r}_2|}
\end{aligned}
\tag{1.7}
$$

Additional correlations may be included in i) the ansatz wavefunctions ϕ_i^A as in the Hartree-Fock-Bogoliubov (HFB) method, which allows a natural treatment of pairing correlations, ii) the concept of symmetry breaking and restoration included in ϕ_i^A which treats shape properties like deformation iii) configuration mixing methods which can tackle collective excitations [24]. Such methods are presented in more detail in Chapter 4.

1.2. Deformation and Shell Evolution from Different Points of View

As early as 1924, Pauli suggested the possibility that nuclei could take non-spherical shapes as an explanation for the hyperfine splitting in atomic systems [25]. The presence of this nuclear deformation was confirmed through the observation of quadrupole moments in europium and lutetium isotopes [26, 27]. The theoretical explanation for the origin of nuclear deformation was provided by Aage Bohr, Ben Wheeler, and Leo Rainwater, for which they received the Nobel Prize in 1975. Very briefly, deformation is an energetically favourable mechanism for nuclei with significant partially filled orbitals, arising naturally from the orbital anisotropy. It is an example of spontaneous symmetry breaking in the so-called intrinsic frame of the nucleus, i.e. where the nuclear density is localized [28, 29]. The signature of deformed shapes can be seen in spectroscopy and observables tightly linked to the expectation value of multipole transitions, like the quadrupole moment.

Deformation has a significant impact on the underlying structure of the nucleus. Single particle states may be plotted as a function of the average value of the quadrupole operator by adding a constraint to the mean-field hamiltonian shown in Equation 1.5. Such a plot is shown in Figure 1.2, where ϵ is a dimensionless axial deformation parameter in cylindrical coordinates introduced by Nilsson [30]. At $\epsilon = 0$, the nucleus is spherical, and all multipoles have an average value of zero. Moving away from $\epsilon = 0$, the nucleus becomes deformed which breaks the degeneracy of magnetic substates, rearranging the single particle levels and corresponding shell-gaps. For example, moving towards $\epsilon = 0.6$, there ceases to be a large energy gap above the $p_{1/2}$ orbital (N or $Z = 8$) but one may open up with the splitting of the $d_{5/2}$ (N or $Z = 10$).

Practically, a deformed single particle basis resulting from a deformed mean field potential is not always used. In the shell model, the impact of deformation on the underlying nuclear structure properties may be understood either through the concept of monopole drift. Mean field methods may treat these effects through symmetry breaking of the mean field potential in Equation 1.6 by imposing a deformed one body density. Each of these methods represents a different paradigm [31], or way of viewing the nucleus, and thus will be discussed separately in the following.

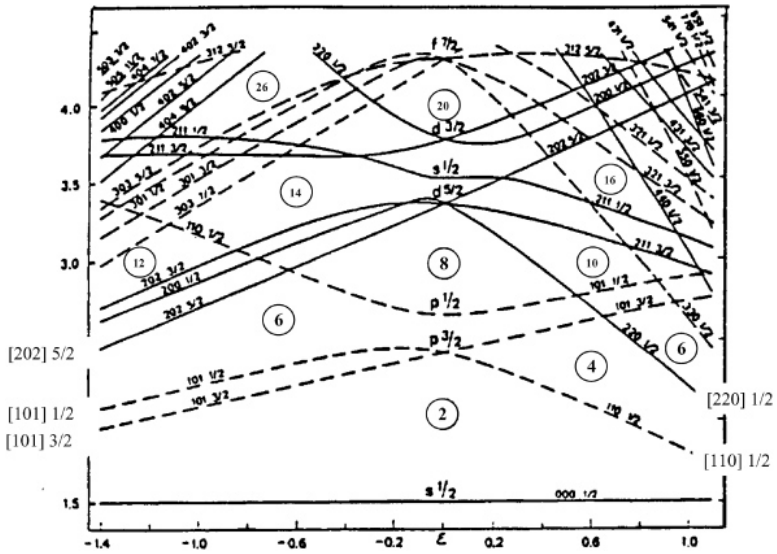

Figure 1.2. Single particle levels as a function of the axial deformation ϵ of the nuclear potential. Each single particle level is indicated by cylindrical symmetry quantum numbers $[N, n_z, m_l]\Omega$, where N is the major oscillator shell, n_z is number of nodes in the plane perpendicular to the symmetry axis, m_l is the projection of the orbital angular momentum onto the symmetry axis, and Ω is the angular momentum projection along the z-axis. Figure from [32].

1.2.1. The Shell Model

Within a spherical[2] shell model, the nucleus is described in the laboratory frame[3], and the wavefunction inherits all the symmetries of the Hamiltonian including time reversal invariance, parity and total angular momentum conservation among others, while being rotationally invariant. The signature of deformation appears thus in the mean value of multipole operators and spectroscopy observables. The shell model hamiltonian may be broken up into two components, a monopole component corresponding with the spherical mean field description of Equation 1.6, and a multipole component that includes residual interactions and quadrupolar, octupolar and hexadecapolar terms.

The modification of single particle levels shown in Figure 1.2 may be most clearly understood through the concept of monopole drift, or the change in the single particle levels resulting from the monopole component of the hamiltonian as nucleons are added. This linear shift in single particle energies as a function of level occupation was first discussed in the 1960s to explain the spin of the ground state of ^{11}Be [33]. Following the formalism of [34], the monopole drift originates in the nucleon-nucleon interaction of Equation 1.3. For two nucleons in orbits j and j', it is defined as the component of the nucleon-nucleon interaction that is averaged over all possible magnetic substate orientations. Considering a monopole interaction $\hat{v}_{nn}$ between two neutron orbitals, the monopole matrix element is

$$V_{nn}(j,j') = \frac{\sum_{m,m'} \langle j,m,j',m'|\, \hat{v}_{nn}\, |j,m;j',m'\rangle}{(2j+1)(2j'+1)} \tag{1.8}$$

[2]Spherical here denotes the coordinate system and the single particle oscillator wavefunctions, i.e. spherical harmonics.

[3]Laboratory and intrinsic frame in the following are not meant to be precise mathematical descriptions of the same wavefunction in two different reference frames, but rather to represent two different ways of constructing models. Laboratory frame for many-body calculations indicates a method that conserves total angular momentum, parity, neutron and proton number, while intrinsic frame refers to variational methods with respect to the single-particle wave function that may explicitly break symmetries.

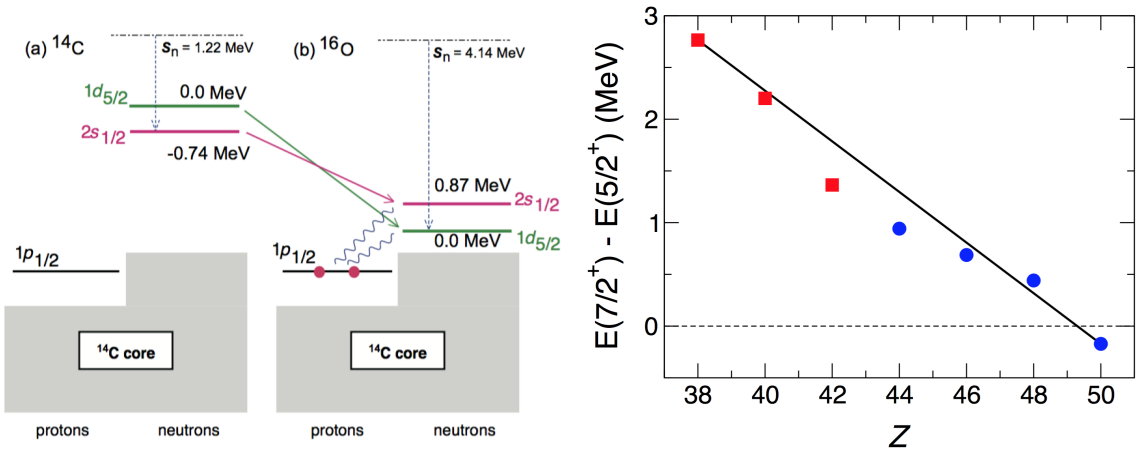

(a) (b)

Figure 1.3. (a) Schematic image of valence orbitals outside a ^{14}C core and the proton neutron monopole interaction (blue lines) that lowers the neutron orbitals as protons are added. (b) Energies of the lowest $7/2^+$ level relative to the $5/2^+$ states for N = 51 isotones. The straight line connects Z=38 and 50. Deviations from the straight line are due to multipole correlations. The different mass regions illustrate the universality of the mechanism. Both Figures from [34].

The monopole interaction leads to a shift of the single particle energies according to the relative occupation of nucleon orbitals. For example, the monopole interaction shifts the single particle energy of the monopole part of the shell model hamiltonian for a neutron on a j-orbit by

$$\Delta\hat{\epsilon}^n_j = \sum_{j'} V_{T=1}(j,j')\Delta\hat{n}^n_{j'} + \sum_{j'} \tilde{V}_{pn}(j,j')\Delta\hat{n}^p_{j'} \tag{1.9}$$

where $\Delta\hat{n}^n_{j'}$ and $\Delta\hat{n}^p_{j'}$ are the number of added neutrons and protons, respectively, and $\tilde{V}_{pn}$ includes T=0 and T=1 components of the proton-neutron interaction. One example of the effects of the monopole interaction is shown schematically in Figure 1.3(a) for the case of protons added outside of a ^{14}C core. As more protons are added, the attractive p-n monopole interaction brings down the neutron orbitals. As is clear from Equation 1.9, the more nucleons added to the j' orbital the more important the monopole shift becomes, for example increasing in strength along an isotopic chain. Certainly the final structure of the nucleus is the result of the monopole and multipole components of the interaction and the two cannot be easily disentangled. The latter can compete with the spherical shell gaps causing sudden shape changes, see for example [35]. However the monopole part is the main driver of the gradual shift in single particle levels along an isotopic chain, concurrent with the development of deformation going towards mid-shell. This may be seen in Figure 1.3(b) which shows the energies of the lowest $7/2^+$ level with significant neutron strength relative to the $5/2^+$ states for N = 51 isotones. The linear trend is attributed to the monopole shift, while deviations from linearity in the Figure may be attributed to multipole correlations.

1.2.2. Mean Field

Within mean field methods, deformation may be treated by transforming to the intrinsic frame of the nucleus. The intrinsic frame is a theoretical construct that represents the localized nucleus and does not obey the symmetry considerations of the Hamiltonian. Following the formalism of [20], the radius of a deformed nucleus in the laboratory frame may be expanded as

$$R(\theta,\phi) = R_0\left(1 + \alpha_{00}\sum_{\lambda=1}\sum_{\mu=-\lambda}^{\lambda}\alpha_{\lambda\mu}Y_{\lambda\mu}(\theta,\phi)\right) \tag{1.10}$$

where R_0 is a length parameter, $\alpha_{\lambda\mu}$ are deformation parameters, λ indicates the multipolarity of the deformation, μ is the projection of λ on the axis of quantization, and $Y_{\lambda\mu}$ are spherical harmonics [36]. Most nuclei are quadrupole deformed, described in first order by parameters α_{20} and α_{22}, while tetrahedral and octahedral deformation is described by $\lambda = 3, 4$, respectively. Transformation to the intrinsic frame where R is invariant under reflection and rotation may be obtained via

$$\alpha_{2\mu} = \sum_{\nu} D^{\lambda=2}_{\mu\nu}(\alpha,\beta,\gamma)a_{2\nu} \tag{1.11}$$

where D is the Wigner D-matrix, a transformation matrix described by the Euler angles (Ω), and $a_{2\nu}$ are the deformation parameters in the intrinsic frame. It is convenient to introduce axial and triaxial deformation parameters β and γ, respectively, where

$$a_{20} = \beta cos(\gamma),\ a_{2,2} = a_{2,-2} = \frac{1}{\sqrt{2}}\beta sin(\gamma) \tag{1.12}$$

Nuclear shapes in the $\beta - \gamma$ plane are shown in Figure 1.4(a). Mean field methods include these deformation degrees of freedom as Lagrange constraints while minimizing the mean field hamiltonian, thus forcing the wavefunction of the system to acquire enforcing the selected shapes. An example of the single particle levels for ^{110}Zr as a function of β deformation is shown in Figure 1.4(b). Inclusion of correlations requires beyond mean field methods, as discussed later in Chapter 4.

1.3. The Spin-Orbit Effect

Other components of the nuclear force may further modify shell structure. Preeminent for this work is the spin-orbit interaction. Beyond the simple, $\mathbf{l}\cdot\mathbf{s}$ coupling of Mayer and Jensen, a modern mean field spin-orbit term enters into the part of the potential that is dependent on the gradient of the density, seen in Equation 1.6. The spin-orbit contribution to the hamiltonian may then be written as

$$V_{LS} = W_0\delta(\mathbf{r}_1 - \mathbf{r}_2)\frac{1}{r}\frac{\partial}{\partial r}(\mathbf{l}\cdot\mathbf{s}) \tag{1.13}$$

where W_0 is the depth of the spin-orbit interaction. For very exotic nuclei, coupling to continuum states may lead to an extremely loosely bound, diffuse nuclear surface [38], meaning a smaller gradient of the radial density, potentially reducing the spin-orbit effect by as much as 40% at the neutron dripline [39, 40]. The implications of this effect on single particle levels is shown in the third column Figure 1.5, and could lead to a shell structure approaching that of a harmonic oscillator[4] [41]. Diffusivity may also lead to an effacement or quenching of shell structure near the dripline, whose effects are shown in the second column of Figure 1.5.

The tensor force may reduce spin-orbit splitting [43], playing a role in both the monopole and multipole components of the shell model interaction. The tensor force acts between specific single particle orbitals and may be attractive or repulsive according to their relative spin configurations and occupation. The tensor force is shown in Equation 1.14[44, 34], where τ and σ denote the isospin and spin vectors of nucleons one and two, $[]^2$ indicates the coupling of the operators to angular momentum $l = 2$, $Y^2(\theta,\phi)$ is the spherical harmonic of rank 2, and f(r) is a function of the relative distance between the two nucleons.

[4]Under the implicit assumption that the harmonic oscillator is a good approximation of the nuclear potential.

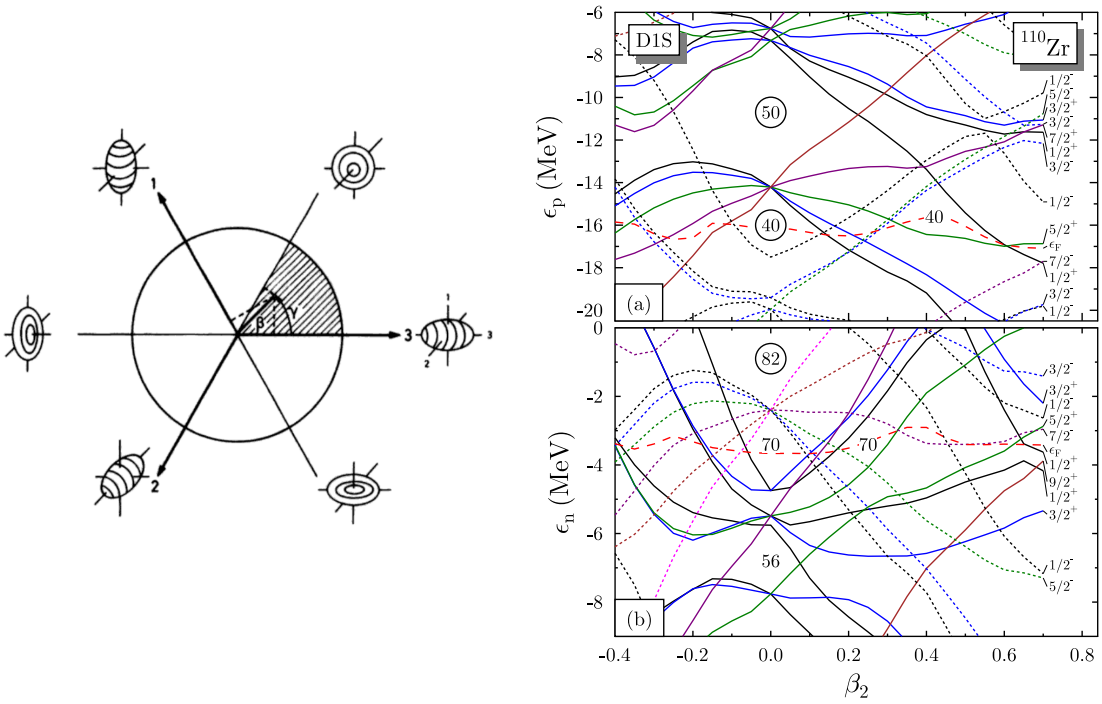

(a) **(b)**

Figure 1.4. (a) Nuclear shapes in the $\beta - \gamma$ plane. Figure from [20]. (b) Single particle (a) proton and (b) neutron levels for ^{110}Zr as a function of β deformation from Gogny D1S mean field calculations. Figure from [37].

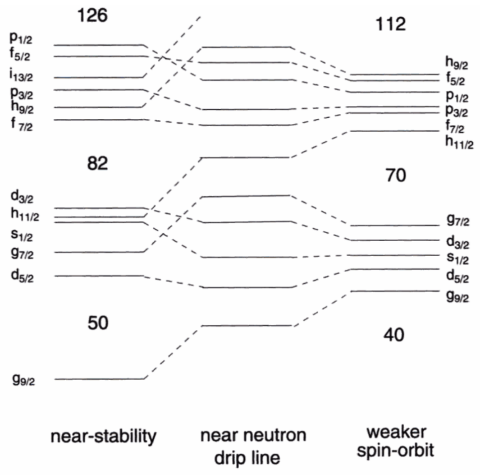

Figure 1.5. Single particle energy levels (left) from a standard mean field potential, (middle) where a more rounded potential is used, and (right) where a more rounded potential is used and the spin-orbit strength has been reduced by 50%. Figure from [42].

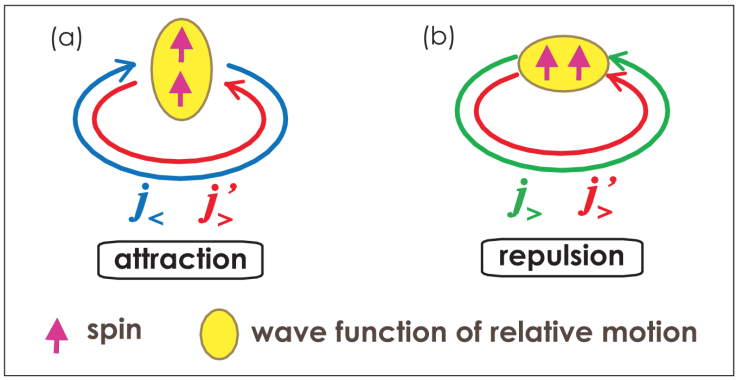

Figure 1.6. Schematic depiction of the tensor force acting between two single particle orbitals j and j'. Figure from [44].

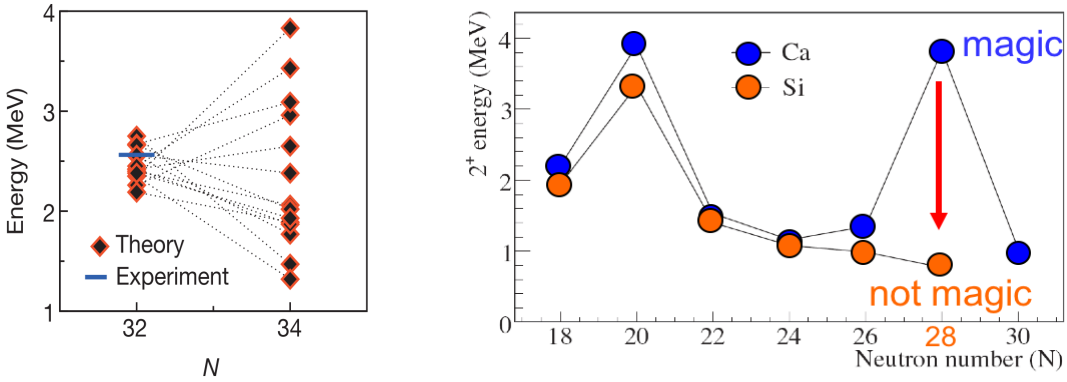

Figure 1.7. Energy of first 2^+ excited state in ^{52,54}Ca as measured (blue) and predicted by theories (black) . Figure from [45]. Evolution of the E_2^+ energies as a function of neutron number for calcium ($Z = 20$) and silicon ($Z = 14$) isotopes. Figure adapted from [46].

$$V_T = (\tau_1 \cdot \tau_2)([\sigma_1 \times \sigma_2]^{(2)} \cdot Y^{(2)}(\theta, \phi))f(|\mathbf{r}_1 - \mathbf{r}_2|) \tag{1.14}$$

An intuitive understanding of the tensor force mechanism is shown in Figure 1.6. For a proton in an orbital $j_< = l - 1/2$ and a neutron in an orbital $j_>^{'} = l' + 1/2$, their spins are parallel, but the relative orientation of their orbitals is opposite, as shown in Figure 1.6(a). These two orbitals may be imagined as current loops, whose opposite orientation causes an attraction between them. Similarly, if we consider the case shown in Figure 1.6(b), for a proton orbital $j_> = l + 1/2$ and neutron orbital $j_>^{'} = l' + 1/2$, now their relative orbits act as repulsive current loops. The tensor force has been invoked to explain the disappearance of the N=20 shell closure in ^{32}Mg [43], and is expected to play a role across the chart of nuclides.

1.4. Mapping Magic Numbers

The collective and single-particle mechanisms, and their interplay, briefly evoked above leads to an evolution of shell structure away from stability. The traditional magic numbers at N=8, 20, and 28 disappear [47, 48, 49, 46], while new ones have been claimed to emerge at N=16, 32, and 34 [50, 51, 52, 45]. So far the dramatic structure changes associated with new and disappearing magic

numbers has been limited to lighter nuclei ($A \leq 70$). No existing data supports a strong variation of the shell structure for heavier nuclei, but only a small fraction of neutron-rich heavy nuclei have been probed.

But how is the presence or absence of a magic number defined? Mayer and her contemporaries arrived at the original classification from purely experimental criteria by looking at correlations among isotopic abundances, binding energies, neutron absorption cross sections, and mass distributions of fission fragments. She then explained these "magic" configurations as resulting from the large gaps in the single particle spectrum associated with these occupancies in her model. The latter however is a strictly unobservable quantity, and gaps in single particle energies may or may not give rise to closed shell configurations. Indeed the presence of gaps in single particle energies is neither a necessary nor sufficient condition for experimental magicity, see [53] for a thorough review.

For this reason, we shall restrict ourselves to the experimental definition of magicity. Today, several observables that are signatures of a spherical shape may be used to indicate a magic number: a small mean-square charge radius $< r^2 >$, a high first 2^+ excited state, low ratio between the lowest 4^+ and 2^+ excited states–R_{42}, high separation energies, and low quadrupole transition probability B(E2)–the correlation among these observables may be seen in [54]. In principle the nuclear shape may be obtained directly through measurement of the multipole moments, but these methods cannot access rare isotopes. Thus we concentrate on those observables that can be obtained for nuclei produced at ≤ 1000 pps.

For the most exotic nuclei, where lifetimes and available beam intensities are low, often the first indicator of magicity is the energy of the first 2^+ excited state, E_2^+. The E_2^+ signature is illustrated in Figure 1.7, where we see two isotopic chains that pass through the traditional shell closure at $N = 28$. For the calcium isotopes, $N = 28$ leads to a large increase in E_2^+, consistent with a shell-closure scenario, but for the silicon isotopes no such elevation is found. This is interpreted as a disappearance of the $N = 28$ magic number for these very neutron rich silicon isotopes [46], though certainly other observables should be measured for conclusive evidence.

The dramatic structural signatures associated with the magic numbers make them a particularly sensitive tool to test the underlying theoretical models. Consider the now historical example of the first excited states in ^{52,54}Ca from advanced shell model and mean-field techniques, shown in Figure 1.7. The large theoretical uncertainty in the first 2^+ energy of ^{54}Ca is linked to the debated role of the spin-isospin interaction that could lead to the development of a subshell gap at $N = 34$. Experimental input was needed to show that, indeed a subshell gap does appear at $N = 34$ [45], suggesting a weakening of the residual attractive proton-neutron interaction between the proton $f_{7/2}$ and neutron $f_{5/2}$ orbitals.

1.5. The Case for ^{110}Zr

1.5.1. The N=70 shell gap

One particular region where competing mechanisms of structural evolution may lead to the development of new magic numbers is around ^{110}Zr ($Z = 40$, $N = 70$). In this region, from $40 \leq Z \leq 50$, protons fill up the $g_{9/2}$ orbital. The tensor mechanism leads to an attraction between these protons and the neutrons in the $g_{7/2}$ orbital, while repelling neutrons in the $h_{11/2}$. The lowering of the neutron $g_{7/2}$ orbital when adding protons to the $g_{9/2}$ was already noted by Federman and Pittel in 1977 to explain the deformation in the zirconium isotopes [55]. They described the mechanism as a sort of "mutual polarization effect", where nucleons may be promoted to valence orbitals to take advantage of the strong neutron-proton interaction when there is a large overlap between the n-p levels. They did not however consider that the effect could also be repulsive, and today this effect is understood as

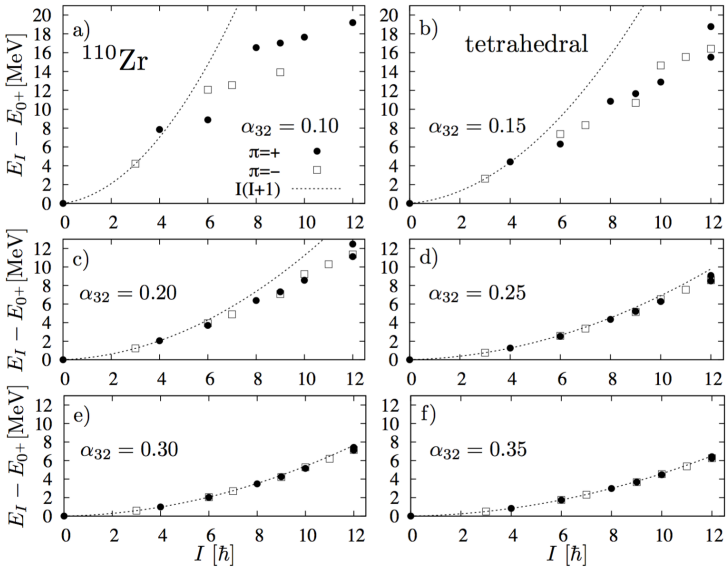

Figure 1.8. Spectroscopic predictions for ^{110}Zr with different degrees of tetrahedral deformation. The dotted line indicates the rigid rotor limit. Figure from [60].

being part of the tensor force. The tensor force attraction between the proton $g_{9/2}$ and neutron $h_{11/2}$ contributes to the N=82 shell gap, but as protons are removed from the $g_{9/2}$, this attraction may become weaker and potentially lead yield a shell gap at $N = 70$.

Shell quenching scenarios linked to coupling to the continuum in mean-field approaches may also favor the development of a subshell gap at $N = 70$. Pfeiffer, Kratz, Dobaczewski, and Moller simulated a shell-quenching scenario by employing a Nilsson potential with a reduced l^2 term [56], and found a reduction of the shell gap at $N = 82$ and an opening of the shell-gap at $N = 70$, the same effect as may be seen in Figure 1.5. As 70 is a harmonic oscillator magic number, these results were consistent with the conclusions of [39], where the harmonic oscillator shell closures may replace the traditional shell closures in a shell-quenching scenario. If either of these mechanisms–tensor interaction or shell quenching– leads to the development of a subshell gap at $N = 70$, is may be visible in ^{110}Zr which combines two ($Z = 40$, $N = 70$) harmonic oscillator shell closures.

Explorations of tetrahedral symmetries in mean field and microscopic-macroscopic techniques also concluded that ^{110}Zr may manifest a magicity relative to neighboring nuclei. Considering again Equation 1.10, tetrahedral deformation corresponds with non-zero α_{32}. When exploring this degree of freedom, it was found that 40 and 70 are both magic numbers associated with large shell gaps for significant a_{32} deformation [57]. This symmetry has never been observed definitely in nuclei, and its emergence is expected to be very sensitive to pairing effects [58]. Mean-field calculations found that the tetrahedral minimum in ^{110}Zr competes strongly with oblate and prolate deformed minima, but for certain interactions, notably using the SLy4 force, the tetrahedral minimum is energetically preferred over the prolate minimum and becomes the ground state [59]. If a tetrahedral configuration persists in the ground state of a nucleus, it would give rise to a unique level ordering, $0^+, 3^-, 4^+, 6^+, 6^-$..., and a rotational spectrum approaching that of a rigid rotor I(I+1), both distinguishable in a simple spectroscopy experiment [60]. The predicted levels for ^{110}Zr with different degrees of tetrahedral deformation are shown in Figure 1.8.

Whether a tetrahedral or spherically stabilized ground state wins out over the competing deformed minima in ^{110}Zr depends intricately on the effective interaction. In the tetrahedral studies employing

various interactions and models, only one calculation (HFB+SLy4) found a tetrahedral configuration for the ground state [59], while Woods-Saxon calculations found that a prolate ground state persists and the tetrahedral band-head lies at 1 MeV [60]. Indeed most predictions of the ^{110}Zr ground state from a variety of approaches show well-deformed prolate or shape coexistent minima [61, 62, 63, 64, 65, 66]. In a similar vein, a systematic study of 11 different tensor force parametrizations in Skyrme mean-field calculations found that only two, albeit unphysical, parametrizations yielded large shell gaps and thus a doubly-magic character for ^{110}Zr. Most parametrizations showed strong competition among prolate, oblate, and spherical minima, highlighting the particular sensitivity of the ground state structure of this nucleus to the details of the effective interaction. Thus while this nucleus is expected to be deformed according to the majority of the calculations, the mechanisms previously discussed may impact ^{110}Zr. Due to the high sensitivity of the structure of this nucleus to the model and interaction employed, ^{110}Zr is an important benchmark for understanding structure evolution for neutron-rich nuclei far from stability.

1.5.2. Implications for the R-process

The structure studies around ^{110}Zr were spurred by their potential implications for understanding the astrophysical rapid neutron capture process (r-process), thought to be responsible for approximately half of the abundances of the heavy elements in the universe. In the traditional conception of the r-process, material is driven to extreme isospin through a series of neutron captures and beta decays in a hot, dense, neutron-rich environment like a type-II supernova wind or a neutron star merger. During the process, material accumulates where beta decay halflives are long, such as near closed shells. When the free neutrons are exhausted and/or the temperature and density decrease (called "freezout"), the n-γ equilibrium is lost and all the material beta-decays back to stability. Peaks in the final abundance distribution correspond with material accumulated at the closed shells far from stability. An example of a classical r-process simulation of the type described here compared to observed solar r-process abundances[5] may be seen in the top panel of Figure 1.9.

The most critical input for r-process simulations is the astrophysical trajectory, i.e. the temperature, density, and neutron/proton ratios of the environment. This trajectory is site dependent, and as the site is currently unknown[6] the trajectory dominates the uncertainties in r-process calculations. However simulations also rely on numerous nuclear data inputs including nuclear masses, beta-decay lifetimes, neutron capture cross sections, and beta delayed neutron branching ratios. And unlike its cousin the slow neutron capture process (s-process) which passes near the valley of stability where the nuclear properties are known, the r-process is traditionally thought to traverse nuclei near the neutron dripline where nuclear structure models diverge. Differences between observed and predicted r-process abundances are thus an entanglement of astrophysics and nuclear physics uncertainties.

It may be seen in the top panel of Figure 1.9 that a large trough persists before the peaks at A=130 and 195 corresponding to the $N = 82$ and $N = 126$ shell closures, respectively. In light of this observation and inspired by the theoretical works cited above, the Extended Thomas Fermi plus Strutinsky Integral mass model (ETFSI), a microscopic-macroscopic approximation for a Hartree-Fock method with Skyrme forces used extensively for r-process simulations, was modified to include a phenomenological shell quenching far from stability for $N = 82$ and $N = 126$, yielding the mass model ETFSI-Q (ETFSI-Quenched). R-process simulations with the ETFSI-Q mass model show a significant improvement as can be seen in Figure 1.9(b). In particular, the previously persistent troughs in the

[5] Solar abundances are obtained from solar emission/absorption lines and analysis of certain meteorites. The simulated s-process component is then subtracted to yield solar r-process abundances.

[6] Though the observation of binary neutron star merger GW170817 in gravitational and electromagnetic waves showed that these events are at least one of the potentially multiple r-process sites [67].

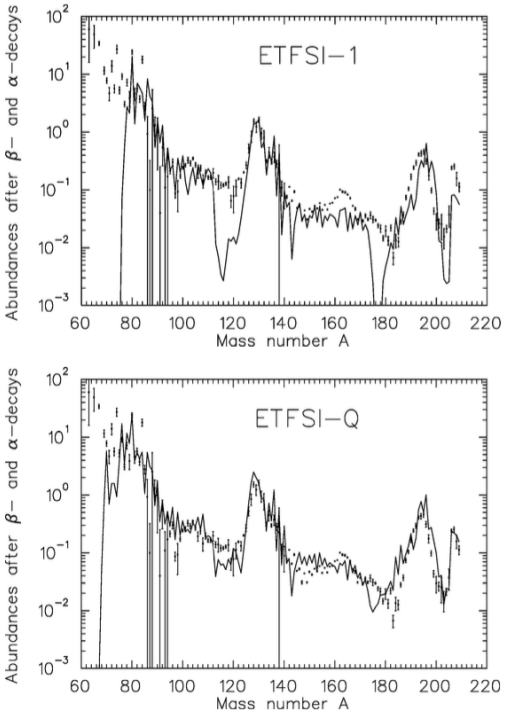

Figure 1.9. R-process calculated abundances (solid line) compared with observed r-process abundances (dots) for simulations with the ETFSI (top) and ETFSI-Q (bottom) mass models. Identical stellar parameters were used in both simulations. Figure from [70].

predicted r-process abundances before the peaks at A=130 and 195 are largely filled in, providing a much better agreement with the experimental r-process abundances. This may be understood as the shell-quenching shifts the r-process path closer to stability where β-decay halflives are longer, leading to relatively more material accumulation before the $N = 82, 126$ shell closures, filling in the respective troughs in the abundance distribution [68]. Some of the same authors continued this investigation by looking specifically at the case of ^{110}Zr, which with its 40 protons and 70 neutrons combines two harmonic oscillator magic numbers. They found that when assuming a strongly quenched $N = 82$ shell, ^{110}Zr may become a near spherical, doubly-magic nucleus [69].

1.6. Current Experimental Debate

Thus we see that significant interest has accrued around ^{110}Zr from the nuclear structure and astrophysical community. Theoretical investigations into shell-quenching spurred hypotheses about the potential stability of this nucleus, these hypotheses were strengthened by discrepancies with abundances predicted by r-process simulations. Experimental evidence for the weakening of the $N = 82$ shell closure was first claimed from β-γ decay spectroscopy of ^{130}Cd and ^{130}In where the measured Q_β value agreed best with predictions from a shell-quenched mass model [71]. This conclusion was challenged by measurements of isomeric decays in ^{130}Cd which showed no evidence of shell quenching [72]. More recently, mass measurements of $^{129-131}$Cd show a reduction of neutron separation energy differences by 1 MeV going from ^{132}Sn to ^{130}Cd, suggesting again a reduction of the $N = 82$ shell gap below ^{132}Sn [73]. So far experiments near ^{110}Zr, including the β-decay half-lives of $^{106-112}$Zr [74], lifetime measurements of the 2+ states in ^{104,106}Zr [75], and spectroscopy of the low-lying excited

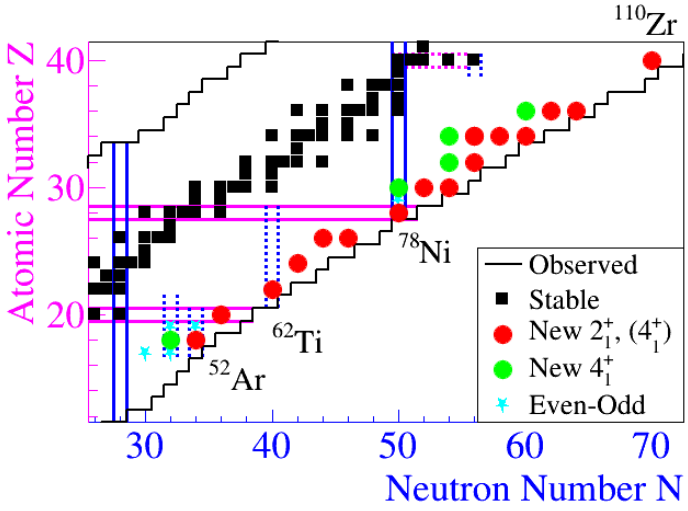

Figure 1.10. Nuclei targeted during the SEASTAR campaign. Figure from the SEASTAR proposal.

states of ^{108}Zr [76], show no hint of a shell gap at $N = 70$ and suggest that the Zr isotopes with $N > 60$ are prolate deformed. Thus in light of conflicting experimental results, a direct measurement of the structure of this nucleus is needed.

1.7. The SEASTAR Campaign

The first spectroscopy of ^{110}Zr presented in this work participates in the global effort to map the evolution of magicity in the most neutron-rich nuclei through spectroscopy of the lowest lying 2^+ excited states. It is part of the multi-year physics program, SEASTAR ("Shell Evolution And Search for Two-plus energies At RIBF"), led by teams from Riken and CEA-Saclay. SEASTAR focuses on multiple regions where significant structure changes are predicted, including the Island of Inversion near $N = 40$, the doubly magic nucleus ^{78}Ni, as well as shell evolution beyond N=60, including ^{110}Zr. The priority nuclei targeted in this campaign are shown in Figure 1.10. The first SEASTAR experiment was conducted in 2014 and focused on the region around ^{78}Ni, the 2015 campaign explored the region beyond $N = 60$ including ^{110}Zr, and the 2017 campaign focused on the lighter nuclei near ^{52}Ar.

SEASTAR harnesses the most intense neutron-rich exotic beams available in the world, provided by the Radioactive Isotope Beam Factory of the RIKEN Nishina Center in Japan. This is the only facility capable of delivering primary and secondary beams of sufficient intensity and energy to perform spectroscopy on exotic nuclei like ^{110}Zr. Primary beam intensities are shown in Table 1.1 for the RIBF and its next competitor, the National Superconducting Cyclotron Laboratory (NSCL) in the USA. Expected secondary beam rates for ^{111}Nb, the parent nucleus of ^{110}Zr when using the proton removal reaction, are 30 pps for the RIBF starting from a ^{238}U primary beam [77], and 0.08 pps for the NSCL starting from a ^{124}Sn beam [78]. The four orders of magnitude gain in intensity at the RIBF makes the choice a no-brainer to attain significant statistics in a reasonable amount of beam time.

To populate the low-lying excited states in these extremely exotic nuclei produced at a few tens of particles per second, SEASTAR uses a thick liquid hydrogen target, part of the MINOS system [4], presented in detail later. Cryogenic hydrogen targets offer significant gains in luminosity and reduced background for optimal energy resolution transitions in exotic nuclei [79], however energy

Table 1.1. Comparison of primary beam energies and intensities between the Radioactive Isotope Beam Factory (RIBF) and National Superconducting Cyclotron Laboratory (NSCL)

	RIBF		**NSCL**	
Primary Beam	E/A (MeV)	Intensity (pnA)	E/A (MeV)	Intensity (pnA)
^{16}O	250	200	150	175
^{48}Ca	345	400	140	80
^{78}Kr	345	300	150	25
^{124}Xe	345	80	140	10
^{238}U	345	30	80	0.2

loss of the ions in the target is approximately 100 MeV/u. The energy of the ^{124}Sn primary beam at NSCL is only 120 MeV/u, meaning that the residual nuclei would be stopped in the MINOS target. A thinner target could be used to minimize the energy loss, but then the time required to attain sufficient statistics increases dramatically. Thus due to intensity and energy considerations, RIBF is the only existing facility where the spectroscopy of ^{110}Zr can be performed.

2
Experimental Setup

The spectroscopy measurements presented in this work were performed at the Radioactive Isotope Beam Factory (RIBF) of the RIKEN laboratory in Japan. While ^{110}Zr ($Z = 40$, $N = 70$) was the physics case of interest, ^{112}Mo ($Z = 42$, $N = 70$) was also present in the data and was measured to further benchmark $N = 70$ structure evolution. Excited states in these nuclei were populated principally through proton knockout via the $^{111}Nb(p,2p)^{110}Zr$ and $^{113}Tc(p,2p)^{112}Mo$ channels. The parent nuclei ^{111}Nb and ^{113}Tc were created via in-flight fission from a ^{238}U primary beam on a 3 mm thick beryllium production target and selected with the BigRIPS Spectrometer. The parent nuclei impinged on a 10 cm thick liquid hydrogen target where the low lying states of interest were populated via proton knockout. Emitted gamma rays were detected in-flight via the DALI2 array and the MINOS time projection chamber allowed reconstruction of the reaction vertex. Reaction residues were detected in the ZeroDegree spectrometer. All nuclei were identified on an event-by-event basis in both spectrometers.

2.1. Ion Source and Acceleration Scheme

The 30 pnA ^{238}U primary beam was created via an electron cyclotron resonance ion source (ECRIS) and accelerated in fixed energy mode of the RIKEN accelerator system through a heavy-ion linac (RILAC) and 4 cyclotrons (RRC, fRC, IRC, SRC), as shown in Figure 2.1. Acceleration of the primary beam in fixed-energy mode includes two stripping stages to augment the charge state of the uranium atoms: first on a He gas stripper after the first cyclotron, and then on a Be disk after the second cyclotron. Ions emerged from the SRC with an energy of 345 keV/nucleon and impinged on a 3-mm thick ^{9}Be production target, creating a cocktail beam of radioactive nuclides via in-flight fission at the F0 focal plane of the BigRIPS in-flight fragment separator [81]. Figure 2.2 shows the measured production cross sections for secondary beams from ^{238}U fragmentation on a Be target, highlighting the vast array of secondary beams than can be created by this method.

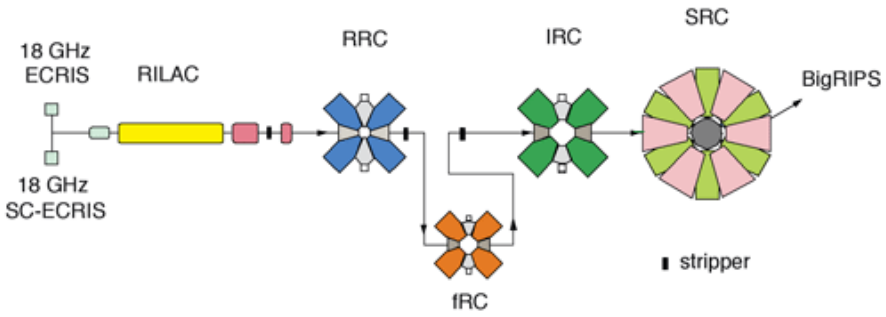

Figure 2.1. Schematic of the acceleration setup for the ^{238}U primary beam in fixed-energy mode at RIBF. Figure adapted from [80].

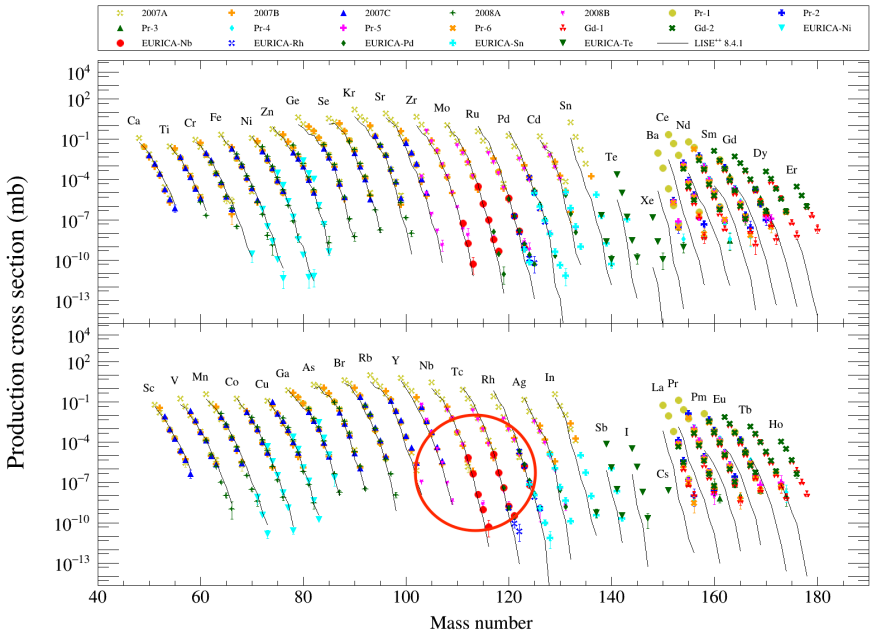

Figure 2.2. Measured production cross sections for secondary beams at RIBF from ^{238}U in-flight fission on a Be target. LISE++ simulations are shown in by the thin black lines. The points are measured values. The region of beams of interest for this work, ^{111}Nb and ^{113}Tc, are indicated by the red circle. Figure adapted from [80].

2.2. BigRIPS and ZeroDegree Spectrometers

Secondary beams produced from fragmentation then enter the BigRIPS spectrometer. BigRIPS is a two stage spectrometer that performs separation and identification of the secondary beams. It features 40 and 50 mrad vertical and horizonal acceptance, respectively, with approximately 50% collection efficiency of fragmentation products, and a two-stage setup to select and identify isotopes of interest. A detailed description of the BigRIPS setup and separation mechanism may be found in [82].

The first stage of BigRIPS is a two-bend achromatic spectrometer that performs a selection of nuclides from the swath of fragmentation products via the $B\rho - \delta E - B\rho$ method. A first dipole (D1) scatters the nuclides transversally according to their magnetic rigidity (Bρ), which depends essentially on their mass to charge ratio A/q, as can be seen by writing down the force equation for a charged particle moving perpendicularly to a magnetic field, shown in Equation 2.1 where B is the dipole magnetic field strength, ρ is the bending radius of dipole, v is the velocity of the ion, γ is the relativistic Lorentz factor, and m is the ion mass, which can be rewritten in terms of the mass number A and the atomic mass unit, u. The energy and hence the velocity emerging from the accelerator is fixed.

$$\begin{aligned} Q\gamma v \times B &= \frac{m\gamma^2 v^2}{\rho} \\ B\rho &= \frac{Au\gamma v}{Q} \end{aligned} \tag{2.1}$$

After the F1 dipole, an aluminum wedge degrader, characterized by its varied thickness in the horizontal plane of the beam axis, performs preliminary isotopic selection via energy loss in the wedge,

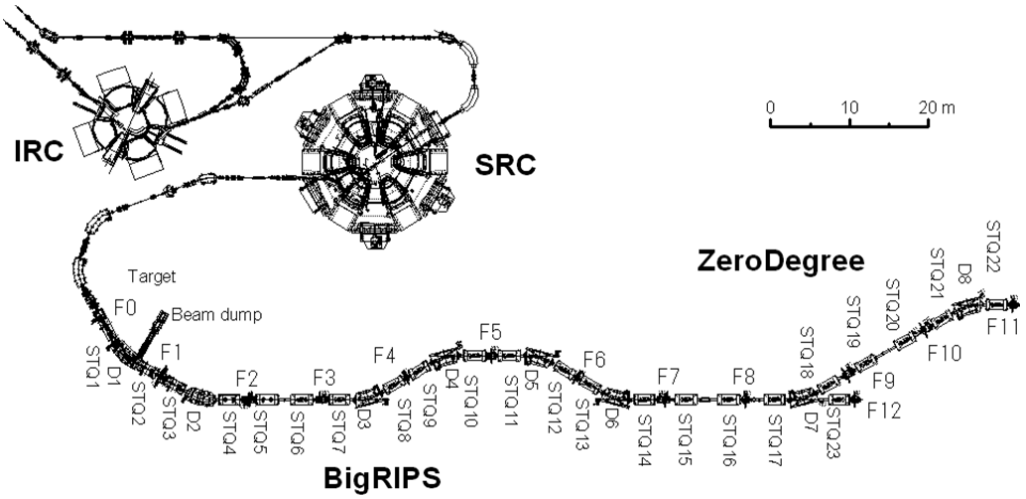

Figure 2.3. Schematic of the BigRIPS and ZeroDegree spectrometers including the superconducting quadrupole triplets (STQ1-STQ22), dipole magnets (D1-D8), and focal planes (F1-F11). Note that the beam direction is from left to right. Figure from [83].

according to Eq 2.2, the Bethe-Bloch formula. In this expression, m_e is the electron mass, e is the elementary charge, z, N, and I are the atomic number, atomic density, and mean excitation potential of the material, respectively

$$\frac{dE}{dX} = \frac{4\pi e^4 Z^2}{m_e v^2} N z \left[ln \frac{2m_e v^2}{I} - ln\left(1-\beta^2\right) - \beta^2 \right] \tag{2.2}$$

Emerging from the wedge at F1, the ions have experienced a preliminary dispersion according to A/q and Z. Dipole D2 is centered on the nucleus of interest and unwanted ions outside the desired beam envelope may be removed by slits at the dispersive F2 focal plane. Then, superconducting quadrupole triplets (STQs) 5-6 focus the cocktail beam centered on the nucleus on interest into the second stage of the separator, as shown in Fig. 2.3.

The second stage of BigRIPS (F3-F7) is a four-bend achromatic spectrometer with high momentum resolution that permits event-by-event identification of Z and A/q via the $B\rho - \Delta E - TOF$ method. This method utilizes combined measurements from parallel plate avalanche counters (PPACs), time of flight scintillators, and multi-sampling ionization chambers (MUSICs) interspersed among the focal planes of the spectrometer. For more details on these detectors, see section 2.5.

A/q may be obtained from the combined measurement of the ion $B\rho$ and TOF (to obtain v) as seen in 2.1. $B\rho$ is obtained from two sets of PPACS installed at each focal plane which measure the position in the X-Y plane of the ions, thus permitting trajectory reconstruction of each ion's path through the spectrometer [84]. This trajectory (or radius ρ), combined with NMR measurements of the magnetic field of each dipole (B) allow then direct calculation of $B\rho$. Plastic scintillators at F3 and F7 measure the time of flight between the focal planes and thus the velocity v of the ions, completing the information needed in Equation 2.1 to extract A/q.

The proton number Z is obtained via the combined measurements in the MUSIC and plastic time-of-flight detectors. The MUSIC detector measures energy loss of the ions in the gas, and this energy loss signal combined with the ion velocity as measured by the scintillators permits Z to be obtained, via equation 2.2. From these combined A/q and Z measurements, a particle identification plot can be reconstructed, as shown in Fig 2.4.

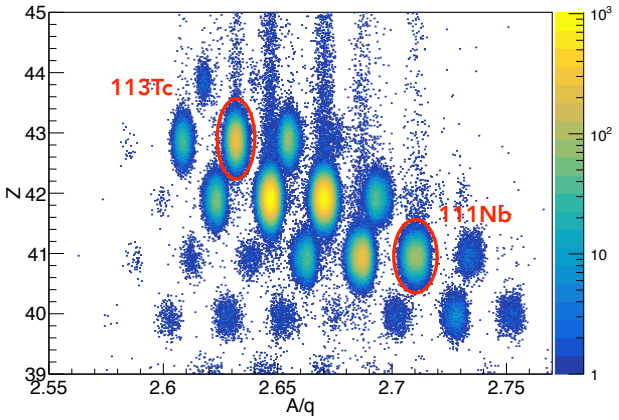

Figure 2.4. Particle identification (PID) plot for the BigRIPS spectrometer. The parent nuclei for the channels of interest are indicated.

After the secondary target, the ZeroDegree spectrometer functions in an identical fashion as BigRIPS to identify the reaction residues by A/q and Z on an event-by-event basis. In this case, no additional separation is needed via wedges, but double PPACs and scintillators at F8 and F11, and a MUSIC chamber at F11, allow precise particle identification via the above described $B\rho - \Delta - TOF$ method.

Note that in this scheme, A and q are not measured independently and charge states may contaminate the PID spectrum. This effect becomes particularly important for high Z ions, such as those studied here. Fortunately as $B\rho$ is measured at multiple intervals along the spectrometer path, jumps in $B\rho$ along the beamline associated with charge exchange reactions can be removed from the final PID spectrum. This method will be exploited later in the data analysis.

A summary of the beam-line settings for the ^{110}Zr experiment is shown in Table 2.1.

2.3. DALI2

At F8, where the nuclei of interest are populated, the emitted gamma rays are detected by the DALI2 (Detector Array for Low Intensity radiation 2) array. DALI2 surrounded the liquid hydrogen target of the MINOS system (see next section) and detected the gamma rays emitted by the de-excitation of the nuclei of interest. DALI2 is a nearly 4π modular array of 186 NaI(Tl) scintillators, adapted for high efficiency detection of in-flight gamma rays, and detailed extensively in [86]. Though there is a large push in the community to move towards tracking germanium arrays for spectroscopy measurements, for very exotic even-even nuclei where beam intensities are low and resolution is not critical, a high efficiency array like DALI2 may be preferable. This aptitude may be quantified through the resolving power (RP) of a 4π spectrometer, given in Equation 2.3 [87], which quantifies the important role that efficiency, resolution, peak-to-total ratio, and granularity play in a spectrometer's ability to measure a given spectrum. In this expression, N is the number of counts in the peak when the peak-to-background ratio is normalized to one, N_0 is the total number of events, ϵ is the full-energy peak efficiency of the array, and $R = 0.76(SE/\delta E)P/T$ is the improvement in the peak-to-background ratio that can be obtained by gating on a peak. In the expression for R, SE is the average energy spacing per transition, δE is the energy resolution, and P/T is the ratio of full energy events to total (full+partial) energy events.

$$RP = exp\,[ln(N_0/N)/(1 - ln\epsilon/lnR)] \tag{2.3}$$

Table 2.1. Summary of beamline settings for ^{110}Zr experiment. BigRIPS includes D1-5 and F1-7. ZeroDegree includes D7-8 and F8-11.

height**Setting**	^{111}**Nb**$\rightarrow$^{110}**Zr**
Primary Beam	^{238}U
Primary Beam Intensity	30 pnA
Be production target	3 mm
F1 Aluminum Degrader	4 mm
F5 Aluminum Degrader	2 mm
D1	7.8 T·m
D2	7.1949 T·m
D3	7.1665 T·m
D4	7.1665 T·m
D5	6.814 T·m
D6	6.814 T·m
D7	4.8338 T·m
D8	4.824 T·m
F1 slits	-30 mm , 64.2 mm
F2 slits	-4.5 mm , 4.5 mm
F5 slits	-120 mm , 60 mm
F7 slits	-16 mm , 16 mm
F8 slits	-50 mm , 50 mm
F9 slits	-120 mm , 120 mm
F10 slits	-120 mm , 120 mm
F11 slits	-170 mm , 170 mm
Secondary Beam intensity at F7	^{111}Nb: 42 Hz; ^{113}Tc: 106 Hz, Total $\sim$ 1 kHz
Daughter intensity at F11	^{110}Zr: 0.04 Hz; ^{112}Mo: 0.15 Hz

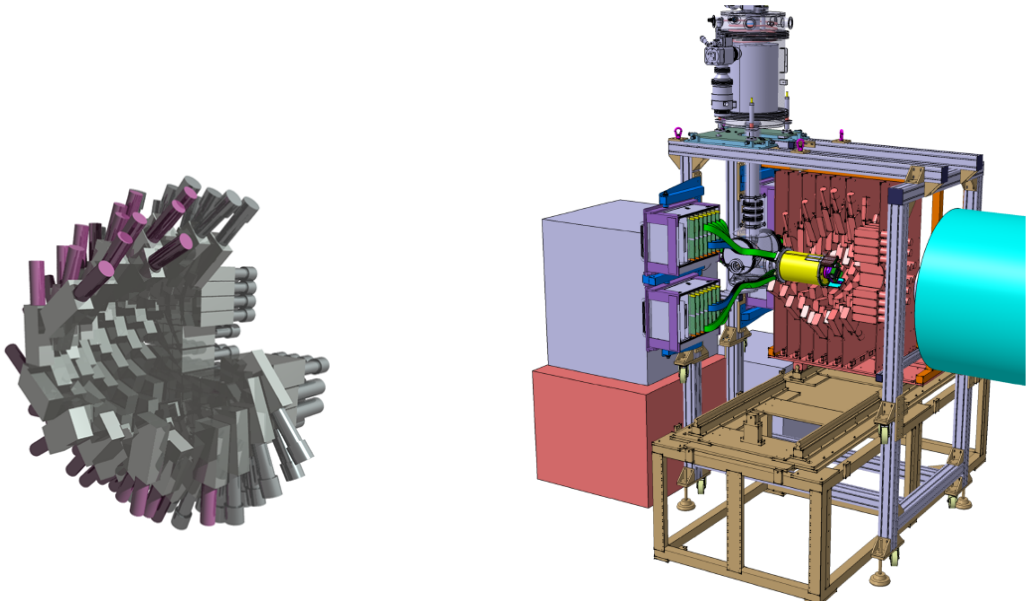

(a) **(b)**

Figure 2.5. (a) Cut-away schematic of the DALI2 array where the superposition of concentric and wall detector arrangements may be seen. (b) Technical drawing showing the MINOS system inside the DALI2 array. Both figures from [85].

Figure 2.6 shows the resolving power of DALI2 compared with the Gammasphere 4π germanium detector array [88], the SEGA 18 detector segmented germanium array [89], and GRETINA the segmented germanium tracking array demonstrator [90]. While certainly germanium detectors with full 4π coverage, as in Gammasphere, provide the highest resolving power, as the average peak spacing SE becomes larger, DALI2 becomes competitive with the germanium arrays, due to its high overall efficiency. The principal peaks in even-even nuclei studied within the SEASTAR campaign have separations of 300-400 keV.

DALI2 consists of three types of scintillators: 66 Saint-Gobain, 89 Scionix, and 31 Bicron crystals. Typical intrinsic efficiency of each scintillator is $\sim 9\%$ for a 662 keV gamma ray. The scintillation light emitted when gamma rays collide with the crystals is converted into a charge signal by Hamamatsu R580 photo multiplier tubes (PMTs). The DALI2 array may be reconfigured according to the specific geometry of each experiment. For these measurements it was arranged with 10 layers of crystals oriented concentrically around the beam-line, and an 11th layer forming a wall at forward angles as shown in Fig. 2.5. This setup covers polar angles of 12-118 degrees in the lab. Intrinsic angular resolution of the array is limited by the size of the detectors themselves and is on average ~ 6 degrees.

The signal output from DALI2 serves both for spectroscopic analysis and it is also used to trigger the DAQ, as may be seen in the electronics diagram shown in Appendix A. The signal from the PMT is fed to a spectroscopic amplifier which then outputs two signals: fast and slow. The fast signal contains no detailed information, it simply shows that there is an event above the threshold. This fast signal is sent through a constant fraction discriminator and if it is in coincidence with good events in F7 and F11 (BigRIPS and ZeroDegree spectrometers respectively), it triggers the TDC, a CAEN V1190A, which sets the time-stamp for the event. If the DAQ is triggered by the fast signal, then the slow signal containing the detailed charge information is digitized for analysis via a CAEN V785 peak-sensing ADC. 30 ns DALI2 timing gates were used for this analysis due to the low energy of the

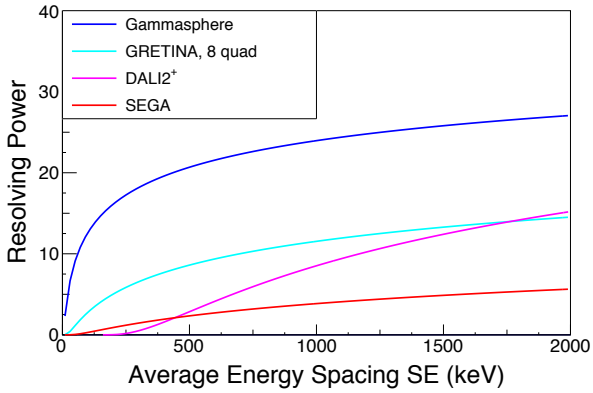

Figure 2.6. Resolving power as a function of SE for DALI, compared with other existing gamma arrays.

transitions.

DALI2 is calibrated before and after each physics measurement with standard sources including ^{137}Cs, ^{60}Co, ^{133}Ba, and ^{88}Y. For the ^{110}Zr setting, the 662 keV peak in the ^{137}Cs calibration source had a 59 keV Full Width at Half Maximum (FWHM), and thus a 9% energy resolution, consistent with benchmarked performance in [86]. Detector thresholds were set around 100 keV. GEANT4 simulations of this setup including a 10 cm liquid hydrogen target, individual experimental DALI2 detector thresholds, energy loss of the gamma-rays in the MINOS structure, and energy reconstruction with no addback[1], yield a 31% full-energy peak detection efficiency for 500 keV γ-rays emitted in-flight [91]. For in-flight emission of gamma rays at β=0.6 with no addback, efficiency ranges from 35% for 500 keV γ-rays to 10% for 2 MeV γ-rays [92].

2.4. MINOS

At the center of the DALI2 array is the MINOS system. MINOS provides the unique combination of a thick proton target and vertex tracker. It was conceived as an improvement to in-beam gamma ray spectroscopy setups for exotic nuclei that historically had to find a compromise between a thick-target to achieve maximum luminosity with low beam rates, and a thin-target to perform precise Doppler correction of the gamma rays emitted in-flight. MINOS provides a solution to this problem by combining a cryogenic liquid hydrogen target within a Time Projection Chamber (TPC), all made to fit inside the DALI2 gamma array [4].The MINOS TPC detects knocked out protons, allowing reaction vertex determination and thus precise Doppler correction. With the TPC providing vertex determination, a thick target can then be used to maximize luminosity for the most exotic beams.

The MINOS TPC is 30 cm long, composed of concentric Rohacell (polymethacrylimide) foam cylinders enclosing the beam-line and gaseous volume respectively. The outer surface of the inner cylinder and the inner surface of the outer cylinder are coated in Kapton foil to define the external electric field cages. A copper cathode serves as the downstream endcap, and establishes the maximum of the potential gradient. The field cage is formed by two chains of 1 mm large strips placed 1.5 mm apart, on opposite sides of a 50 μm thick Kapton foil. This makes the effective spacing between strip

[1] This is an analysis technique wherein the energies of γ-rays that hit within a given radius of the fired crystal (normally 15cm) are summed together. This technique may improve resolution by "adding back" counts that are lost to Compton scattering, but this technique was not used for this analysis as explained in the next chapter.

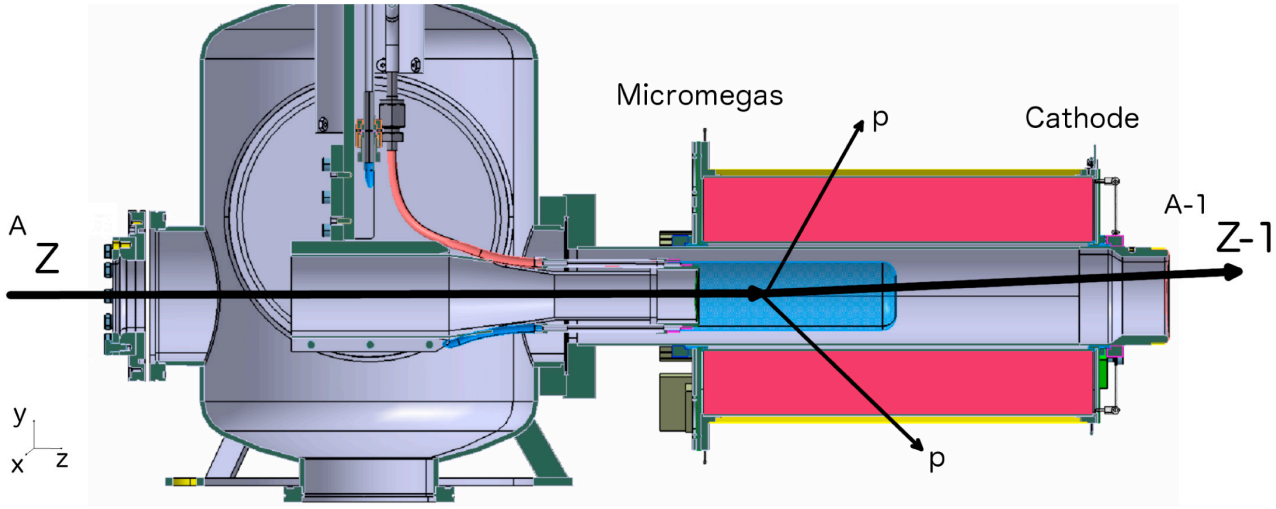

Figure 2.7. Schematic of the MINOS liquid hydrogen target, its associated cryostat, and the time projection chamber system. Note that a 150 mm long target cell is shown, whereas this experiment used a 100 mm long target cell. Figure from [5].

0.75 mm to decrease the potential uniformly towards the anode plane within minimal distortions due to edge effects [2].

The MINOS TPC uses Micro-MEsh GAseous Structure detector (Micromegas) technology, developed by CEA-Saclay [93]. A Micromegas consists of a biased mesh suspended above a segmented detection plane of "pads". The mesh divides the TPC volume into two regions: a drift region, and an amplification region. In the drift region, which is the majority of the TPC volume, electrons liberated by an ion traversing the gas drift in the electric field towards the mesh. When the electrons hit the mesh, they create an avalanche of electrons in the amplification region which are collected on the pads. The gap between the mesh and the pads is very small (128 μm) and the field gradient in this amplification region is very high (40-70 kV/cm), which allows short signal rise times on the pads and thus high event rates to be sustained, up to a few kHz. A summary of the MINOS TPC electric characteristics is shown in Table 2.2 [4].

Table 2.2. Summary of MINOS electrical and timing settings for the ^{110}Zr setting

Cathode	-6000 V
Mesh	-480 V
Threshold	25 V
Time Bins	30 ns
Shaping Time	333 ns

The 6 L TPC volume is filled with Ar(82%)-isobutane(3%)-CF_4(15%) gas mixture, optimized for maximal electron transport and Micromegas gain with minimal sparking. As gas impurities can impact the drift-velocity by attracting and capturing electrons, water and oxygen levels in the gas are monitored continually throughout the experiment, and the TPC is flushed if impurity levels become too high. Average impurities for this setting were $\sim$ 100 ppm of oxygen and $\sim$100-1000 ppm of water.

The MINOS target system was developed by the Accelerators, Magnetism and Cryogenics Lab of CEA-Saclay. It consists of a cold head to liquify the hydrogen located in the experimental area, and

[2] A more detailed discussion of these effects is presented in Chapter 8.

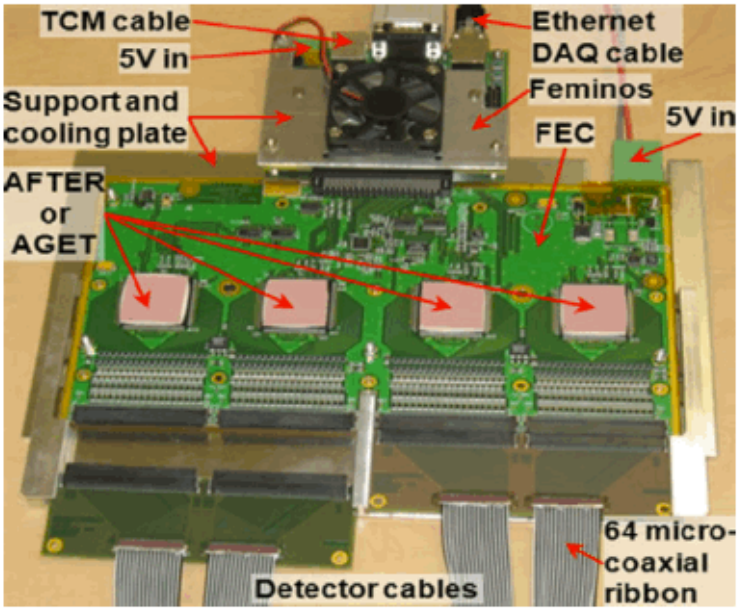

Figure 2.8. A FEC+Feminos for TPC signal processing. Figure from [4].

an external control/command unit located in the data analysis room with the room-temperature tank of hydrogen gas. This division allows remote monitoring and filling of the target, and ensures safe hydrogen transfer in the experimental area. The target cell itself is 10 cm long (though a 15 cm long target may also be used) and is made of Mylar ($C_{10}H_8O_4$) films sealed to a stainless-steel holder. The entrance and exit windows are 110 and 150 μm thick Mylar respectively, and the latter becomes concave deformed when the target is filled. This flexing adds approximately 2.0(4) mm of additional length which needs to be considered later when calculating energy loss in the target.

MINOS utilizes custom electronics developed at CEA-Saclay and based on the AGET chips developed by the GET collaboration[3]. These chips were chosen as a cost-effective, reliable solution to handle the 4608 channels of TPC readout with an event rate that can reach a few kHz. AGET chips feature a discriminator on each channel and can thus selectively digitize only the channels with a signal above threshold, dramatically reducing readout times compared to traditional chips. Each chip contains 64 channels, and four AGET chips are mounted on each front end card (FEC). Each FEC is in turn controlled by a Feminos, a custom board that performs basic data readout and communicates with the so-called "Trigger Clock Module" (TCM) for synchronization to a common clock and trigger distribution. Due to space constraints, the entirety of the TPC signal processing system is located outside the DALI2 structure and signals are relayed from the Micromegas via ribbon cables. An example of a FEC and Feminos is shown in Fig 2.8. Simulations of MINOS performance for detecting protons coming from knockout reactions show that the system has a 92(1)% efficiency for detecting at least one proton from (p,2p) reactions, and a reaction vertex resolution (see Chapter 3) of less than 5 mm [5].

While the details of the development of the MINOS system are described extensively in the thesis of Clémentine Santamaria [94], a few firmware improvements were implemented for this experiment and used in subsequent experiments. The first improvement resulted from the problem that sometimes occurred during the experiment wherein the timestamp of one Feminos would become offset with

[3]GET (acronym for General Electronics for TPCs) is a joint project between CEA-IRFU, CENBG, GANIL (France) and NSCL (USA) laboratories.The project has been funded by the French funding agency ANR and the DOE (US).

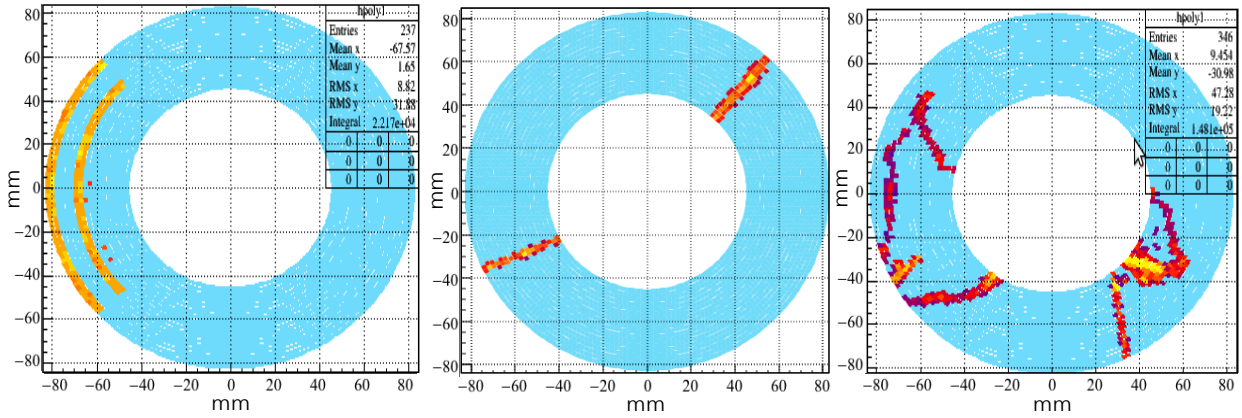

Figure 2.9. (left) a noisy AGET chip, no real events, (middle) a good (p,2p) event, (right) a busy event with too many tracks to be analysed. Figure from Denis Calvet.

respect to the other Feminos cards. This offset blocked the entire DAQ system, which requires the timestamps from events with the same trigger to match. The robustness of the MINOS DAQ was improved by allowing a timestamp mismatch of one or two units for the same event number. This introduces a potential error of ± 10 ns for the very small fraction of concerned events, without deteriorating the overall data quality [95].

Another firmware update was aimed at reducing the deadtime coming from noisy pads or busy events. Figure 2.9 compares a good event and two noisy events that cannot be exploited. These latter events, due to either electronic noise (b) or a physical event with many delta electrons (c) take a significant amount of time to readout because there are many pads touched, dramatically increasing the deadtime, while the event remains unusable. Thus is it preferable to be able to filter these sorts of events during the acquisition phase to prevent them from being written to disk. This is done by placing an upper limit on the number of hit channels on each AGET, and if this limit is breached the channel register on the chip is erased such that it appears the chip has no data and thus will not be readout. This threshold must be placed with care, as a chip could have one or more good tracks and be eliminated due to noise on a few channels. The hit channel limit can be set between 4 and 32 channels, a limit of 12 was found to be safe for rejecting unwanted background while not eliminating good tracks. This improvement reduced the average number of hit AGET channels by 50%, and correspondingly reduced the deadtime by 50%, since the deadtime is proportional to the number of channels to readout on the busiest chip [95]. Typical MINOS deadtime is $\sim 140\ \mu s$, corresponding to ∼5 channels hit on average for the busiest AGET chip of every event. A MINOS dead time histogram is shown in Figure 2.10.

2.5. Beamline Detectors

The other detectors used in analysis are the beamline detectors for PID reconstruction, i.e. the plastic scintillators, the MUSIC chambers, and the PPAC detectors interspersed among the focal planes. Here the setup and functioning of these detectors are briefly described.

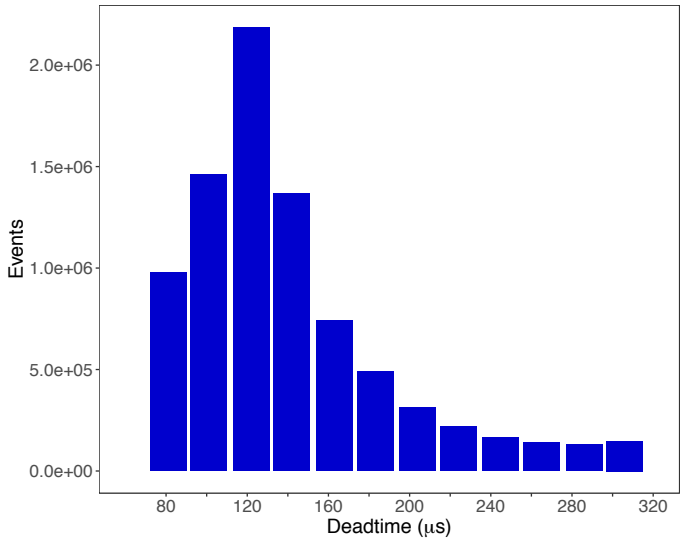

Figure 2.10. MINOS deadtime histogram from three runs of the Samurai 2015 experiment, as a function of the number of events in MINOS. Data courtesy of Denis Calvet.

2.5.1. PPAC detectors

Position monitoring of the beam at each focal plane is performed with sets of Parallel Plate Avalanche Counter (PPAC) detectors. PPACs consist of two parallel electrode planes, an anode and a cathode, with gas in between. When an ion passes through the planes, it ionizes the gas creating an electron avalanche that induces a charge on the electrodes. Due to the small space between the plates (few mm) and the high electron mobility, the rise time of the signals is very short (few ns), providing good timing properties. Furthermore, the cathode plane can be segmented to obtain position information. In this scheme, the cathode planes are attached to delay lines, and when a charge is induced on a segment of the plane the time difference between the signal at the ends of the delay line provides the timing information. Though the cathode planes are only segmented in one direction, pairs of anode-cathode planes may be coupled together to provide X-Y position information.

PPAC detectors are preferred to other sorts of beam-monitoring detectors because of the low-density of scattering centers that the beam has to pass through. These detectors have 1/10th the material of traditional position-sensitive gaseous detectors such as multi-wire proportional chambers or multi-wire drift chambers. This means better transmission through the beam line–essential for the most exotic beams. Figure 2.11 shows a schematic and photo of the double PPAC detectors used at RIKEN. These PPACs have aluminum deposited polyester windows of approximately 10 μm thick, a sensitive area of 240 mm x 150 mm, and a root-mean-squared position resolution of 0.25 mm [96].

The efficiency of the PPAC detectors is monitored continually during the experiment by comparing the number of events in each PPAC plane with the number of triggered events. Generally the efficiency for one PPAC (anode+cathode) is between 95-99%. To maximize efficiency, the double PPACs are combined in sets of 2 or 3 to yield a total PPAC efficiency at each focal plane of nearly 100%.

2.5.2. MUSIC detectors

Multi-sampling Ionization Chamber (MUSIC) detectors are used at F7 and F11 to provide Z identification of the ions. Each MUSIC detector consists of tilted alternating anode and cathode planes enclosed in a chamber filled with gas. A schematic MUSIC is shown in Figure 2.12. When an ion

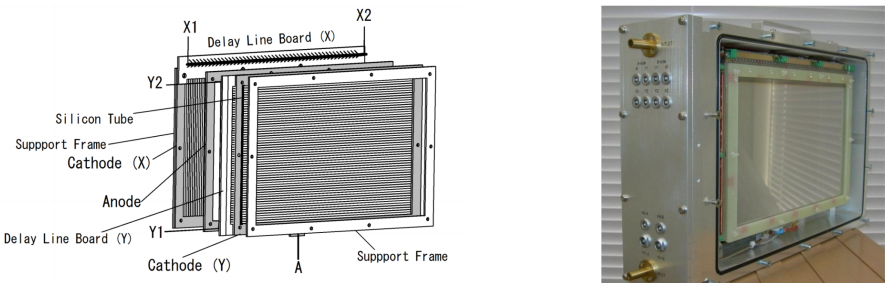

(a) (b)

Figure 2.11. (a) Schematic of double PPAC and (b) photo of double PPAC from RIKEN. Figures from [84].

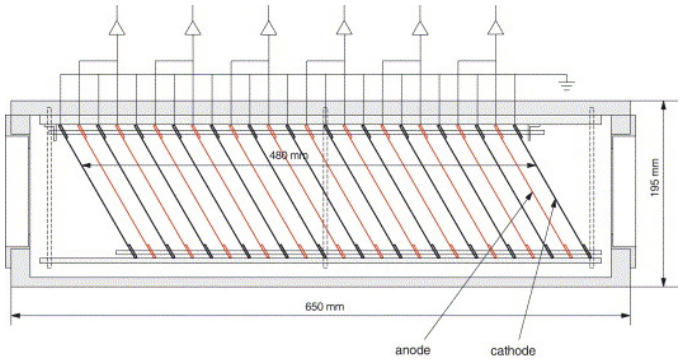

Figure 2.12. Schematic of a MUSIC detector with tilted electrode planes. Figure from [97].

from the beam passes through the chamber, it liberates electrons and positive ions that travel to the electrode planes. Because the electrode planes are tilted with respect to the beam axis, the electrons and ions move away from the particle trajectory, minimizing recombination. When these charges hit the planes they induce a drop in potential proportional to the number of incident charges, which is in turn proportional to the energy loss of the beam ions in the gas.

The MUSIC detectors used at RIKEN feature 12 anode and 13 cathode planes, spaced by 20mm and tilted by 30 degrees with respect to the beam axis. $Ar - CH_4$ gas is used which yields an electron signal rise time of 0.3 μs. The proton number Z of the ion traversing the gas can be obtained by combining the energy loss signal with a time of flight measurement, as seen in Equation 2.2. The MUSIC detectors have a Z resolution of 0.2-0.3 for ^{40}Ar at 95 A·MeV. They can handle event rates up to 1 MHz, but beyond 300 kHz the efficiency starts to decrease greatly [97]. This is largely sufficient for our experiment where rates are generally less than 10 kHz.

Because the MUSIC detectors at F7 and F11 are integral to the PID and thus the event selection, we cannot determine the absolute efficiency of each MUSIC. However we can determine the relative efficiency of each electrode plane, to determine if any one plane is malfunctioning, which would affect the Z identification. This relative efficiency may be obtained by dividing the total number of counts in the ADC associated with each plane with the total number of triggered events at the focal plane. For the ^{110}Zr setting, we found that all planes were functioning with better than 99% relative efficiency.

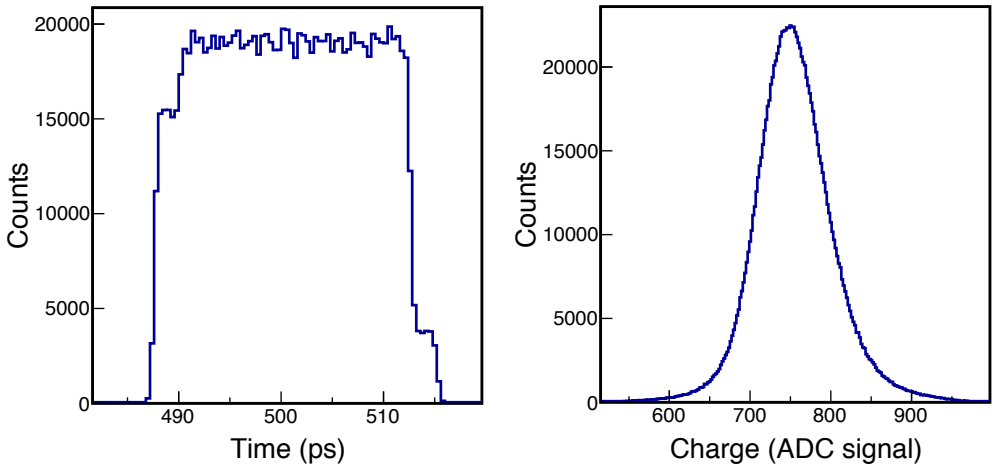

Figure 2.13. Timing and raw charge signal (ADC signal) from F7 plastic detector from run 8 of the ^{110}Zr setting.

2.5.3. Plastic detectors

The time-of-flight (TOF) measurements at F3, F7, F8, F11 are performed with Elgen EJ-212 and EJ-230 plastic scintillator detectors. These detectors consist of a 0.2 mm plastic material that emits light when hit by an ion. This light is collected on each end of the scintillator by a Hammamatsu H1949-50MOD or H2431-51MOD photo-multiplier tubes, which provides TOF resolution on the order of 40 ps [81]. An example timing signal and charge signal from the F7 plastic is shown in Figure 2.13.

Because these plastic scintillators are integral to the event trigger, an absolute efficiency measurement cannot be obtained from our data. We assume that the plastic detectors have 100% efficiency and compare known physical plastic signals with raw plastic signals to determine any detectors that are particularly noisy. In this case a physical signal is defined as one where there is a coincidence with F11, and we can compare the raw charge in the plastic signal gated on the F11 coincidence with the raw charge in the plastic. With this method we indeed find that all the plastic detectors are 99.99 percent efficient.

2.6. DAQ: Trigger and Dead time

For this setup, the RIBF data acquisition system (DAQ)–consisting of the beamline detectors previously described and DALI2–coordinates the event triggers and timestamps while the MINOS DAQ is a slave. This means that a signal in MINOS cannot serve as a trigger to start data acquisition, but if the DAQ is triggered, then MINOS takes data. When the DAQ is triggered, all detectors (RIBF+DALI2+MINOS) operate in common-dead time mode, which means that all individual DAQs wait until the last detector has finished its readout before accepting new triggers. Typically the beamline detectors (due to old CAMAC crates) have the longest deadtime, between 100 and 200 μs.

The trigger logic is coordinated by the General Trigger Operator (GTO) module and the Coincidence Register Module. The GTO takes the trigger signals from the various acquisition systems and performs the coincidence to trigger the DAQ. It also awaits the End of Busy signals from each detector system to signal the end of the acquisition/dead time. A logic diagram for the GTO module is shown in Figure 2.14. For physics runs, the DAQ can be triggered by GTO channel 0, corresponding to the downscaled beam trigger from the plastic detector at focal plane F7 (DSF7), GTO channel

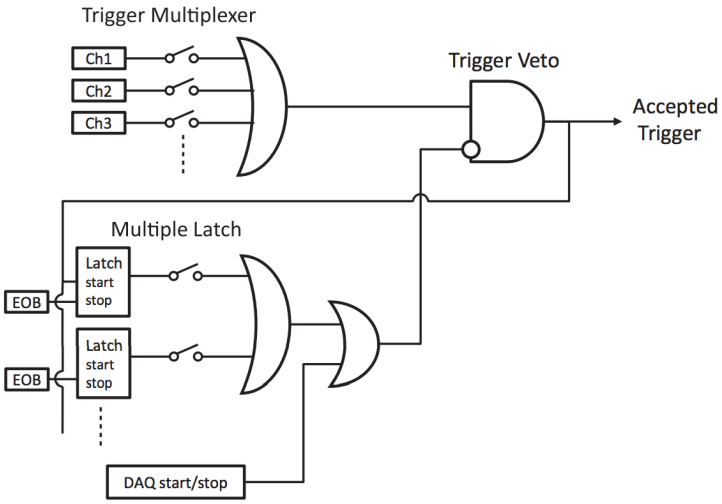

Figure 2.14. Logic diagram of GTO module. Figure from [98].

1, a coincidence between the plastic detectors at F7 and F11, or GTO channel 2, a coincidence among plastic detectors at F7 and F11, and DALI. DSF7 allows monitoring of the beam during the experiment, and for the ^{110}Zr setting the downscale factor was 20. F7 X F11 X DALI selects events most likely to give gamma rays of interest. The total coincidence window is $\sim$ 200 ns. For transmission runs, only GTO channel 0, DSF7, is used to trigger the DAQ and the downscale factor is set to 1 to allow monitoring of the direct beam through the beamline.

The GTO then sends the coincidence information to the Coincidence Register Module that assigns a “trigger bit" value to the event, which is recorded in the data to identify the different types of triggered events during analysis. The trigger bit values assigned by the Coincidence Module are shown in Table 2.3, and example trigger bit spectra are shown in Figure 2.15 for a physics run and the transmission run. For the physics run, events correspond to combinations of the two triggers: DSF7 (trigger bit=1) and F7 X F11 X DALI (trigger bit=4). The most counts are found in trigger bit 6, which corresponds to the F7 X F11 X DALI + F7 X F11 trigger (trigger bit 4+2=6). Due to the downscale factor, fewer events are found in combination with DSF7 (trigger bit 1), DSF7 + F7 X F11 (trigger bit 1+2=3), and DSF7 + F7 X F11 + F7 X F11 X DALI (trigger bit 1+2+4=7). Considering the ratio between the number of counts in trigger bits 6 and 7 for the physics run, we see that it corresponds approximately to the downscale factor, 20. Conversely for the transmission run, since the downscale factor was set to 1 and only DSF7 triggered the DAQ, we see most of the counts in the DSF7 + F7 X F11 bin (trigger bit 1+2=3). This may be understood as most ions that traverse the beamline produce at least Bremsstrahlung in the target that triggers DALI, so with no downscale factor any beam particle triggers DALI2 as well. There was a problem during the experiment with some triggers from DALI not being correctly transmitted to the coincidence module, thus there are slightly fewer counts in the sum trigger bit 7 relative to 3, but this has no significant impact on the analysis presented here.

Trigger Bit	Detector Coincidence
1	Downscaled F7
2	F7∩F11
4	F7∩F11∩DALI

Table 2.3. Coincidence Register Module: Triggers and their associated Trigger Bits used during the experiment.

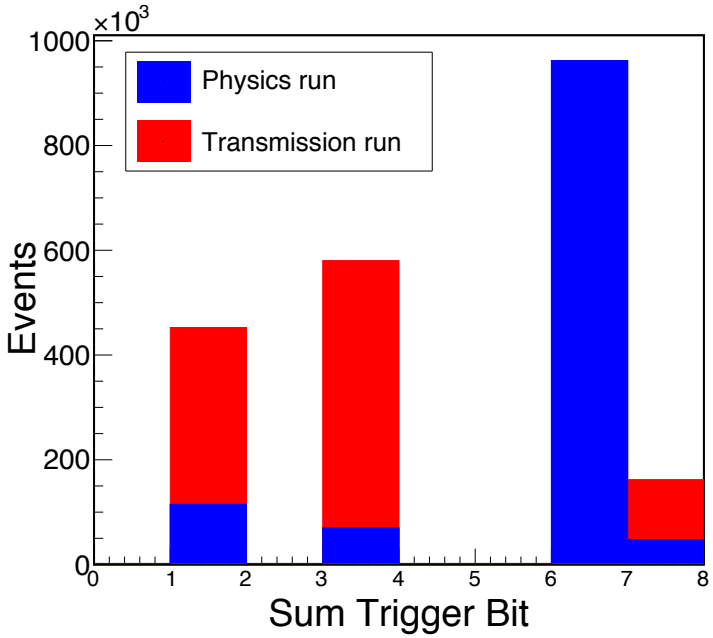

Figure 2.15. Trigger spectra for a physics and transmission run, where the histograms have been normalized to the same number of events. The sum trigger bit values are combinations of the trigger bits in Table 2.3.

In God we trust. All others must bring data.

W. Edwards Deming

3 Data Analysis

The data analysis proceeded through three main steps. First all detectors must be calibrated and major background events removed to obtain clean events. Then the doppler correction of the gamma rays is performed using the vertex from MINOS. Finally this doppler corrected gamma spectrum is analyzed by fitting with simulated detector response functions. This analysis featured a few non-standard tricks due to particularly low energy transitions, including subtraction of the Bremsstrahlung background and a refined fitting procedure to account for lifetime effects.

3.1. Cleaning and Calibrating

3.1.1. PID corrections

The general method for A/q and Z particle identification (PID) has already been explained in the previous chapter, however this explanation brushed over the fact that the $B\rho$ mapping of an individual ion with respect to the central trajectory requires knowledge of the ion optical transfer matrix through the spectrometer. In reality, the parameters of the optical matrix must be calibrated with respect to known nuclides [99, 81]. In BigRIPS, the ion optical corrections are done during the experiment by the accelerator team, while the physics team is responsible for ZeroDegree corrections.

Consider a simple transfer matrix between two focal planes, ignoring the angular degrees of freedom for simplicity. There is a linear relationship between the positions, as shown in Equation 3.1. The matrix elements can be obtained directly from the experimental data by plotting the two quantities as a function of each other, and fitting a line to the resulting distribution, as shown in [81]. Practically, as we are interested in the final PID spectrum, only non-linearities that affect A/q and Z reconstruction are important. Thus the beamline measurements can be plotted directly as a function of these quantities and the correction applied to the A/q and Z reconstruction. The BigRIPS PID spectrum is normally corrected up to 3rd order by the accelerator team. Calculated ZeroDegree matrix elements are used in online analysis, and then they are refined up to second order during offline analysis to correct for slight misalignments among beamline elements.

$$\begin{pmatrix} a & 0 \\ 0 & b \end{pmatrix} \begin{pmatrix} F3_x \\ F3_y \end{pmatrix} = \begin{pmatrix} F5_x \\ F5_y \end{pmatrix} \tag{3.1}$$

In practice, the ZeroDegree PID corrections are determined empirically by considering the beamline measurements as a function of A/q, shown in Figure 3.1 before and after correction. While A/q corrections have the largest impact on the PID spectrum, a velocity ($\beta = v/c$) dependence was also

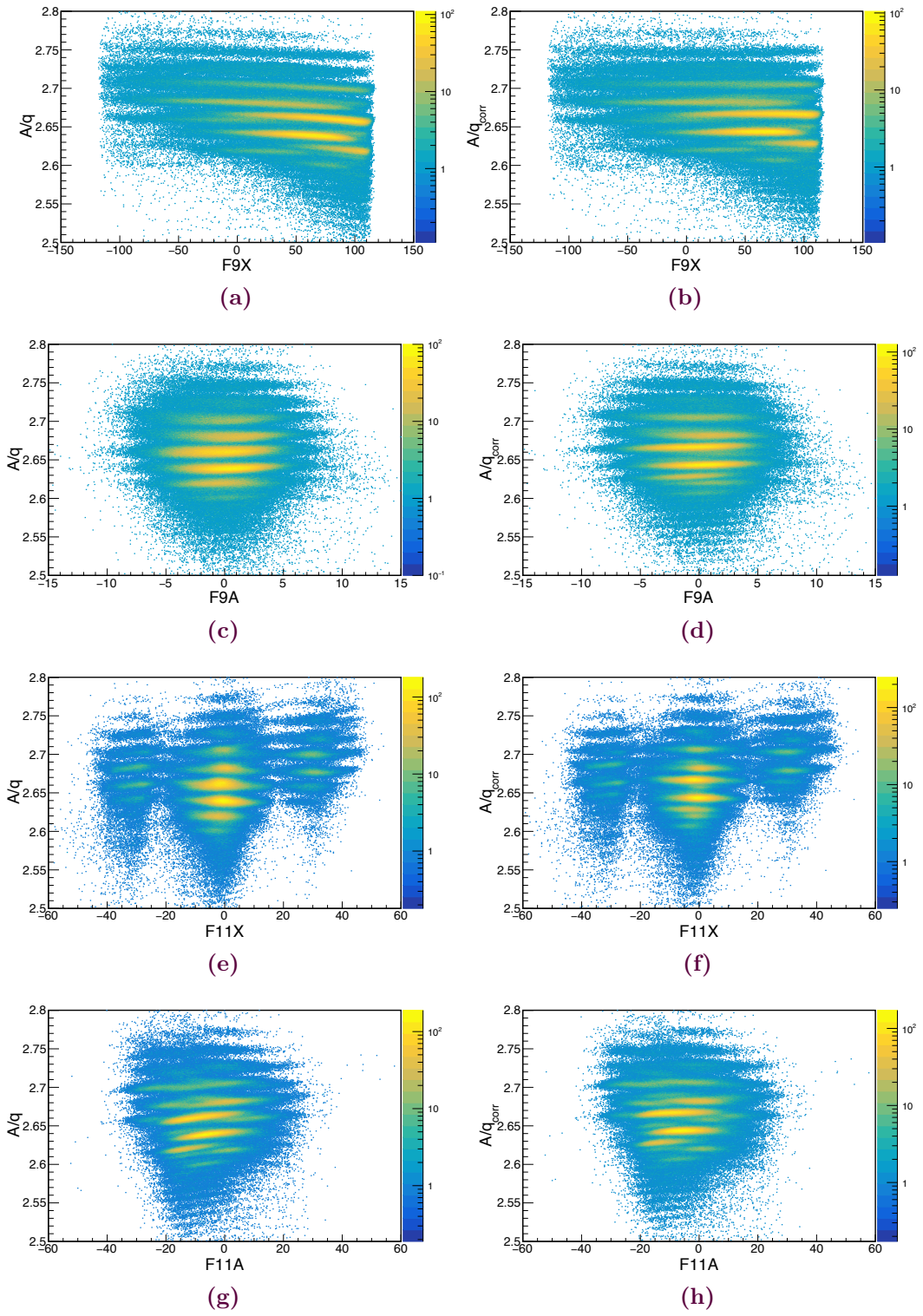

Figure 3.1. Beamline measurements of position (X) and angle (A) as a function of ZeroDegree A/q before (a,c,e,g) and after (b,d,f,h) ZeroDegree PID corrections.

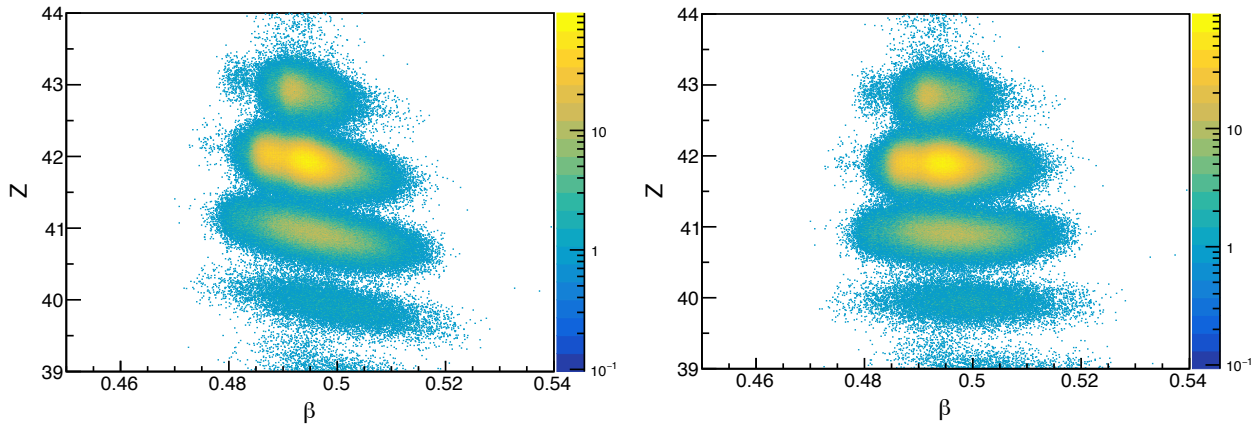

Figure 3.2. Velocity $\beta = v/c$ in ZeroDegree as a function of Z before (left) and after (right) correction.

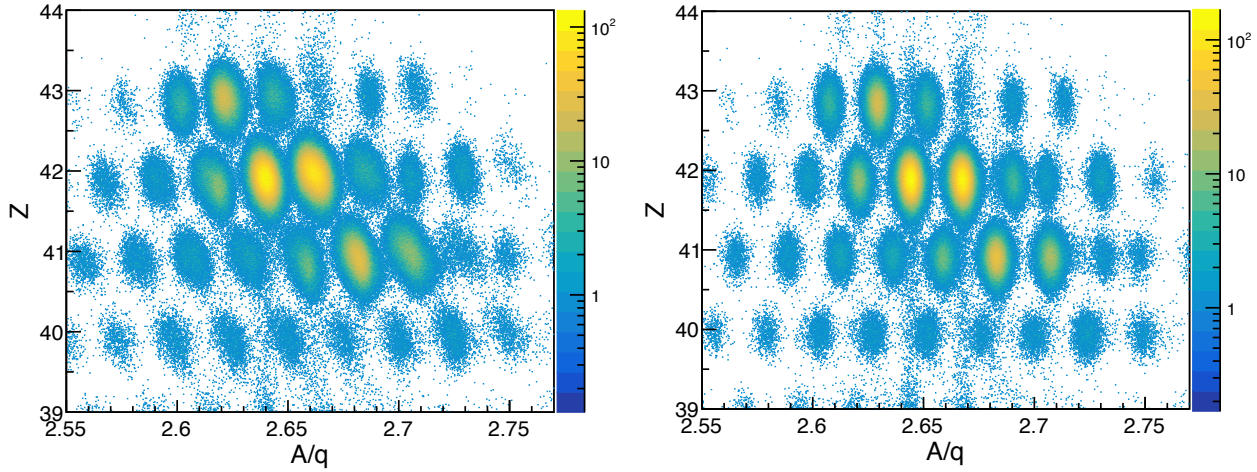

Figure 3.3. ZeroDegree PID plot before (left) and after (right) PID corrections.

found in the Z reconstruction and corrected, as shown in Figure 3.2. Note that due to $B\rho$ and Z dependence of the beam-line transport elements, simple PID corrections that improve resolution for a given (Z,A/q), may degrade resolution for other nuclei. Thus these corrections are specific for a given set of nuclei in the PID plot, and may need to be adapted if a broad range of nuclei are to be analyzed simultaneously. The PID corrections shown for the zirconium setting are however good enough to be used for identification of all reaction channels, and will be used later on for cross section analysis in Part II. The corrections applied to the ZeroDegree PID elements are shown in Appendix B. The ZeroDegree PID spectrum before and after A/q corrections are shown in Figure 3.3.

3.1.2. Cleaning Up Contamination

The focal plane detectors can also be used to clean up the PID spectrum, as detailed extensively in [81]. In this analysis, we applied these techniques to remove charge state contamination and noise in the plastic scintillators, the former being the principle source of contamination for the ^{110}Zr setting.

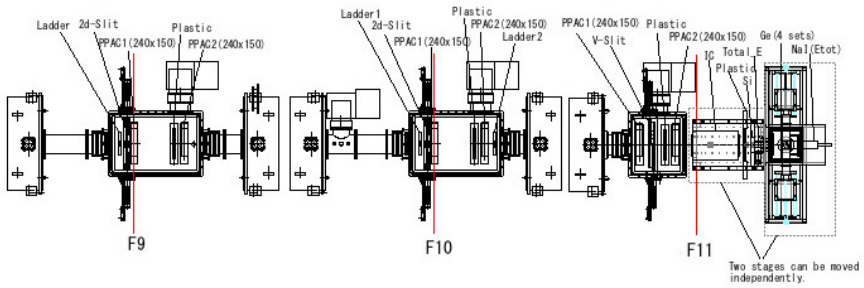

Figure 3.4. Schematic of ZeroDegree spectrometer and its elements. Figure from [80].

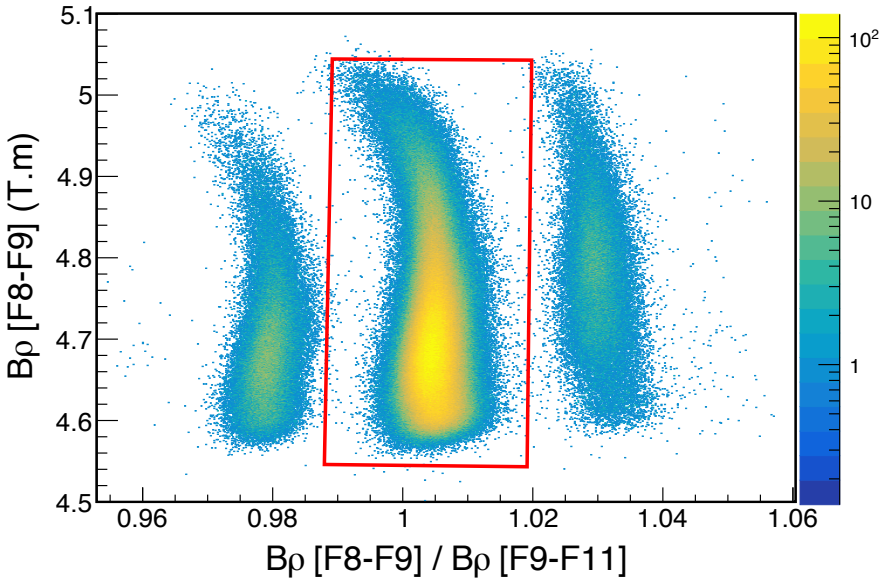

Figure 3.5. $B\rho$ between focals planes 8-9 as a function of the $B\rho$ ratio between focal planes 8-9 and 9-11. Events where no charge exchange occurred have a $\beta\rho[F8-9]/\beta\rho[F9-11]=1$. The cut used in the analysis to remove charge states is shown in red.

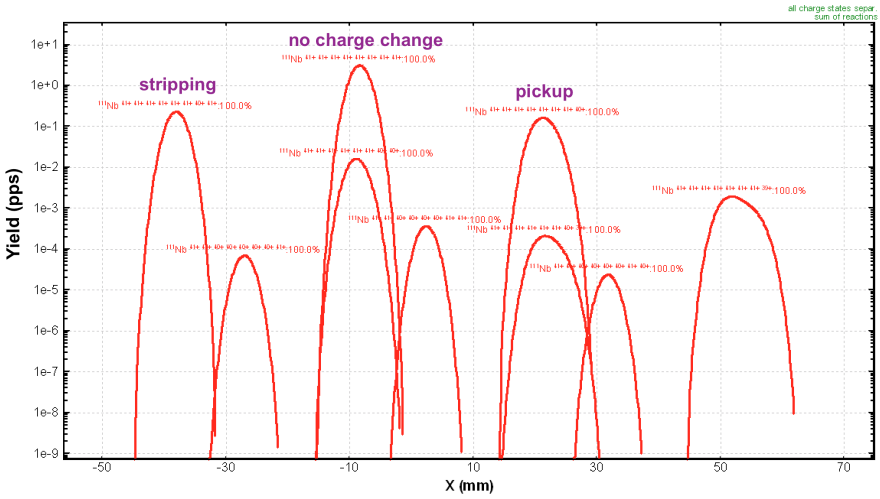

Figure 3.6. LISE++ simulation of charge states of ions at F11 window, after PPAC and plastic detectors.

As mentioned previously, the $B\rho - \Delta E - TOF$ method assumes that A/q is constant, and that the ion is fully stripped. However if an ion picks up an electron in the ZeroDegree detectors after the target, or picks up an electron in the target and then loses it again in the ZeroDegree detectors, the velocity β will not be calculated properly which will lead to incorrect A/q identification in the PID spectrum. An overview of the ZeroDegree spectrometer with its detectors and mechanical devices is shown in Figure 3.4. This effect can be immediately seen upon inspection of the uncorrected ZeroDegree PID spectrum in Figure 3.3, where a smearing is evidenced along the A/q axis. These events can be identified by comparing $B\rho$ between two focal plane intervals. By selecting the events where $B\rho$ is unchanged between focal plane segments, in this case where $B\rho[8-9]/B\rho[9-11] = 1$, charge state contamination can be removed as shown in Figure 3.5. The ratio of magnetic rigidities is inversely proportional to the charge state ratio, ie $B\rho[F8-F9]/B\rho[F9-F11] \sim Q[F9-F11]/Q[F8-F9]$. The spots to the right and left of 1 correspond thus to electron pick-up and stripping, respectively, and we see that they indeed correspond to approximately $40/41 = 0.975$ and $41/40 = 1.025$. Charge state cleaning removed about 20% of entire statistics for the ^{110}Zr run. LISE++ simulations [77] confirm that at F11 there are about a factor of 10 fewer pickup and stripping events each than the fully-stripped events, as shown in Figure 3.6, confirming the ratio seen in the data.

Additional cleaning of background events can be obtained by exploiting the physics of the plastic TOF detectors [81]. These detectors have PMTs at each end of the scintillator bars, and the position of the incident nucleus along the scintillator can be obtained by comparing the charge signals between the right and left PMTs. The charge signals obey the relation shown in Eq 3.2, where q_l, q_r are the charge signals from the left and right PMTs respectively, q_0 is the signal of the original scintillation, x is the location of the charge deposit, L is the length of the scintillator bar, and λ is the attenuation length of charge in the cylinder.

$$q_l = q_0 exp(-\frac{L+x}{\lambda}), q_r = q_0 exp(-\frac{L-x}{\lambda}) \tag{3.2}$$

Solving Equation 3.2 for x yields Equation 3.3. The timing information from the PMTs can also be exploited to obtain Equation 3.4, where V is the propagation speed of light in the scintillator, and t_r and t_l are the timing signals in the right and left PMTs respectively. Eqs 3.3 and 3.4 can be combined to obtain Eq. 3.5 which can then be plotted for each plastic detector. Physical events should lie on

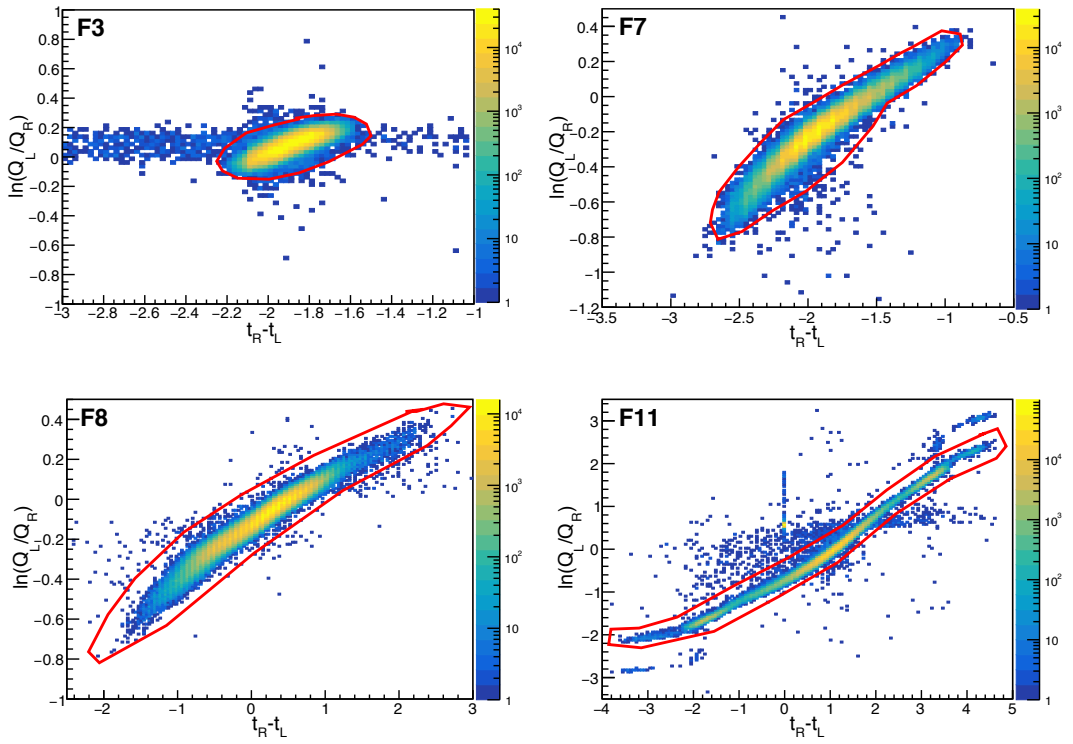

Figure 3.7. Cleaning cuts applied to F3, F7, F8, and F11 plastic detectors. The events visible at $t_R - t_L = 0$ in the F11 plot are events outside ZeroDegree momentum acceptance.

the line Y=X, and background events can be omitted by cutting on this relationship, as shown in Figure 3.7, for the F3, F7, F8, and F11 plastic detectors.

$$x = -\frac{\lambda}{2} ln\left(\frac{q_l}{q_r}\right) \tag{3.3}$$

$$x = -\frac{V}{2}(t_r - tl) \tag{3.4}$$

$$\lambda ln\left(\frac{q_l}{q_r}\right) = V(t_r - t_l) \tag{3.5}$$

3.1.3. DALI2 Calibration

DALI2 was calibrated before and after each physics setting in the SEASTAR campaign with standard gamma-ray sources covering the energy range of interest. The sources were taped onto the downstream end of the TPC, as shown in Figure 3.8. In case of a long run, DALI2 is calibrated approximately every 2 days, to be able to trace any ADC drifts. The detector responses are also sensitive to the fields of the quadrupoles, located before and after the array, thus any change in $B\rho$ settings of the beamline necessitates recalibration. For this experiment DALI2 was calibrated before and after the experiment.

The ^{110}Zr experiment used the calibration sources shown in Table 3.1. The ^{152}Eu and ^{133}Ba sources are not part of the standard DALI2 calibration, but after online analysis indicated that the principal

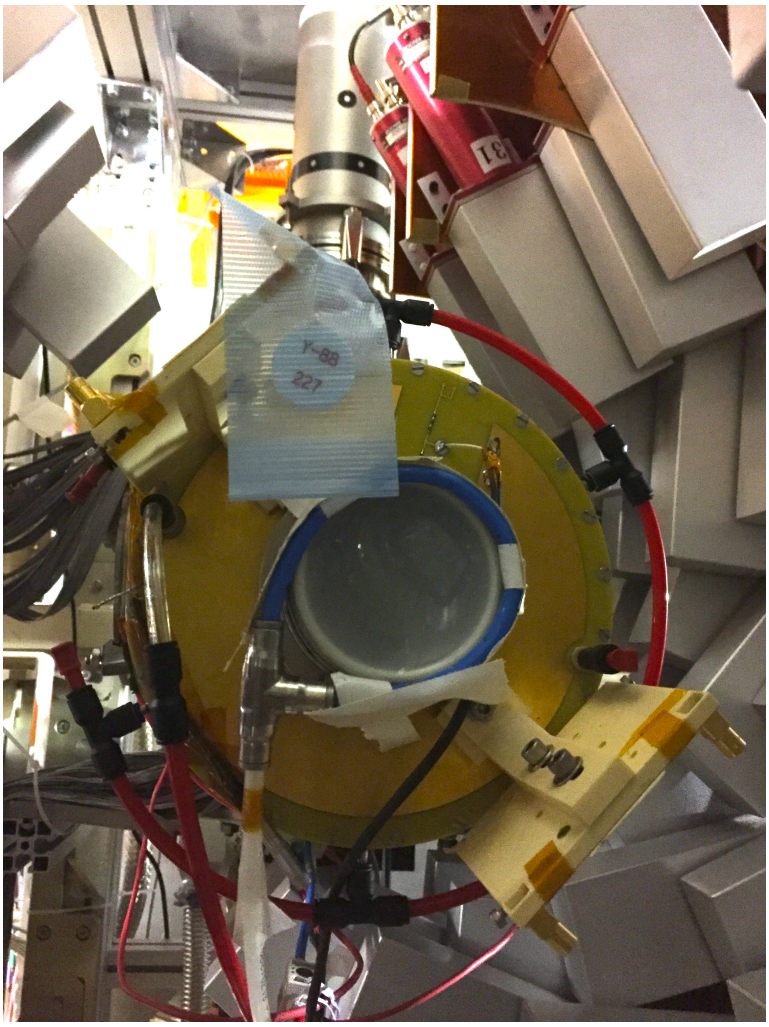

Figure 3.8. Calibration source taped onto the downstream end of the TPC. Note that wrapped around the end of the target is a flexible tube with holes that delivers compressed air to avoid condensation on the exit window. Photo courtesy of Sidong Chen.

Table 3.1. Gamma sources used for ^{110}Zr experiment

Source	Photopeak Energy (keV)
^{152}Eu	121.77
^{137}Cs	661.66
^{133}Ba	302.85,356.01
^{60}Co	1173.24,1332.50

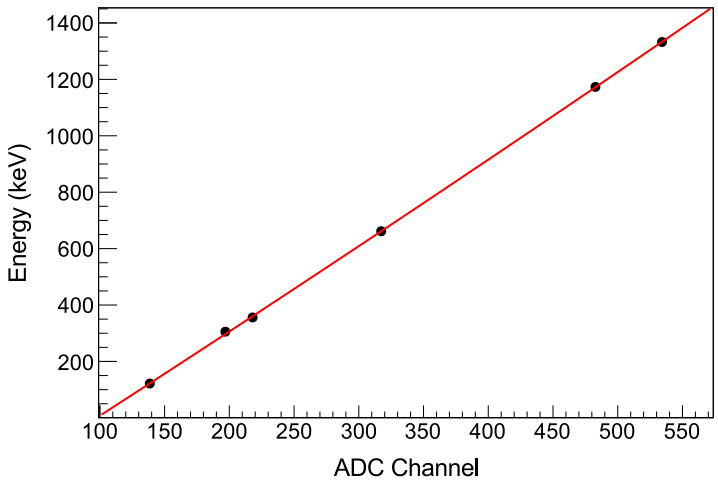

Figure 3.9. ADC channel as a function of known energy for the calibration peaks used in this analysis. Data shown is for DALI2 detector 185.

peak of interest was most likely at low energy, these sources were used to calibrate DALI2 at the end of the experiment. For this reason, our ability to track low-energy ADC drift between the beginning and the end of the setting is limited to energies above 600 keV.

To calibrate DALI2, the calibration photo-peaks of interest in the raw ADC spectrum are fit with a gaussian+exponential. The centroids of the gaussians with their corresponding sigmas are then plotted as a function of the known peak energies and fit to obtain the peak energy as a function of ADC channel for each crystal, as shown in Figure 3.9. Normally the mapping from ADC channel to energy is taken to be linear for these types of measurements with DALI2, but since the transitions of interest here are at low energy where NaI(Tl) detectors start to manifest non-linearities (see for example, Fig 8.8 of [100], a second-order calibration was used. Note that the ^{152}Eu peak was either not visible or not resolvable for 30% of the DALI2 detectors. Additionally, because the ^{133}Ba peaks lie close in energy, for some crystals these peaks were poorly resolved. Thus the number of source transitions used to calibrate each crystal varied from 3 to 6, depending on each individual crystal's response and resolution at low energy.

The difference between known and reconstructed energies of the source peaks for each detector is shown in Figure 3.10. All the residuals are well below 10 keV. Note that detectors 4 and 167 are completely dead and are not used. When using all the crystals together to reconstruct the photopeaks of the sources used for calibration, a calibration error of 1 keV is obtained, consistent with benchmarked DALI2 performance [92]. The DALI2 spectra for ^{137}Cs is shown in Figure 3.11.

Due to the fact that additional low-energy calibration sources were used at the end of the experiment that were not used at the beginning of the experiment, it was impossible to track individual detector

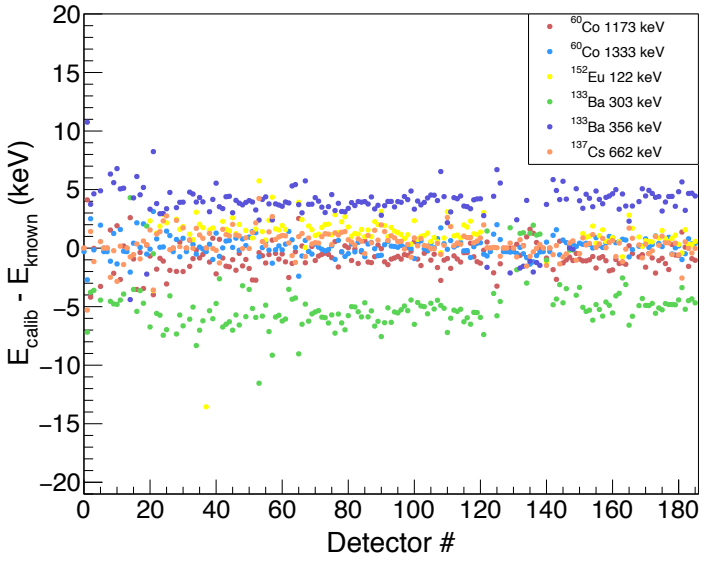

Figure 3.10. Residuals (known energy-calibrated energy) for the six calibration peaks and all 186 DALI2 detectors.

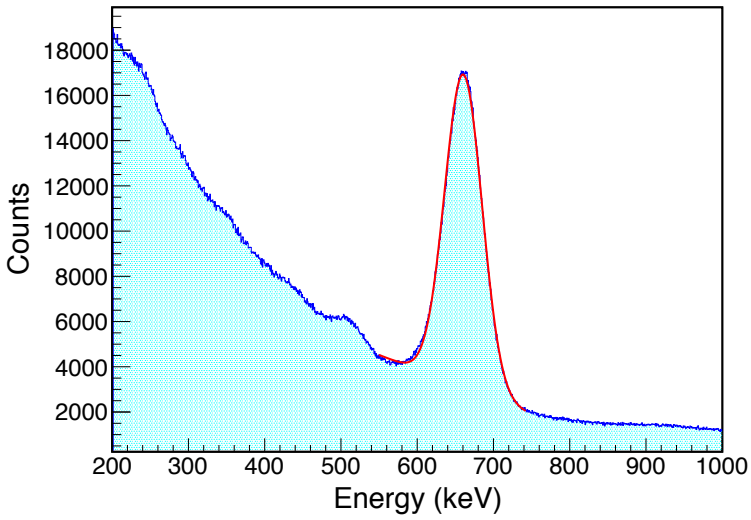

Figure 3.11. Gamma spectra with gaussian+linear fit of the photopeak for the ^{137}Cs calibration source. The agreement with known energy is 1.1 keV.

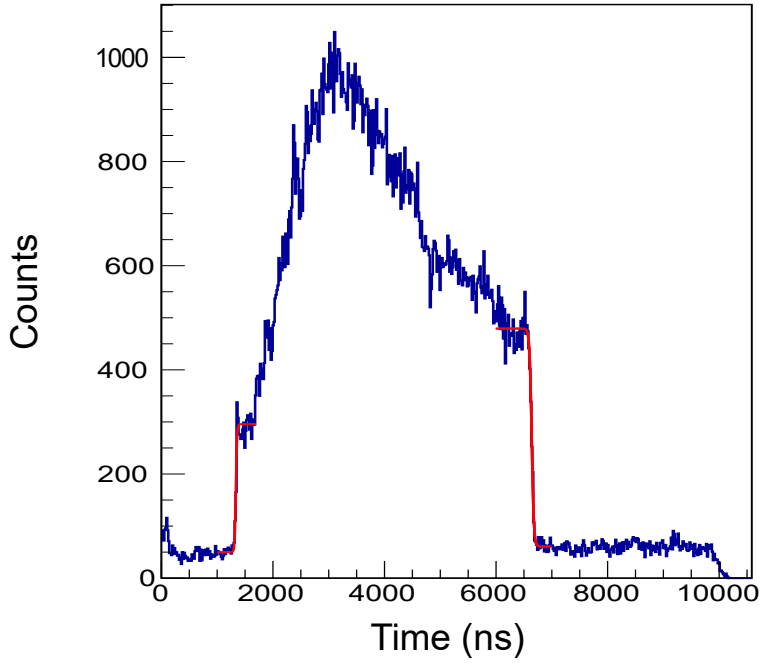

Figure 3.12. MINOS time spectrum for a single physics run. The red curves indicate the fits of beginning and end of the spectrum that are used to determine the drift velocity.

drift over the entire relevant energy range during the course of the experiment. However the ^{60}Co source was used before and after the experiment and can be used to benchmark this quantity. By applying the calibration from the source measurements performed after the experiment, to the ^{60}Co data from before the experiment, it was determined that seven detectors exhibited a drift of larger than 15 keV. However since the principal limitation in this measurement was statistics, these crystals were not removed from the analysis.

3.1.4. MINOS Calibration

In the MINOS system, the principal quantity to be calibrated is the drift velocity (v_{drift}) of the electrons in the gas, needed to set the metric for the proton track lengths. The drift velocity is highly sensitive to water and oxygen impurities in the gas, as these molecules can attract and capture electrons, respectively, slowing the electron transport through the gas to the Micromegas plane. Due to this potential variability, the drift velocity is calculated for each run, as described below.

The drift velocity can be obtained from the Micromegas time spectrum, as shown in Figure 3.12. The peak at small times (t_{start}) corresponds to electrons that are ionized right next to the Micromegas mesh. This signal does not depend on gas impurities, therefore it remains a constant for given TDC settings. The tail end of the spectrum (t_{stop}) corresponds to the time it takes for electrons ionized near the cathode to traverse the entire TPC before arriving at the Micromegas mesh. This time is obviously dependent on the gas conditions, and is the variable quantity in the run-by-run v_{drift} calculation. t_{start} and t_{stop} are obtained by fitting Fermi functions to the left and right-hand sides of the time spectrum, respectively. The Fermi functions take the form shown in Equation 3.6, where $\pm$t is the electron drift time and the variables A,B,C, and D are fit to the distribution. B corresponds to t_{start} for $-t$ and t_{stop} for $+t$.

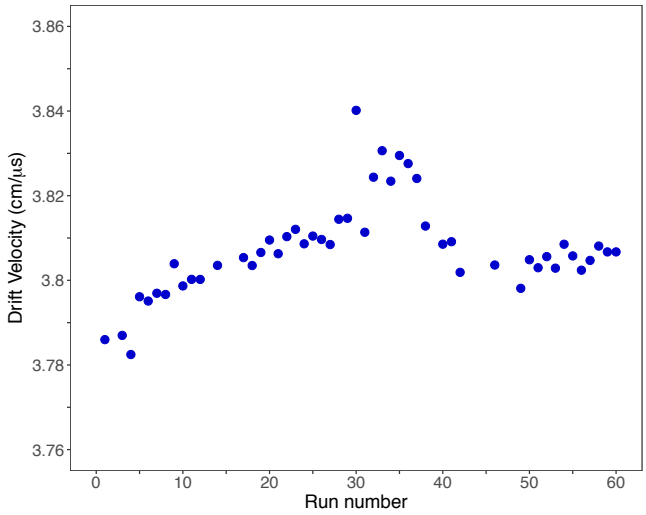

Figure 3.13. Electron drift velocity in the TPC (v_{drift}) during the 60 runs of the ^{110}Zr setting.

$$counts = \frac{A}{\left(exp(\frac{\pm t - B}{C} + 1)\right)} + D \tag{3.6}$$

With t_{start} and t_{stop}, v_{drift} can be trivially obtained by dividing the length of the TPC (L_{TPC}=300mm) by the time it takes for the electrons to traverse this distance, as shown in Equation 3.7. This drift velocity is monitored during the experiment as an indication of the conditions in the TPC. During the analysis it is also used for track reconstruction to set the vertex position along the z-axis. Figure 3.13 shows the evolution of the drift velocity during the ^{110}Zr experiment. The evolution is relatively flat and there were no major problems with impurities in the TPC gas.

$$v_{drift} = \frac{L_{TPC}}{(t_{stop} - t_{start})} \tag{3.7}$$

The v_{drift} calibration may be checked by looking at the distribution of reaction vertices reconstructed from the physics data, as shown in Figure 3.14. These vertices should cover the entire 100 mm length of the MINOS target. If we fit Fermi functions, as in Equation 3.6, to the ends of this distribution, the target length can be obtained as the difference between these two endpoints. Performing this calculation, here we recover a target length of 98.5(5)mm, which is a bit too short compared to the known target length of 102(2)mm. However all independent analyses from this campaign found target lengths between 98-99 mm, thus it appears to be a systematic anomaly whose origin lies likely in field inhomogeneities in the TPC, but which is not expected to have a significant impact on this analysis.

The rotational orientation of MINOS is also calibrated offline to correct for imperfect alignment. The TPC is free to rotate around the beam pipe, therefore the x and y axes may not coincide with those of the beamline detectors. This alignment issue may be seen in the data by looking at the reconstructed reaction vertices in the x and y planes as determined from MINOS and using the PPAC detectors. If the x and y components of the TPC are aligned correctly, the vertex coordinates reconstructed with MINOS should agree with those reconstructed using the beamline detectors and a linear correspondence should be visible between the two. However the standard MINOS reconstruction, shown for example for the x coordinate in Figure 3.15(a) does not show a linear mapping between the MINOS and beamline vertex coordinates. This misalignment could adversely affect the Doppler correction for events where the vertex does not lie directly on the beam axis. This is corrected by

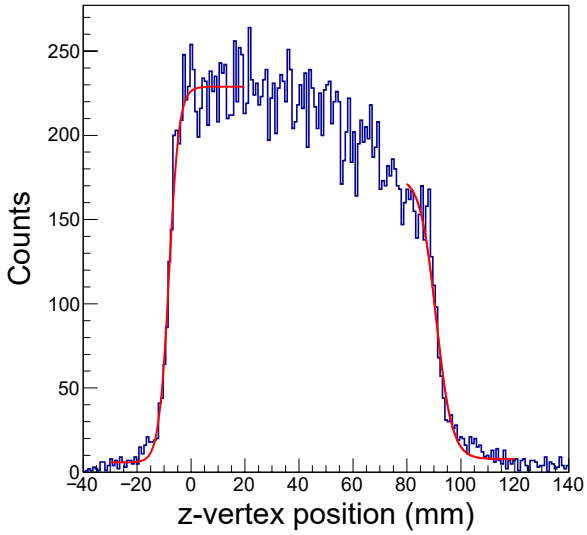

Figure 3.14. Reconstruction of reaction vertices along the z-axis of the MINOS target. The target length is extracted by fitting the left and right hand sides of this distribution with Fermi functions.

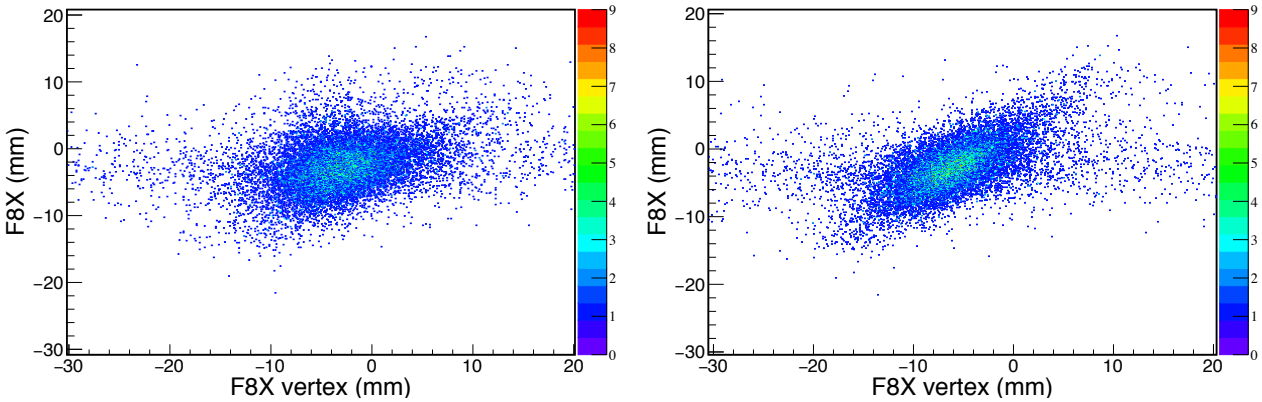

(a) **(b)**

Figure 3.15. F8X position as reconstructed with two proton tracks in MINOS (F8 vertex) versus as reconstructed with one track and the beam axis from the F8 PPAC (F8X) (a) with a bad rotation angle and (b) after calibrating the MINOS rotation angle.

applying a MINOS rotation angle in the analysis code. The optimum rotation angle was found to be $-30(330)°$, the rotated x reconstruction is shown in Figure 3.15(b). Even after rotation it is clear that the distribution is not centered at zero, and linear x and y offsets of -3.5 mm and 2 mm, respectively, were also applied to the TPC pad plane coordinates.

3.2. MINOS Vertex Reconstruction

The MINOS track reconstruction algorithm has been developed and extensively detailed in the thesis of Clémentine Santamaria (CEA-Saclay, 2015), therefore only the highlights relevant for understanding this data analysis will be mentioned here.

The MINOS data acquisition system collects time and charge signals from the individual Micromegas

pads, as well as the pad-position location. As a first step, only the pad-position information is retained, and an algorithm based on a Hough transform selects the events where the hit pads form a straight line in the (x,y) plane, with a minimum of 10 pads hit. Then, the timing information is recovered for these tracks, such that a 3D reconstruction may be made with the track projection along the z-axis. An additional Hough filter, identical to that used to select straight lines in (x,y) is applied to make sure that these tracks are straight lines in (x,y,z) dimensions. The filtered tracks are then fit in three dimensions by performing a minimization of each of the (x,y,z) points, weighted by their charge. This fit allows each track to be parametrized according to four parameters in the 3D space, as shown in Equation 3.8, where l_a is the line describing a single track, and p_{0-3} are fit parameters.

$$l_a : \begin{cases} x = p_0 + p_1 z \\ y = p_2 + p_3 z \end{cases} \tag{3.8}$$

For two reconstructed tracks in the TPC, the segment of minimal distance, or closest approach between the two lines is identified. The vertex position is taken as the midway point of this segment. If there is only one track in the TPC, the vertex is calculated between the track and the beamline axis (as measured from the PPAC detectors before and after the hydrogen target). This technique yields a proton track reconstruction efficiency of better than 95%, and a vertex resolution of 5 mm FWHM, as demonstrated in [101, 5].

3.3. Gamma Analysis

3.3.1. Doppler Correction

With the gamma-ray energy from DALI2 and the vertex position from MINOS, the gamma spectrum can be doppler corrected, according to Equation 3.9, where E_γ is the gamma-ray energy in the lab frame, β is the nucleus velocity at the reaction vertex ($\beta = v/c$), θ_γ is the gamma emission angle relative to the beam-axis, and $E_{doppler}$ is the doppler-corrected gamma-ray energy.

$$E_{doppler} = \frac{1 - \beta cos(\theta_\gamma)}{\sqrt{1-\beta^2}} E_\gamma \tag{3.9}$$

For each event, E_γ is determined by applying the DALI2 calibration to the ADC signal, θ_γ is calculated from the MINOS vertex position and the Geant4 simulated first interaction point for the DALI2 crystal where the gamma ray was detected, and β is calculated from a $B\rho$ measurement between F5 and F7 just before the target, and the reaction vertex position, assuming linear energy loss in the liquid hydrogen target.

Thus Doppler-corrected gamma-ray spectra can be constructed for the channels of interest, ^{113}Tc(p,2p)^{112}Mo, and ^{111}Nb(p,2p)^{110}Zr, as shown in Figure 3.20 by the solid gray lines. Note that there is a method to improve the Doppler correction by "adding-back" the energy lost to Compton scattering in a given radius. However due to the low-energy of the transitions of interest in this measurement, this technique was not used as photoelectric absorption is expected to dominate, as may be seen by comparing the photoabsorption and Compton cross sections at 200 MeV in Figure 3.16. The MINOS spectrum with and without addback is shown in Figure 3.17, and we see indeed that using addback provides no gain in the peak-to-background ratio for the transitions of interest.

3.3.2. Bremsstrahlung Subtraction

A quick examination of the Doppler-corrected ^{110}Zr gamma ray spectra of Figure 3.17 shows that the peaks of interest lie very close in energy to exponential low energy background attributed to

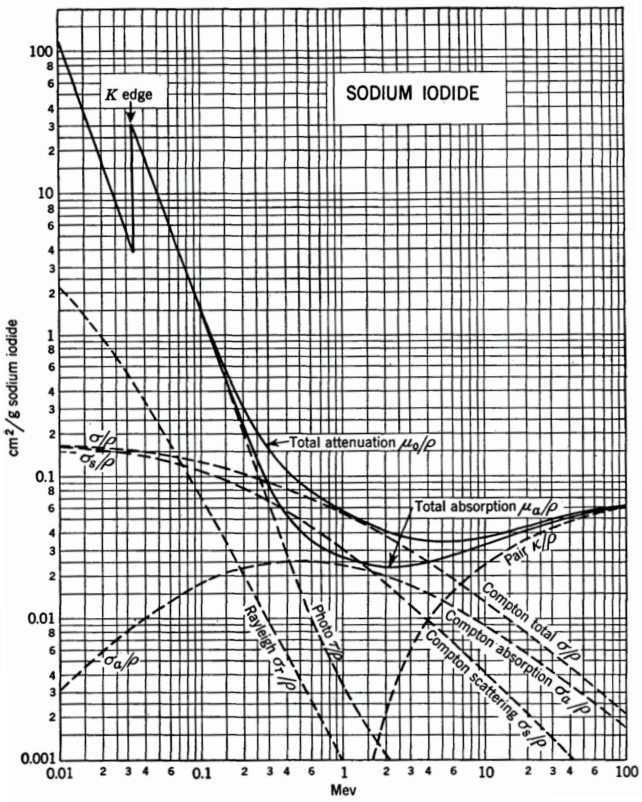

Figure 3.16. Energy dependence of the cross sections for the various gamma ray interaction processes in a NaI detector. Figure from [102].

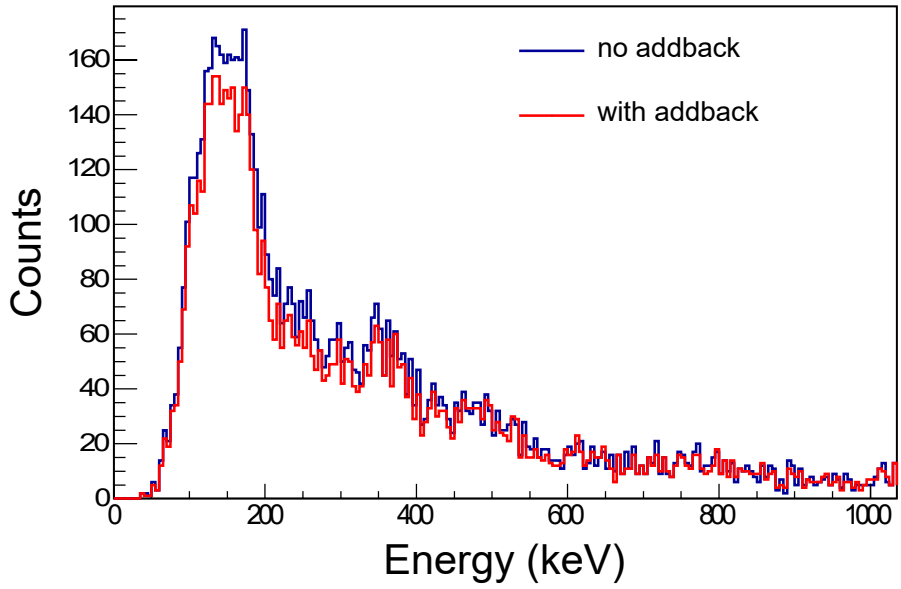

Figure 3.17. Doppler corrected gamma ray spectrum for ^{110}Zr without (blue) and with (red) addback in a 15 cm radius.

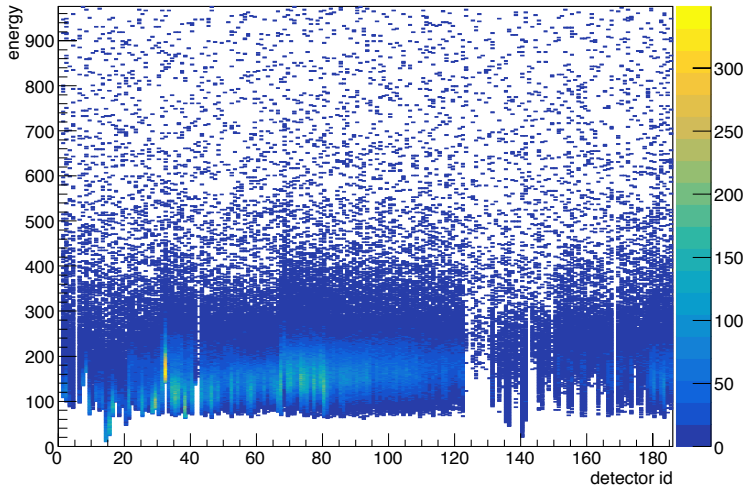

Figure 3.18. Doppler corrected gamma energy as a function of DALI2 detector ID. High id numbers correspond with forward angles, and low id numbers correspond with backward angles. Note that detectors 120 to 140 are shielded by detectors 110-120, so low energy gamma rays never reach them.

Bremsstrahlung events. This Bremsstrahlung background has two main components. The first, primary Bremsstrahlung, is when electrons in the hydrogen target are captured onto continuum states of the projectile nucleus [103]. This process has a cross section that scales as $Z_t Z_p^2$, where Z_t is the atomic number of the target material, and Z_p is the atomic number of the projectile. This component has an angular dependence in the lab frame, as the radiation is forward focused with the beam particles. The second, and principle contribution for high Z projectiles comes from secondary Bremsstrahlung. This is a two-step process wherein the relativistic projectile nucleus knocks out a target electron, and then this electron emits photons as it slows down in target. Since the electron may undergo multiple scattering events in the target, this component is isotropic in the lab frame. The cross section for secondary bremsstrahlung scales as $Z_t^2 Z_p^2$. The isotropic secondary Bremsstrahlung dominates, as may be seen in the un-Doppler corrected gamma spectrum for the ^{112}Mo(p,p)^{112}Mo channel, shown in Figure 3.18.

Fortunately, because of the event-by-event data tagging, this Bremsstrahlung background component can be isolated experimentally, and subtracted from our Doppler-corrected gamma spectrum. This component is isolated by considering only the direct beam channel, that is X(p,p)X, such that we are only seeing background events induced from the nucleus of interest passing through the target material. Certainly some inelastic excitations are expected in this channel, but they are negligible compared to the Bremsstrahlung component for these nuclei. This Bremsstrahlung spectrum is then normalized with a factor N according to the relative number of nuclei incident on the liquid hydrogen target in the X(p,p)X and Y(p,2p)X channels, calculated from the F7DS trigger, as shown in Equation 3.10. Then the normalized Bremsstrahlung spectrum is subtracted from the Y(p,2p)X gamma spectrum, as shown in Figure 3.20 for ^{112}Mo and ^{110}Zr. Upon subtraction, the main peaks in both spectra emerge cleanly. While the peak in ^{112}Mo could be seen without subtraction, the peak in ^{110}Z is completely hidden behind the Bremsstrahlung background and this subtraction method was necessary to analyse the spectrum. The peak in ^{110}Zr may however be seen at forward angles in the DALI2 spectrum (without MINOS, where all gamma rays are assumed to originate at the center of the target for doppler correction), as shown in Figure 3.19. The improved reconstruction of the peak

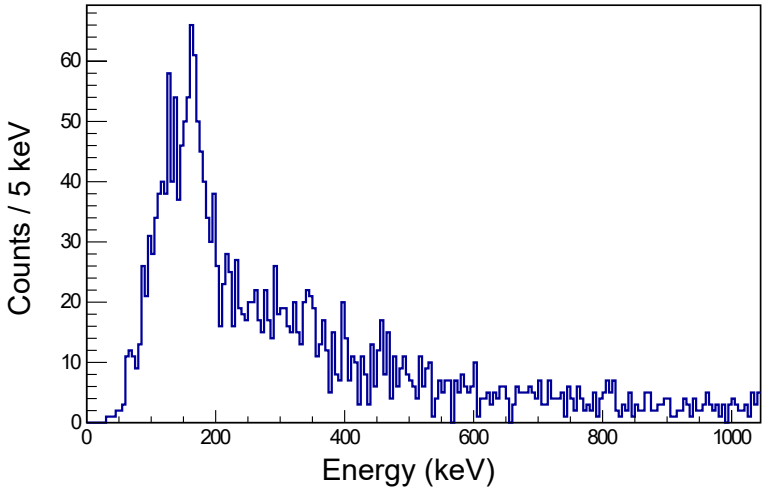

Figure 3.19. Forward angle DALI2 doppler-corrected γ-ray spectrum of ^{110}Zr.

without MINOS is attributed to the long lifetime of the transition, such that the gamma rays are emitted beyond the liquid hydrogen target.

$$N = \frac{F7DS_{p2p}}{F7DS_{pp}} \tag{3.10}$$

To verify that this subtraction does not create any artificial peaks, the method was tested on another nucleus from the same experimental campaign,^{86}Ge, where the principle peak lies at high energy and is well-separated from the Bremsstrahlung background. The resultant spectrum is shown in Figure 3.21, and displays a smooth behavior in the subtraction region with no spurious peak.

3.3.3. Other Background Contributions

As can be seen in Figure 3.20, even after removing the Bremsstrahlung component, there is still a non-negligible background that remains. This is attributed to unresolvable high energy transitions and potentially from ejected protons that deposit energy in the gamma array. This background is generally taken to be an exponential with a long tail at high energies, however the behaviour at low energies near the DALI2 thresholds has an unknown form. For this analysis, the background was fit with an exponential cut off with an error-function, of the form shown in Equation 3.11, where x is gamma ray energy and A,B,C, and D are free parameters.

$$b(x) = A\left[1 - erf(\frac{B-x}{C})e^{-Dx}\right] \tag{3.11}$$

Attempts were made to fix parameters B and C, corresponding with the half-rise point and slope of the low-energy cutoff respectively, by fitting this functional to the experimentally obtained Bremsstrahlung spectrum. Normally the low-energy cutoff in the Bremsstrahlung background and the continuum background have the same origin–the effect of the DALI2 thresholds, thus we expect that they should have common cutoff parameters. Unfortunately while Equation 3.11 does reproduce reasonably well the general form of the Bremsstrahlung spectrum, the cutoff parameters obtained from fitting this spectrum fail to reproduce the cutoff of the continuum background in the subtracted spectrum. Therefore all four parameters of the continuum background were left free during the fitting procedure, described below.

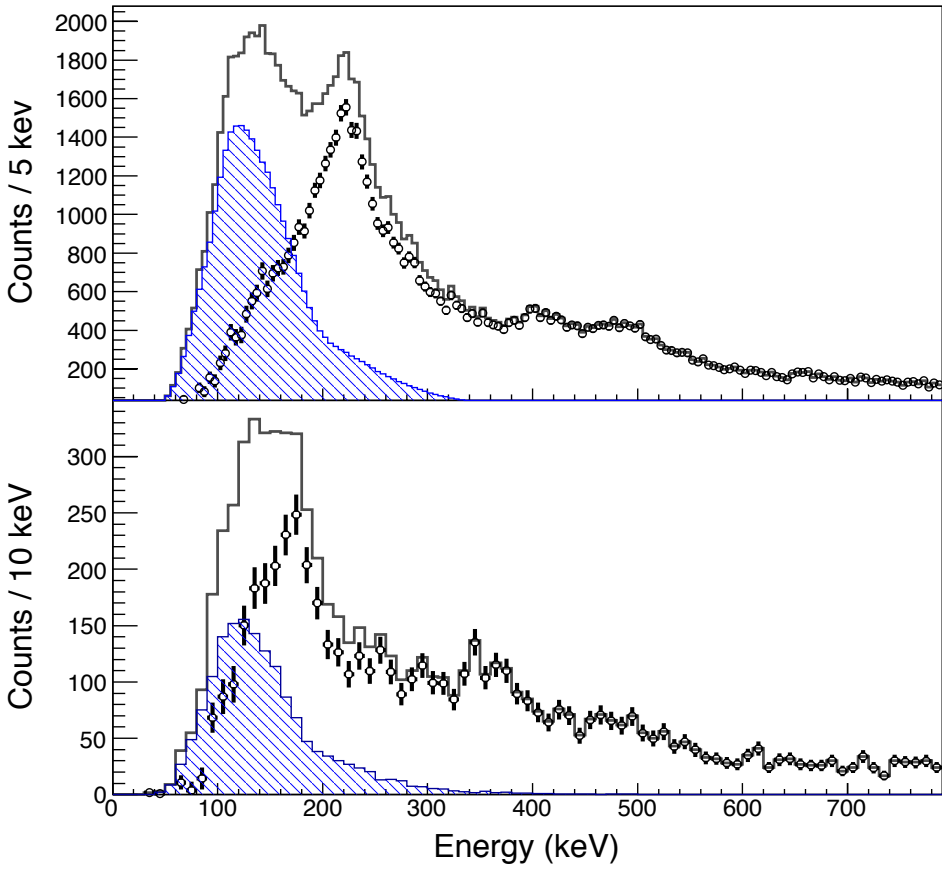

Figure 3.20. Doppler corrected gamma spectrum for ^{112}Mo (top) and ^{110}Zr (bottom) shown by solid gray lines. Normalized Bremsstrahlung component (blue) is subtracted from the gamma spectrum to yield the subtracted spectrum (dots) for each case.

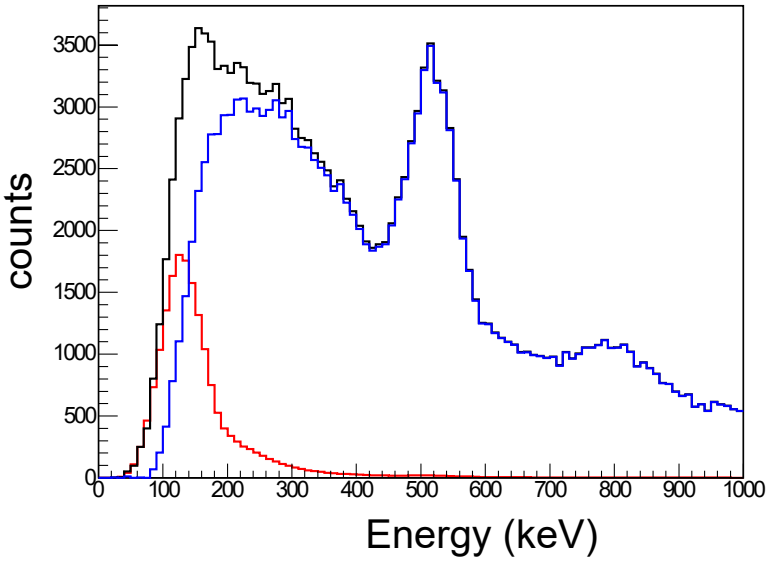

Figure 3.21. Doppler corrected gamma spectrum for ^{86}Ge (black), normalized Bremsstrahlung background (red), and subtracted spectrum (blue).

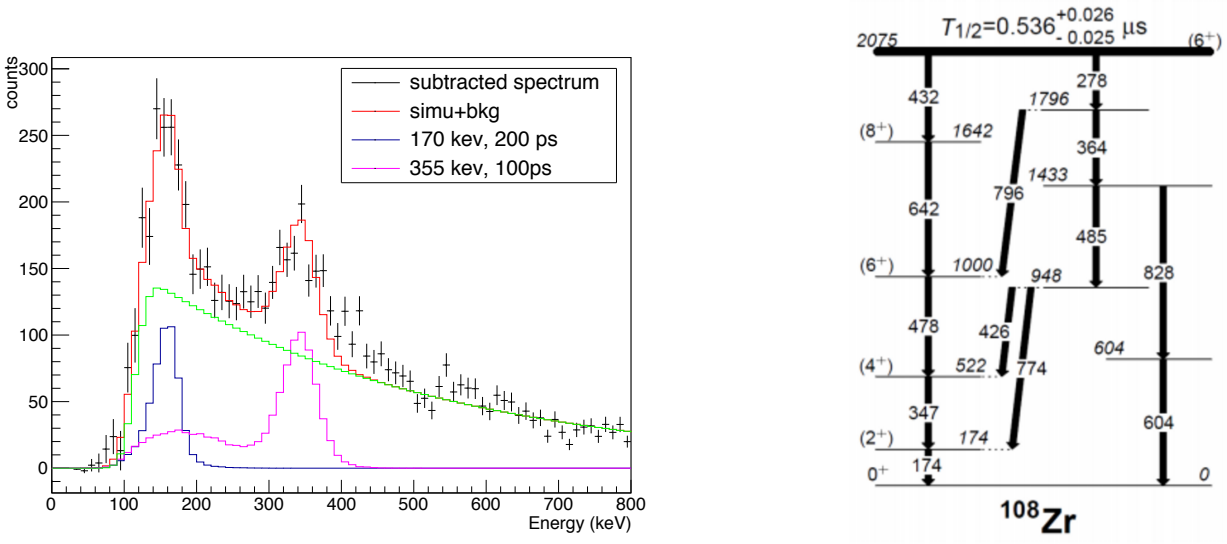

(a) **(b)**

Figure 3.22. (a) Bremsstrahlung subtracted spectrum of ^{108}Zr, fit with the two indicated simulated response functions and a background of the form shown in Equation 3.11. (b) The published ^{108}Zr level scheme from [104].

3.4. ^{108}Zr Benchmark

As a test of the subtraction procedure, ^{108}Zr was also analyzed. The spectroscopy of this nucleus has already been measured at the RIBF and published in [76] and [104]. The subtracted spectrum fit with simulation response functions (see next section) and the published level scheme is shown in Figure 3.22. Good agreement is found, validating the subtraction procedure.

3.5. Simulations and Fitting

To extract the energies of the transitions, the Bremsstrahlung subtracted Doppler-corrected gamma spectra were fit with DALI2 detector response functions simulated with GEANT4 [91]. The DALI2 simulation package, ShogunSim, is a common tool to the collaboration developed by Pieter Doornenbal from the RIBF [105]. ShogunSim has been benchmarked on known in-flight transitions and has a precision of 1 keV. It features three stages: 1) the Event Generator, which simulates a heavy ion beam hitting a target and subsequent emission of gamma rays with given lifetimes and population probabilities. 2) the Event Builder, which takes the gamma rays from the Event Generator, distributes them in the DALI2 geometry, and simulates the detector response. 3) the Event Reconstructor, which takes the gamma ray spectrum from the Event Builder and performs the Doppler correction in an analogous way as the data analysis codes.

A number of experimental quantities are used to optimize the ShogunSim for a given setup. Standard utilization involves including the experimental detector-by-detector DALI2 calibration and the parameters describing the individual resolutions of each crystal in the Event Builder stage. For this analysis, to optimize the simulation at low energy for our transitions of interest, the experimental DALI2 thresholds were extracted detector-by-detector and added to the Event Reconstructor phase with a Gaussian smoothing. Additionally, the physical structure of the TPC was included in the Event Builder to account for absorption of gamma rays in the TPC materials. This addition principally

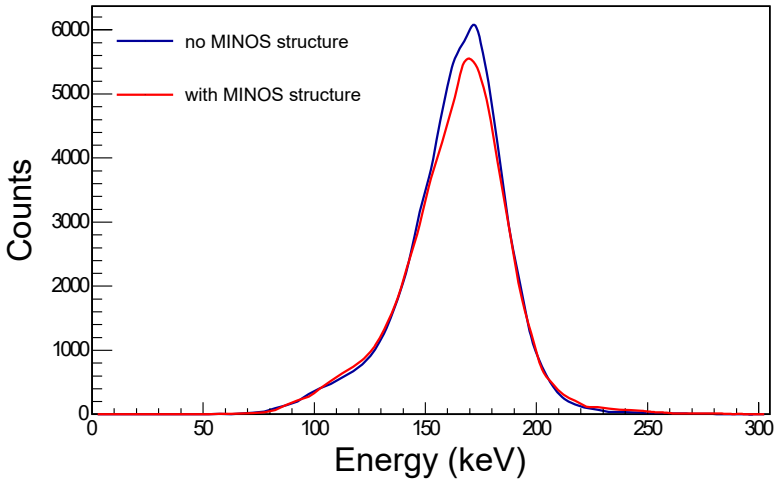

Figure 3.23. Simulated response function for 180keV, 200 ps halflife transition in ^{110}Zr when including (red) and not including (blue) the physical structure of MINOS in the Event Builder.

affects the Doppler-corrected gamma ray spectrum at low energy, as shown in Figure 3.23.

After the principle peaks were identified by examining the full and multiplicity gated spectra at forward and backward angles, an array of response functions was simulated for each peak for different lifetimes and energies. This step was necessary as the lifetimes of these transitions are unknown, but non-zero lifetimes significantly alter the detector response function through centroid shift and degraded resolution.

The centroid shift can be understood by examining the doppler shift formula, Equation 3.9. If the nucleus has a non-zero lifetime and travels along the z-axis before decaying, then the real gamma emission angle $\theta_{\gamma R}$ will be larger than the angle assumed for the Doppler correction. Then the $(1 - \beta cos(\theta_\gamma))$ term will be artificially small, and the gamma ray will be over Doppler shifted to lower energies. Similarly, if the real gamma emission occurs farther along the Z-axis in the target, then the real velocity β_R will be smaller than the β used for the Doppler correction due to energy loss in the target, again leading to a Doppler correction shifted to lower energies.

Non-zero lifetimes also contribute to peak broadening, which can be understood since de-excitation follows Poisson statistics, therefore the gamma ray is not emitted promptly after a certain-time τ. Instead, the gamma-ray emission time is sampled from a distribution characterized by τ, leading to a convolution of the lifetime distribution with the prompt gamma-ray response function. Practically, this means that non-zero lifetimes smear out the reconstructed photopeaks, leading to lumpy plateau structures instead of clean, Gaussian-like peaks. The combined result of these aforementioned lifetime effects is illustrated in Figure 3.24, showing simulated peaks of a 180 keV transition in ^{110}Zr for various half-lives.

Both these effects are correctly treated in ShogunSim, therefore it is sufficient to sample the appropriate range of energies and lifetimes for each simulation. The general scheme to find the energies of the transitions was:

1) Simulate an array of response functions for each peak covering the possible energy/lifetime (e/τ) variable space in 5 keV/ 50 ps steps
2) Fit the subtracted spectrum with all combinations of the peak arrays and extract the χ^2
3) Determine the most-probable response function (e/τ) for each peak
4) Extract one sigma regions of confidence for each peak

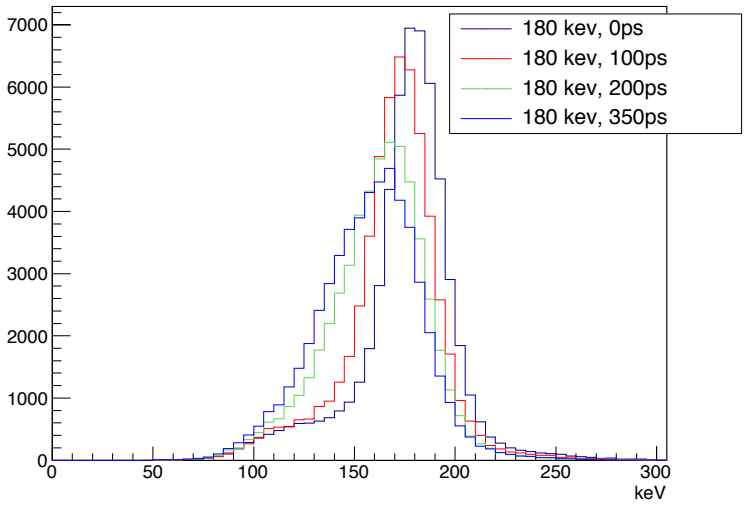

Figure 3.24. Simulated response functions for a 180 keV transition in ^{110}Zr emitted in-flight, for various half-lives.

The fitting procedure was the most time consuming and sensitive part of the process. Because the Compton tails of the response functions extend to low energy and may overlap with photopeaks of other response functions, we were concerned about cross talk and potential bias that might arise from sequential peak fitting (i.e. fitting a single peak while keeping the others constant). Thus all peaks were fit simultaneously, which meant considering all possible combinations off the peak arrays generated in step 1 of the fitting procedure. This required a separate code to generate the input file for the fitting routine, taking three or four lists of response functions (each list containing the energy/half-life combinations for a given peak), and calculating all the possible combinations of the lists. Note that calculating all possible combinations of a given number of arrays very quickly becomes numerically burdensome. For this analysis, four peaks was the limit for which the all-possible-combinations input file for the fitting routine could be generated for the ROOT fitting routine within a reasonable amount of time (less than 1 minute), which translated into a fitting procedure that could run in less than one day for a single spectrum.

Due to the sheer magnitude of the number of response functions, the fitting procedure was completely automated. Dynamic ROOT routines took a given number of simulated response functions, fit the subtracted spectra, and wrote out the fit results to a text file. The fitting function f(x) is shown in Equation 3.12 for the case of three peaks where x is energy, p_i are the fit parameters, the first term is the background introduced in Equation 3.11, and $R_i(x)$ are the simulated response functions. Minimization was performed using ROOT's TMinuit package using a Pearson's χ^2 as the goodness-of-fit metric, defined in Equation 3.13, where and d(x) is the experimental spectrum. The energies and half-lives identifying each R_i, and the χ^2 value, were retained from the fitting procedure.

$$f(x) = p_1 \left[1 - erf(\frac{p_2 - x}{p_3})e^{-p_4 x}\right] + p_5 R_1(x) + p_6 R_2(x) + p_7 R_3(x) \tag{3.12}$$

$$\chi^2 = \frac{(f(x) - d(x))^2}{d(x)} \tag{3.13}$$

The results from the fitting procedure can be projected onto the energy/half-life plane for each

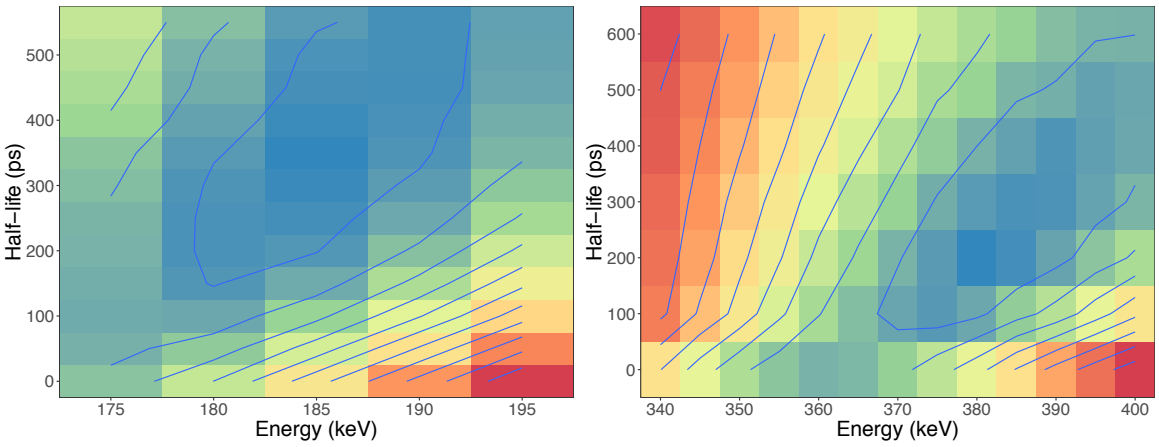

(a) (b)

Figure 3.25. χ^2 surfaces and interpolated contour lines for the (a) $2^+ \rightarrow 0^+$ and (b) $4^+ \rightarrow 2^+$ transitions in ^{110}Zr. Blue(red) is lowest(highest) χ^2.

fitted peak to identify the minimum in the χ^2 surface, and thus the response function for each peak that gives the overall best fit to the subtracted spectra. The χ^2 surfaces with interpolated contour lines for the $2^+ \rightarrow 0^+$ and $4^+ \rightarrow 2^+$ transitions in ^{110}Zr are shown in Figure 3.25.

Regions of confidence were obtained by converting the χ^2 data to probability. Gamma-ray emission follows Poisson statistics, but for many counts the Poisson distribution approaches the normal distribution. Thus it is reasonable to assume that our system, with multiple peaks and thousands of counts, can be described by a multivariate gaussian probability density functional, as shown in Equation 3.14 [106]. In this expression, p(x,N) is the probability as function of energy x and number of counts N, σ_i are the uncertainties on the measurement, which is just the square root of the number of counts, i.e. $\sigma_i = \sqrt{N_i}$. The expression for χ^2 appears naturally, and the probability reduces to essentially the exponential of χ^2, modulo a normalization factor out front.

$$\begin{aligned} p(x,N) &= \prod_{i=1}^{n} \frac{1}{\sqrt{2\pi}\sigma_i} exp\left(-\frac{1}{2}\frac{(x_i - M_i)^2}{\sigma_i^2}\right) \\ &= \frac{1}{\sqrt{(2\pi)^n}\prod_{i=1}^{N}\sigma_i} exp\left(-\frac{1}{2}\sum_{i=1}^{N}\frac{(x_i - M_i)^2}{\sigma_i^2}\right) \\ &= \frac{1}{\sqrt{(2\pi)^n}\prod_{i=1}^{N}\sigma_i} exp\left(-\frac{1}{2}\chi^2\right) \\ &= C\ exp\left(-\frac{1}{2}\chi^2\right) \end{aligned} \tag{3.14}$$

Thus the χ^2 surfaces in energy and half-life coordinates for each peak can be converted into a probability surface, and regions of confidence can be extracted around the most probable energy/half-life coordinate. The probability surfaces were normalized to unity in the energy/half-life regime explored, and one sigma regions of confidence were found recursively around the probability maximum. Probability surface and regions of confidence for the $2^+ \rightarrow 0^+$ and $4^+ \rightarrow 2^+$ transitions in ^{110}Zr and ^{112}Mo are shown in Figure 3.26. The probability and regions of confidence calculations were done using the a code written with the statistics toolkit and programming suite R [107].

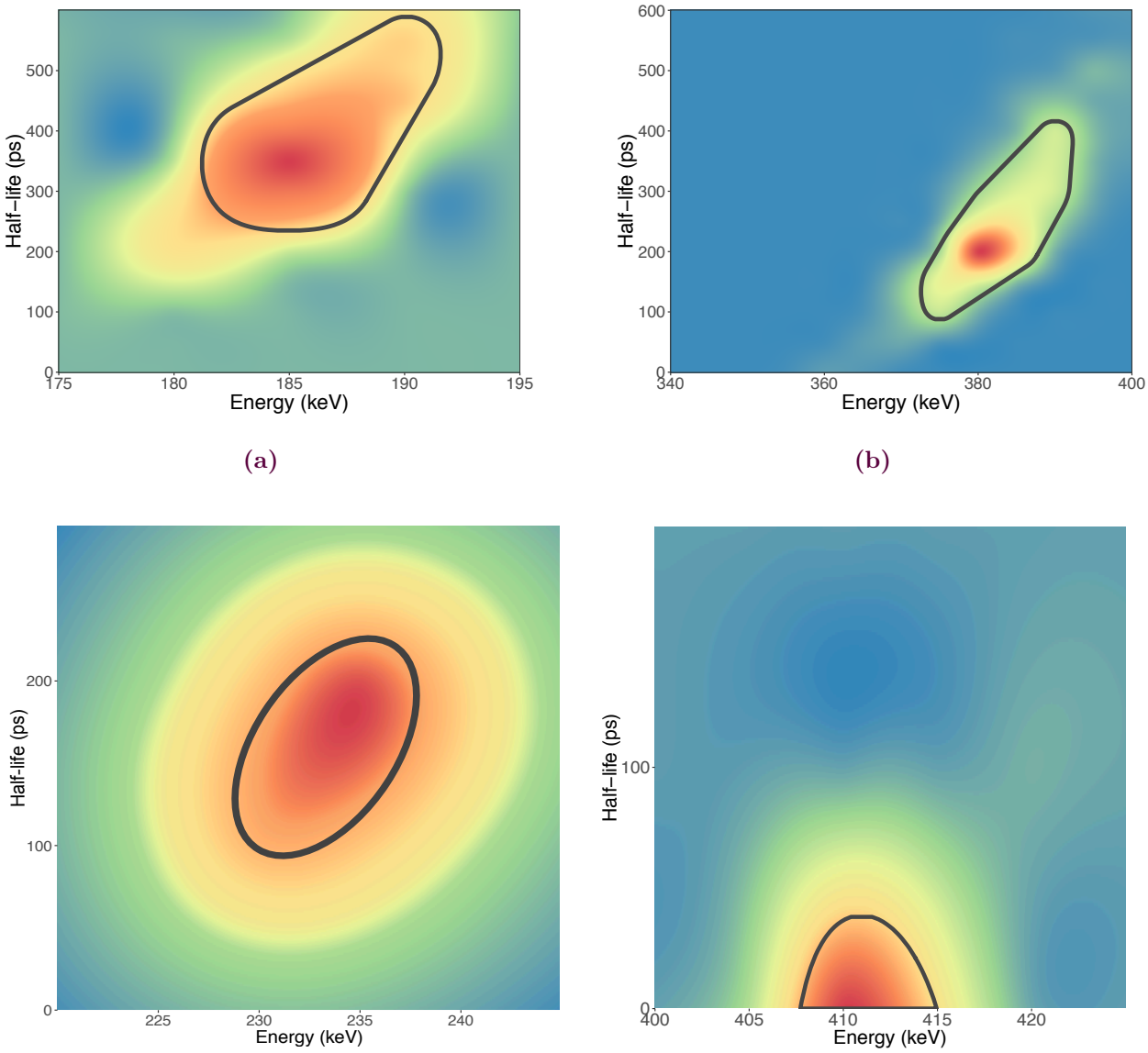

Figure 3.26. Probability surfaces and 1-σ regions of confidence (black lines) for $2_1 \rightarrow 0_1$(a,c) and $4_1 \rightarrow 2_1$ (b,d) transitions in ^{110}Zr (a,b) and ^{112}Mo (c,d). Probability surfaces and regions of confidence have been smoothed via interpolation and normalized to one in the shown parameter space of transition energy and half-life. Red is most probable, blue is least probable.

To test the robustness of this analysis, we also analysed the spectra by dividing the data up between very forward (26-68 degrees) and other angles (69-149 degrees), which we will refer to as backward angles in the following for simplicity. The remaining background after subtraction has a different form at low energy between these two spectra, thus this analysis provides a check on any potential bias introduced by the free fit of the background parameters with the response function intensities. For this analysis, the Bremsstrahlung background was subtracted independently from both forward and backward spectra (this is trivial, the Bremsstrahlung spectrum can be broken up between forward/backward angles as well and the normalization factor is unchanged). Then, the response functions were simulated with the same angular divisions, and the forward/backward subtracted data spectra were fit simultaneously with the forward/backward simulated response functions. For this fit, the response function intensities were constrained between the spectra, but all the background parameters were free in each spectra. Thus for the fit of ^{112}Mo, the free parameters were the four response function intensities, the four parameters describing the background at forward angles, and the four parameters describing the background at backward angles. The rest of the fitting procedure including all combinations of response function arrays was unchanged from the previously described analysis of the full spectra.

It was discovered during this angular divided fitting procedure that the detector efficiencies at backward angles are overestimated in ShogunSim. This was evident when the peak intensities at low energy were always overestimated at backward angles, and underestimated at forward angles (remember that the intensity was constrained between the two spectra). This could have been anticipated as all poorly functioning detectors are placed at backward angles, as confirmed by the DALI2 team at RIBF during this investigation. The relative efficiency as a function of energy was benchmarked by comparing the photopeaks from source measurements with simulated response functions, using the same angular divisions. Indeed poorer efficiency relative to the simulation was found at backward angles and additionally at low energies, though the granularity of the benchmarked trend was limited by positions of source peaks. From these comparisons we were able to extract a backward scaling factor, defined as shown in Equation 3.15, where F is the backward scaling factor, F_{data}/B_{data} is the ratio of photopeak intensities obtained by fitting the data directly with a gaussian+first order polynomial, and F_{sim}/B_{sim} is the ratio of photopeak intensities fit in the same way but in a simulated spectrum. The ratio of simulated and real photopeak intensities at forward angles is taken to be 1. This scaling factor needed to be applied to the simulated response functions at backward angles to account for the overestimated efficiency relative to forward angles in the simulation.

$$\begin{aligned} F &= \frac{\frac{F_{sim}}{B_{sim}}}{\frac{F_{data}}{B_{data}}} \\ &= \frac{B_{data}}{B_{sim}}\frac{F_{sim}}{F_{data}} \\ &= \frac{B_{data}}{B_{sim}} \cdot 1 \end{aligned} \tag{3.15}$$

By benchmarking this F factor at different energies, limited by the available source measurements (see section on DALI calibration), we then fit a line to this trend to extract the evolution of the backward scaling factor as a function of energy. Then this scaling factor was applied to the simulated response functions at backward angles to improve the agreement with the data. An example of the optimum angular divided fit, after accounting for the mismatch in efficiency at backward angles and low energy, is shown for ^{112}Mo in Figure 3.28.

The transition energies found with the angular divided fitting method are consistent with those

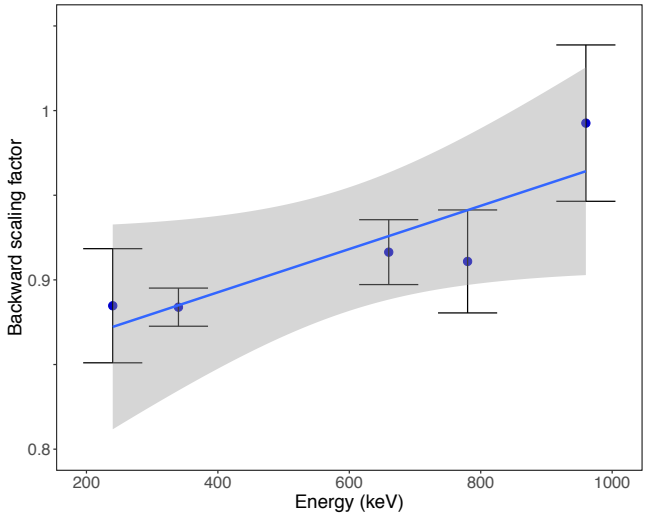

Figure 3.27. Backward scaling factor as a function of energy, as obtained from source measurements. The linear regression is shown by the solid blue line and the gray bar indicates the 90% confidence region.

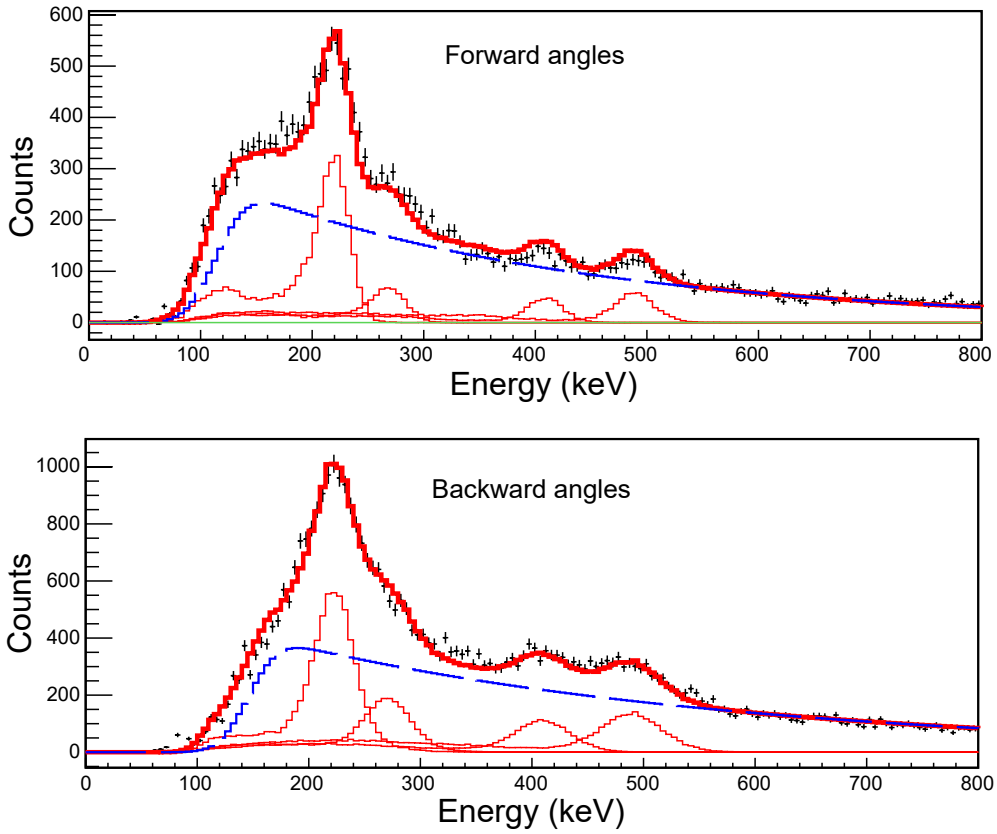

Figure 3.28. Angular divided fit for ^{112}Mo after applying backward scaling method.

Table 3.2. Comparison of results from fitting procedure from full spectrum (FS), and angular divided (FB) fit

Nucleus	Transition	E_{FS}	$T_{FS}^{1/2}$ (ps)	E_{FB}	$T_{FB}^{1/2}$ (ps)
^{112}Mo	$2_1 \rightarrow 0_1$	235 (5)	200 (100)	235 (5)	200 (100)
	$4_1 \rightarrow 2_1$	410 (5)	0 (100)	425 (5)	100 (100)
	$2_2 \rightarrow 0_1$	485 (25)	0 (100)	490 (5)	0 (100)
^{110}Zr	$2_1 \rightarrow 0_1$	185 (5)	350 $(^{+200}_{-100})$	185 $(^{+5}_{-10})$	350 $(^{+50}_{-300})$
	$4_1 \rightarrow 2_1$	380 (10)	200 $(^{+200}_{-100})$	375 $(^{+10}_{-15})$	100 (100)
	$2_2 \rightarrow 0_1$	485 (5)	0	490 (5)	0

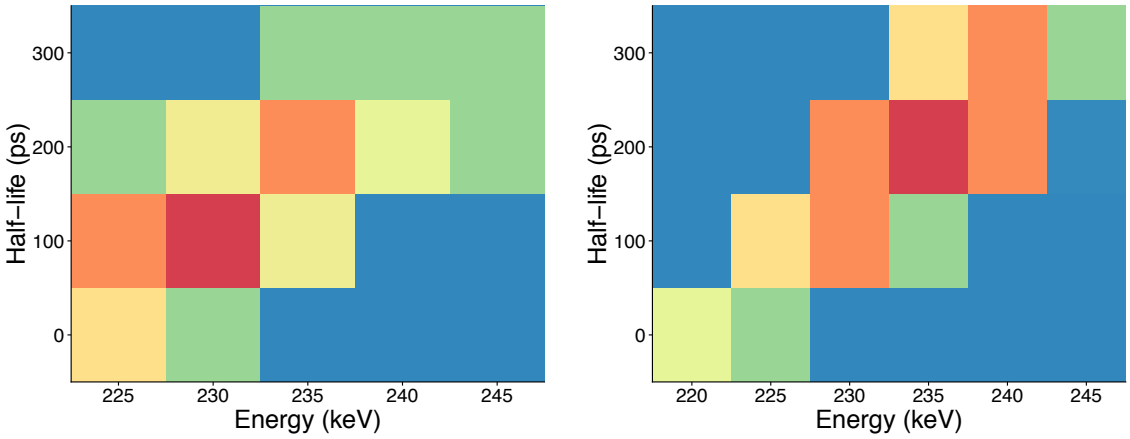

(a) **(b)**

Figure 3.29. Probability surface for the $2_1^+ \rightarrow 0_1^+$ transitions in ^{112}Mo when considering the angular divided (a) and full spectrum (b) fits. Probability surfaces are shown binned as resulting from the fitting procedure, red indicates most probable, blue is least probable.

found from fitting the full spectrum within the regions of confidence. The probability surfaces for the $2_1^+ \rightarrow 0_1^+$ transitions in ^{112}Mo are compared in Figure 3.29 for both the angular divided and full spectrum fits. It is clear from the figure that the most probable transition energy only changes by 5 kev, which is the level of the precision of the Geant4 simulation, but the allowed half-lives vary by 100 ps. This is because the full and angular divided spectra have different backgrounds, and the fit of the free parameters describing this background can partially compensate for peak broadening induced by lifetime effects. For this reason, we believe that the half-lives obtained from the fitting procedure are “effective" half-lives, and cannot be taken literally due to their inextracability from the background parameters. Thus they are only used to define the regions of confidence that set the error bars on the energy uncertainties. The angular divided fitting results and comparison with the full spectrum fit for ^{110}Zr may be found in Appendix B.

Table 3.2 shows the energies and uncertainties for all the peaks obtained with both methods. Note that for the $2_2^+ \rightarrow 0_1^+$ transition in ^{110}Zr, non-zero half-lives were not considered as the equivalent transition in ^{112}Mo was only ever consistent with zero-lifetime transitions. To obtain the final transition energies and uncertainties, the full spectrum fit was used as it has better statistics, fewer free fit parameters (only one exponential background), and to avoid the added systematic uncertainty due to the efficiency correction at backward angles.

Table 3.3. Comparison of results from fitting procedure for ^{110}Zr when feeding to the 2_1^+ state is considered

Nucleus	Feeding time to 2_1^+	E_{FS}	$T_{FS}^{1/2}$	E_{FB}	$T_{FB}^{1/2}$ (ps)
^{110}Zr	200 ps	$185(^{+5}_{-10})$	100 $(^{+250}_{-100})$	180 $(^{+10}_{-5})$	50 $(^{+150}_{-50})$
	350 ps	180(5)	0 (100)	180 (5)	0 (50)

As can be seen in Figures 3.29, 3.26 many of the regions of confidence encompass half-lives that are quite long. This invites the question then, if a higher-lying transition like a $4_1^+ \rightarrow 2_1^+$ has a significant non-zero lifetime, then how is the subsequent $2_1^+ \rightarrow 0_1^+$ transition affected? To answer this question, the DALI2 response functions were resimulated to include these delayed feeding effects. This was done by adding a second decay of the desired gamma ray energy+1 (ShogunSim does not accept a transition energy of 0) to the level of interest, with a half-life corresponding to the feeding time. We then simulated all the potential feeding times allowed in the regions of confidence for the $4_1^+ \rightarrow 2_1^+$ and $2_2^+ \rightarrow 2_1^+$ transitions for both ^{112}Mo and ^{110}Zr, and reran the fitting procedure with the delayed $2_1^+ \rightarrow 0_1^+$ transitions. Results of the fitting procedure for $T^{1/2}$=200 and 350 ps feeding to the 2_1^+ state in ^{110}Zr are shown in Table 3.3. These values correspond to the central and upper-limit of the half-life of the $4_1^+ \rightarrow 2_1^+$ transition. We see that the $2_1^+ \rightarrow 0_1^+$ energy is unchanged when considering 200 ps of feeding, and only shifts by 5 keV when the upper limit feeding case is considered. A feeding of 150 ps to the 2_1^+ in ^{112}Mo was also considered (the upper limit on the half-life of the $4_1^+ \rightarrow 2_1^+$ transition), which only shifted the most probable half-life of the $2_1^+ \rightarrow 0_1^+$ by 5 keV, therefore it was neglected. In general there is a linear mapping towards lower energies and thus shorter half-lives when feeding effects are included, as expected from the peak-shift discussed previously. Considering the possible feeding to the 2_1^+ states in ^{110}Zr and ^{112}Mo does not change the previously obtained transition energies, but we did use this study to expand the regions of confidence to include the regions when feeding effects are considered.

The final fits of the subtracted spectra are shown in Figure 3.30.

3.6. $\gamma - \gamma$ Coincidences and Level Scheme Construction

The level schemes for these nuclei were constructed via known systematics in the region and by examining the gamma-gamma coincidence spectra. The most intense peak is taken to be the $2_1^+ \rightarrow 0_1^+$, based on the fact that these are even-even nuclei, and this is the trend seen in similar measurements of neighboring nuclei. Due to the limited statistics, only the coincidence spectra gated on the most intense transition could be exploited for data analysis. The background was taken far away from the transitions of interest (above 1 MeV), and normalized according to the relative intensity between the gated and background region of the sum of Bremsstrahlung and fit exponential backgrounds. Background subtracted coincidence spectra are shown in the insets of Figure 3.31 for ^{112}Mo and ^{110}Zr.

When gating on the $2_1^+ \rightarrow 0_1^+$ transition in ^{112}Mo, there are clear coincidence peaks around 400 and 300 keV respectively. The former is also visible in the doppler corrected spectrum, and thus we take it to be the $4_1^+ \rightarrow 2_1^+$ transition. The latter is hidden in the shoulder to the right of the $2_1^+ \rightarrow 0_1^+$ transition in the full spectrum of Figure 3.30. The peak near 500 keV is not in coincidence with the $2_1^+ \rightarrow 0_1^+$ transition, and its intensity relative to the background does not seem to change when considering spectra for different gamma ray multiplicities, therefore we take it to be a $2_2^+ \rightarrow 0_1^+$ transition. In light of this, the transition near 300 keV is consistent with a potential assignment as the $2_2^+ \rightarrow 2_1^+$ transition, but unfortunately statistics are too limited to confirm this with gamma-gamma

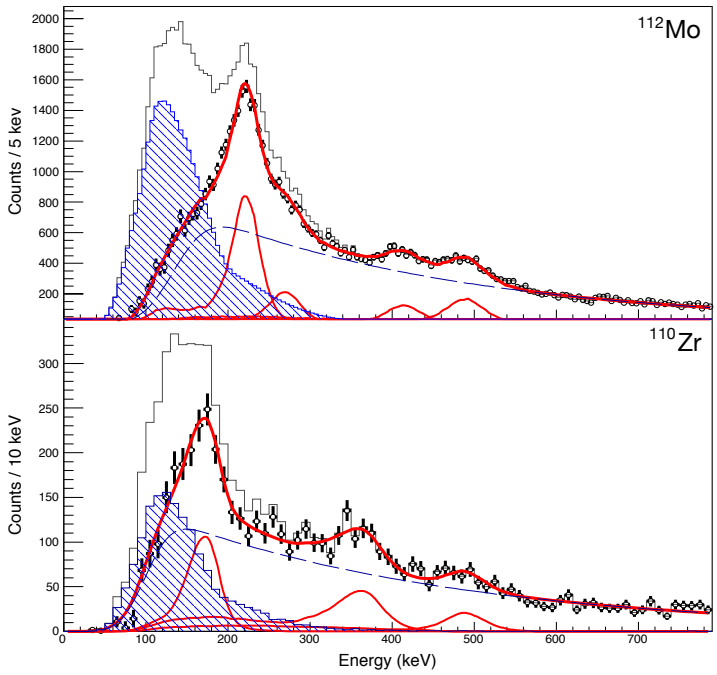

Figure 3.30. ^{112}Mo and ^{110}Zr doppler corrected (black line), the normalized Bremsstrahlung (blue line), and the subtracted spectra (black dots). The individual simulated response functions and total fit are shown in red.

coincidences.

A very similar picture emerges for ^{110}Zr, though the statistics are more severely limited. When gating on the $2_1^+ \to 0_1^+$ transition, the peak between 300 and 400 keV clearly emerges, thus we take it to be the $4_1^+ \to 2_1^+$ transition. The peak near 500 keV is not in coincidence with the $2_1^+ \to 0_1^+$ transition, and its intensity does not evolve with γ multiplicity, thus we take it to be the $2_2^+ \to 0_1^+$ transition. There are perhaps other peaks hiding between the $2_1^+ \to 0_1^+$ and $4_1^+ \to 2_1^+$, but the resolution of this data does not permit us to analyse them. The final level schemes are shown in Figure 3.32.

3.7. Uncertainties

The principal source of uncertainty in the spectroscopy analysis described above is the region of confidence in the energy/half-life plane for each transition, including both the fit to the full spectrum, the angular divided fitting, and including feeding effects. Other sources include DALI2 calibration (1 keV) and systematic uncertainties (5 keV). Unfortunately due to the few available reference peaks in this region where the energy and lifetime are known, we are forced to estimate this systematic uncertainty. 5 keV is a modest estimate that includes principally the reliability of the simulated response functions for the energies and lifetimes considered. All uncertainties were added in quadrature to obtain the final level schemes shown in Figure 3.32. The error bars were symmetrized, while keeping the central value, for simplicity–i.e. if the energy from the fit was $185(^{+5}_{-10})$ keV, 185(10) was used. To illustrate the error bar calculation, consider the 4_1^+ state in ^{112}Mo. This state is made by the sum of the $4_1^+ \to 2_1^+$ and $2_1^+ \to 0_1^+$ transitions, but the systematic errors are common to both measurements. The error bar calculation is shown in Equation 3.16. Note that the published error

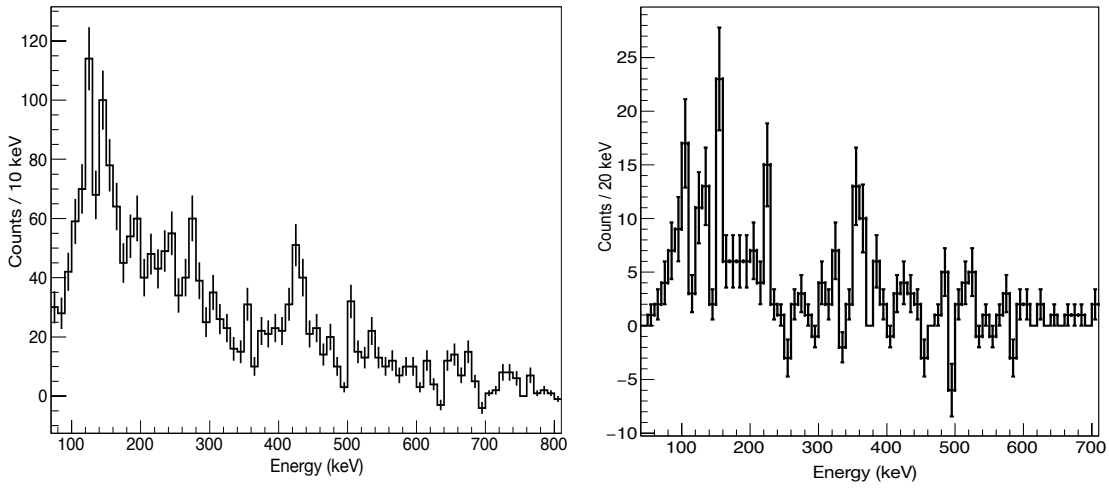

(a) **(b)**

Figure 3.31. $\gamma - \gamma$ coincident spectra gated on the most intense peak for (a) ^{112}Mo and (b) ^{110}Zr.

bars are ever so slightly smaller than the ones obtained via this method for the $4_1^+ \rightarrow 2_1^+$ transitions, due to lack of accounting for the systematic errors twice. However this difference is approximately 1 keV, and the statistical errors were already enlarged for symmetry and simplicity reasons, thus the impact on the final result is negligible. Note that the large error bar on the $4_1^+ \rightarrow 2_1^+$ transition in ^{110}Zr is because the particularly large contribution to the region of confidence from the feeding and angular divided fits.

$$\begin{aligned} \sigma &= \sqrt{\sigma_{stat_1}^2 + \sigma_{stat_2}^2 + \sigma_{sys_1}^2 + \sigma_{sys_2}^2} \\ \sigma_{E4^+} &= \sqrt{5^2 + 10^2 + 5^2 + 5^2 + 1^2 + 1^2} = 13 \end{aligned} \tag{3.16}$$

(a) **(b)**

Figure 3.32. Level schemes for ^{112}Mo and ^{110}Zr obtained from this work.

4 Interpretation

4.1. Beyond Mean-Field Calculations

The spectroscopy measurements of this work are compared with calculations from multiple beyond mean field models. As discussed in Chapter 1, currently mean-field methods are the only models capable of predicting the properties of the ensemble of the chart of the nuclides within the same framework. They are particularly adapted for medium-mass deformed nuclei, such as those studied here. These approaches focus on specific degrees of freedom that drive the low-energy properties of these nuclei, like pairing and deformation. This work uses calculations with two different phenomenological mean field potentials, the Gogny D1S [23] and the Skyrme SLyMR0 [108] interactions. The fundamental difference between Gogny and Skyrme interactions is the range of the effective interaction: finite range (Gogny) or zero range (Skyrme). SLyMR0 was specifically designed to be used with beyond mean field techniques, such as those employed here, used to calculate excited states with proper angular momentum and shape correlations [1].

In mean field approaches, the Hartree Fock Bogoliubov (HFB) method is routinely employed [20]. The HFB wavefunction is a vacuum of quasiparticles, a linear combination of particle and hole states, which allows a natural treatment of pairing. The HFB method numerically solves

$$\delta\left(\langle\Psi|H-\lambda_Z Z-\lambda_N N-\sum_{\lambda\mu}\nu_{\lambda\mu}Q_{\lambda\mu}|\Psi\rangle\right)=0 \tag{4.1}$$

where Z is the number of protons, N is the number of neutrons, $Q_{\lambda\mu}$ is the multipole operator which is proportional to the spherical harmonic $Y_{\lambda\mu}$, and λ_z, λ_N, and μ are Lagrange multipliers. For a given nucleus, the result of this minimization yields a potential energy surface as a function of deformation parameters. Standard mean-field calculations explore the deformation space of β and γ related to the $\lambda = 2$ multipole moments, as discussed in Chapter 1, but higher multipoles may be needed, as seen in the exploration of tetrahedral symmetries later in this chapter. A potential energy surface resulting from a HFB minimization for ^{110}Zr using the Gogny D1S interaction is shown in Figure 4.1.

This mean field procedure provides a description of the minimum energy of all possible quasiparticle vacua for a given $\langle Q_{\lambda\mu}\rangle$, treating only pairing and effects that can be included in the density dependent potential. Exotic systems are however sensitive to many-body correlations such as collective excitations. A possible path to describe real nuclei is to consider a superposition of these basis states, as real nuclei may or may not be well described by the minimum in the potential energy surface. Furthermore, by only minimizing the energy with respect to deformation parameters, angular momentum and parity quantum numbers have in general been lost. To recover these symmetries and treat collective excitations, additional steps are needed.

[1] Traditional Skyrme interactions developed for mean-field approaches led to spurious energy contributions when coupled with beyond mean field techniques. But the SLyMR0 interaction was constructed to avoid these unphysical divergences. See [109] for a detailed explanation.

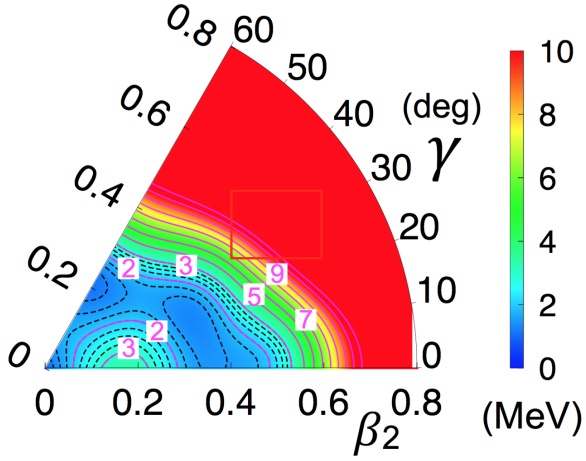

Figure 4.1. Potential energy surface of ^{110}Zr from Gogny-D1S HFB Calculation. Figure from Tomas Rodriguez.

The next step is to go beyond the mean field description and mix the quasiparticle states obtained from the HFB procedure. This may be done via the projected configuration mixing approach (PCM), also known as the symmetry conserving configuration mixing model (SCCM) [110] or projected generator coordinate method pGCM [24]. With these methods, a new wave function is constructed based on a superposition of the mean field configurations. Taking as an example the Skyrme and Gogny PCM calculations presented here, the quasiparticle states are first projected onto good angular momentum and particle quantum numbers, then those projected states are mixed to construct a realistic wavefunction as shown in Equation 4.2, where a indicates the deformation parameters, Λ indicates the particle number and angular momentum quantum numbers, $\phi(a, \Lambda)$ are projected quasiparticle states, and $f(a)$ is a variational parameter that gives the relative mixing between the different deformed configurations. This non-orthogonal basis may then be used in a variational method and leads to a renormalized eigenvalue problem, shown in Equation 4.3, known as the Hill-Wheeler-Griffin equation. Solving this equation yields the correlated ground state and excited state spectrum.

$$|\Psi(\Lambda)\rangle = \int da\, f_\Lambda(a)\, |\phi(\Lambda, a)\rangle \tag{4.2}$$

$$\int da' \, \langle \Phi(\Lambda, a)|\, H\, |\Phi(\Lambda, a')\rangle\, f_\Lambda(a') = E \int \langle \Phi(\Lambda, a)|\Phi(\Lambda, a')\rangle\, f_\Lambda(a') \tag{4.3}$$

In the past, the Hill-Wheeler-Griffin equation was considered computationally cumbersome, and an approximation was made in terms of a collective Hamiltonian [111], famously incarnated in the Five Dimensional Collective Hamiltonian (5DCH) used with the Gogny D1S interaction [62]. Instead of projecting onto good quantum numbers and directly calculating the relative mixing among the basis states of different deformation parameters, collective degrees of freedom are absorbed into the parametrization of the Hamiltonian itself. A simple collective Hamiltonian is shown in Equation 4.4, where $V(q)$ is the potential energy surface from the mean field calculation, and M_q is the tensor of inertia. This tensor of inertia contains moments of inertia around the axes of symmetry to account for rotation, and collective masses to account for vibrations. Thus the collective Hamiltonian contains all the ingredients to treat rotation, vibration, and the coupling between these modes, mimicking the brute force mixing of quasiparticle states in the PCM approach. In this scheme, the results of the

HFB calculation are used exclusively as input for the collective Hamiltonian and a requantification in the collective coordinates is done through a new Schrödinger equation as shown in Equation 4.5. The wavefunctions Ψ_i are written in terms of deformation and angular momentum coordinates, and are found with the energy spectrum by numerically solving Equation 4.5. Note again that here particle number and angular momentum quantum numbers have been lost.

$$H_{coll} = \sum_{ij} \frac{\partial}{\partial q_i}[M^{-1}(q)]_{ij}\frac{\partial}{\partial q_j} + V(q) \tag{4.4}$$

$$H_{coll}\,|\Psi_i\rangle = E_i\,|\Psi_i\rangle \tag{4.5}$$

4.2. Tetrahedral Deformation

Most mean field based calculations consider the nuclear deformation up to $\lambda = 2$, to account for the most commonly encountered prolate and oblate deformation. These methods can be extended to higher multipolarities to explore other more exotic shapes. As ^{110}Zr's nucleons correspond with the magic numbers of the tetrahedral symmetry, mean field calculations have also been performed for this nucleus specifically including the octupole deformation coordinate $\lambda_{3\mu}$, which includes the leading order tetrahedral deformation, λ_{32}, and hexadecapole, $\lambda_{3\mu}$, degrees of freedom. These calculations were performed using a microscopic-macroscopic interaction, which treat the nucleus as a liquid-droplet with shell and pairing corrections [112]. These mean field calculations including the tetrahedral degree of freedom may be coupled to beyond mean field methods, similar to those presented previously, to obtain the excited states for a tetrahedral nucleus. Such methods are used in [113, 60].

4.3. Monte Carlo Shell Model Calculations

Valence space shell model calculations are always limited by the large number of possible many-body states. The Monte Carlo Shell Model (MCSM) method [43, 114] addresses this issue by representing the theoretically numerous many-body states with a few number of highly selected states, making an importance truncation based on lowest energy considerations . Then these states (angular momentum and parity projected Slater determinants) are minimized with the Hamiltonian containing the effective interaction to obtain the coefficients of the states and the energy spectrum, analogously to solving to the Hill-Wheeler-Griffin Equation 4.3.

4.4. Results from Beyond Mean Field Calculations

For this work, we had access to five calculations for the structure of ^{110}Zr: three independent HFB calculations for the N=70 isotonic chain featuring two different interactions and two different beyond mean field techniques, in addition to MCSM and tetrahedral calculations for ^{110}Zr. The first four of these calculations are compared with our E_2^+ and R_{42} data in Figure 4.2.

First consider the Gogny-D1S based calculations. With this interaction, we have two ways of calculating excited states-5DCH [62] and the PCM approach [110], shown in Figure 4.2 by the blue circles and triangles, respectively. Both D1S calculations reproduce well the global N=70 trends consisting of a high E_2^+ at the $Z = 50$ closed shell (^{120}Sn) which gradually descends moving towards midshell. If we consider that the next proton shell closure occurs at $Z = 28$ (^{98}Ni), then the maximum of collectivity should occur at $Z \sim 39$, very near to ^{110}Zr, as shown in the D1S+5DCH calculations. D1S+PCM calculations for the N=70 chain were performed for this work and are only available through ^{108}Sr. Despite this overall good agreement, both D1S calculations overestimate the E_2^+

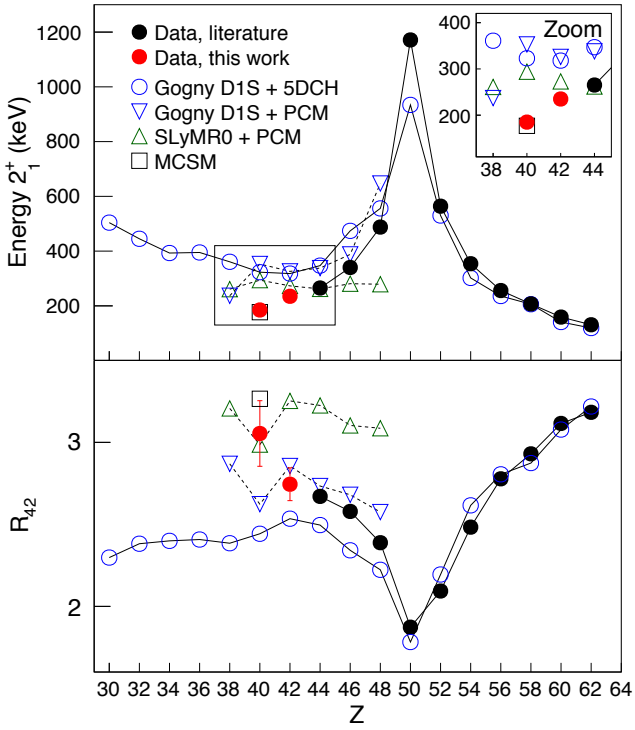

Figure 4.2. $N = 70$ systematics including previously published values (black dots), the transitions measured in this work (red dots), and the calculations used in this interpretation (open markers).

energy of the nuclei measured in this work by approximately the same amount. The discrepancy is small for ^{112}Mo (∼100 keV), but becomes larger for ^{110}Zr (∼200 keV).

Looking at the R_{42} ratios, we see the first hints of a difference between the two D1S calculations. The 5DCH calculations show a smooth R_{42} trend with values for both nuclei around 2.4, while the PCM calculations show a higher R_{42} for ^{112}Mo, in agreement with the experimental value, and a sharp drop at ^{110}Zr, opposite of the behavior observed in the data.

The potential energy surfaces for the $N = 70$ isotones resulting from these D1S+PCM calculations are shown in Figure 4.3. These plots give a good overall picture of the shape evolution along the isotonic chain, common to both D1S calculations. A sharp minimum at small prolate deformation is clear at ^{118}Cd which gradually becomes more extended in gamma and moves towards a soft prolate, oblate, shape coexistent scenario towards mid-shell. In the ground state wave-functions, ^{110}Zr is firmly triaxial, but marks a transition point between the oblate ground state in ^{112}Mo and the prolate ground state in ^{108}Sr. This is one possible explanation for the kink at ^{110}Zr observed in the R_{42} systematics. No kink is expected in the 5DCH calculations due to the lack of projection on good particle number, which leads to smooth trends.

PCM calculations using the SLyMR0 interaction are shown in green in Figure 4.2. Contrary to the D1S calculations using the same method, these calculations do not reproduce the global trend of the $N = 70$ isotones, but show a relatively flat behavior in both observables and do not reproduce the shell closure at $Z = 50$. Despite this, the predicted E_2^+ and R_{42} values fall close to our measured values, but this is likely by chance. This interaction was benchmarked in the lighter Mg isotopes, and despite its advanced formalism, is known to reproduce less reliably the global nuclear structure trends. It is interesting to note that the SLyMR0 calculations show the same kink in the R_{42} ratio at ^{110}Zr as was seen in the D1S+PCM calculation, though an oblate-prolate transition is not clearly

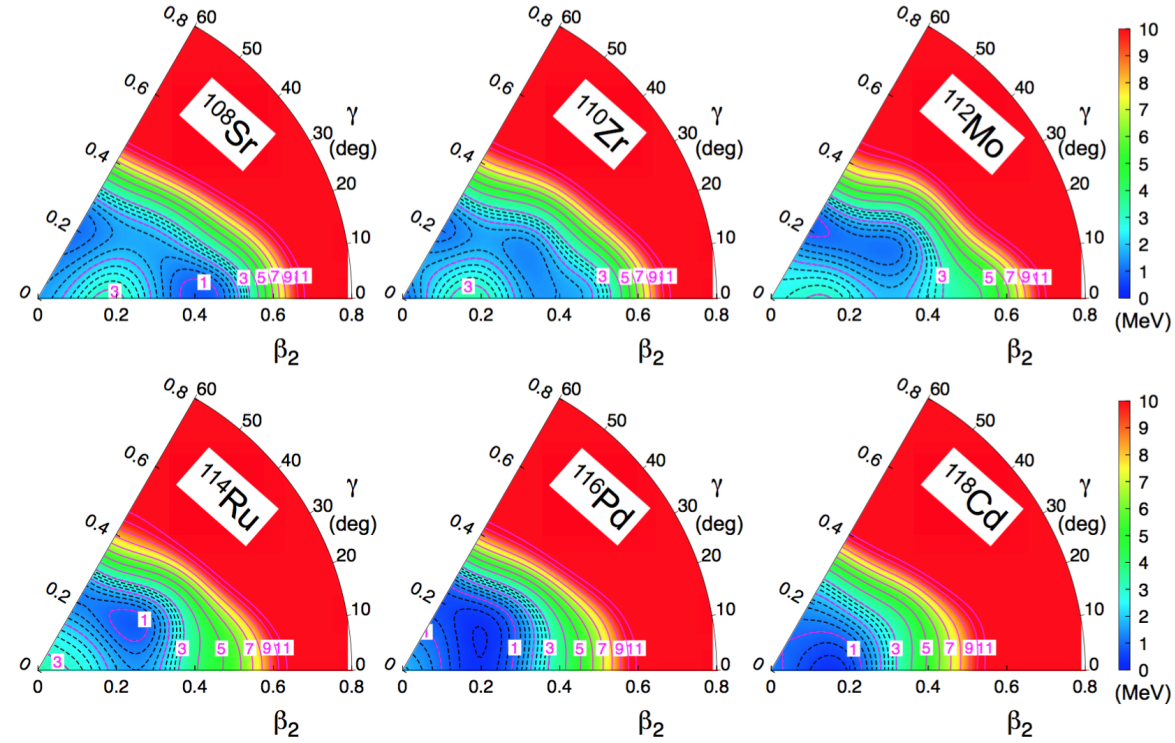

(a)

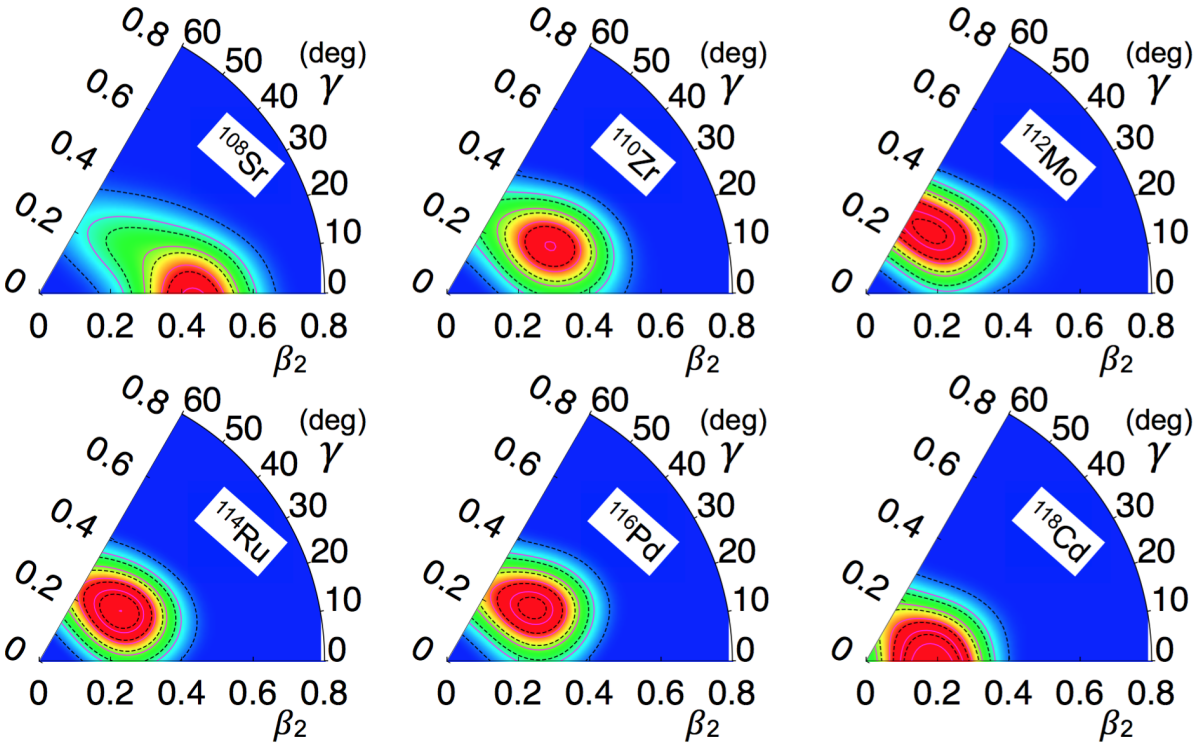

(b)

Figure 4.3. (a) Potential energy surfaces for the N=70 isotones, and (b) ground state collective wave functions from the D1S+PCM calculations from Tomas Rodriguez.

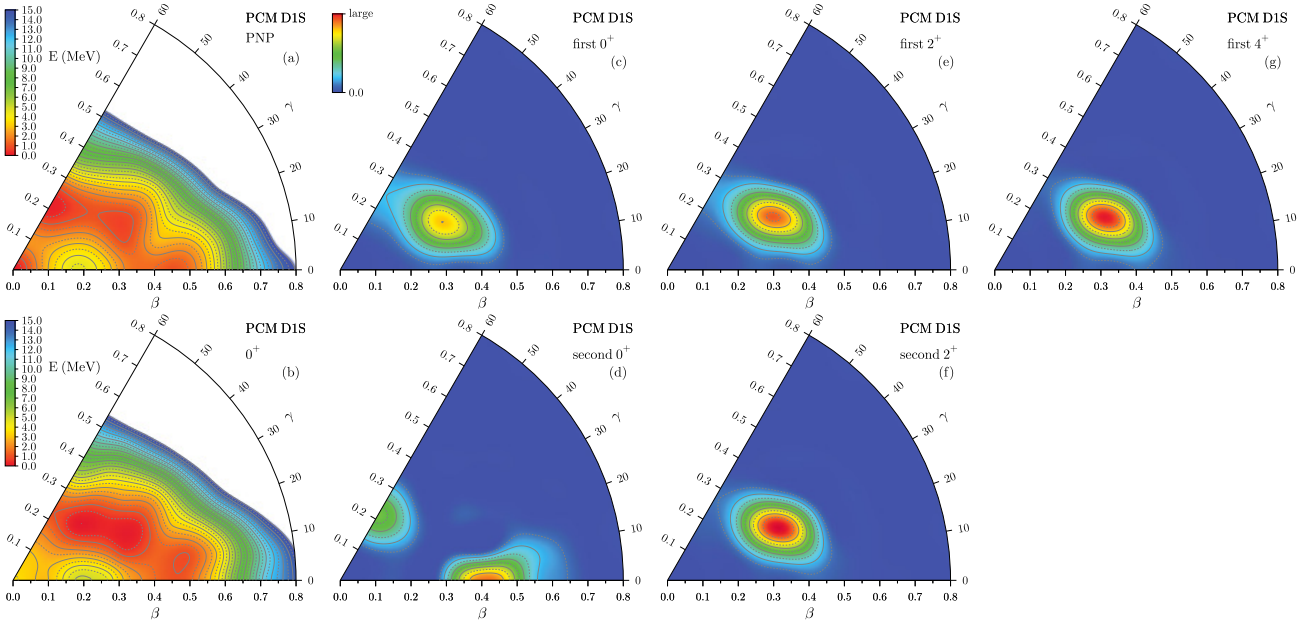

Figure 4.4. Deformation energy surfaces and the square of the collective wave function of selected states obtained in PCM calculations with the Gogny D1S interaction . All squared wave functions are plotted in the same arbitrary units. Figure from [37].

evidenced as in the D1S+PCM calculations. Instead the entire isotonic chain as calculated with the SLyMR0 interaction is more or less oblate.

Now we consider more in detail the predictions for ^{110}Zr. The mean field potential energy surfaces and collective wavefunctions for the first few excited states are shown in Figures 4.4, 4.5, and 4.6 for D1S+PCM, D1S+5DCH, and SLyMR0+PCM, respectively. Considering just the ground state of this nucleus, all calculations predict a triaxial configuration, but the SLyMR0 calculations tend towards a more oblate symmetry. Both D1S calculations predict a strongly prolate-oblate shape coexistent 0_2^+, while the SLyMR0 finds a triaxial 0_2^+ that is not significantly different from the ground state. This shape-coexistent scenario with strong competing minima is characteristic for this region beyond N=60, and similar results are seen in the krypton and selenium isotopic chains [115, 116] . Going beyond the mean field and looking in detail at the level schemes predicted by these approaches, shown in Figure 4.7, all these HFB calculations are in good qualitative agreement with our data, though the energies are overestimated. Notably the 2_2^+ lies lower in energy than the 4_1^+, a signature of gamma softness [117], and supports the hypothesis that this nucleus is triaxial, as predicted by the calculations.

Next we consider the Monte Carlo Shell Model calculations for ^{110}Zr [118]. Unfortunately these calculations were performed for the isotopic chain and not the isotonic chain, therefore we only have predictions for ^{110}Zr. The MCSM calculations give the best agreement with our data, showing a low E_2^+ and a high R_{42}, in agreement with the measured values. These calculations also reproduce well the trend of the Zr isotopic chain, attributing the large collectivity in the heavier Zr isotopes to a modification of the neutron single particle energies due to deformation triggered promotion of protons from the fp shell to the $g_{9/2}$ shell. This mechanism is attributed to spin-isospin coupling between valence orbitals driven by the tensor interaction. Considering the collective wavefunctions from the MCSM calculations, shown in Figure 4.8, though shape coexistence is present, a stronger prolate deformation is found compared to the HFB calculations presented above. In light of the excellent

agreement with the level scheme, we can conclude that this MCSM picture is more representative of the real structure of ^{110}Zr. These calculations predict however a low-lying 0_2^+ state below the 2_2^+ that we do not observe. If this level lies very close in energy the 2_1^+, it is possible that the $0_2^+ \rightarrow 2_1^+$ transition energy lies below the DALI2 thresholds. A more refined experiment preferably with the capacity to measure conversion electrons and thus see the $0_2^+ \rightarrow 2_1^+$ transition would be required to differentiate between the structure proposed by the MCSM and HFB calculations.

We also compare our ^{110}Zr data with beyond mean field calculations including tetrahedral deformation [60]. These predictions are also shown in Figure 4.7, denoted by the mean field method employed, a Wood-Saxon potential with a HFB mean field calculation, and then projection technique to obtain excited states (WS-HFB+PCM). These calculations predict that the lowest excited state is a 3^-, which means that the strongest transition should be the $3^- \rightarrow 0^+$ E3 transition. However an E3 transition in this energy range ($\sim$ 200 keV), would have a lifetime on the order of tens of milliseconds, and thus would decay far down the beamline beyond our gamma-ray detectors and we would never detect it, as may be seen by comparing the Weisskopf estimates of the E3 and E2 lifetimes. One could imagine then that the two coincident peaks that we see correspond to the $4^+ \rightarrow 3^-$ and $6^- \rightarrow 4^+$ transitions, but for significant tetrahedral deformation the ratio of these transition energies should be ~ 2, far from our measured value of ~ 3. For these reasons we conclude that the ground state band we observe does not manifest a tetrahedral symmetry, though we cannot exclude the possibility that this symmetry persists in an excited configuration.

Our colleagues who performed the D1S+5DCH calculations, with whom we worked closely for the interpretation of these results, were inspired to perform a local sensitivity test to try to understand the underestimated collectivity in ^{110}Zr with respect to our data. To mimic this effect in their approach, the spin-orbit term of the D1S interaction was increased from -130 to -140 MeV fm^5, with no changes to the other terms. These results show a lowering of the 2_1^+ excitation energies in ^{110}Zr and ^{112}Mo down to 215 and 259 keV respectively, in much better agreement with our data. The R_{42} agreement

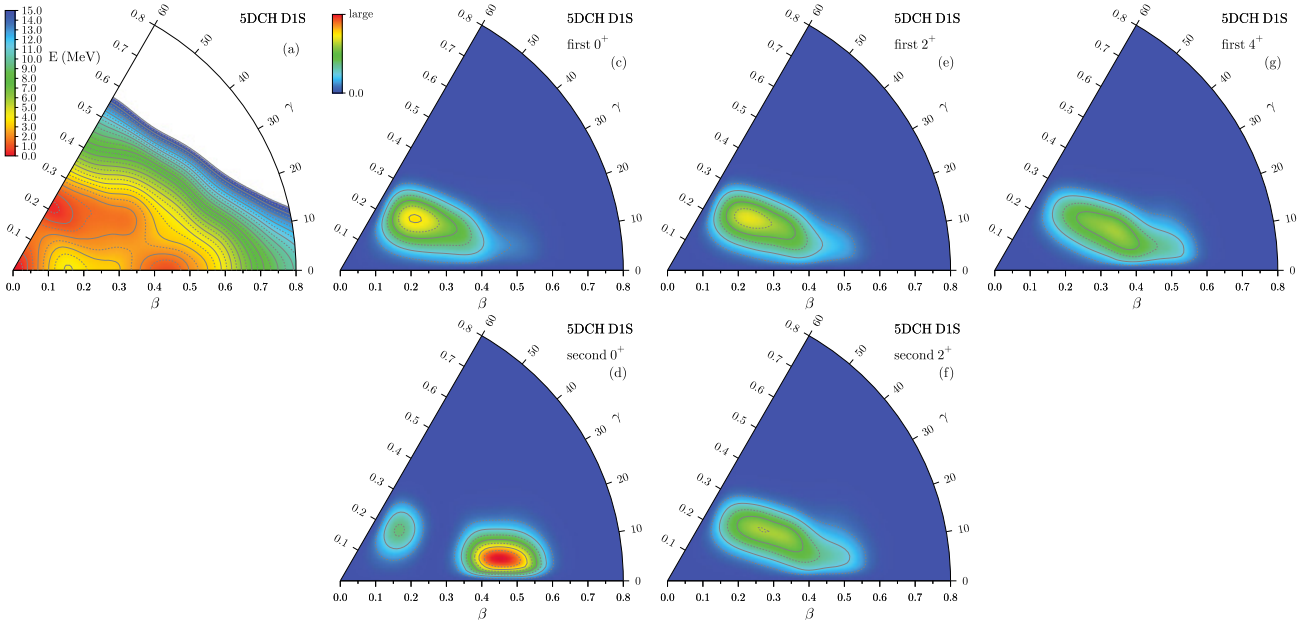

Figure 4.5. Deformation energy and probability densities obtained with the 5-dimensional collective Hamiltonian with the Gogny D1S interaction. All probability densities are plotted in the same arbitrary units. Figure from [37].

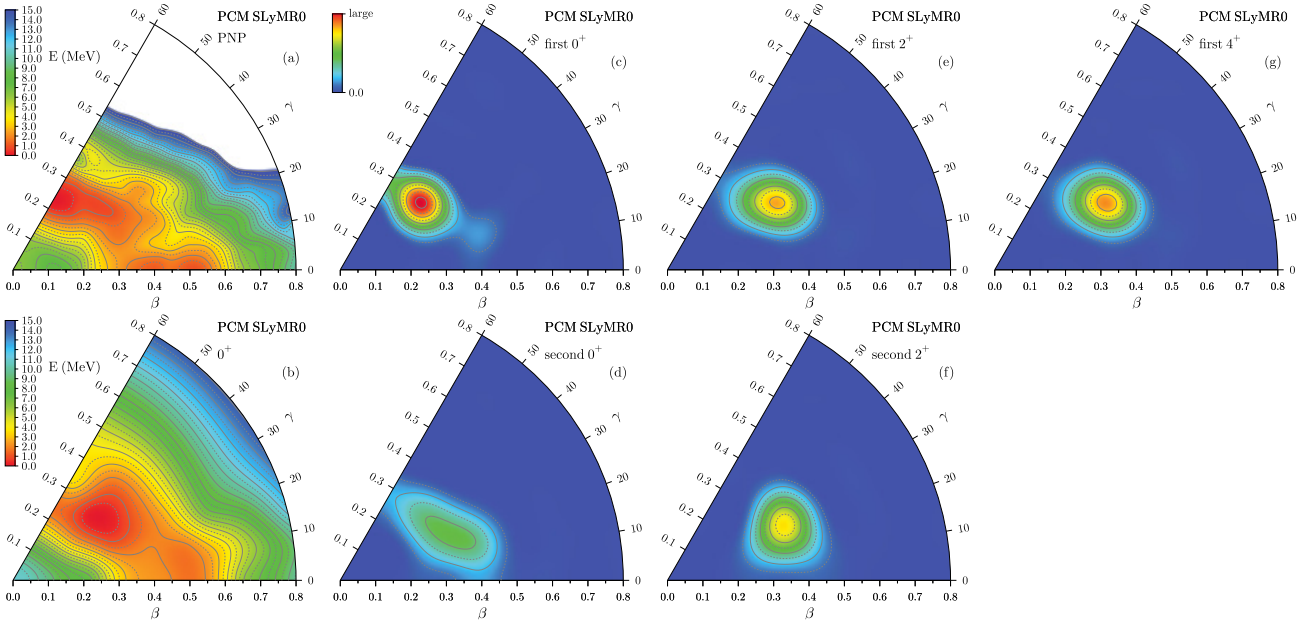

Figure 4.6. Same as Fig. 4.4, but obtained with the Skyrme SLyMR0 interaction. Figure from [37].

is also improved, going to 2.8 and 2.4 for ^{110}Zr and ^{112}Mo, respectively. The impact on the collective wavefunctions and potential energy surface may be seen in Figure 4.9. The ground state band is shifted more prolate, and the prolate minimum in the 0_2^+ becomes more localized in β. Furthermore, considering the $g_{9/2}$ occupancy at the prolate minimum, increasing the spin-orbit strength corresponds with an increased occupancy by 0.3 protons. This is consistent with the mechanism driving the deformation in ^{110}Zr proposed by the MCSM calculations where the collectivity is concurrent with protons promoted into the $g_{9/2}$ orbital.

4.5. Implications

We have performed the first spectroscopy of the most exotic $N = 70$ isotones ^{112}Mo and ^{110}Zr. For both these isotopes we find low E_2^+ and high R_{42} values, suggesting that these nuclei are well deformed. No surprising structure is found in ^{110}Zr that would indicate a stabilization effect due to its 40 protons and 70 neutrons. We can thus reject the hypothesis that a subshell closure in ^{110}Zr is responsible for failure of models to describe the r-process abundance distribution before the $A = 130$ peak. Indeed considering the evolution of single particle levels as predicted by the calculations, for example the representative case of PCM-D1S shown in Figure 4.10, moving towards more exotic nuclei the N=70 gap is predicted to get smaller, not larger.

The measured transitions also invalidate the hypothesis that the ground state of ^{110}Zr manifests a tetrahedral symmetry. Instead, we find that ^{110}Zr is even more deformed than predicted by beyond mean field methods with Gogny and Skryme interactions, though the general structure of the level scheme is consistent with the shape coexistent scenario proposed by these calculations. This data points to a deficiency in the commonly used mean field based methods to properly account for collectivity in the most exotic nuclei. Best agreement is found with MCSM calculations that show a strong deformation in ^{110}Zr due to proton-neutron interactions originating in the tensor force. Sensitivity studies with the D1S+5DCH approach support this interpretation. Potential work parametrizing the spin-orbit force in terms of isospin may be envisaged to improve structure predictions in very

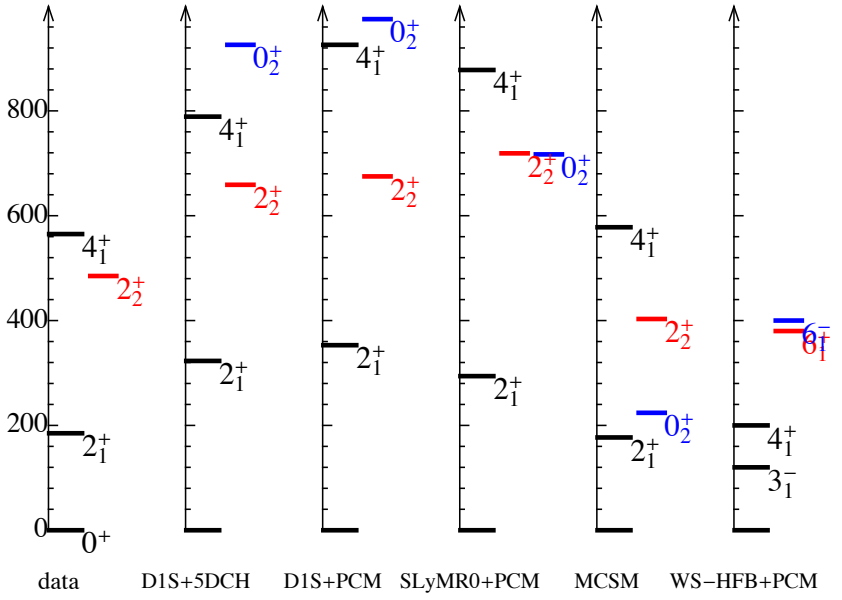

Figure 4.7. ^{110}Zr level scheme comparison between the data and the theoretical predictions discussed in this work. The Woods-Saxon (WS)-HFB+PCM calculations are the tetrahedral predictions from [60].

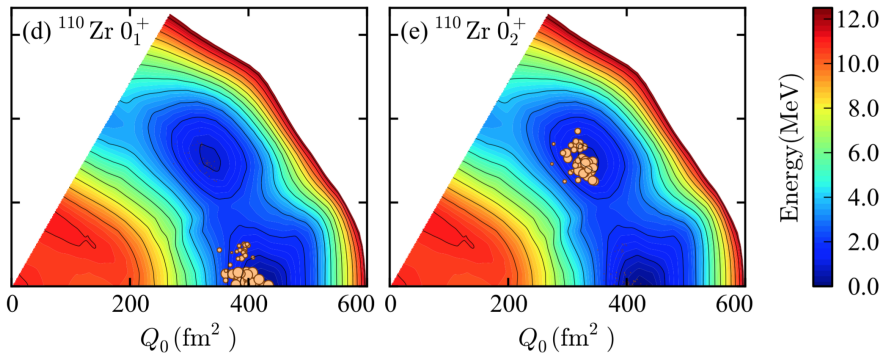

Figure 4.8. T-plots, analogous to collective wavefunctions for MCSM calculations of ^{110}Zr. Figure from [118].

neutron-rich nuclei.

The E_2^+ systematics in this region are shown in Figure 4.11, where measurements made within the SEASTAR collaboration are shown as open circles. The krypton and selenium measurements were published in [115, 116], respectively. The data in this work shows a continuation of the strong deformation in the zirconium isotopic chain that occurs after the N=60 subshell closure, with no significant difference from $62 \leq N \leq 70$. We also see that as protons are removed from the $g_{9/2}$ orbital, the strong onset of deformation at N=60, visible in the plunging E_2^+, becomes less dramatic and comparisons of the most neutron-rich measurements of the Zr, Kr, and Se isotopic chains with calculations suggest complicated shape coexistence. Precision measurements of the level structure of ^{110}Zr, notably the identification of the 0_2^+ state, could differentiate whether the tensor-force driven prolate deformation of the MCSM predictions or the the triaxial shape coexistence predicted by the mean field more accurately describes shell evolution beyond N=60 for these nuclei.

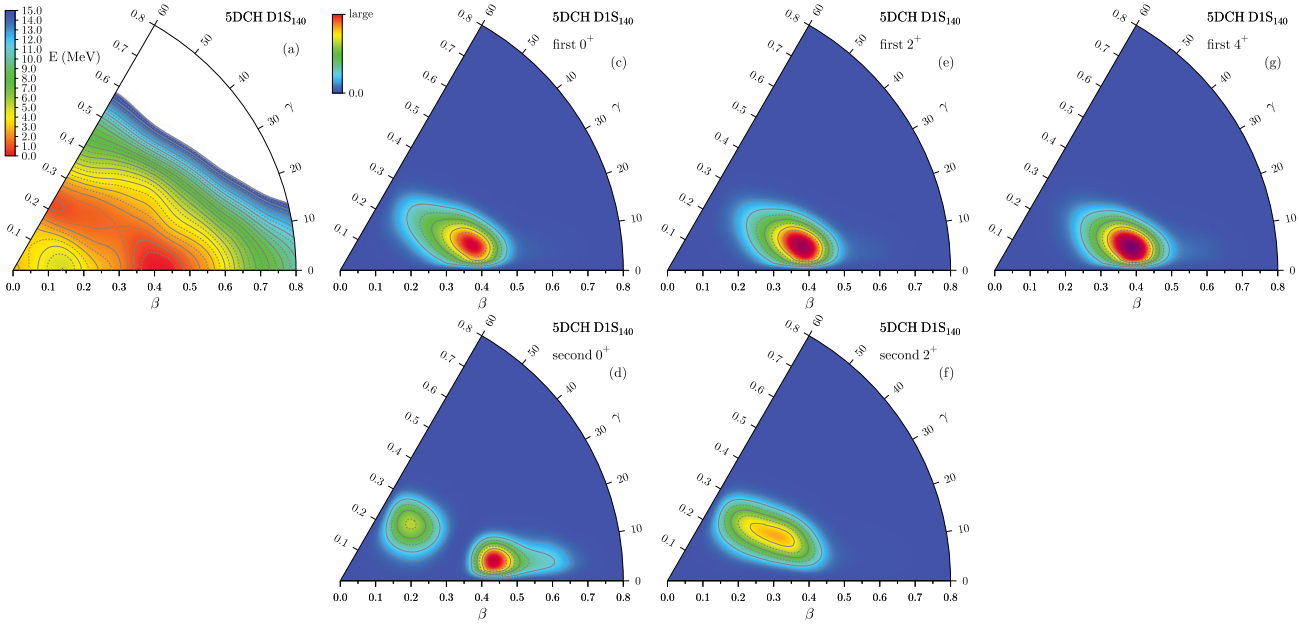

Figure 4.9. Potential energy surface and probability densities prepared in exactly the same way as Fig. 4.5, but using a modified Gogny D1S interaction for which the spin-orbit coupling constant has been changed from −130 to −140 MeV fm^5. Figure from [37].

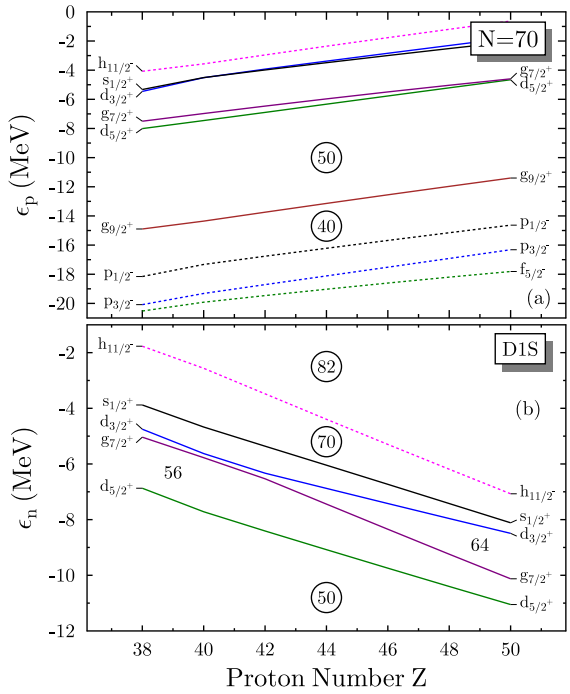

Figure 4.10. Spectrum of single-particle energies, i.e. the eigenvalues of the single-particle Hamiltonian, of protons (a) and neutrons (b) as obtained from spherical HFB calculations of even-even $N = 70$ isotones with the Gogny D1S force as a function of proton number Z. Solid (dotted) lines represent levels of single-particle states with positive (negative) parity. The colors indicate the states' mean value of total angular momentum.

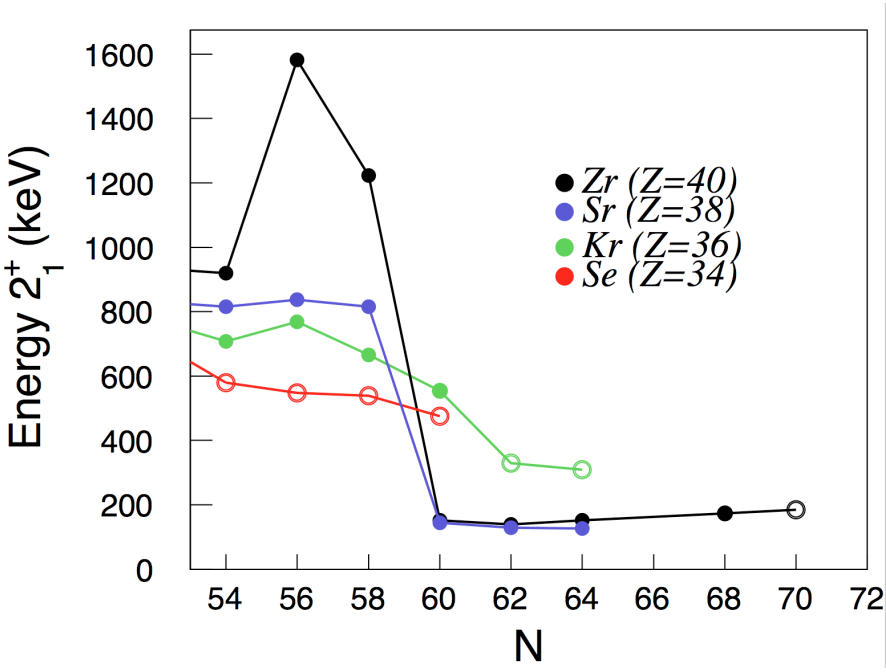

Figure 4.11. Systematics of E_2^+ beyond N=60. Data shown as open circles were measured as part of the SEASTAR campaign.

Part II.

Quasifree Scattering Cross Sections

How wonderful that we have met with a paradox. Now we have some hope of making progress.

Niels Bohr

5 Introduction

5.1. Quasifree Scattering

The birth of quasifree scattering studies may be traced to Berkeley, California in the early 1950s, when Owen Chamberlain and Emilio Segrè irradiated a lithium target with a proton beam at 350 MeV and observed proton pairs emerge in coincidence in the laboratory at approximately 90 degrees [119][1]. They interpreted the data via a model wherein the incident proton collided with a proton in the nucleus that could be considered as "free". Within this billiard-ball conception, the target can be described as an inert core and a valence proton, illustrated schematically in Figure 5.1. If the incident energy of the projectile is much larger than the binding energy of the nucleon to be removed, ideally between 200-800 MeV/u corresponding with the minimum in the nucleon-nucleon scattering cross sections, shown in Figure 5.1, the incident proton removes the valence proton via a single collision, known as the impulse approximation, with minimal distortion of the ingoing and outgoing channels [120, 121]. Of course the nucleon is indeed bound to the core, and Chamberlain and Segrè explained the small deviations from 90 degrees that they observed as originating from the binding energy of the valence proton and a small bit of excitation energy (5 MeV) given to the residual nucleus. These reactions were thus dubbed "*Quasi*free Scattering" (QFS).

Concurrent studies showed that the angular correlation of the pairs and the separation energy distribution of the knocked out proton corresponded to the momentum distribution and binding energy of the proton in the nucleus, respectively. Thus these reactions permitted to measure the properties of the nucleus, showing the power of QFS to probe structure [123]. A historical example of a (p,2p) energy spectrum is shown in Figure 5.3.

Complementary studies employed electron beams to remove valence protons. As only the Coulomb interaction is at play, electrons have a higher mean free path in the nucleus, perturbing less the core and allowing more interior orbitals to be probed. Reviews of the (p,2p) and (e,e'p) studies may be found in [124, 125, 126].

Under the assumption that the scattering occurs in one step, the nucleon removal cross section is proportional to the occupancy of the level probed, loosely referred to as the spectroscopic factor. If the cross section to a given single particle level is calculated, then the experimental cross section may be obtained via a factor loosely connected to the occupation probability of the level. This is shown in Equation 5.1, where σ_{sp} is the theoretical single particle cross section and SF is the spectroscopic factor. The ratio between experimental cross sections from (e,e'p) measurements and predictions

[1] Chamberlain and Segrè would later win the Nobel prize for the discovery of the antiproton, discussed in Part III as an alternative probe for nuclear structure.

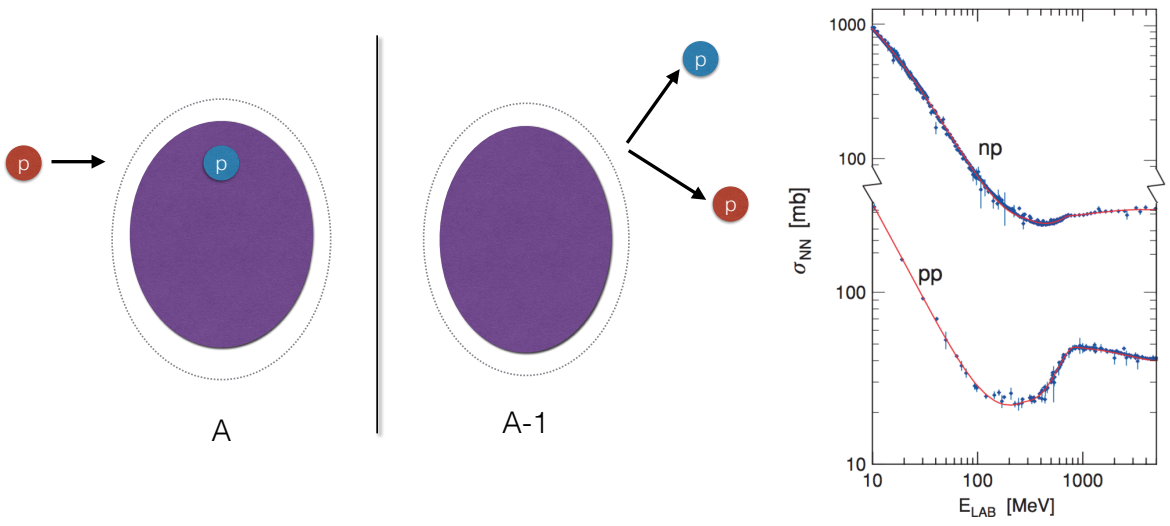

(a) **(b)**

Figure 5.1. (a) Schematic illustration of a quasifree scattering reaction.The incident proton (red) removes a valence proton from the nucleus, leaving the core mostly undisturbed. To minimize distortions in the entrance/exit channels, incident energies >200 MeV/u are used. (b) Nucleon-nucleon scattering cross sections. Figure from [122].

from the independent particle model have been systematically measured across a range of masses for quasifree scattering with electrons. The results, shown in Figure 5.2, reveal a ratio of 60-70%, evidencing a reduction of the experimental cross section compared to the independent particle picture, attributed to nucleon-nucleon correlations in the nucleus.

$$\sigma = SF \times \sigma_{sp} \tag{5.1}$$

5.2. Microscopic Description of QFS

Historically, the formal structure commonly used to describe quasifree scattering is the Distorted Wave Impulse Approximation (DWIA). This model assumes that the reaction proceeds principally via a single interaction between the projectile and removed nucleon. Multiple scattering and absorption of the entrance and exit channels are treated through distorted waves resulting from a mean nuclear potential. Following the formalism of [125], the DWIA transition amplitude for the reaction A(p,pN)B is

$$T_{p,pN} = \sqrt{S(lj)}\langle \chi_p^- \chi_N^- | \tau_{pN} | \chi_p^+ \psi_{jlm} \rangle \tag{5.2}$$

where $\chi_{p,N}^-$ are the distorted waves of the outgoing proton and nucleon, χ_p^+ is the distorted wave of the incoming proton, ψ_{jlm} is the bound state wavefunction of the removed nucleon, $\sqrt{S(lj)}$ is the spectroscopic factor for a bound nucleon with quantum numbers l,j, and τ_{pN} is the two-body scattering matrix. Standard DWIA calculations give good agreement for exclusive QFS measurements, as may be seen in the historic example in Figure 5.3.

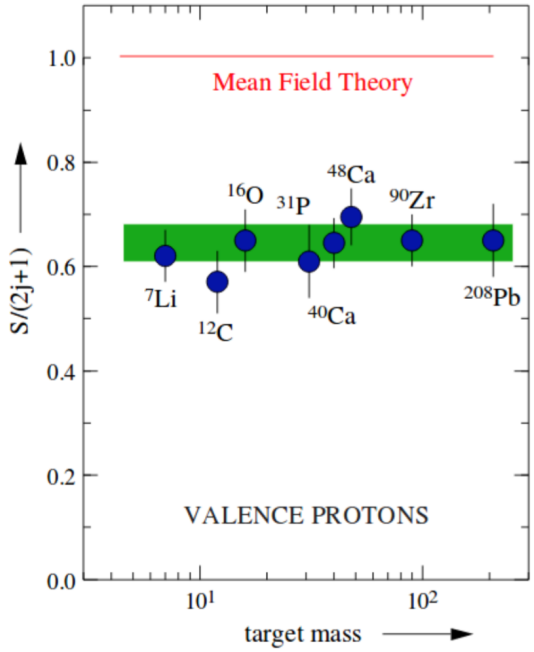

Figure 5.2. Ratio between experimentally measured (e,e'p) cross sections and predictions from the Independent Particle Model. Figure modified by M. Gomez-Ramos from [127].

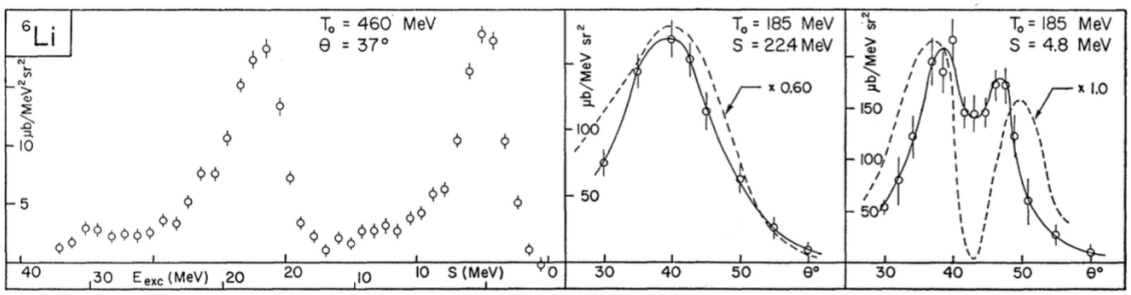

Figure 5.3. Energy spectrum and angular correlations for ^{6}Li (p, 2p)^{5}He. The dotted lines are DWIA calculations multiplied by the indicated factors. Figure from [124].

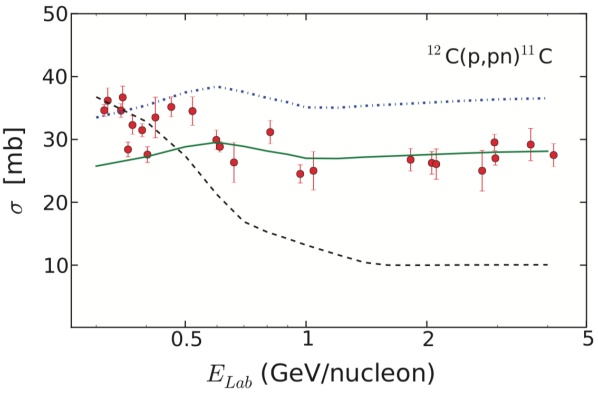

Figure 5.4. Experimental data for (p,pn) cross sections from ^{12}C at different energies (red points) compared with DWIA predictions within the eikonal approximation (dashed-dotted blue line), and these DWIA predictions multiplied by 0.77 (solid green line). Figure from [128].

A simplification may be obtained if the projectile and outgoing protons are assumed to follow straight line trajectories–known as the eikonal approximation [128]. Recent results for neutron removal from carbon isotopes is shown in Figure 5.4. Good agreement is found with the global trend of the data, though calculations overestimate the experimental cross section by ∼20%. The discrepancy may be attributed in part to the fact that these measurements are inclusive and thus non-QFS events may be present, particularly inelastic excitation of the core at low energies. Fully exclusive measurements such as those recently demonstrated in [129] may provide more useful comparison with calculations, and are the target of future experimental campaigns for example at R3B at GSI, at SAMURAI at RIKEN.

5.3. Knockout Reactions

The advent of radioactive ion beam facilities in the 1980's ushered in a new era, with the ability to perform nucleon removal reactions in inverse kinematics and probe the structure of exotic species [130]. Due to the difficulty of working with proton targets, experiments commonly employed composite targets like carbon or beryllium. The outgoing projectile and the removed nucleon are generally not detected, rather the properties of the (A-1) core including its momentum and the cross sections to individual valence states are studied. See [131] for an overview. Within these conditions, the QFS paradigm can no longer be invoked, but due to the simplicity of the method to easily populate and study the low-lying states in exotic species, experiments abounded under the general term of "knockout reactions". These reactions have a large cross section, and are highly peripheral, as deep penetration of the projectile into the nucleus generally leads to breakup of the core.

Though the interaction between the projectile and the core are more complicated in knockout reactions, the peripherality of these reactions permits the same approximations used to describe quasifree scattering–the impulse and eikonal approximations. As depicted in Figure 5.1, the projectile removes the nucleon via a single hit with minimal interaction with the core, and both the projectile and removed nucleon follow outgoing straight-line trajectories. It is assumed that processes involving a strong interaction between the projectile and the target do not contribute to the cross section. The cross section may then be expressed as the sum of stripping and diffraction components, shown in Equations 5.3,5.4, respectively. The stripping component describes the removal of the nucleon including interaction with the core, leaving the core in an excited state. The diffraction component

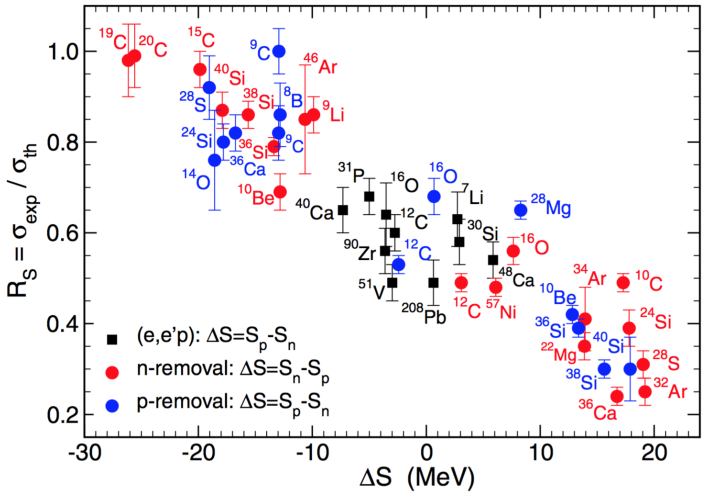

Figure 5.5. Ratio between experimental and theoretical inclusive cross sections as calculated within the S-matrix formalism, as a function of neutron-proton asymmetry. Figure from [133].

describes the removal of the nucleon while leaving the target in its ground state. In these expressions, S_n, S_c are the S-matrices that describe the nucleon-projectile and core-projectile systems, related to the survival probabilities of the nucleon and core. ϕ is the removed nucleon-core relative motion wavefunction. In this case, the S-matrices are determined from phenomenological complex optical potentials [132].

$$\sigma_{str} = \int db \, \langle \phi | \, (1 - |S_n|^2) |S_c|^2 \, | \phi \rangle \tag{5.3}$$

$$\sigma_{diff} = \int db \, \langle \phi | \, |1 - S_c S_n|^2 \, | \phi \rangle - | \, \langle \phi | \, 1 - S_c S_n \, | \phi \rangle \, |^2 \tag{5.4}$$

The relative simplicity of the S-matrix formalism has led to its application to a multitude of single nucleon removal reactions from composite targets. However, divergences are seen when describing deeply bound nucleon removal, seen in Figure 5.5, which shows the ratio of experimental and theoretical inclusive cross sections calculated with the S-matrix formalism combined with Shell Model inputs, as a function of proton-neutron asymmetry $\Delta S = (S_n - S_p)$ for neutron removal, or $(S_p - S_n)$ for proton removal. It is clear that moving towards more deeply bound nucleon removal (large ΔS in Figure 5.5), the theory increasingly overestimates the cross section. This has been attributed to missing correlations between removed nucleon and the rest of the core that become significant when the nucleon is deeply bound [133] or invalidity of the eikonal approximation in the energy regime studied [134].

It should be noted that this slope of R with asymmetry is a new feature not seen in electron scattering as shown in Figure 5.2, nor in transfer reactions [135, 136, 134] as may be seen in Figure 5.6. The origin of this discrepancy is still an active subject of debate in the community, and is part of the motivation of recent quasifree scattering studies, such as the work undertaken here.

5.4. Semi-Microscopic Techniques

The microscopic methods previously presented are adept for single nucleon removal. However when describing broad fragmentation or spallation data including single and multinucleon removal, semi-

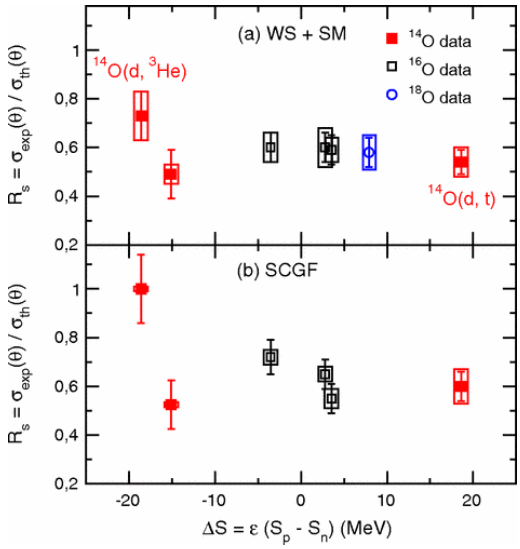

Figure 5.6. R calculated with two different microscopic models as a function of asymmetry for transfer reactions at 18 MeV/A. Figure from [137].

microscopic methods may be instead employed. With few parameters fit on stable data, they offer the ability to predict a broad range of reaction data within the same framework with minimal computational burden. These methods may also be useful where detailed structure information is not known, as in the very exotic nuclei studied in this work.

The semi-microscopic methods used here–the Fragmentation-Evaporation (FE, also called Glauber) framework, and the Liège Intranuclear Cascade Model (INCL)–are two step collision and de-excitation models. In the first step, binary collisions occur between nucleons, obeying essentially classical kinematics. After a certain timescale, the collisions are stopped and the energy left in the system is released with an evaporation code for gamma and particle emission. As will be seen in the following sections, FE and INCL differ principally in the geometry within which the collisions take place, and the way that the excitation energy of the fragment is calculated.

5.4.1. Fragmentation-Evaporation

The Fragmentation-Evaporation (FE), or Glauber framework [138], models nucleon removal as a collision between two spheres of nucleons, and differentiates between the strongly interacting region (the collision zone), and the non-interacting region (the spectator zone). Binary collisions may occur between nucleons in the collision zone along a cylindrical tube whose longitudinal axis is defined by the momentum of the projectile, and radius defined by the impact parameter of the reaction. Nucleons outside the collision zone remain undisturbed. The model assumes that whenever a collision occurs, the participant nucleons are ejected from the projectile. Following the formalism in Section 8.3 of [139], the abrasion cross section[2] from a given projectile nucleus $(Z, N)_p$ to a fragment $(Z, N)_f$ is given by Equation 5.5, where P_n and P_z are the single neutron and proton survival probabilities, and b is the impact parameter. As the identity of the fragment is defined by the case where the neutrons and protons are stripped, the integral is over $1 - P_n$, $1 - P_z$. The prefactor before the integral is a binomial coefficient that accounts for all the ways of obtaining $(Z, N)_f$ from $(Z, N)_p$.

[2]The term abrasion is used to indicate the stripping or direct removal of nucleons during collisions.

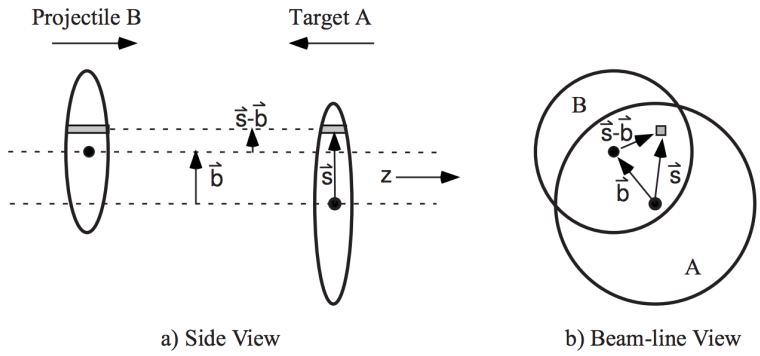

Figure 5.7. Schematic of reaction geometry in Fragmentation framework. Figure from [140].

$$\sigma_{abrasion} = N(Z_p, N_p; Z_f, N_f) \int d^2b \left[1 - P_p(b)\right]^{Z_p - Z_f} P_p(b)^{Z_f} \left[1 - P_n(b)\right]^{N_p - N_f} P_n(b)^{N_f} \tag{5.5}$$

Considering for example single neutron removal, the single nucleon survival probability is given by

$$P_n(b) = \int ds dz \rho_n^P(s,z) \exp\left[- \sigma_{nn} Z_T \int dz \rho_p^T(b-s,z) - \sigma_{pn} N_T \int dz \rho_n^T(b-s,z) \right] \tag{5.6}$$

Note that here, an interaction potential does not enter explicitly, rather we find the neutron-neutron (σ_{nn}), proton-neutron (σ_{pn}), and proton-proton (σ_{pp}) total cross sections obtained from a fit to experimental data as in [122]. Th proton and neutron densities, ρ_p, ρ_n may be obtained from HFB calculations. The superscripts T and P indicate the target and projectile, respectively, and s is the radius of the overlapping tube where the calculation is performed, as shown in Figure 5.7. An equivalent expression may be written for $P_p(b)$.

The excitation energy of the residual nucleus after the fragmentation step is calculated based on the energy of the resultant particle hole configuration. Each removed nucleon leaves a hole state, and then the density of states, $\rho(E_x, Z_f, N_f)$ is obtained by counting the possible configurations of the resultant hole states consistent with the identify of the fragment. The distribution is normalized such that the lowest level is the ground state. The single particle energies come from HFB calculations of the parent nucleus, under the assumption that no mean-field rearrangements have time to occur within the abrasion stage. Note that all particle-hole configurations generated through the abrasion process are treated as equally likely, and the preferential population of certain configurations based on structure overlap is not treated. The cross sections for a given excitation energy are then calculated according to

$$\frac{d\sigma}{dE_x} = \rho(E_x, Z, A)\sigma_{abrasion} \tag{5.7}$$

Unbound fragments are de-excited using an evaporation code based on the Weisskopf-Ewing formalism [141]. Within this framework, the decay width of an initial nucleus with excitation energy E_i into a final nucleus with excitation energy E_f via emission of a particle ν with kinetic energy ϵ_ν is given by

$$\Gamma_\nu(E_i) = \frac{2s_\nu + 1}{2\pi\rho(E_i)} \frac{2m_\nu}{\pi\hbar^2} \int_0^{E_i - S_\nu - B_\nu} \sigma_c(\epsilon_\nu)\rho_f(E_f)(\epsilon_\nu - B_\nu)dE_f \tag{5.8}$$

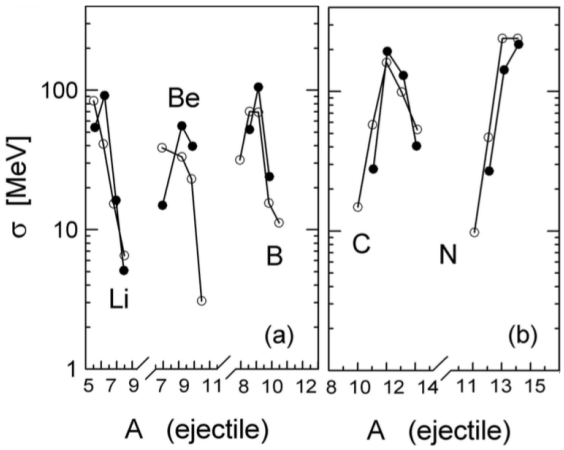

Figure 5.8. Yields from the ^{16}O+ ^{208}Pb reaction as calculated with the FE formalism are shown as full circles. Open circles are experimental data from [146]. Figure from [139].

In this expression, s_ν is the spin of the emitted particle, $_\nu$ is the mass of the emitted particle, σ_c is the inverse cross section for particle emission, ρ_i and ρ_f are the level densities of the initial and final nuclei, S_ν is the nucleon separation energy, and B_ν is the Coulomb barrier for charged particle emission. The level densities are based on a Fermi-gas model [142]. Modern evaporation codes like ABLA07 [143] include additional refinements such as changes in the decay width based on the angular momentum of the emitted particle, and vibrational and rotational enhancement of level densities.

The final secondary yield is then given by integrating over the product of the evaporation probability, which may be obtained from Equation 5.8 and the abrasion cross section for a given excitation energy from Equation 5.11 according to

$$\sigma_{FE}(Z,A) = \sum_{Z_f,A_f} \int dE\, P_{evap}(Z,A;E,Z_f,A_f) \frac{d\sigma}{dE}(E,Z_f,A_f) \tag{5.9}$$

Fragmentation-Evaporation (FE) calculations have been used to describe single and many nucleon removal from heavy-ion collisions for the last half a century [144], and provide good overall agreement for fragmentation data, as may be seen in Figure 5.8. However, systematic overestimations of the cross section appear when this method is applied to single deeply bound nucleon removal, as seen in Figure 5.9 from [145] which shows the experimental inclusive single nucleon removal cross sections along the tin isotopic chain compared with FE predictions. The black line shows the primary yields before evaporation, the dashed blue line is the cross section after evaporation, and the dotted blue line is when the excitation energy has been phenomenologically enhanced. The figure shows that when loosely bound nucleons are removed, for example protons at mass 104, or neutrons above mass 110, good agreement is found. However when more deeply bound nucleons are removed, for example protons from isotopes with $A \geq 110$, the FE predictions overestimate by a factor of 2 the cross section, and good agreement may be found only by artificially enhancing the excitation energy of the fragment before evaporation.

5.4.2. INCL

A similar semi-microscopic framework is the Liège Intranuclear Cascade Model [147, 148, 149]. Within the binary collision step of INCL, no differentiation is made between participant and spectator

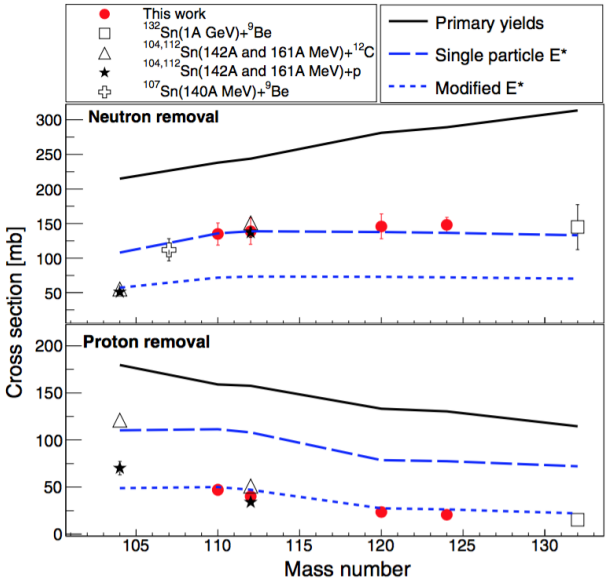

Figure 5.9. Inclusive cross sections for the Sn isotopes measured at GSI compared with Fragmentation-Evaporation (FE) predictions (blue dashed lines), and FE predictions where the excitation energy has been phenomenologically enhanced (blue dotted lines). Figure from [145].

nucleons, rather all collide within a square potential well whose radius depends on the nucleon's kinetic energy. The nucleons are followed individually as they traverse the spherical volume, and emission of nucleons and light clusters is possible. The collisions are allowed to continue until the system shows signs of thermalization, determined dynamically based on the excitation energy evolution of the system. The kinetic energy of the system in the lab frame at any moment of the collision process can be written as

$$T_{lab} = \sum_{j=1}^{A_{ej}} \bar{T}_j + W_\pi + \sum_{i \in A_{rem}} \bar{T}_i - \left[T_i^0 - (A_T - A_{rem}) T_F \right] + S \tag{5.10}$$

where A_{ej} is the number of ejected nucleons, $\bar{T}_j$ is the kinetic energy of the ejected nucleons, W_π is the total energy of the pions, A_T and A_{rem} are the number of nucleons in the target (parent) and remnant, respectively, T_i^0 is the initial kinetic energy of the nucleons in the remnant, $\bar{T}_i$ is the final kinetic energy of the nucleons in the remnant, T_f is the fermi kinetic energy of the nucleus, and S is the total separation energy of the projectile, i.e. the energy required to remove $A_T - A_{rem}$ nucleons. Note that in standard INCL calculations, S is for simplicity taken as the total separation energy of the parent nucleus. Equation 5.10 may be understood as the sum of the kinetic energy of the ejected nucleon and pions, the excitation energy of the nucleus, and the separation energy liberated by removing the nucleons, respectively. When the collisions are stopped, the excitation energy of the fragment is then given by Equation 5.11. This energy is evaporated via gamma and particle emission with an evaporation code, in our case ABLA07 [143].

$$E^* = \sum_{i \in A_{rem}} \bar{T}_i - \left[T_i^0 - (A_T - A_{rem}) T_F \right] \tag{5.11}$$

Most recent versions of INCL have the additional feature that fluctuations of the surface of the potential well are permitted, controlled by a fuzziness parameter, f (0<f<1). This empirically

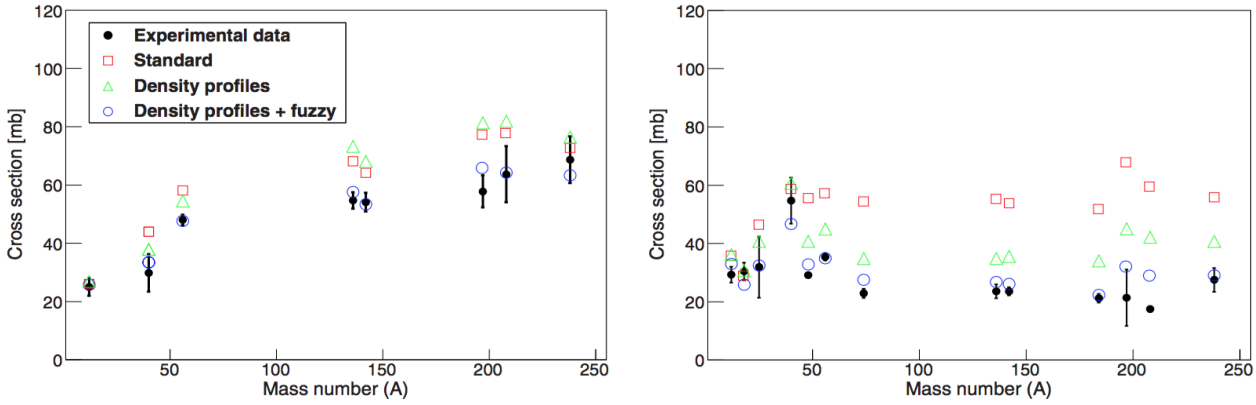

(a) (b)

Figure 5.10. Single neutron (a) and proton (b) removal cross sections for proton-induced reactions at 1 GeV kinetic energy as a function of the target mass. The blue circles indicate the most recent INCL calculations including HFB densities and fuzziness parameter. Figure from [145].

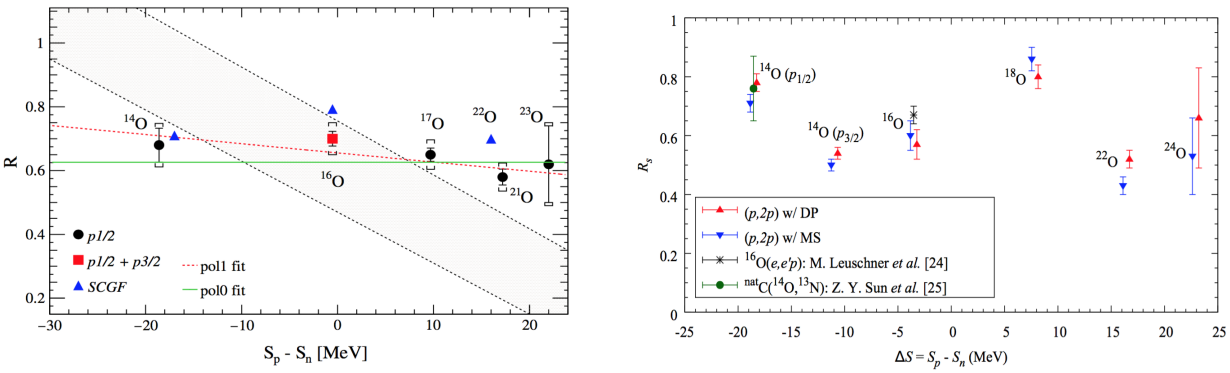

(a) (b)

Figure 5.11. Recent results showing the ratio of experimental and theoretical exclusive cross sections for the QFS on oxygen isotopes from [150](a) and [151](b).

determined parameter smears out the surface of the potential well, mimicking the quantum effect wherein a nucleon may be found beyond its classical turning point, and consequently increases the probability that a deeply bound nucleon may be removed from a surface collision [148] . This phenomenological adjustment is aimed at improving the description of deeply bound nucleon removal, such as those studied in this work. Good agreement is found for one neutron and one proton removal cross sections from stable nuclides at energies around 1 GeV, as shown in Figure 5.10.

5.5. Current State of Affairs

The various methods presented here to describe single nucleon removal with proton or composite targets are linked by two common themes. First, microscopic calculations systematically overpredict inclusive cross sections, as seen in Figures 5.4 and 5.5, a long-known problem that has been attributed to missing correlations in the reaction mechanism, or invalidity of the assumptions employed in the reaction mechanism formalism as suggested by comparison with transfer studies, shown in Figure 5.6.

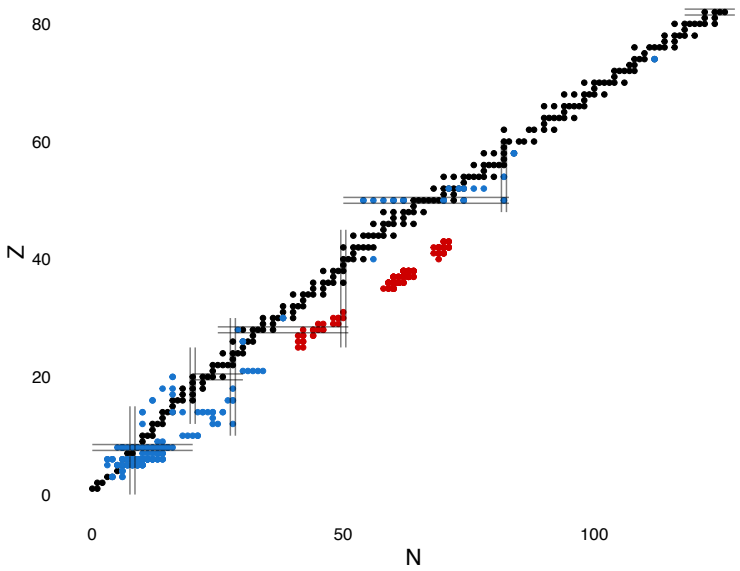

Figure 5.12. Chart of the nuclides showing existing single nucleon removal inclusive cross section studies at intermediate energy (blue), and the cross sections measured in this work (red).

Semi-microscopic models show similar trends, as seen in Figure 5.9, though the agreement is expected to be worse based on the lack of structure information and the fact that the few free parameters in the models are generally fit on stable data.

Secondly, both microscopic and semi-microscopic methods are poorly benchmarked when moving towards more exotic species. Figure 5.12 shows in blue the existing cross section studies of single nucleon removal reactions at intermediate energies. Some studies have moved away from stability for light nuclei, but very little data exists for medium and heavy mass neutron rich nuclei. The existing nucleon removal studies away from the valley of stability have largely employed composite targets at energies around $\sim$ 100 MeV/u, revealing the asymmetry dilemma of Figure 5.5.

For these reasons, there has been a recent refocus on quasifree scattering experiments using proton targets to try to understand the single nucleon removal reaction mechanism, within the cleanest experimental conditions possible–i.e. with proton targets at energies >200 MeV/u. Ideally fully exclusive measurements may be performed, as recently demonstrated in [129], for a most realistic comparison with microscopic theories. Two recent quasifree scattering studies of the oxygen isotopes have shown promising results, as shown in Figure 5.11. The experiments, conducted at RIKEN (250MeV/u) and GSI (300-400 MeV/u), measured the exclusive cross sections to low lying states across a broad range of asymmetries. When compared with both S-matrix based and state-of-the-art *ab initio* calculations, though a 20% reduction factor is found, no slope appears with ΔS and the methods show consistent results amongst each other. In the following, we have explored QFS through inclusive measurements of neutron-rich nuclei far from stability, shown in red, and extend significantly the available systematics for single nucleon removal studies, particularly for large neutron-proton asymmetries in medium mass nuclei.

6 Analysis

6.1. Experimental Setup: SEASTAR 2014-2015

The cross sections presented in this work were obtained from the SEASTAR campaigns of 2014 and 2015 at the RIBF. The setup, common to both campaigns, was presented in detail in Part 1, and utilized a ^{238}U primary beam whose fission fragments impinged on a 10 cm liquid hydrogen target at the F8 focal plane of the BigRIPS spectrometer. Resulting reaction products were identified in the ZeroDegree spectrometer. The principal variable components of the setup during these experiments were the magnetic settings of the spectrometers, centered according to the nuclei of interest. The settings for the two campaigns and rates for some of the principal nuclei of interest at the F7 focal plane are shown in Table 6.1.

6.2. How to Measure a Thick Target Cross Section?

First consider the general expression used to calculate thick-target cross sections, which will put in perspective the quantities that need to be extracted from the analysis procedure. Consider a thick target of length L, and a (p,2p) reaction that occurs at a position x inside the target, as shown in Figure 6.1. The number of projectile ions incident on the target is N_0, the number of daughter ions detected after the target is $N_f(L)$. Taking an infinitesimal target thickness dx at position x the attenuation of the incident beam is due to flux to other reactions and scattering. This is shown in Equation 6.2, where σ_R is the reaction cross section and η is the density of the target in atoms/cm^3. This differential equation may then be solved trivially to attain the number of projectile ions at position x, $N_i(x)$, also shown in Equation 6.2, where N_0 is the number of incident nuclei at the beginning of the target.

$$dN_i = -N_i \sigma_R \eta dx \tag{6.1}$$

$$N_i(x) = N_0 e^{-\sigma_R \eta x} \tag{6.2}$$

Table 6.1. Summary of settings for SEASTAR campaigns.

SEASTAR	Setting	E_{mid} (MeV/u)	rate (pps)
2015	^{111}Nb	201	20
	^{95}Br	213	50
	^{101}Rb	215	16
2014	^{67}Mn	238	12
	^{73}Co	225	6
	^{80}Zn	227	260

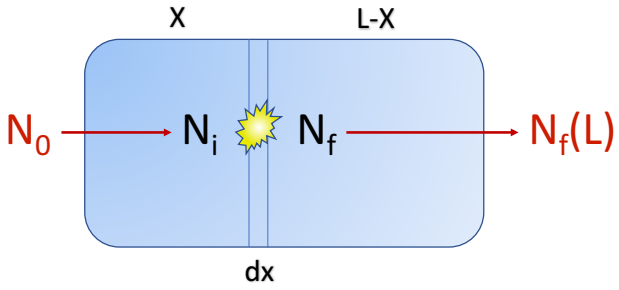

Figure 6.1. Schematic of a reaction occurring at position x along the beam axis in a target of length L.

Similarly, consider the infinitesimal change in the number of daughter nuclei of interest at position x, $N_f(x)$. Daughter nuclei are created due to the incident nuclei according to the (p,2p) cross section, and the existing daughter may also be destroyed due to attenuation in the target. Assume for simplicity that the reaction cross section for destruction of the daughter is the same as for the projectile, this assumption is validated later in the analysis. The differential equation for N_f is shown in Equation 6.3. This expression is an example of a first order differential equation that may be solved via an integrating factor, according to Equation 6.4.

$$\frac{dN_f(x)}{dx} + \sigma_R \eta N_f = \sigma_{p2p} \eta N_i \tag{6.3}$$

$$\begin{aligned} \frac{dy}{dx} + p(x)y &= q(x) \\ y &= \frac{\int_0^x u(x')q(x')dx' + C}{u(x)} \\ u(x) &= \exp\left\{\int_0^x p(x')dx'\right\} \end{aligned} \tag{6.4}$$

Applying this solution to the differential equation 6.3, and inserting the previously obtained expression for $N_i(x)$, we obtain the expression for the number of daughter nuclei at any position in the target, $N_f(x)$.

$$\begin{aligned} N_f(x) &= \frac{\int_0^x e^{\sigma_R \eta x'} N_0 \eta \sigma_{p2p} e^{-\sigma_R \eta x'} dx'}{e^{\sigma_R \eta x}} \\ &= \frac{N_0 \sigma_{p2p} \eta x}{e^{\sigma_R \eta x}} \end{aligned} \tag{6.5}$$

This expression can then be evaluated at the end of the target to obtain $N_f(L)$, the experimentally measurable quantity.

$$N_f(L) = \frac{N_0 \sigma_{p2p} \eta L}{e^{\sigma_R \eta L}} \tag{6.6}$$

In principle, the attenuation of the beam, $e^{\sigma_R \eta L}$ may be obtained by measuring the direct beam transmission $N_i(L)/N_0$. In reality however what is measured is rather $\epsilon e^{\sigma_R \eta L} \equiv T$ which includes the

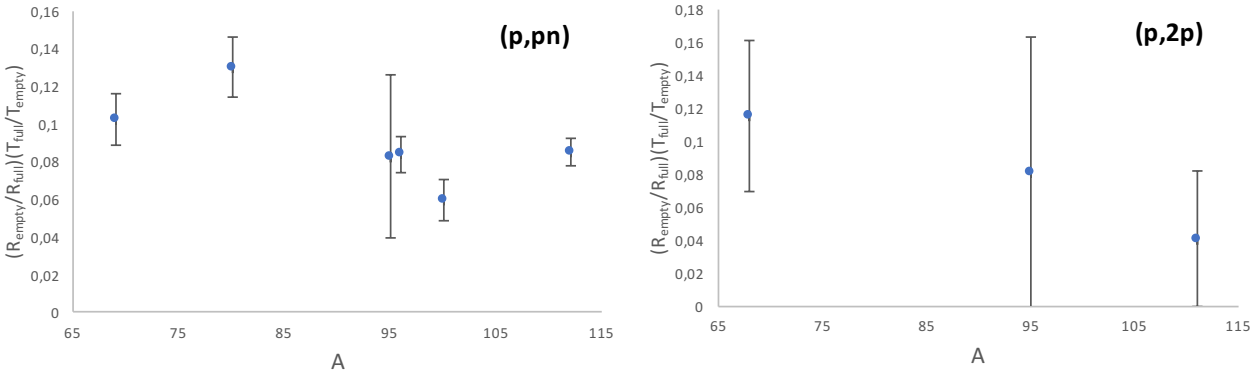

Figure 6.2. $(R_{empty}/R_{full})(T_{full}/T_{empty})$ for (p,pn) and (p,2p) channels. The mass of the projectile is indicated.

detection efficiency and transmission through the beamline. Inserting this into the expression above we obtain the (p,2p) cross section

$$\sigma_{p2p} = \frac{N_f(L)}{N_0 \eta L T} = \frac{R}{\eta L T} \tag{6.7}$$

The fundamental quantity extracted from the experiment is the daughter to parent ratio, R.

In reality, the beamline material before and after the target can contribute to either create or attenuate the daughter nuclei of interest. For this reason, the contribution of the beamline elements to the channel of interest must be considered, meaning that the real (p,2p) cross section is given by

$$\sigma_{p2p} = \frac{R(1-\gamma)}{\eta L T} \tag{6.8}$$

where $\gamma = \frac{R_{empty}}{R_{full}} \frac{T_{full}}{T_{empty}}$ is the percentage of daughter nuclei contributed by the empty target and beamline elements. This expression is derived in Appendix D. The (p,2p) and (p,pn) beamline contribution as measured from high statistics channels are shown in Figure 6.2. Practically, due to limited statistics it was impossible to extract $R_{empty}^{p2p,ppn}$ for every channel. R_{empty}^{ppn} could be extracted using the F5X fit method for approximately one channel per setting. Statistics prohibited the extraction of R_{empty}^{p2p} using the fit method, therefore central channels were selected and simply the number of counts of the daughter nucleus in ZeroDegree were compared to the number of counts of the incident parent. The empty target contributions for both (p,2p) and (p,pn) are higher for 2014 data (A<90 in the figure above) relative to 2015 data, as expected due to the presence of a double-sided silicon strip detector before the LH2 target in 2014. This detector is expected to contribute approximately 30% more scattering centers, consistent with relative increase seen in the γ factor. As γ is expected to be a constant for a given setup, $\gamma_{ppn}^{2015,2014}$ were taken to be 0.08(2) and 0.12(2), respectively. $\gamma_{p2p}^{2015,2014}$ were taken as 0.08(8) and 0.12(4), respectively. The uncertainty on γ accounts for the dispersion in the data.

6.3. PID

As explained in Part 1, to obtain an unambiguous PID, the ZeroDegree beamline elements must be calibrated. This requires adjusting time-of-flight offsets and making phenomenological corrections to

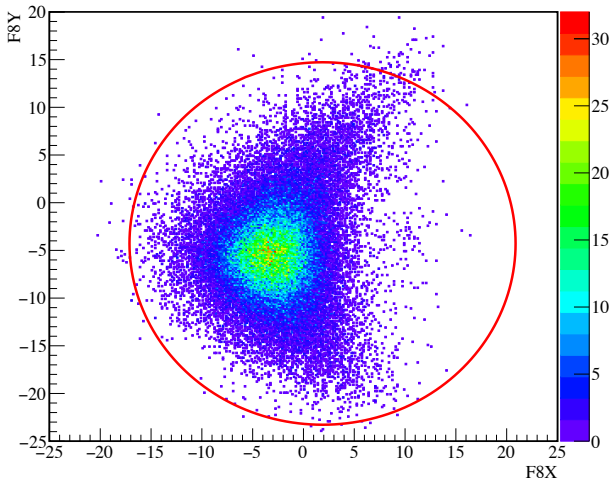

Figure 6.3. Reconstruction of beam that passes through LH2 target at target entrance window (focal plan F8), triggered on F7, F11, and DALI, and corresponding cut on the target entrance window.

A/q and Z, described in detail for the ^{110}Zr analysis. The PID corrections for each setting are shown in Appendix C. Once clean PID spectra were obtained for a given setting, cuts on the ingoing/outgoing nuclei of interest were defined by hand. Despite this rudimentary manner of making PID cuts, testing multiple equivalent cuts showed that the uncertainty in the number of counts with this method is 0.3%, much smaller than the corresponding statistical uncertainty. Note that only events that triggered the downscaled beam trigger were counted, i.e. Fbit=1,3, or 7 for SEASTAR2015, and the equivalent for SEASTAR2014, though the numbers are different, Fbit=5,13, or 15. See the previous section on the ^{110}Zr analysis for an explanation of trigger patterns.

6.4. Other Cuts

As for the ^{110}Zr analysis, cleaning cuts were applied to the F3, F7, F8, and F11 plastic detectors to remove unwanted noise. Examples of these cuts for the ^{111}Nb setting were already presented in the previous section. Charge states were also removed from the ZeroDegree spectrometer, when present, as described in the previous chapter for the ^{110}Zr analysis. Their presence should however make no contribution to the cross section, as they are removed from the transmission runs as well. Analysis of the ^{80}Zn setting with and without cleaning cuts showed that the cross section calculated both ways agreed to 1% or better, taken as a source of systematic uncertainty.

A cut was also applied to the beamspot on the target entrance window at F8, as reconstructed by the PPAC detectors. This cut ensures that all the nuclei considered for the cross section calculation actually impinge on the LH2 target. This cut was defined by considering a direct beam run and demanding only events that trigger F7, F11, and DALI. The DALI condition insures that the beam passed through the target, as Bremsstrahlung in the target dominates the DALI spectrum at low energy. These conditions yield a beam spot at F8 as shown in Figure 6.3, upon which a 19 mm radius circle was drawn, corresponding to the size of the target entrance window. Note that the missing counts on the right hand side are due to ZeroDegree acceptance effects. The F8XY cut was checked by making a smaller 10 mm radius cut, and the results were found to be consistent.

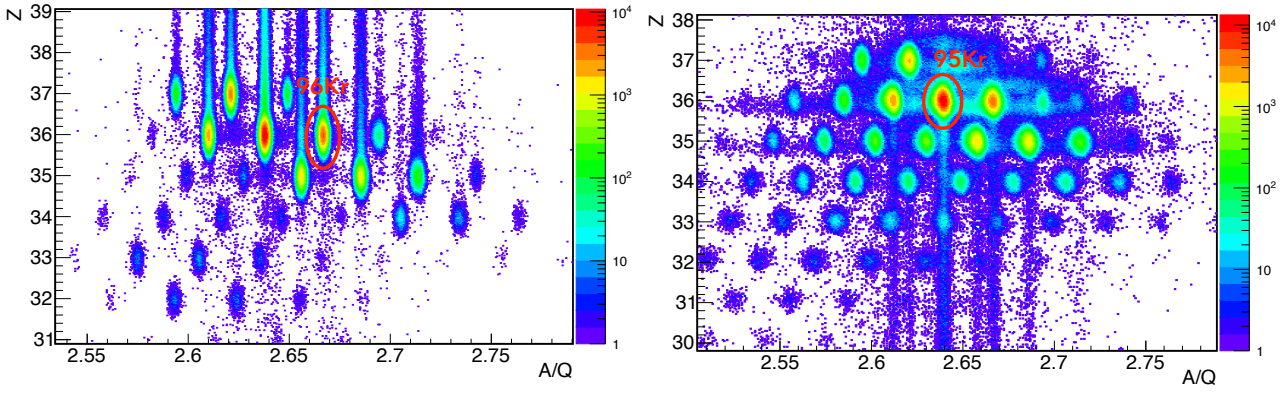

(a) **(b)**

Figure 6.4. PID plot showing ^{96}Kr in BigRIPS (a) and the reaction products of ^{96}Kr in ZeroDegree (b) from which ^{95}Kr may be identified for the neutron removal analysis.

6.5. Ratio extraction

The heart of the cross section measurement is the determination of R, as shown in Equation 6.8. To demonstrate how this ratio is obtained, consider the example, ^{96}Kr(p,pn)^{95}Kr. For the physics runs, ^{96}Kr is selected in the BigRIPS PID plot, and ^{95}Kr coincident with the ^{96}Kr projectile is selected in the ZeroDegree PID plot, as shown in Figure 6.4, demanding only events that triggered the downscaled beam detector before the target. If the acceptance of the ZeroDegree spectrometer were 100%, this would be sufficient to obtain R. However, as ZeroDegree is operated in large acceptance achromatic mode with a momentum acceptance of 3% [152], and the change in Bρ for single nucleon knockout ranges from 2.5 to 3% for the considered nuclei, acceptance effects need to be considered for all non-central trajectories.

This is done by examining the position distribution in the BigRIPS dispersive focal plane, F5. Figure 6.5(a) shows the F5X distribution for ^{96}Kr in BigRIPS (black), and then the part of this distribution that yields ^{95}Kr in ZeroDegree (red). The red distribution is clearly cut at low F5X. The origin of this cut may be seen by examining the dispersive focal plane in ZeroDegree, F9X, as shown in Figure 6.5(b), where the ^{96}Kr direct beam is shown in black, the ^{95}Kr resulting from the (p,pn) reaction in the target is shown in blue, and for reference the ^{95}Br resulting from (p,2p) in the target is shown in red. It is clear that the ZeroDegree spectrometer is optimized for the (p,2p) channel, and that the (p,pn) channel is cut by the slits at high F9X, which maps to low F5X.

There are two possibilities to account for these acceptance effects. The first is to have knowledge, either from a simulation or via extraction from the data, of acceptance of each channel considered. This approach may be useful particularly when the statistics are limited. Alternatively, the regions where the acceptance is shown to be <100% may be excluded from the analysis. The latter path was chosen due to uncontrolled uncertainty associated with extraction of acceptance values from simulations or data.

Identifying the regions where acceptance was <100% was done by taking the ratio of the F5X distributions with a PID cut on the parent nucleus in BigRIPS, and with PID cuts on the parent in BigRIPS and daughter nuclei in ZeroDegree. Both distributions include all downscaled beam triggers. The F5X ratio plot for the ^{96}Kr(p,pn)^{95}Kr example case is shown in Figure 6.6. The cut at low x (corresponding to large F9X) is clearly seen, and the flat region may be fit to extract directly R. R values for this analysis range from 0.00036 to 0.017. Note that this method requires relatively high

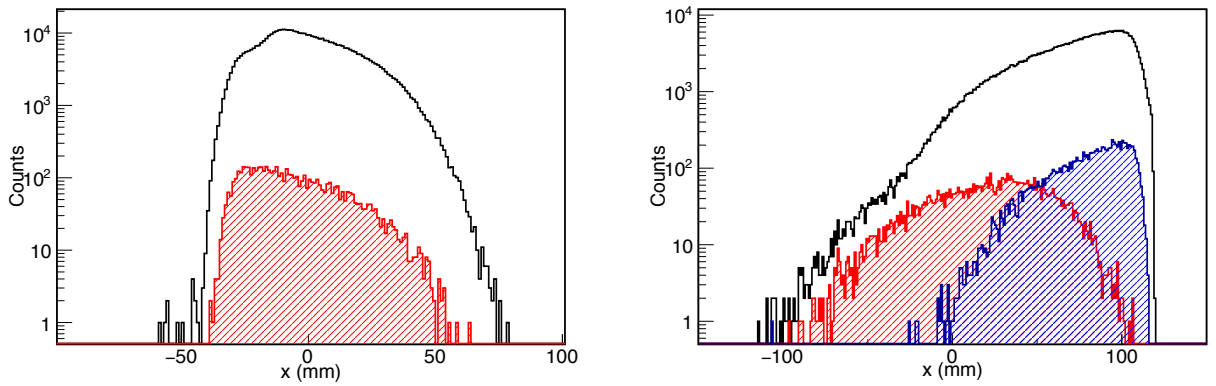

(a) **(b)**

Figure 6.5. (a) ^{96}Kr (black) distribution in the BigRIPS dispersive focal plane, and the part of the ^{96}Kr distribution that yields ^{95}Kr in the ZeroDegree spectrometer (red). (b) ZeroDegree dispersive focal plane distributions (F9) for ^{96}Kr (black) direct beam,^{95}Kr (blue) resulting from ^{96}Kr(p,pn) in the target, and ^{95}Br (red) resulting from ^{96}Kr(p,2p) in the target.

statistics in order to differentiate between flat and non-flat regions, thus no low statistics channels are reported here. Any channels where a flat region could not be clearly identified, by the automatic fitting routine and later verified by eye, were removed. In practice, the inverse ratio, $\frac{N_0}{N_f} = 1/R$, was fit for the simplicity of working with whole numbers.

As our data obeys Poisson statistics, a weighted-log-likelihood method was used to determine the fit parameters. The fit limits were calculated dynamically by determining the largest region where a flat line could be fit with a statistical probability (1 - statistical p-value) of greater than 0.001 [1]. A study was performed to determine the impact of this probability threshold on the fit result, and the value of the R was found to be relatively insensitive to the limit, as summarized in Figure 6.7, where the fitted value of $\frac{N_0}{N_f} = 1/R$ is shown as a function of the probability threshold. The principal effect of augmenting the probability limit was to remove channels capable of being fit with the regression method. With a threshold of 0.001, approximately 50% of the total channels analysed may be fit (400 channels for single and many nucleon removal). Raising the threshold to 0.01 removes 80% of the channels, leaving only 50. Due to the insensitivity of R to the probability threshold, 0.001 was chosen to optimize the accuracy of the fit without removing channels. The uncertainty on the fit was as the statistical uncertainty on $1/R$.

6.5.1. Isomeric Contamination

A number of isomers were present in the beam and measured by the EURICA array at F11 [153]. Table 6.2 shows the fractional isomeric contamination (FC) in the beam at F7, extrapolated from the measurement at F11. Values were provided by our collaborators [154]. The isomeric ratios were calculated using the known efficiency of EURICA, the multipolarities were not determined experimentally but based on expectations from the level schemes. Some level schemes are partially unknown but other decay paths are expected to have a minor contribution. The gamma intensities are integrated up to 500 ns, based on a 300-400 ns flight time, which may contribute additional

[1] The p-value quantifies the likelihood that the null hypothesis is true, in this case that the data cannot be described by a line. A low p-value indicates that the null hypothesis can be rejected, though the exact cut-off value is not well defined and thus must be determined empirically based on the application.

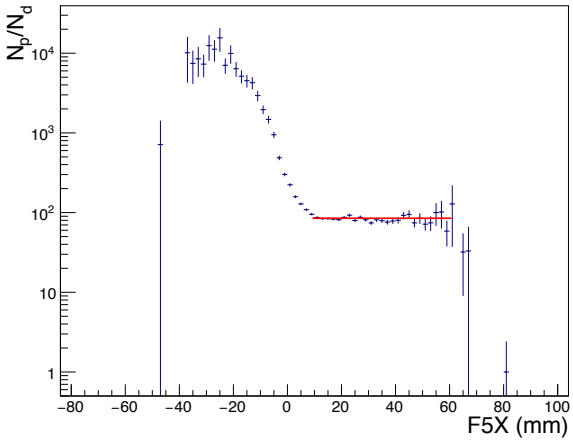

Figure 6.6. Ratio of ^{96}Kr incident distribution in F5X relative to the distribution of ^{96}Kr that yields ^{95}Kr in ZeroDegree. The fit to obtain $\frac{N_f}{N_0}$ is shown in red.

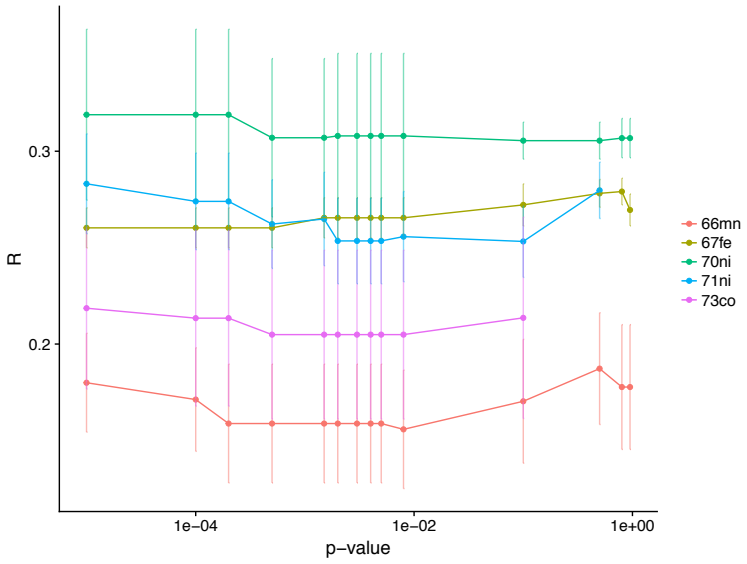

Figure 6.7. R as extracted from the fitting routine, as a function of the probability limit imposed on the regression. The legend indicates the parent nucleus.

Beam	Fractional Contamination (FC)
^{67}Fe	0.354
^{70}Ni	0.069
^{78}Zn	0.077
^{100}Sr	0.0242
^{95}Kr	0.5233
^{94}Br	0.2247
^{95}Br	0.1342
^{96}Rb	0.0311
^{97}Rb	0.0502
^{98}Rb	0.2733
^{100}Sr	0.024
^{75}Cu	0.050
^{78}Zn	0.078

Table 6.2. List of isomers present in the beam, with fractional contamination as measured by EURICA.

error if the isomer is very short lived. All these assumptions are acceptable however, as the isomeric contamination is considered as an additional uncertainty on R, added in quadrature to the fitting uncertainty according to

$$\left(\frac{\delta_R}{R}\right)^2 = \left(\frac{\delta_{fit}}{R}\right)^2 + FC^2 \tag{6.9}$$

6.6. Transmission

The absorption of the parent and daughter nuclei in the target and transmission through beamline elements are described by a transmission factor, T, as shown in Equation 6.7. The transmission is measured from a direct beam, full target run, where both BigRIPS and ZeroDegree spectrometers are centered on the same nucleus. It is defined as the percentage of direct beam detected in ZeroDegree, after passing through the LH2 target. The method of extracting T is identical to that used to extract R, using the F5X fit method described above.

This method assumes implicitly that the absorption of the parent and daughter nuclei is the same. This was checked by calculating the cross sections for a two cases i) using T of the parent nucleus and ii) using T of the daughter nucleus. The results were found to be consistent within the uncertainties, though in general a slightly higher cross section was found when the transmission of the parent was used. For the analysis, the statistically weighted average of the parent and daughter transmissions was used when available, otherwise whichever transmission was available (parent or daughter) was used. The transmission ranged between ∼40-70% for the nuclei analysed. Variations in transmission within a given setting are linked to different magnetic rigidities, and global drifts from setting to setting are linked to changing detector efficiencies. The latter are responsible for the largest deviations, generally transmission within a given setting varies by $\sim 10\%$.

Empty target transmission was also measured, used to calculate reaction cross sections and subtract background contributions. Empty target transmission ranged from ∼70-90%.

6.7. Target Density

The target density n (atoms/cm^2) is calculated according to Equation 6.10, where ρ_{target} is the target density as determined by measuring the vapor pressure above the liquid hydrogen in the cryostat, L_{target} is the target length as physically measured and then checked by reconstructing the reaction vertices, as shown in Part 1, N_A is Avogadro's number 6.022×10^{23}, and M_H is the molar mass of Hydrogen, 1.008 g/mol.

$$\eta = \frac{\rho_{target} L_{target} N_A}{M_H} \tag{6.10}$$

For SEASTAR2014, ρ_{target} was 70.973 kg/m^3 and L_{target} was 102(1) mm, leading to a density of $\eta = 4.32(0.04) \times 10^{23}$ atoms/cm^2 For SEASTAR2015, ρ_{target} was 73.22(8) kg/m^3 and L_{target} was 99(1) mm, leading to a density of $\eta = 4.33(0.04) \times 10^{23}$ atoms/cm^2.

6.8. Uncertainties

The uncertainties on the inclusive cross sections are dominated by statistical uncertainties, ranging from 0.6 to 52% for T, and 2-30% for R. The general formula employed to determine the uncertainty on the cross section is shown in Equation 6.11. Systematic uncertainty on R and T stemming from plastic and charge states cuts contributes 1% to the cross section, shown as δ_{cuts}, and uncertainty on particle identification cuts contributes 0.3% to R and T, shown simply as $\delta T(R)_{sys}$. Note that the uncertainty on R may contain an additional contribution from isomeric contamination, as shown in Equation 6.12.

$$\frac{\delta_\sigma}{\sigma} = \sqrt{\left(\frac{\delta_R}{R}\right)^2 + \left(\frac{\delta_T}{T}\right)^2 + \left(\frac{\delta_\eta}{\eta}\right)^2 + \left(\frac{\delta_L}{L}\right)^2 + \left(\frac{\delta_\gamma}{1-\gamma}\right)^2 + \delta_{cuts}^2} \tag{6.11}$$

$$\left(\frac{\delta_R}{R}\right)^2 = \left(\frac{\delta R_{fit}}{R}\right)^2 + \left(\frac{\delta R_{isomer}}{R}\right)^2 + \left(\frac{\delta R_{sys}}{R}\right)^2 \tag{6.12}$$

$$\left(\frac{\delta_T}{T}\right)^2 = \left(\frac{\delta T_{stat}}{T}\right)^2 + \left(\frac{\delta T_{sys}}{T}\right)^2 \tag{6.13}$$

Taking again the example of ^{96}Kr(p,pn)^{95}Kr, $R = 0.01177$, with a fitting uncertainty $\delta R_{fit} = 4.9\%$ and no isomeric contamination in the beam. Transmission of the parent and daughter are 58.32(5.3)% and 58.21(5.2) %, respectively, yielding a weighted transmission of 58.3(5.2) %. Additional 0.3% uncertainties on T and R are included to account for the PID cuts. Including these with the 0.92% uncertainty on η and 1% uncertainty on L_{target} the final uncertainty is 7.3%, as broken down in Table 6.3.

Table 6.3. Breakdown of uncertainty calculation for ^{96}Kr(p,pn)^{95}Kr cross section

$\delta_R/R = 0.0491$	$\delta R_{fit}/R = 0.049$	$\delta R_{isomer}/R = 0$	$\delta R_{sys}/R = 0.003$
$\delta_T/T = 0.0521$	$\delta T_{fit}/T = 0.052$	$\delta R_{sys}/R = 0.003$	
$\delta_\eta/\eta = 0.0092$			
$\delta_L/L = 0.01$			
$\delta_\gamma/(1-\gamma) = 0.022$			
$\delta_{cuts} = 0.01$			
$\delta_\sigma/\sigma = 0.0768$	$\rightarrow \sigma = 43(3)mb$		

7
Results and Discussion

No particular trends were anticipated a priori in this data set, as similar systematic studies of inclusive cross sections in this mass region do not exist in the literature. Thus, when examining the data, the results were explored as a function of what we deemed to be reasonable quantities–A,N,Z,S_p, S_n. In the following, the data will first be presented and discussed in terms of simple arguments, then in a second step the results will be compared with semi-microscopic INCL and FE calculations. A table of measured cross sections and predictions may be found in Appendix E.

7.1. (p,2p)

The results for single proton removal inclusive cross sections are shown in Figure 7.1 as a function of proton separation energy of the projectile nucleus, and then neutron separation energy of the daughter nucleus. In the figure, even-Z projectiles are shown as open circles, and odd-Z projectiles are shown as closed circles. All (p,2p) cross sections fall between 2 and 12 mb. It is clear that the even-Z projectiles have a ∼50% larger cross section than the odd-Z neighbors, and no strong trend is visible as a function of S_p. Since within QFS dynamics, the projectile energy is much larger than the binding energy of the nucleon to be removed, the relative binding of the proton is not expected to influence significantly the cross section. Indeed if it did, one would expect the opposite trend, i.e. a reduction of the cross section for larger S_p. The (p,2p) systematics as a function of $-S_n$ of the daughter nucleus, shown in Figure 7.1(b) reveal additionally a general decreasing trend with -S_n, i.e. moving towards the neutron dripline.

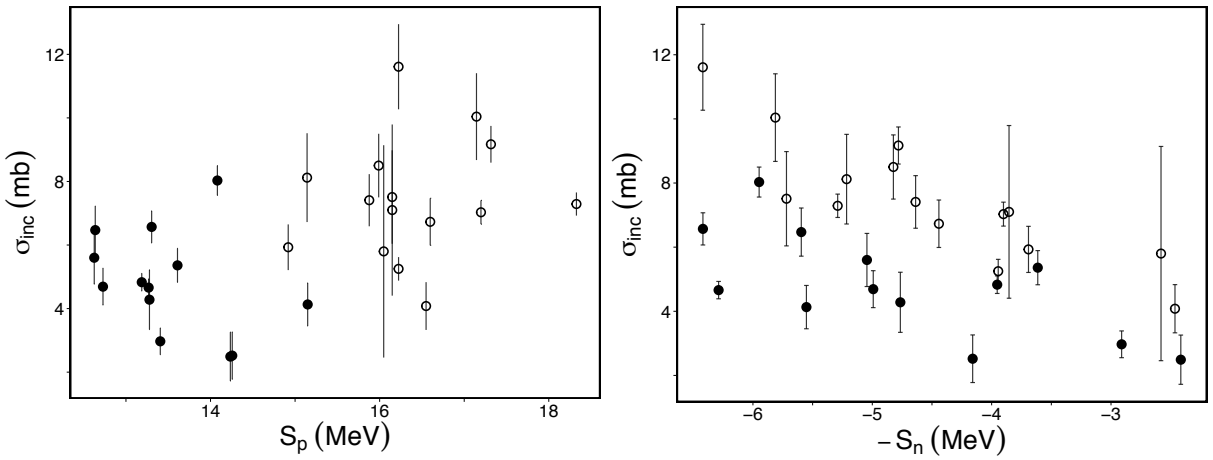

(a) **(b)**

Figure 7.1. (p,2p) inclusive cross sections as a function of S_p of the projectile (a) and -S_n of the daughter nucleus (b). Even(odd)-Z projectiles are shown as open(filled) circles.

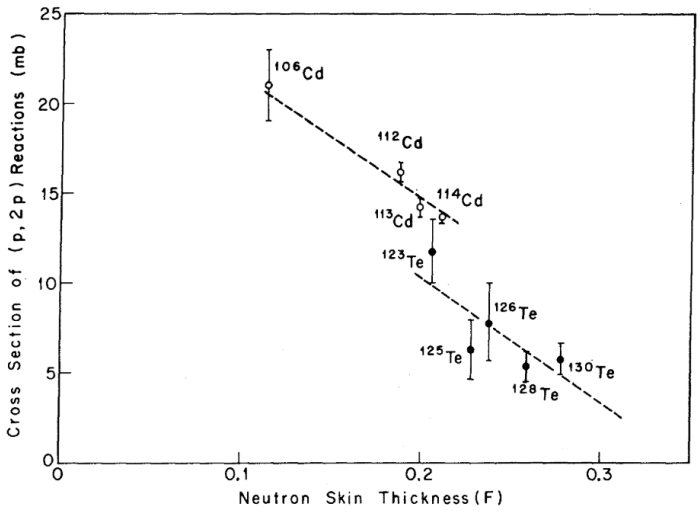

Figure 7.2. Figure from early measurement of inclusive (p,2p) cross sections showing the same decreasing trend as seen in this data, as neutron skin thickness maps qualitatively to -S_n for this data. Figure from [155].

Both of these features can be explained by examining the bound state spectrum of the daughter nucleus. As the neutron separation energy decreases, the number of bound states in the daughter nucleus decreases correspondingly. The inclusive cross section reflects the sum of strength to the bound single particle states, thus as the number of bound states decreases, the cross section may be expected to decrease correspondingly, as seen in the slope of the data in Figure 7.1(b). The same effect can be seen in some of the earliest studies of (p,2p) reactions, such as in Figure 7.1 from [155], where the neutron skin thickness was calculated with a liquid drop model, but corresponds qualitatively as moving towards -S_n.

The odd-even Z splitting may be understood by considering the finer details of the excitation energy spectrum. Proton removal from an odd-Z projectile yields an even-Z fragment. In even-Z nuclei, the pairing interaction produces a gap between the ground state and the first excited state, Δ_p that may be expressed empirically as in Equation 7.1 [156]. In odd-Z nuclei no such gap exists and the overall level density is higher, shown schematically in Figure 7.3. A real-example may be seen comparing the ground state bands in ^{64}Ni(Z=28,N=36) and ^{65}Cu(Z=29, N=36) also shown in Figure 7.3, where not only does the first excited state in the even-Z nucleus starts at approximately twice the energy of the first excited state in the odd-Z case, but counting just the number of states up to $\sim$ 3 MeV, there are twice the number of states in the odd-Z nucleus. Assuming that these same proportions hold for exotic neutron-rich nuclei, and using again the argument that the inclusive cross section is proportional to the number of bound states, we then expect a $\sim$50% larger cross section for the odd-Z fragment (even-Z projectiles), commensurate with the differences seen in Figure 7.1. Unfortunately existing studies have focused on even-Z isotopic chains however, and thus no effect linked to even-odd Z effects in (p,2p) reactions has been previously noted in the literature.

$$\Delta_p = (-1)^{Z-1}[S_p(Z+1,N) - S_p(Z,N)] \tag{7.1}$$

Note that in both these arguments, the cross section has been assumed to be proportional to the total number of bound states in the daughter nucleus. Realistically it is rather the total strength of states where there is a significant overlap between the parent and daughter wavefunctions that

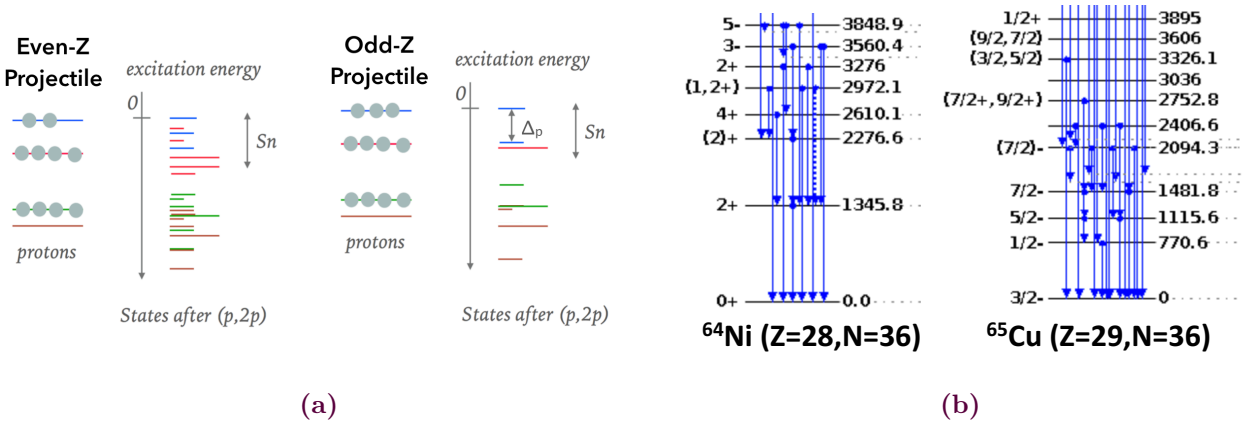

(a) (b)

Figure 7.3. (a) Schematic image of the excitation energy spectra of fragments resulting from proton removal from even-Z and odd-Z projectiles, (b) and real-life example of ground state band spectra for odd, even Z neighbors ^{64}Ni and ^{65}Cu. Note that the spectra have been cut at ∼3 MeV. Figure adapted from [157] (right).

contributes to the inclusive (p,2p) cross section. In the absence of measured spectroscopic strength in these nuclei, assessing the total number of bound states is thus an approximation. Shell model calculations could be envisaged to determine the proton strength distribution, but calculations for all nuclides studied here would be highly computationally demanding and at this stage are beyond the scope of this work. No other significant features were seen in the (p,2p) data as a function of A, N, or Z.

7.2. (p,pn)

The (p,pn) inclusive cross sections are shown in Figure 7.4 as a function of the number of nucleons, A, and -S_n of the projectile. Even-N projectiles are shown as open circles, and odd-N projectiles are shown as closed circles. For a given projectile, the (p,pn) cross sections are ∼ 10 times larger than the corresponding (p,2p) cross sections. No strong trend was found as a function of A, N, Z, S_p or S_n, rather the cross sections are randomly distributed around 60 mb. While one might expect a linear increase along isotopic chains as neutrons are added (with increasing A in the Figure), no such trend is visible. This may be because along an isotopic chain, as A increases, S_n decreases going towards more neutron-rich nuclei. Though the probability to remove a neutron from the projectile increases with A, the separation energy of the daughter also decreases correspondingly, leading to fewer bound states in the daughter nucleus. These combined effects lead to the overall flat trend seen in the data as a function of A.

Examining the (p,pn) trends as a function of S_n, there is no odd-even staggering as was seen in the (p,2p) data. This may be understood by examining the interplay of S_n and bound state level density, the same arguments used to explain the (p,2p) systematics. Consider neutron removal from an odd-N projectile: the resulting even-N daughter has a higher S_n, but a reduced level density suggesting that the total integrated strength should not change significantly for neutron removal along an isotopic chain. Yet, there is still a marked difference between the even and odd N projectiles. The even-N projectiles show essentially flat cross sections as a function of S_n, whereas the odd-N projectiles show a decreasing cross section going towards the neutron dripline. This may be understood by considering again the density of states in the daughter nucleus. For odd-N projectiles, the even-N daughters have

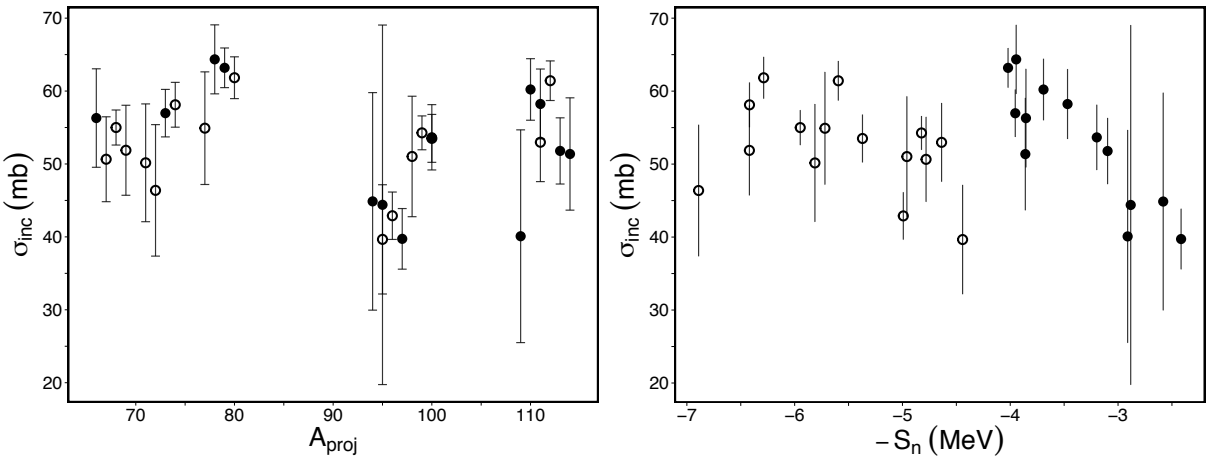

(a) **(b)**

Figure 7.4. (p,pn) inclusive cross sections as a function of (a) the nucleon number of the projectile and (b) -S_n of the parent nucleus. Even(odd)-N projectiles are shown as open(filled) circles.

a low density of states, and thus the reduction in the number of bound states going towards the neutron dripline is more pronounced than for odd-N daughters.

7.3. Theory Comparison

These results were compared with two semi-macroscopic models: the latest version of the Liège Intranuclear Cascade Model (INCL) [147, 148, 149], and Fragmentation-Evaporation (FE) calculations within a Glauber framework [138, 122], both presented in the previous chapter.

Comparisons between our proton removal cross sections and INCL calculations are shown in Figure 7.5, following the odd-even convention introduced in Figure 7.1. The overall global linear trend is well reproduced by the model. Within the INCL framework, the slope as a function of -S_n appears after the evaporation stage, as fragments with an excitation energy above S_n are lost to neutron evaporation. The odd-even splitting is not however reproduced by INCL. This is to be expected as INCL calculations do not include level densities.

Modified INCL calculations were performed, trying to mimic the odd-even effect seen in the (p,2p) data. This was done by applying an empirical correction to the excitation energy of odd-Z projectiles used for evaporation, equal to the separation energy difference between the parent and daughter nuclides, as shown in Equation 7.2, where E_{ex} is the standard excitation energy from INCL from Equation 5.11, and it is modified by the difference between projectile and daughter separation energies according to

$$E_{ex}^{mod} = E_{ex} + (S^{daughter} - S^{projectile}) \tag{7.2}$$

where S indicates the proton(neutron) separation energy for proton(neutron) removal. This phenomenological correction shifts the strength to higher excitation energy, correcting for the shift induced by pairing, and consequently reducing the final yields after evaporation.

INCL standard and modified calculations were also compared with the (p,pn) cross sections, as shown in Figure 7.6 in blue and red, respectively. On average the standard INCL predictions reproduce well the cross sections, however there is a strong odd-even staggering in the calculations, linked to the

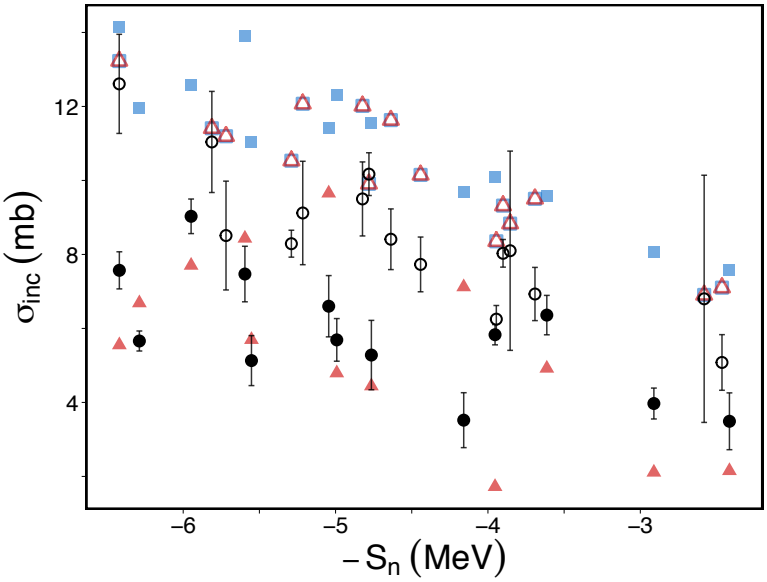

Figure 7.5. (p,2p) inclusive cross sections compared with standard (blue) and modified (red) INCL predictions. Even(odd)-z projectiles are shown as open(filled) markers.

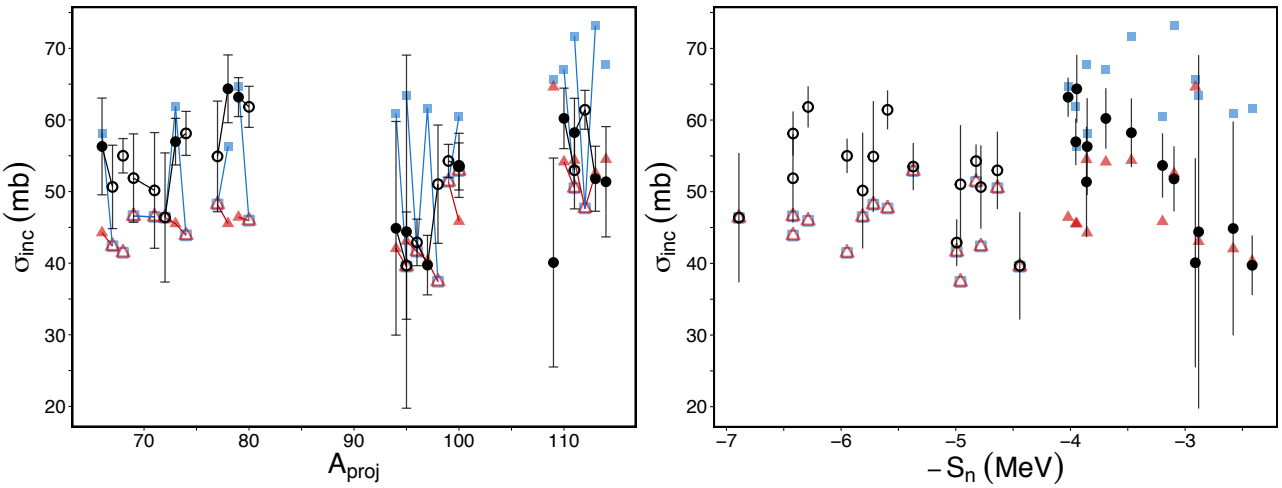

(a) **(b)**

Figure 7.6. (p,pn) inclusive cross sections compared with standard (blue) and modified (red) INCL predictions as a function of the mass of the projectile (a) and -S_n of the parent nucleus (b). Even(odd) N projectiles are shown as open(filled) markers and isotopic chains are connected by lines in (a).

neutron separation energies, that is not present in the data. As in the (p,2p) case, this is likely due to the lack of a microscopic description of the excitation energy spectrum that includes pairing effects. While even neutron numbers yield a higher S_n, and thus larger range in excitation energy, the pairing effect reduces the overall number of bound states, leading to the flat tendency seen in the data. The INCL calculations include the S_n effect, but not the impact on the level density, leading to the strong odd-even staggering. Examining the INCL primary yields, shown in Figure 7.7, we see the expected

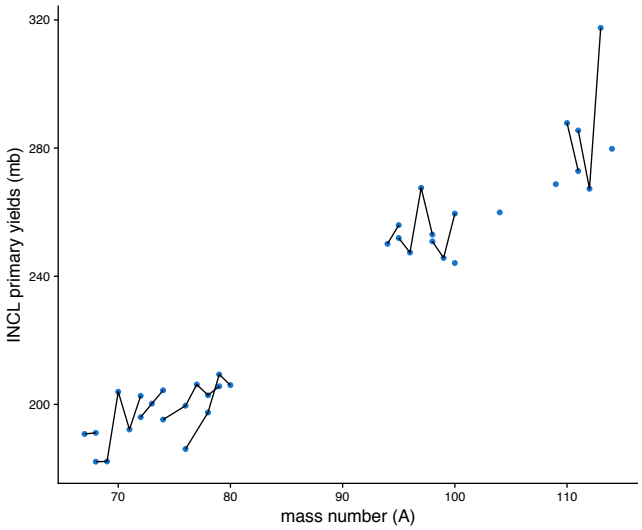

Figure 7.7. INCL (p,pn) primary yields. Isotopic chains are connected by lines.

linear increase with A, that is then flattened after evaporation due to the decreasing separation energy. It is also clear that some of the odd-even staggering is induced in the primary yields, while more is added after evaporation. The modified INCL calculations reduce the odd-even staggering from the evaporation step, confirming qualitatively our understanding of the origin of this effect.

The results were also compared with the FE model already presented in Section 2.1. Proton and neutron removal cross sections compared with these two models are shown in Figure 7.8. The first observation is that the FE predictions are significantly above both the data and INCL predictions, by factors of 2-3. This is somehow surprising due to the relative similarity between the approaches. Already in the primary yields before evaporation, FE exceeds INCL by factors of 1.3-1.5, which becomes factors of 2-4 after evaporation. While the origin of this discrepancy has not been quantified, it could originate in the different geometries of the two models. FE restricts collisions to a cylindrical zone along the z-axis defined by the overlapping projectile and target regions, while INCL allows nucleons to explore the entirety of the nuclear volume during the collision process, potentially increasing absorption and reducing the overall number of collisions. The enhanced divergence between the two models after evaporation may also be linked to the different ways that the two models calculate the excitation energy. While both approaches are based on single particle configurations from HFB calculations, the smoothing of these densities with the fuzzy parameter in INCL allows more deeply bound nucleons to be removed, which increases the resulting excitation energy and should lead to smaller final yields relative to the FE calculations. Beyond this gross offset however, FE reproduces well the linear slope of the (p,2p) systematics, and the overall flat tendency of the (p,pn) systematics. In the (p,pn) systematics we note again a strong odd-even staggering not seen in the data, presumably due to the lack of a microscopic excitation energy spectrum as for INCL.

As a final step, consider the ratio of experimental and theoretical cross sections as a function of asymmetry ΔS, as shown in Figure 7.9. Both FE and standard INCL predictions show worse agreement for more deeply bound (proton in this case) nucleon removal, as has already been noted in [158, 148, 145]. However here we also reveal a general trend of increasing theoretical estimation with increased asymmetry ΔS. This is reminiscent of the overestimation seen when describing knockout reactions with the S-matrix formalism as in Figure 5.5, but due to the dramatic differences between the models a direct link may not be drawn. Based on the structure of these models, it is likely that

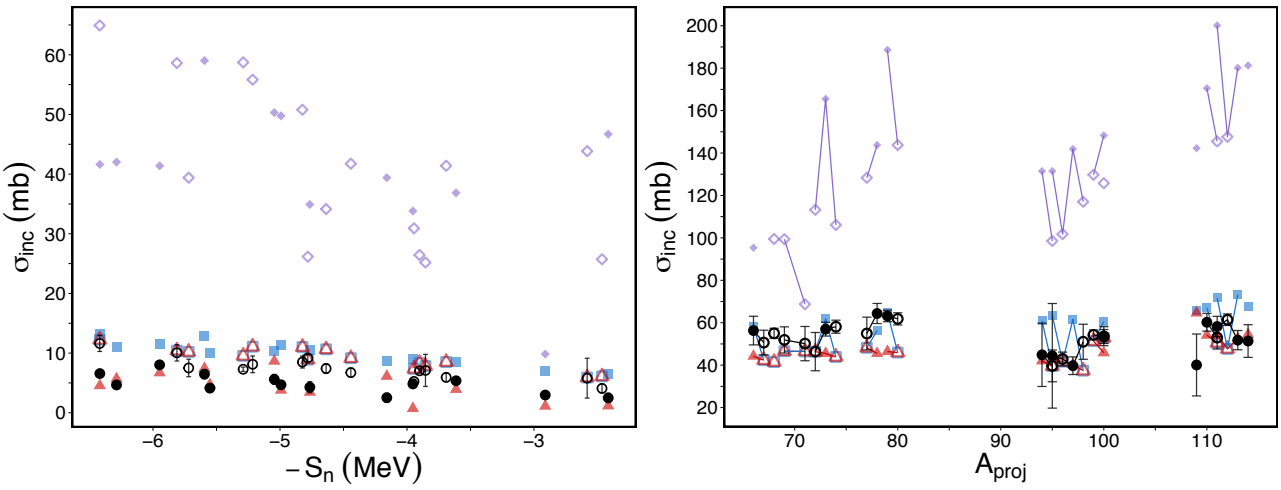

(a) (b)

Figure 7.8. (p,2p) (left) and (p,pn) (right) cross sections compared with INCL (blue), INCL-mod (red), and Fragmentation-Evaporation (purple) predictions. Even(odd) nucleon projectiles are shown as open(filled) markers.

the excitation energy is generally underestimated, an effect that becomes amplified as more deeply bound nucleons are removed. The phenomenological enhancement of the excitation energy for odd-Z projectiles removes the slope for proton removal, confirming this interpretation. The slope remains for neutron removal however, suggesting that a more microscopic description of the excitation energy spectrum is needed to reliably predict cross sections for the most exotic nuclei.

7.4. Outlook

We have measured 56 single nucleon removal inclusive cross sections from medium-mass neutron rich nuclei. Proton removal cross sections range between 2 and 12 mb, and neutron removal cross sections average around 60 mb. The systematics of the data can be explained through simple arguments of bound state level density and neutron separation energy. Semi-microscopic methods reproduce well the global trends however they fail to reproduce the presence of odd-even splitting in the proton removal cross sections, and the absence of such splitting in neutron removal cross sections. This is attributed to the lack of a realistic bound state spectrum in the models, a known drawback of using methods without true microscopic structure. Improvement may be found through a phenomenological correction to the INCL excitation energy, mimicking the impact of pairing correlations on the level density. Our results also highlight a systematic underestimation of the excitation energy as calculated with these models, a known problem as was seen in Figure 5.9, but that may present a fundamental limitation for calculating deeply bound nucleon removal.

These results reveal that the fine features of low energy level structure, particularly pairing correlations, play an important role in determining inclusive cross sections in these loosely bound nuclei. The data serves as a benchmark for microscopic calculations, which unfortunately hardly exist due to the difficulty in reliably predicting all bound states while the mechanisms of neutron-rich structure evolution remain unconstrained. Another area of exploration would be a refined study of the relationship between these low-energy correlations and the relative stability of the nucleus. It is expected that the importance of these correlations should diminish for nuclides near stability–the

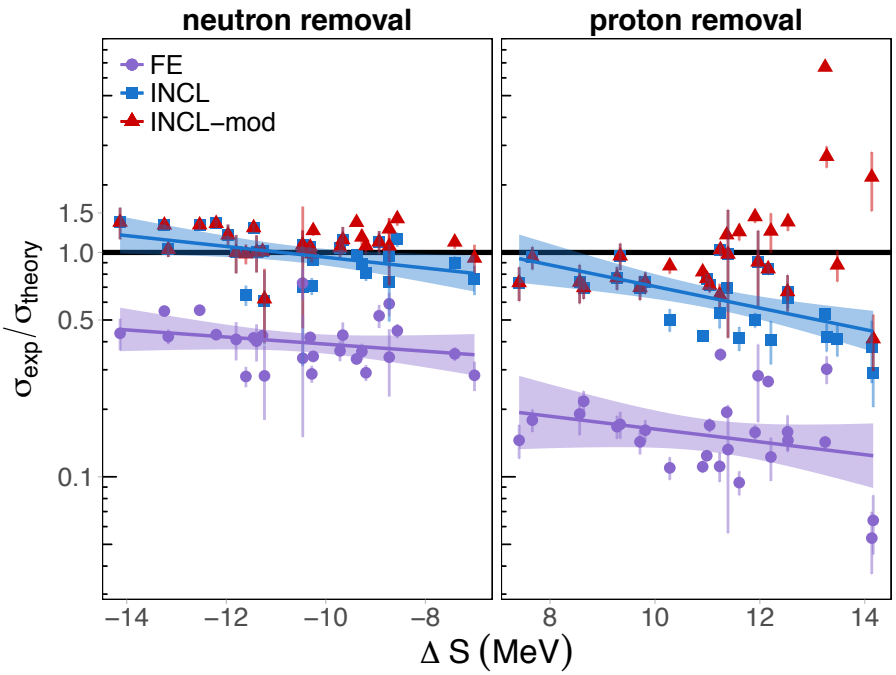

Figure 7.9. Ratio between experimental and theoretical inclusive cross sections as a function of asymmetry.

effect being washed out as the total number of bound states increases–unfortunately comparable systematics have not been found in the literature.

Part III.

PUMA

I like to say that while antimatter may seem strange, it is strange in the sense that Luxembourgeois are strange. They are not really strange; it is just that one rarely meets them.

adapted from Lawrence M. Krauss, A Universe from Nothing: Why There Is Something Rather Than Nothing

8 PUMA

8.1. Nuclear Physics with Antiprotons?

The PUMA project (antiProton Unstable Matter Annihilation) is a future experiment at CERN that aims at furthering our understanding of exotic nuclei through a new probe–**antiprotons** [6]. The first nuclear structure studies with antiprotons were performed at Brookhaven National Laboratory in the 1970s [159]. In these experiments, an antiproton beam impinged on stable C, Ti, Ta, and Pb targets, and annihilation products were detected in a bubble chamber. By determining the total charge of the reaction products based on prong analysis, neutron to proton annihilation ratios were extracted for each target. After accounting for detection efficiency and differences in neutron and proton annihilation probabilities, and normalizing to ^{12}C, neutron to proton annihilation ratios significantly larger than N/Z were found for the Ti, Ta, and Pb targets. This result was interpreted as evidence of neutron skins. Precision measurements were performed later at the Low Energy Antiproton Ring (LEAR) of CERN, where nucleon-antiproton and nucleus-antiproton collisions were studied principally via X-ray spectroscopy [160, 161, 162], but measurements of neutron skins were restricted to stable species.

A neutron skin is an accumulation of neutrons on the surface of the nucleus, so far observed in stable and light nuclei [163]. Extreme cases may become neutron halos where the majority of the neutron probability density is located at large radii in the classically forbidden region [130, 164, 165]. Neutron halos were discovered in ^{11}Li [130] and so far have only been evidenced in light, dripline nuclei. Though only s-wave halos have been confirmed, p-wave halos are claimed in Ne and Mg isotopes [166, 167]. Whether neutron halos may develop in medium-mass nuclei deformed nuclei is unknown, with little theoretical work and no conclusive experimental evidence. The development of thick neutron skins in exotic nuclei is predicted by microscopic models, but different calculations diverge wildly. Figure 8.1, also seen in the introduction, shows the predicted neutron skin thickness as a function of isospin asymmetry $I = (N - Z)/A$ for different nuclides ranging from mass 40 to 208 as calculated using different effective interactions in mean field methods. The discrepancy reaches as much as a factor 15 for the most neutron-rich systems. Constraining neutron skins in exotic nuclei would thus serve as a particularly sensitive probe to distinguish between microscopic structure models.

Thick neutron skins present a unique example of low-density pure neutron matter on earth, and understanding them is of astrophysical interest to constrain the equation of state of neutron stars. The neutron skin thickness is strongly correlated with the radius of low-mass neutron stars, as both share a common origin in the pressure of nuclear matter defined by the equation of state (EOS) [169]. The EOS may be parametrized as

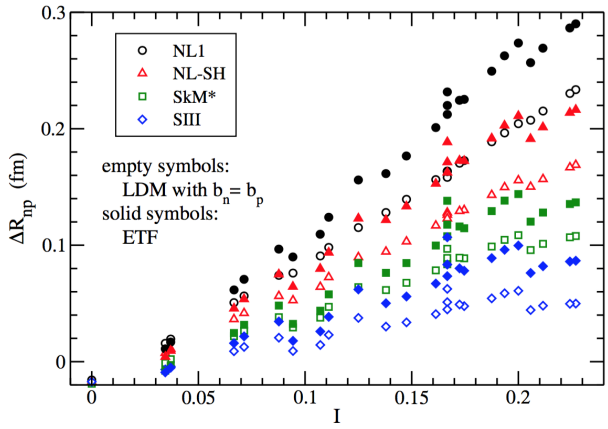

Figure 8.1. Neutron skin thicknesses as a function of isospin asymmetry I=(N-Z)/A using different effective interactions in mean field calculations. The nuclides cover the mass range $40 \leq A \leq 208$. Figure from [168].

$$E(\rho, \delta) = E(\rho, \delta = 0) + E_{sym}(\rho)\delta^2 \tag{8.1}$$

where E is the energy of the system, $\rho = \rho_n + \rho_p$ is the total density of the system, and $\delta = (\rho_n - \rho_p)/(\rho_n + \rho_p)$ is the isospin asymmetry. The first term in the above expression represents symmetric nuclear matter, and the second term is the symmetry energy that becomes increasingly important for asymmetric (neutron-rich for our purposes) systems. The symmetry energy may in turn be expanded around saturation density ρ_0 according to

$$E_{sym}(\rho) = E_{sym}(\rho_0) + \frac{L}{3}\frac{\rho - \rho_0}{\rho_0} + \frac{K}{18}\left(\frac{\rho - \rho_0}{\rho_0}\right)^2 \tag{8.2}$$

where L and K characterize the slope and curvature of the symmetry energy, respectively. E_{sym} opposes the creation of asymmetric nuclear matter, and neutron skin thicknesses reflect thus the relative strength of the symmetry energy going from saturation density to less dense regions at the periphery of the nucleus. Accordingly, neutron skin thickness have been shown to be strongly correlated with L around saturation density, as shown in Figure 8.2. Constraining neutron skin thicknesses can help pin down L, and thus the EOS. The applicability for neutron stars may be limited by the fact that neutron skin thicknesses in the laboratory are measured at the fermi density, ρ_f, and neutron stars are thought to have densities of $3\rho_f$ where correlations, such as clustering, may play a role [170]. Nevertheless constraining neutron skins should significantly reduce the EOS parameter space [1]. The PREX electron scattering experiment at Jefferson Laboratory has measured the neutron skin in ^{208}Pb via electron scattering, but the approximately 50% error bar is too large to place significant constraints on the EOS. A precision of ~1% (0.02 fm) is needed for this, which has currently only been demonstrated with the antiproton method on stable nuclei [171]. Indirect methods like resonance experiments [172] can obtain a 0.2 fm precision. Neutron removal cross section analysis has been proposed to provide similar precision as the antiproton method, but has yet to be demonstrated [173].

PUMA offers an alternative approach to understand neutron skins in exotic nuclei. When an antiproton encounters a nucleus, if the incident energy is lower than the separation energy, the

[1] The observation of gravitational waves from the neutron star merger GW170817 has already ruled out a number of previously proposed EOSs [67]

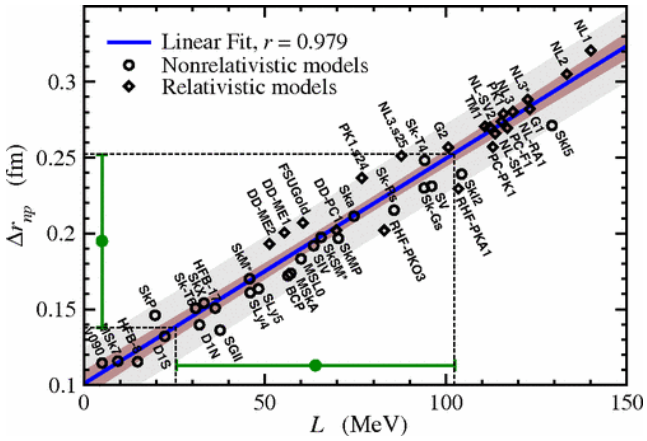

Figure 8.2. Neutron skin thicknesses in ^{208}Pb as a function of the density dependence of the symmetry energy, as calculated with various models. Figure from [3].

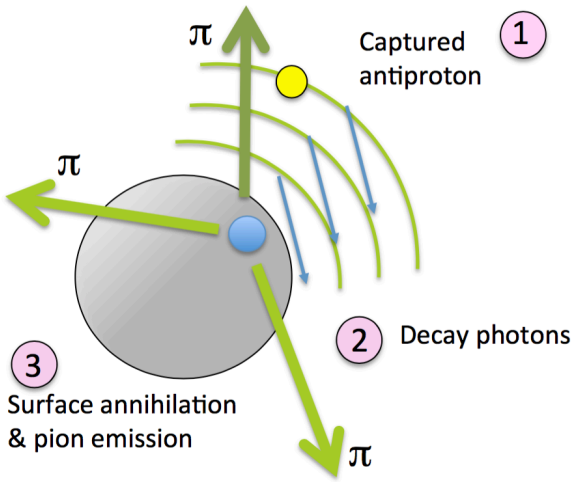

Figure 8.3. Schematic depiction of the decay and subsequent annihilation of an antiprotonic atom via electron, X-ray, and pion emission. Figure from A. Obertelli.

Coulomb interaction may lead it to collide with one of the electrons, ejecting the electron, and capturing onto one of the electronic orbitals of the atom. It then decays down the electronic orbitals by Auger electron and x-ray emission. When the wavefunctions of the antiproton and nucleus start to overlap, the antiproton annihilates with a nucleon, emitting pions. Due to charge conservation, by detecting the charge of the pions emitted during annihilation, either 0 or -1, one can determine whether the antiproton annihilated with a proton or neutron, respectively. A schematic of the de-excitation and annihilation process of an antiprotonic atomic system is shown in Figure 8.3.

The relative number of neutron to proton annihilations for a given species may be used to obtain the ratio of proton to neutron densities at the annihilation site, as shown in Equation 8.3 [171], where ρ_n, ρ_p are the neutron and proton densities, N_n, N_p are the detected number of neutron and proton annihilations, $\sigma_{pbar-p}, \sigma_{pbar-n}$ are the absorptive parts of the antiproton-proton and antiproton-neutron scattering amplitudes (obtained from theory), and ϵ is the detection efficiency. The annihilation ratio is thus complementary to neutron skin thickness measurements.

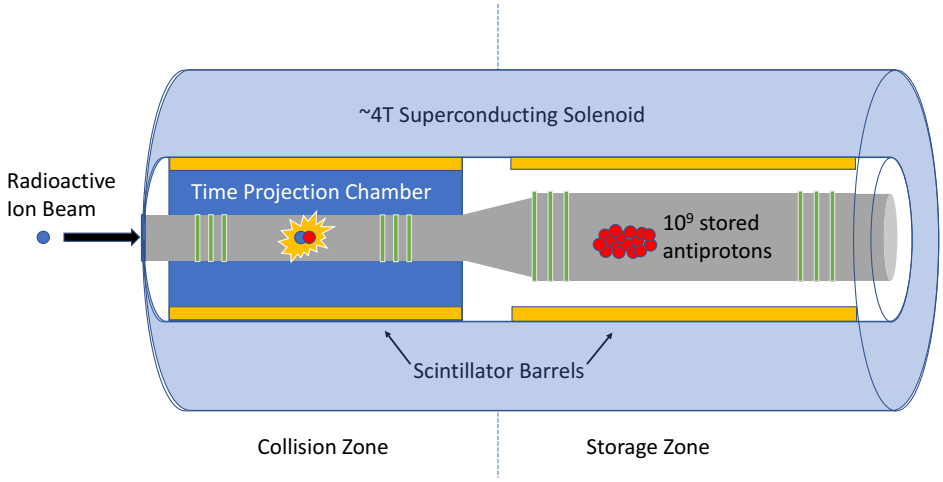

Figure 8.4. Schematic depiction of the PUMA system.

$$\frac{\rho_n}{\rho_p}\Big|_{surface} \sim \frac{N_n}{N_p} \times \frac{\sigma_{pbar-p}}{\sigma_{pbar-n}} \times \epsilon \tag{8.3}$$

The antiproton probe is unique inasmuch as the annihilations are shown to occur in the very tail of the nuclear density, as opposed to electron scattering experiments which probe the mid-rise point. Antiproton-nucleus annihilations also feature extremely large cross sections, up to 1 Megabarn at low energies [174], meaning that measurements can be performed for exotic beams with low intensities <1 kHz. Contrarily, electron scattering, proton elastic scattering, or isotopes shifts require at least 10^4 Hz [175]. This makes this method well adapted for studying the elusive species needed to test nuclear structure models.

8.2. Setup and Detection Requirements

PUMA is a two stage experiment. The first step consists in trapping 1 billion antiprotons from the CERN antiproton ring ELENA in a large capacity cryogenic cylindrical Malmberg-Penning trap. The trap will then be loaded onto a truck, delivered to the ISOLDE facility, and attached to the ISOLDE beamline, such that exotic nuclides may be injected into the antiproton cloud.

A schematic of the PUMA apparatus[2] is shown in Figure 8.4. It consists of a two-zone cylindrical trap, whose schematic electrodes are indicated in green in Figure 8.4, located inside a 4 Tesla superconducting solenoid. The trap confines the ions axially, while the solenoid provides radial confinement as the ions undergo magnetron motion in the B field. A large radius storage zone accumulates and stocks the antiprotons from the ELENA ring, and a scintillator barrel outside the collision zone monitors the decay rate of the stocked antiprotons. Once at ISOLDE, smaller bunches of antiprotons ($\sim 10^6$) are transferred from the storage zone to the collision zone. Nuclei are then injected and subsequently trapped with the antiprotons in the collision zone. Annihilation pions are detected in the TPC located outside the collision zone. The trajectory of the pions in the B field indicates the charge of the pions, as seen in the simulated event on the TPC detection plane

[2]excluding the PUMA truck

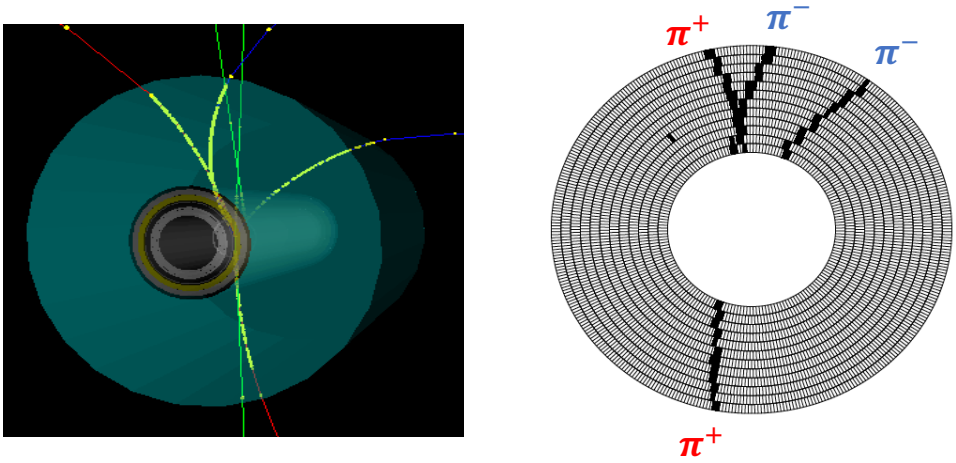

Figure 8.5. Geant4 simulated antiproton-proton annihilation event, and corresponding tracks on TPC pad plane. Figure from A. Corsi.

of Figure 8.5. A plastic scintillator barrel on the outside of the TPC provides the trigger from the outgoing pions. Note that the event shown in Figure 8.5 is a perfect scenario where all four pions emitted in the annihilation process are detected in the TPC without undergoing additional interactions. In reality, the outgoing pions may interact with the residual nucleus, and these final state interactions must be considered and compared with simulations to determine the neutron to proton annihilation ratio.

This work focuses on the development of the PUMA TPC, whose field cage and electronic components are designed by CEA-Irfu, with mechanical design and construction provided by the CERN detector lab. The design of the PUMA TPC is very similar to the MINOS TPC, as the MINOS demonstrated the feasibility of a compact TPC with high resolution and efficiency. The principal constraints on the PUMA TPC design are those of compactness, longevity, and electromechanical stability. The TPC needs to fit inside the solenoid with the Penning trap and trigger barrel. The internal diameter of the solenoid is limited to 270 mm for cost reasons, the trap and vacuum chamber take up 100 mm, leaving only 170 mm for the TPC. As the charge of the pions is determined by their trajectory in the magnetic field, the active volume of the TPC needs to be as large as possible to maximize efficiency. The constraints lead to a physical profile of the PUMA TPC very similar to that of MINOS. It is approximately 300 mm long, with an external diameter of 220 mm and an internal diameter of 100 mm, fixed by the trigger barrel and penning trap, respectively. A 5 mm copper cathode biased at 6 kV provides the electron drift potential, and a field cage consisting of 1 mm long, 200 μm thick copper electrodes spaced 0.5 mm apart insure uniform field degradation down to the grounded anode, a resistive Micromegas plane [176]. The field cage electrodes are mounted onto a flexible PCB which forms the structural basis of the TPC, behind which a gap, filled with gas, provides electric field insulation between the PCB and the grounded aluminum outer shell. The active and insulating regions of the TPC are filled with a gas mixture of argon and isobutane to optimize electron drift while minimizing sparking. The presence of this gas in the insulating region minimizes the risk of gas contamination from impurities. This work focuses on the first two points in the list above, through optimization of the cathode, anode, fieldcage, and insulating layer (PCB+gas) geometries of the TPC for a homogeneous electric field.

Additionally, PUMA experimental campaigns are quite long, about 1 month, due to the necessary trapping→transport→collision steps. All equipment located inside the magnet, including the TPC,

needs to be stable and require no maintenance during this time. This requires a design as simple and robust as possible, with benchmarked performance over months. Furthermore, the entire system will be moved in a truck from ELENA to ISOLDE, thus it needs to be stable in a vibrational environment. The goal is thus to achieve a TPC design that maximizes the active volume of the TPC, with the fewest mechanical complications possible, while limiting sparking risks. The electromechanical design goals of the TPC are as follows:

- Minimized sparking risk
- Maximized electric field homogenity
- Maximum active area for vertex resolution and curvature determination
- No gas leaks
- No point to point electrode contacts in vibrational environment
- Stable performance under temperature variation
- Radiation resistant electronics
- Minimum material budget for maximum transmission of pions to the scintillator trigger barrel

This work focuses on the first three points in the list above, through optimization of the cathode, anode, fieldcage, and insulating layer geometries of the TPC.

8.3. TPC Simulations

To attain these design goals, electrostatic simulations of the PUMA TPC have been performed with the engineering suite COMSOL[177]. COMSOL is a multiphysics simulation software package that performs finite element analysis [178] of coupled systems of partial differential equations. For our purposes we use the electrostatics module which solves Laplace's equation for a given charge and material configuration.

COMSOL functions through a multistep process. First, the user defines a geometry in two or three dimensions with different materials and associated electric potentials. Then, the geometry is broken up into small finite elements, a process called "meshing". COMSOL employs an adaptive meshing technique where a finer mesh is automatically used where the field is expected to change quickly, such as on the edges of electrodes or on non-uniform surfaces. Then, Laplace's equation is solved numerically between the vertices of the mesh, allowing computationally tractable discretization methods to be applied to complex geometries. An example of a small geometry and adaptive mesh is shown in Figure 8.7 for the cathode corner study (see next section).

The PUMA TPC simulations detailed here involved two-dimensional optimizations of specific regions of interest where field inhomogeneities are expected. These optimized configurations will then be combined into a full-scale two dimensional simulation, and eventually a realistic electron-drift calculation with the Garfield code developed by CERN [179]. The Garfield simulations will allow to see the resolution of the signal collected on the anode for a given field, and then the geometry can be refined again in COMSOL if needed. Eventually, the finalized geometry and electron drift will be integrated into a Geant4 simulation.

The regions of interest are shown in Figure 8.6. They consist of the interfaces between 1) the cathode and field cage, 2) the field cage and gas volume, and 3) the anode and field cage. Each of these regions will be discussed separately in the sections that follow.

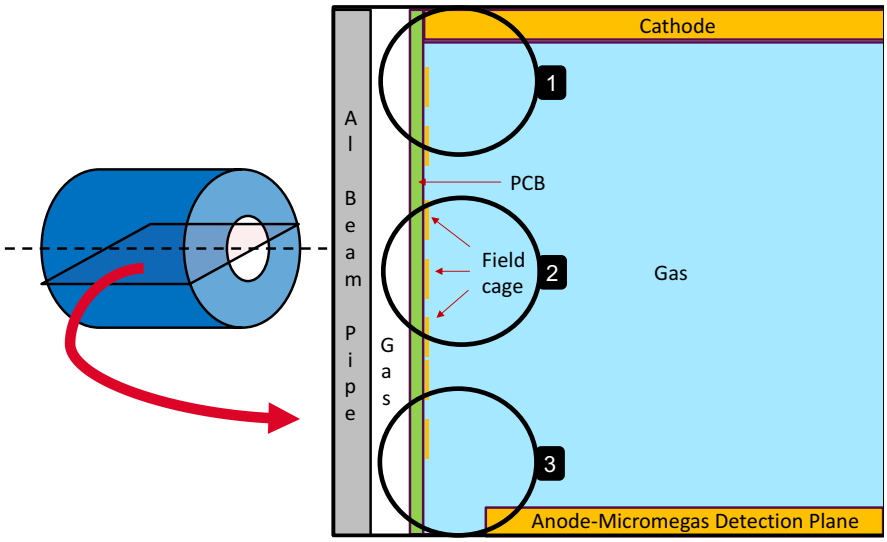

Figure 8.6. Schematic depiction cross section of half of the TPC, with the three specific regions of interest for the field cage optimization studies indicated by the black circles.

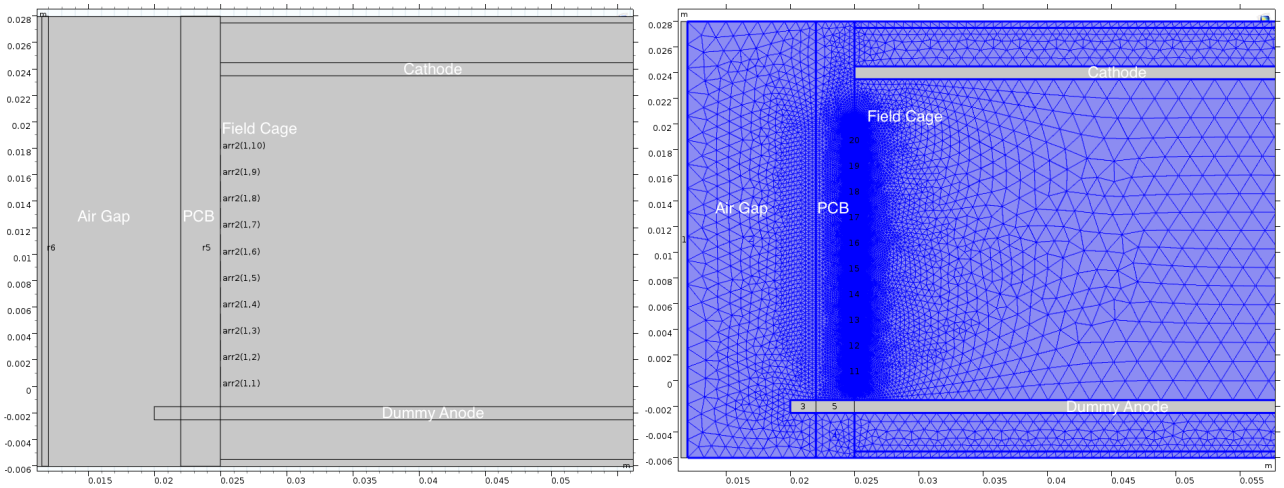

(a) (b)

Figure 8.7. Example of geometry (a) and subsequent adaptive mesh (b) from COMSOL. Distances are shown in meters.

8.3.1. Cathode Corner

The first area of study is the interface between copper cathode and the first degrader electrode of the field cage, as may be seen in region 1 of Figure 8.6. For this simulation, only 20 field cage electrodes were used, and a thick, dummy anode at the end insures a uniform field. The 5 mm thick cathode is biased at -6000 V, presents a significant sparking risk. The first strips of the field cage maintain a 160 V/cm electric field gradient along the z-axis of the TPC. In MINOS, mechanical and sparking considerations led to a 4.5 mm gap between these two objects, which induces significant distortions in the electric field, as may be seen in Figure 8.8(a). These distortions are due to the combined edge effects of the cathode and first strip, and lead to essentially a dead zone in the corners of the TPC of

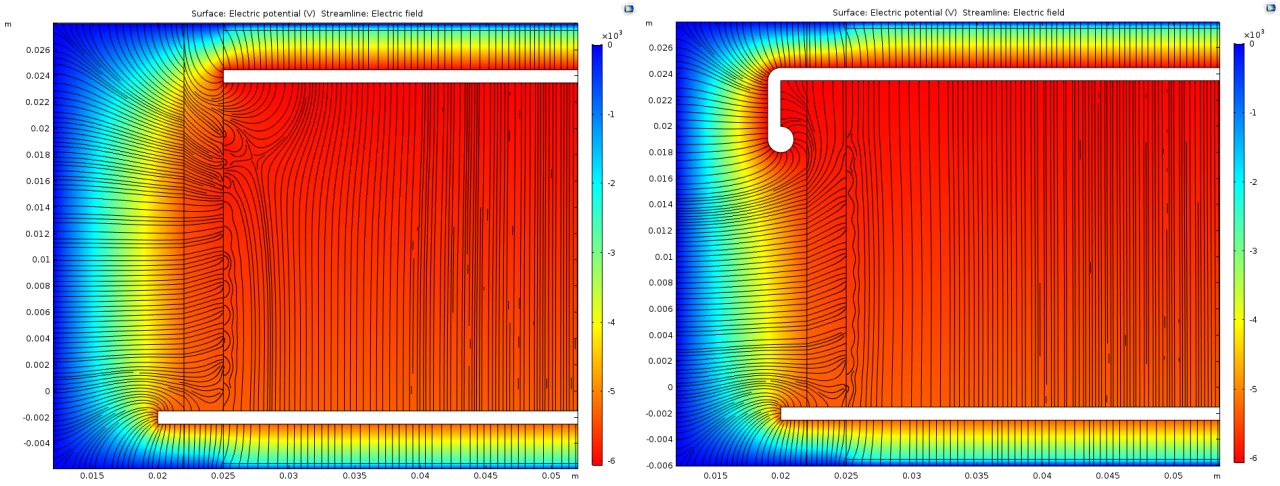

(a) **(b)**

Figure 8.8. (a) Cathode corner where distorted electric fields lines are induced by the 4.5mm gap between the end of the field cage and the cathode. (b) The same geometry with a biased wing. Distances are shown in meters.

about 20 mm^2, or 0.1% of the active volume of the TPC. This dead zone may be negligible for our purposes, but the optimization of this zone serves as a good study case for the subsequent regions due to its simplicity. A solution, proposed by Emmanuel Pollacco, consists in extending the cathode beyond the active volume of the TPC and introducing a biased wing behind the field cage in the TPC air gap. This displaces the edge effects outside the active volume, and significantly improves the field homogeneity, as may be see in Figure 8.8(b). This solution is inspired by the geometry of a Van der Graaff accelerator, as seen in Figure 8.9, where the rounded terminal of the cathode shields the first rings of the field cage, reducing the sparking risk compared to the situation where the field cage is exposed to ground, and increasing field uniformity.

8.3.2. Anode Corner

Similar concepts may be applied to the anode corner, where field homogeneity is much more important as any radial dead spaces above the anode can mean that electrons in that radial zone along the entire length of the TPC are lost. The anode corner consists of the interface between the last strip of the field cage and the Micromegas detection plane. The latter has a grounded mesh, insulating diamond-like carbon layer biased at 500V, and then a grounded pad plane. A small 1 mm wide coverlay on the edge of the detection plane holds the mesh in place. Baseline field calculations for a 5 mm gap between the last field cage electrode (also called the last strip) and the Micromegas mesh are shown in Figure 8.10(a). Note that the radial gap between the wall of the TPC and the anode plane is due to known field inhomogeneities from the field cage, to be addressed in the next section. In the past, solutions have been found via the introduction of guard rings, such as in [181]. Based on the cathode corner study, we applied a biased wing solution, as shown in Figure 8.10(b), and the distortions are reduced to approximately 1 mm of radial zone, as compared to 5-10 mm without correction.

Unfortunately the biased wing solution is less practical in this case, as biasing cables and gas connections (not shown in the figure) need to pass through the same region occupied by the wing. Instead, a simpler solution may be obtained by simply approaching the anode surface and the field

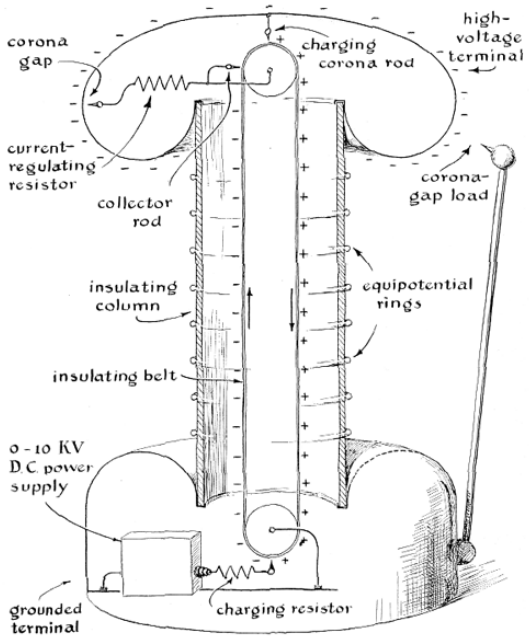

Figure 8.9. Schematic image of a Van der Graaff accelerator. Figure from [180].

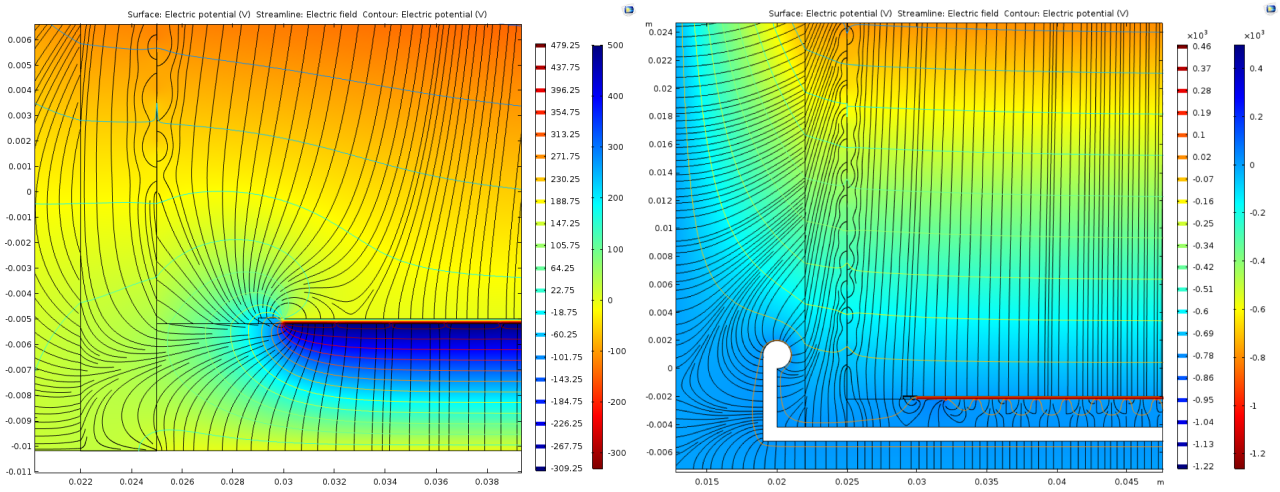

(a) **(b)**

Figure 8.10. (a) Anode corner with standard 5 mm gap between bottom of field cage and Micromegas plane. (b) The same geometry with a biased wing. Distances are shown in meters.

cage. While the MINOS field cage could be placed a minimum of 1.5 mm from the anode, the CERN detector lab can approach the two as close as 0.5 mm, the same as the inter-electrode distance in the field cage. The result of reducing this distance is shown in Figure 8.11. The Micromegas plane has also been moved flush against the wall of the TPC. Here we see another potential problem develop, wherein field lines from near the wall are directed inwards towards the detection plane, but at least these regions are not lost. In principle, such effects of non-linear mapping can be treated later though data analysis. The feasibility of each of these two solutions will eventually be determined after electron drift simulations and more detailed discussions regarding mechanical construction with the CERN

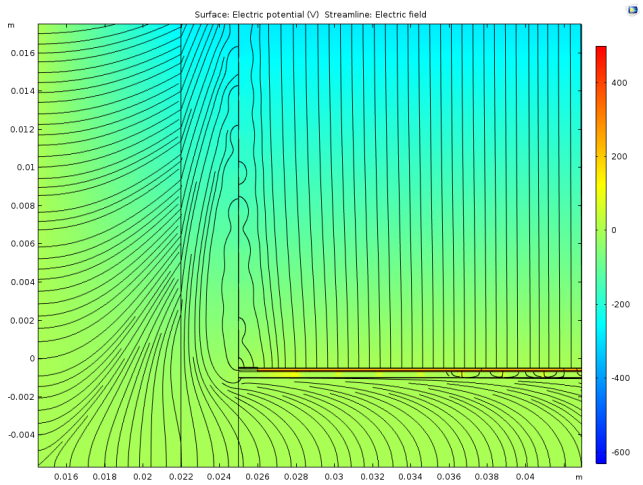

Figure 8.11. Anode corner where the Micromegas plane has been made flush with the wall of the TPC and the distance between the field cage and Micromegas mesh is 0.5 mm, and same as the inter-electrode spacing in the field cage. Distances are shown in meters.

detector lab.

8.3.3. Field Cage and the Wall

The last region of study is the structure of the field cage itself, and the insulation with respect to the external grounded cage of the TPC. While the 3mm PCB insulating layer is considered fixed as it forms the rigid mechanical body of the TPC, the gas gap and the geometry of the field cage strips may be optimized. The first concern regards sparking of the field cage to the outside. Realistic sparking including avalanches and streamers[3] can be simulated with COMSOL, but requires an additional software component that was not available for this work. A simple approximation of the sparking limit, or breakdown voltage between two electrodes in a gas is given by Paschen's Law, shown in Equation 8.4, where d is the distance in meters between the two electrodes, p is pressure in Pascals, γ_{SE} is the voltage and pressure dependent secondary electron coefficient, and A and B are experimentally determined constants [183]. For example $A = 112.50(kPa \cdot cm)^{-1}$ and $B = 2737.50V(kPa \cdot cm)^{-1}$ in air [184]. The secondary electron must be measured in principle, therefore the breakdown voltage was calculated in air across a broad range of γ_{SE} and possible distances between the field cage and the grounded outer surface, as shown in Table 8.1. Note that the insulating PCB layer is not included in this calculation, so the results can be considered as a "worst-case" scenario. It is clear that a 3 mm gap provides sufficient protection from sparking.

$$V_{BD} = \frac{Bpd}{ln(Apd) - ln[ln(1 - \frac{1}{\gamma_{SE}})]} \tag{8.4}$$

The air gap also helps insure field cage uniformity in the TPC, as may be seen in Figure 8.12. Too small of a gap leads to edge effects distorting the field inside the TPC. The effect of varying air gap thickness on the z-component of the field (E_z) is shown in Figure 8.13. The E_z should be constant along the length of the TPC. Significant gains in field uniformity are found going from 0.5 to 2.5 mm,

[3] A streamer occurs when sufficient space charge accumulates in electron avalanches such that a self propagating discharge structure emerges in a given direction [182].

Table 8.1. Breakdown voltages

Distance (mm)	γ_{SE}	$V_{BD}(V)$
1	0.1	4500
2	0.1	8090
3	0.1	11458
5	0.1	17842
10	0.1	32763
2	0.01	8944
2	1.0	6850

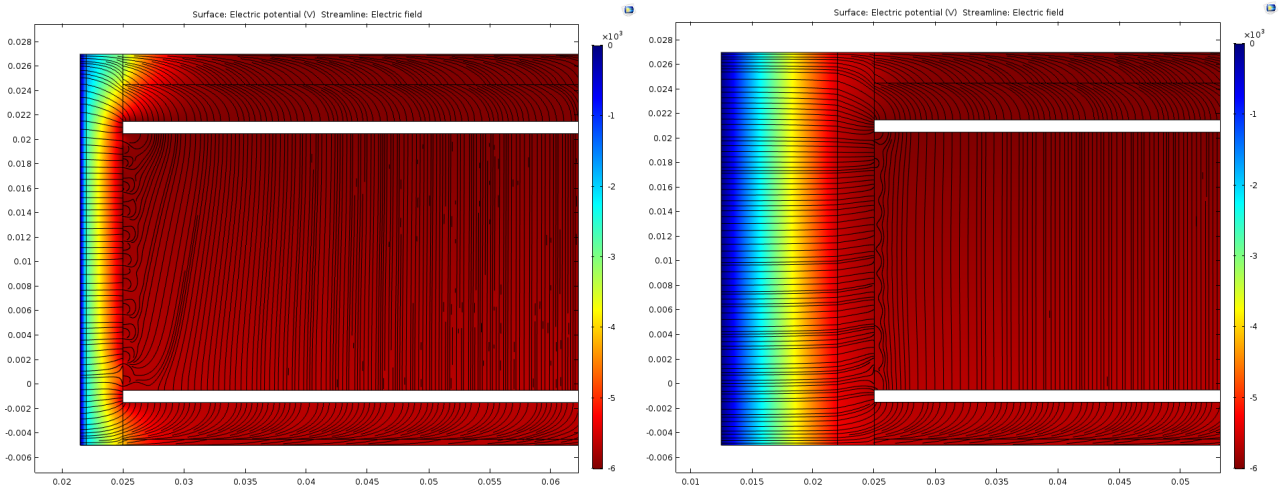

(a) (b)

Figure 8.12. (a) Field lines with 0.5mm gap between the PCB and the outer grounded shell of the TPC (b) The same setup with a 9.5 mm air gap. Distances are shown in meters.

but then the effect is mitigated for larger thicknesses. Thus a minimal thickness of 3 mm, consistent with what was found from the Paschen voltage analysis, is needed.

Finally we consider the radial field uniformities arising from the field cage. It is clear from Figure 8.12 that the discrete structure of the field cage leads to distortions. The previously shown figures include a single field cage, but these distortions may be reduced by introducing a double field cage, as used in MINOS. The field maps for single and double field cages are shown in Figure 8.14. A slight reduction in the radial extent of the inhomogeneities is found for a double field cage, but the gains are not significant. This solution is thus put aside, as a double field cages adds significant complexity for minimal gains. Instead, the length of electrodes and distance between subsequent electrodes will be reduced as much as possible, to limit these field inhomogeneities. Another solution would involve a single, homogeneous resistive material to provide the field degradation, removing this phenomenon altogether, but such a solution is currently considered too complex to be implemented here.

8.4. Outlook

Two dimensional simulations have been performed to optimize the field homogeneity of the PUMA TPC. Solutions for the anode and cathode corners were found either in terms of an extended biased

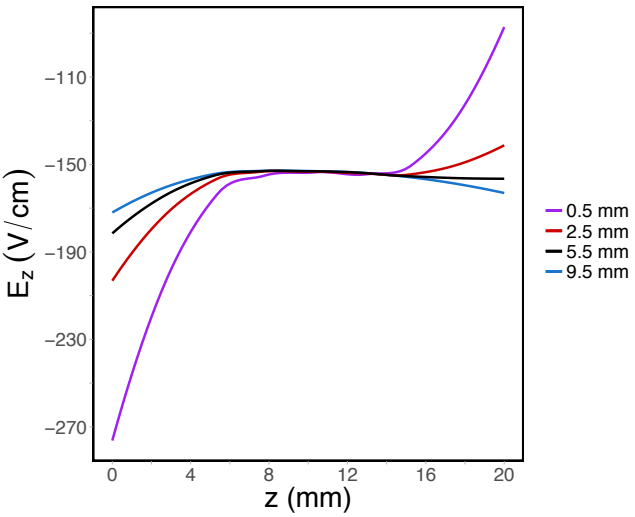

Figure 8.13. Plot of the z-component of the electric field as a function of distance z along the TPC for different air gap thicknesses for the geometry shown in Figure 8.12. The divergences at the extremities are due to anode and cathode edge effects.

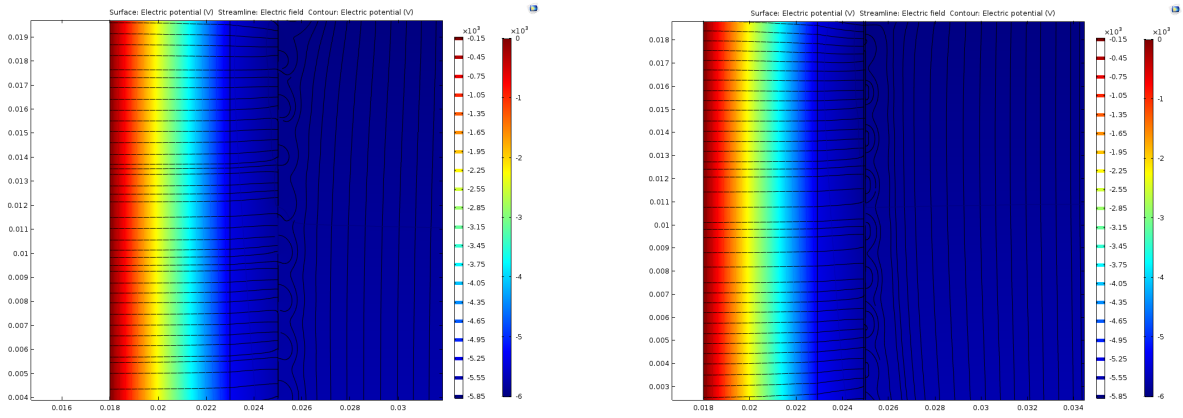

(a) **(b)**

Figure 8.14. Map of field around field cage electrodes (a) for single field cage (b) for double field cage. Distances are shown in meters.

wing electrode, or reduced mechanical spacings between the field cage and endcaps. An insulating gas gap of 3 mm for the body of the TPC was identified by studying breakdown voltages and field homogeneities, and it was discovered that a double field cage, as used in MINOS, did not provide significant gains. Other possibilities to be explored include non-uniform voltage steps on the last few field cage electrodes before the anode plane, and mirrored electrodes behind the anode plane and or the PCB. These optimizations have begun to be incorporated into a full 2D simulation. Currently however the solutions found in the regional simulations do not give the desired field uniformity on the full simulation, for reasons that remain to be explored. Once an acceptable configuration is found in the full simulation, the resulting field map will be used in a realistic electron drift calculation using the CERN software Garfield++ [179]. While steps towards these goals were made, the full realisation was beyond the timeline of this thesis.

Conclusion

This work probed some of the most exotic neutron rich nuclei accessible today through single nucleon removal reactions on a thick proton target, part of the MINOS system. I analysed the spectroscopy data of ^{110}Zr and ^{112}Mo, developing methods for background subtraction and robust fitting techniques to analyse the γ-ray spectrum. The results show no evidence for the emergence of a subshell gap at N=70 arising from a spherical or tetrahedral symmetry, and instead this nucleus is even more deformed than expected compared with mean field models. The large deformation in this nucleus was only reproducible through Monte Carlo shell model calculations with a locally fit effective interaction, or mean field predictions with an artificially enhanced spin-orbit interaction. This work, combined with other recent measurements from the SEASTAR campaign, suggests that the structure of nuclei in this region $Z \leq 40$ and $60 \leq N \leq 70$ manifests complicated shape coexistence, whose details remain to be resolved.

A complementary study explored the systematics of inclusive single nucleon removal cross sections on the thick proton target where I performed a consistent analysis of (p,2p) and (p,pn) inclusive cross sections from two years of experimental campaigns. The (p,2p) systematics show values between 2 and 12 mb and a decreasing trend with $-S_n$. An enhanced cross section from even-Z projectiles is also evidenced here for the first time in these reactions. The (p,pn) systematics show cross sections approximately a factor of 10 larger than (p,2p) cross section for a given projectile, with scattered values around 60 mb. Comparison with semi-microscopic Fragmentation-Evaporation and Intranuclear Cascade models shows that, while the calculations capture the overall trends with separation energy and mass, the finer details, notably the presence and lack of odd even staggering in the proton and neutron removal cross sections, respectively, are not reproduced. These results highlight the importance of microscopic low-lying bound state level densities, particularly pairing effects, to accurately describe nucleon removal from loosely bound neutron rich nuclei.

Both of these studies show the limitations of commonly employed theories to describe the most exotic neutron rich nuclei. How then can we build on these results such that the missing physics ingredients emerge? Francis Bacon said, "Truth emerges more readily from error than from confusion"[185]. One possible path is to remove some of the confusion in interpreting results by performing higher precision measurements, with the maximum observables possible for a given phenomenon. When multiple observables must be reproduced, the available parameter space for making phenomenological corrections should be reduced and the relevant degrees of freedom emerge more clearly. Consider for example the spectroscopy of ^{110}Zr. We were unable in our interpretation to distinguish between the structure scenarios proposed by MCSM and Gogny D1S predictions due to uncertainty on the J^π of the transition in the second band. If such a measurement were performed with a higher precision γ-ray array, and ideally the possibility to detect conversion electrons, the nature of this band could perhaps have been identified. Such efforts are underway, for example of combining high performance gamma ray tracking arrays, like GRETINA or AGATA with thick target systems like MINOS. Information on the energy of the outgoing proton could also provide information on the single particle level from which it was removed to inform level scheme construction. Combining a segmented silicon array outside the liquid hydrogen target has been proposed for a next-generation MINOS device at RIKEN that when paired with a gamma ray tracking array will provide more than a factor of 10 improvement in energy resolution.

A similar approach can be applied for reaction studies. Due to the inclusive nature of the data collected in this work, we restricted ourselves to semi-classical approaches capable of capturing broad systematic trends in the data but clearly missing important structure components like details of single

particle structure. More microscopic approaches exist, but comparing predictions with inclusive cross sections is notoriously difficult due to the entanglement between the structure and reaction ingredients of the models. Such difficulties have been seen historically in the discussion of reduction factors seen with S-matrix methods. Disentangling the two can begin to be achieved through fully exclusive, complete kinematics measurements, which provide full information on both the scattering process and the single particle structure of the states probed, such as demonstrated in [129]. Experimental setups like SAMURAI at RIKEN or R^3B at GSI will perform precision cross section studies with the ability to constrain the reaction mechanism and simultaneously describe the nature of the populated states. One could imagine systematic studies such as the one pursued here with a reconstruction of the outgoing proton kinematics and identification of the nature of the single particle state of the removed nucleon, which would then be able to be compared with microscopic models. R^3B will notably extend the quasifree scattering studies to higher energies around 700 MeV/u where the nucleon-nucleon cross section has its minimum and thus final state interactions are minimized and more interior regions of the nucleus may be probed.

Finally, the last perhaps most exciting alternative is to forget exclusive, precision measurements, and make new measurements of observables where no data exists. Such is the philosophy of the PUMA project which will apply the antiproton method to probe neutron skins in exotic neutron-rich nuclei where theories don't just disagree on the details but are wildly unconstrained. I have contributed to this project by working on the design of the field cage for the PUMA TPC, whose homogeneity is integral to extracting the pion signal from the annihilation data. Next steps will integrate a finalized field cage design into a Geant4 simulation with realistic pion emission to benchmark the detection and reconstruction efficiency. Much development remains for the PUMA project, but once the feasibility of the measurement is demonstrated, it may open the doors to other types of new data, such as gamma spectroscopy of neutron-rich hypernuclei produced from antiproton-nucleus interactions, or even spectroscopy of super-heavy elements from nucleon annihilation, paving the way for a future antiproton-ion collider at CERN or FAIR.

Appendices

A

Appendix A: DALI2 electronics diagram

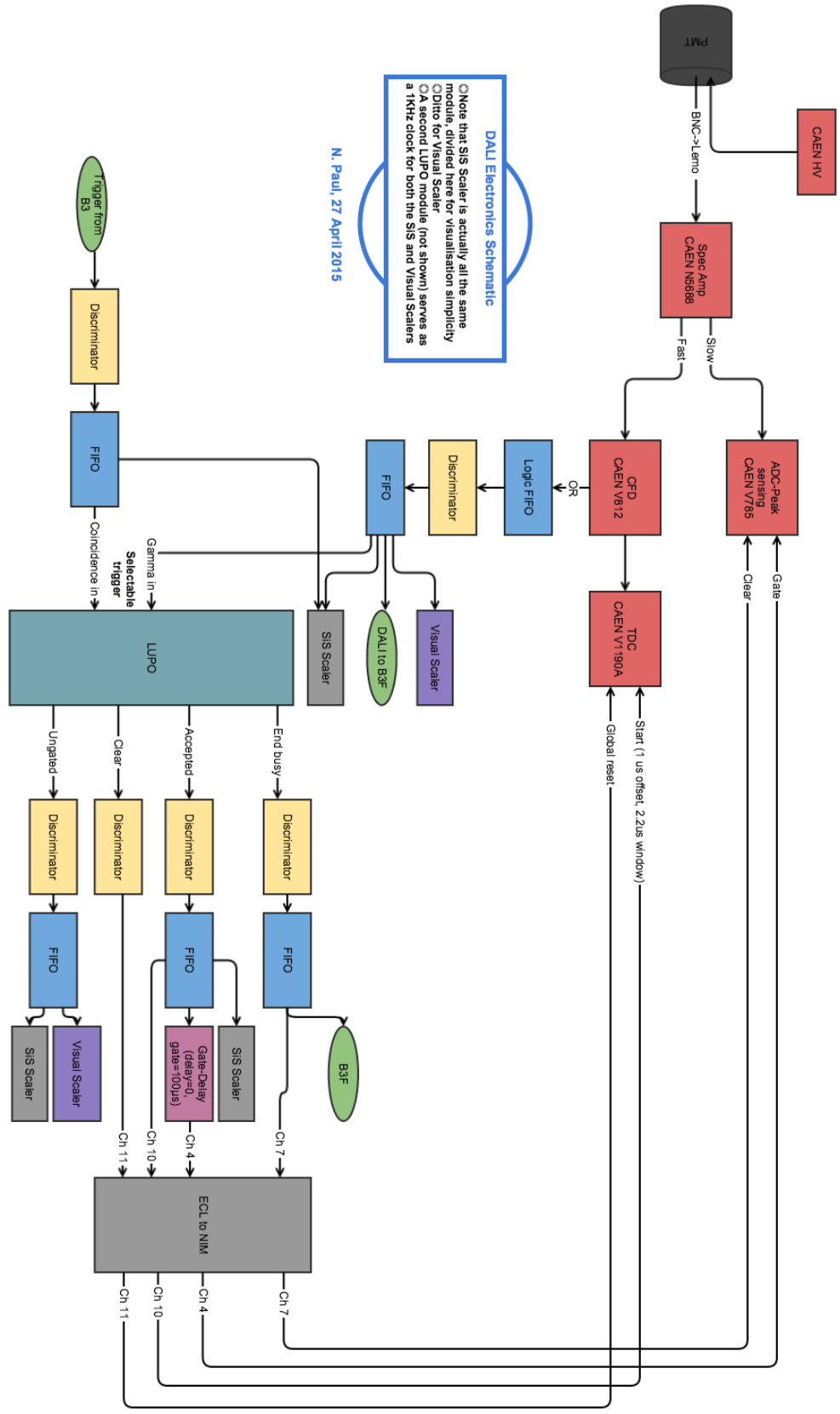

Figure A.1. Schematic of the DALI2 signal processing and trigger scheme

B

Appendix B: ^{110}Zr Angular Divided Fit Comparison

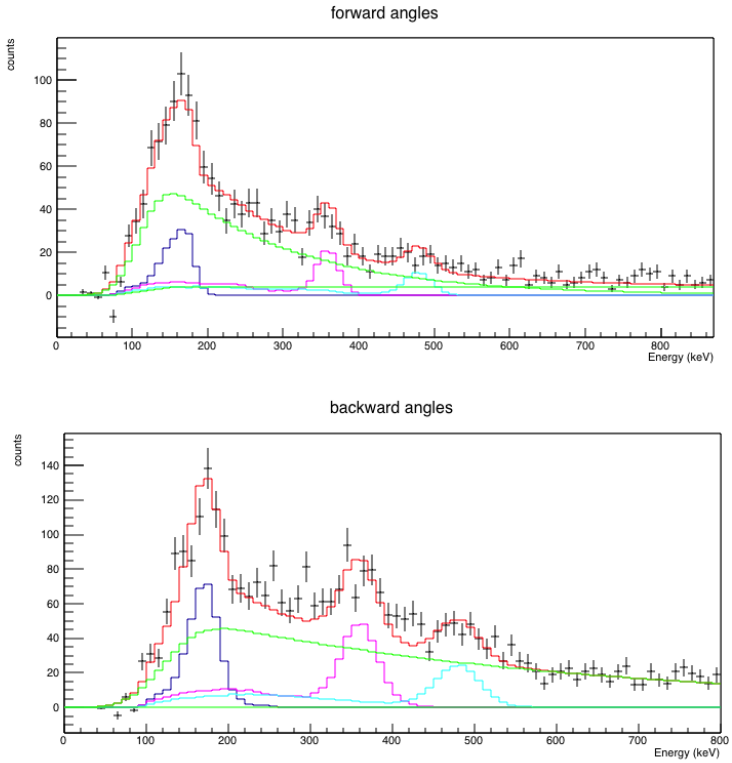

Figure B.1. Angular divided fit for ^{110}Zr after applying backward scaling method as described in Chapter 3.

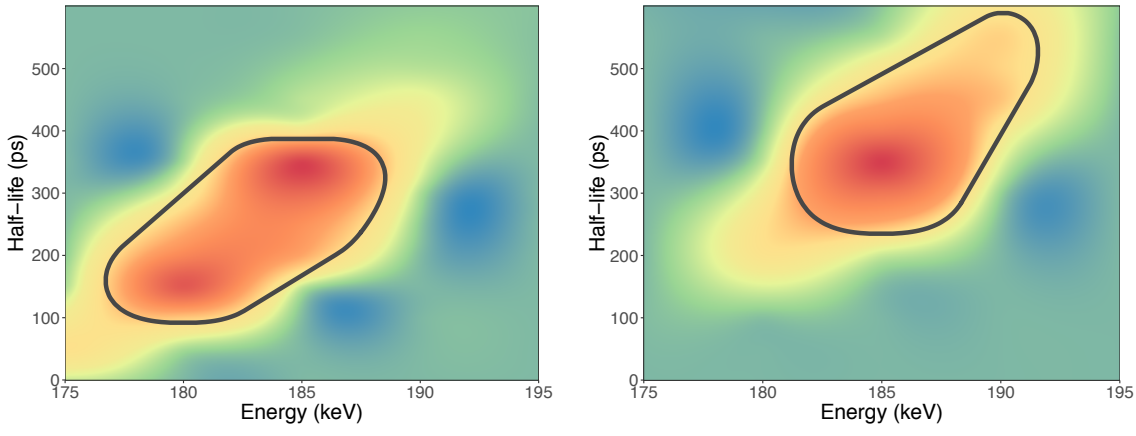

(a) **(b)**

Figure B.2. Probability surfaces and 1-σ regions of confidence (black lines) for $2_1^+ \rightarrow 0_1^+$ transitions in ^{110}Zr when considering the angular divided (a) and full spectrum (b) fits. Note that the probability surfaces and regions of confidence have been smoothed with standard interpolation methods.

C

Appendix C: PID corrections

The PID corrections used for the ^{110}Zr spectroscopy and SEASTAR cross section analysis are as follows:

^{111}Nb Setting:

$$
\begin{aligned}
Z_{corr} &= Z + (\beta - 0.4974) \times 12 \\
A/q_{corr} &= A/q + 0.000065 * F9X + 0.00000025 * (F9X - 20) * (F9X - 20) + 0.0001 * F9A \\
&\quad - 0.00003 * F9A * F9A - 0.0001 * F11X - 0.00006 * F11A \\
&\quad - 0.000001 * (F11A + 6) * (F11A + 6)
\end{aligned}
$$

^{101}Rb Setting:

$$
\begin{aligned}
A/q_{corr} &= A/q - 0.00015 * F8X - 0.000015 * F8X * F8X - 0.00007 * F8A + 0.00008 * F9X \\
&\quad + 0.0000002 * F9X * F9X - 0.0002 * F9A - 0.00002 * F9A * F9A - 0.00025 * F11X \\
&\quad - 0.0002 * F11A + 0.000015 * F11A * F11A
\end{aligned}
$$

^{67}Mn Setting:

$$A/q_{corr} = A/q$$

^{73}Co Setting:

$$A/q_{corr} = A/q + 0.001 * F8X + 0.0006 * F9A$$

^{80}Zn Setting:

$$
\begin{aligned}
A/q_{corr} &= A/q - 0.0002 * (F11X - 8) - 0.0000003 * (F11X - 8) * (F11X - 8) * (F11X - 8) \\
&\quad - 0.0000005 * (F9X) * (F9X) + 0.000000005 * (F9X + 10) * (F9X + 10) * (F9X + 10)
\end{aligned}
$$

Fe Setting:

$$A/q_{corr} = A/q + 0.0007 * F8X + 0.0006 * F9A$$

D

Appendix D: Beamline Contribution to Thick Target Cross Section

It is possible that reactions of the projectile in the beamline elements yield the daughters of interest. This contribution may be incorporated by analysing the number of daughter nuclides created in the empty target runs, and subtracting this from the daughter nuclei measured in the physics runs.

Consider the beamline as being composed of three targets, i) before the LH2 target including the F8 PPACs, TOF detector, DSSSD (SEASTAR2014) and the LH2 target entrance windows, ii) the LH2 target, and iii) the exit windows and ZeroDegree beamline elements. Such a schematic is shown in Figure D.1. The detectable quantities are the number of incident nuclei in BigRIPS, N_i, and the number of outgoing nuclei either of the incident species, N_i^{ZD}, or of the daughter of interest, N_f, for both empty and full target runs. The number of incident nuclei remaining after the first target is N_i', attenuated according to

$$N_i' = N_i e^{-\alpha_1} \tag{D.1}$$

where $\alpha_1 = \sigma_{R1}\eta' L_1$. Similarly, the number of daughter nuclei created after the first target is

$$N_f' = N_i \beta_1 \tag{D.2}$$

where $\beta_1 = \sigma_{-p}\eta' L_1$. Following this logic, as the densities and cross sections are different in each target material, the attenuation and creation coefficients for each target will be denoted as α_n and β_n, respectively, where n is the target number.

For the empty target case, $N_f' = N_f''$, and $N_i' = N_i''$. Then the number of incident and daughter species at the end of target three may be written as

$$N_i^{ZD} = N_i' e^{-\alpha_3} = N_i e^{-\alpha_1} e^{-\alpha_3} \tag{D.3}$$

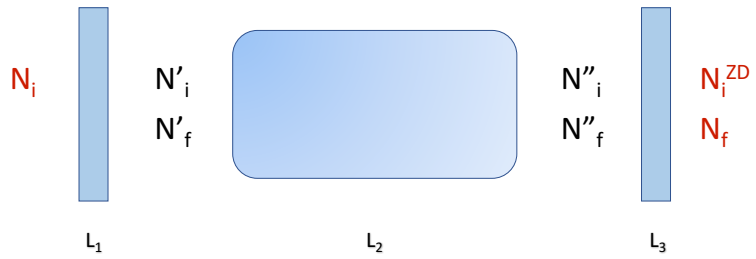

Figure D.1. Three target schematic, with the quantities used to calculated the cross section including subtraction of events in the beamline elements

$$N_f = N_i' \beta_3 - N_f' e^{-\alpha_3} \tag{D.4}$$

Note that the expression for N_f includes both creation of the daughters of interest in the third target as well as attenuation of daughters already created. The two measurable quantities from the empty target run are $\frac{N_f}{N_i}$ and $\frac{N_i^{ZD}}{N_i}$ which may be then expressed as

$$\frac{N_f}{N_i} = e^{-\alpha_1}\beta_3 - \beta_1 e^{-\alpha_3} \equiv R_{empty} \tag{D.5}$$

$$\frac{N_i^{ZD}}{N_i} = e^{-\alpha_1} e^{-\alpha_3} \equiv T_{empty} \tag{D.6}$$

Going to the full target case, N_i' and N_f' are unchanged from the empty target case, and the incident and daughter nuclides at the end of the LH2 cell were already derived in Equation 6.7 as

$$N_i'' = N_i' e^{-\sigma_R \eta L_2} \tag{D.7}$$

$$N_f'' = N_i' \sigma_{p2p} \eta L_2 e^{-\sigma_R \eta L_2} + N_f' e^{-\sigma_R \eta L_2} \tag{D.8}$$

We can use the previous results to simplify this expression for the full target transmission, $\frac{N_i^{ZD}}{N_i} = T_{full}$, which is clearly a product of the transmissions through the three targets.

$$T_{full} = e^{-\sigma_R \eta L_2} e^{-\alpha_1} e^{-\alpha_3} \tag{D.9}$$

$$= e^{-\sigma_R \eta L_2} T_{empty} \tag{D.10}$$

The expression $\frac{N_f}{N_i}$ in this three target configuration may also be simplified to

$$\frac{N_f}{N_i} = e^{-\sigma_R L_2 \eta} e^{-\alpha_1} e^{-\alpha_3} L_2 \eta \sigma_{p2p} + \beta_1 e^{-\alpha_3} + \beta_3 e^{-\alpha_1} \tag{D.11}$$

$$= T_{full} L_2 \eta \sigma_{p2p} - R_{empty} e^{-\sigma_R \eta L_2} \tag{D.12}$$

$$\equiv R_{full} \tag{D.13}$$

Using the fact that $\frac{T_{full}}{T_{empty}} = e^{-\sigma_R \eta L_2}$, this expression may be rearranged to obtain the (p,2p) cross section in this three target configuration

$$\sigma_{p2p} = \frac{R_{full}}{T_{full} L_2 \eta} \left(1 - \frac{R_{empty}}{R_{full}} \frac{T_{full}}{T_{empty}}\right) \tag{D.14}$$

$$= \frac{R_{full}}{T_{full} L_2 \eta} (1 - \gamma) \tag{D.15}$$

Appendix E: Inclusive Cross Sections

The following table shows the (p,2p) and (p,pn) cross sections measured in this work, compared with predictions from INCL and Fragmentation-Evaporation models. Experimental mid-target energies used in the calculations and the setting in which the data was taken are also indicated. The uncertainty includes statistical, systematic, isomeric effects, and empty target subtraction.

Table E.1.

Parent	Daughter	Setting	E_{mid} (MeV/u)	σ (mb)	INCL	FE
^{66}Mn	^{65}Mn	1	247	56(7)	58	95
^{67}Mn	^{66}Mn	1	237	51(6)	42	97
^{68}Fe	^{67}Fe	1	244	55(2)	41	100
^{69}Co	^{68}Co	1	247	52(6)	47	99
^{71}Co	^{70}Co	2	242	50(8)	46	69
^{72}Ni	^{71}Ni	2	242	46(9)	46	113
^{73}Ni	^{72}Ni	2	259	57(3)	62	166
^{74}Ni	^{73}Ni	2	234	58(3)	44	106
^{77}Cu	^{76}Cu	3	251	55(8)	48	128
^{78}Cu	^{77}Cu	3	248	64(5)	56	144
^{79}Zn	^{78}Zn	3	252	63(3)	65	189
^{80}Zn	^{79}Zn	3	248	62(3)	46	144
^{94}Br	^{93}Br	4	221	45(15)	61	131
^{95}Br	^{94}Br	4	213	40(7)	40	99
^{96}Kr	^{95}Kr	4	217	43(3)	42	102
^{97}Kr	^{96}Kr	4	211	40(4)	62	142
^{98}Kr	^{97}Kr	5	220	51(8)	37	117
^{99}Rb	^{98}Rb	5	223	54(2)	51	130
^{100}Rb	^{99}Rb	5	216	54(4)	61	148
^{100}Sr	^{99}Sr	5	226	54(3)	53	126
^{109}Zr	^{108}Zr	6	207	40(15)	66	142
^{110}Nb	^{109}Nb	6	207	60(4)	67	171
^{111}Nb	^{110}Nb	6	201	53(5)	50	145
^{111}Mo	^{110}Mo	6	210	58(5)	72	200
^{112}Mo	^{111}Mo	6	204	61(3)	48	148
^{113}Mo	^{112}Mo	6	199	52(5)	73	180
^{114}Tc	^{113}Tc	6	204	51(8)	68	181
^{67}Fe	^{66}Mn	1	258	7(3)	8	25
^{68}Fe	^{67}Mn	1	244	9.2(6)	9	26
^{68}Co	^{67}Fe	1	254	5.4(5)	9	37
^{69}Co	^{68}Fe	1	247	8.0(5)	12	41

^{70}Ni	^{69}Co	1	251	12(1)	12	65
^{71}Co	^{70}Fe	2	247	4.1(7)	12	41
^{72}Ni	^{71}Co	2	242	10(1)	10	59
^{73}Ni	^{72}Co	2	259	7.0(4)	8	26
^{74}Ni	^{73}Co	2	234	7.3(4)	10	59
^{74}Cu	^{73}Ni	2	262	4.8(3)	9	34
^{75}Cu	^{74}Ni	2	256	6.6(5)	13	42
^{78}Zn	^{77}Cu	3	256	8(1)	10	40
^{79}Zn	^{78}Cu	3	252	5.3(4)	7	31
^{81}Ga	^{80}Zn	3	251	4.7(3)	11	42
^{95}Br	^{94}Se	4	213	2.5(7)	9	39
^{95}Kr	^{94}Br	4	222	6(3)	6	44
^{96}Kr	^{95}Br	4	217	6.7(7)	9	42
^{97}Kr	^{96}Br	4	211	4.1(8)	6	26
^{97}Rb	^{96}Kr	4	222	4.7(6)	11	50
^{98}Rb	^{97}Kr	4	217	2.5(8)	7	47
^{100}Sr	^{99}Rb	5	226	9(1)	11	51
^{109}Nb	^{108}Zr	6	214	5.6(8)	10	50
^{110}Nb	^{109}Zr	6	207	3.0(4)	7	10
^{110}Mo	^{109}Nb	6	214	8(1)	11	56
^{111}Nb	^{110}Zr	6	201	4.3(9)	11	35
^{111}Mo	^{110}Nb	6	210	5.9(7)	9	41
^{112}Mo	^{111}Nb	6	204	7.4(8)	11	34
^{113}Tc	^{112}Mo	6	209	6.5(7)	13	59

Appendix F–Résumé en francais

Le noyau atomique est un système complexe. Avec ses protons et neutrons liés par l'interaction forte, il est à la fois sujet aux forces Coulombiennes et des corrélations à plusieurs corps. À basse énergie ($\leq$ 1 GeV), la théorie de la chromodynamique quantique (QCD) qui gouverne l'interaction forte est non-perturbatrice. Bien que l'extraction d'une interaction nucléon-nucléon directement à partir de la QCD sur réseau semble prometteuse, elle ne peut actuellement être réalisée que pour les systèmes $A = 2$ avec des masses de pions non physiques, voir par exemple [1]. On peut tirer parti de la séparation d'échelles rendue possible par la suppression de la symétrie chirale, ce qui signifie qu'aux énergies typiques de la physique nucléaire, seuls les nucléons et les pions sont des degrés de liberté explicites nécessaires, tandis que les degrés de liberté nucléoniques internes peuvent être pris en compte de manière effective par des termes de contact. Cependant, même en utilisant une interaction effective dérivée de la théorie de champ effectif chirale[1], le nombre extrêmement élevé de degrés de liberté rend les calculs exacts rapidement difficiles à résoudre. La résolution brute de fonderie de l'équation de Schrödinger pour un système à cinq nucléons nécessite des dizaines de millions d'heures de traitement sur les plus gros supercalculateurs du monde, et la mise en œuvre de telles approches pour des masses supérieures à 10 n'est pas possible avec la technologie actuelle. Etant donné que l'interaction et le problème multi corps ne peuvent être résolus microscopiquement que pour les systèmes les plus simples, les efforts modernes ne cherchent pas à tirer toute la physique d'une théorie unificatrice, mais plutôt à construire une série de théories effectives, chacune adaptée à un domaine d'observation [2]. Le succès de telles théories effectives dépend de leur capacité à identifier et à décrire les degrés de liberté pertinents qui régissent les observables d'une échelle énergétique donnée.

C'est là que nous, expérimentateurs, entrons en scène. La mesure d'observables fondamentales dans des régions où les prévisions théoriques divergent peut aider à cerner la physique pertinente à l'origine de l'évolution des structures des noyaux exotiques. Les noyaux les plus riches en neutrons sont souvent étudiés dans des installations de fragmentation, telles que le RIBF au Japon, où les données présentées dans ce travail ont été obtenues. Le RIBF est la seule installation de fragmentation de nouvelle génération actuellement opérationnelle, mais d'autres suivront prochainement, telles que FAIR en Allemagne ou FRIB aux États-Unis. Les faisceaux relativistes avec des cibles épaisses fournissent la luminosité la plus élevée de noyaux rares, mais historiquement, ces gains étaient limités par une faible résolution spectroscopique due à une correction Doppler imprécise. Une avancée majeure a été réalisée avec le système MINOS, qui associe une cible d'hydrogène liquide épaisse à un trajectrographe de protons permettant simultanément une luminosité et une résolution élevées via la reconstruction du vertex de réaction [4, 5]. Ce travail utilise des réactions d'arrachage de proton avec le système MINOS pour étudier la structure du noyau de référence clé ^{110}Zr, participant à l'effort mondial visant à réaliser des mesures ciblées des espèces les plus exotiques dans des régions contestées de l'évolution de la structure nucléaire.

[1] une expansion contrôlée à basse énergie basée sur le comptage de puissance et l'ajustement à des propriétés de basse énergie

Le noyau de ^{110}Zr se situe au centre de nombreux débats théoriques sur l'évolution de la structure riche en neutrons. Une extinction potentielle de la fermeture de la couche $N = 82$ dans des noyaux riches en neutrons entraînée par un affaiblissement d'effet spin-orbite a été proposée pour conduire à une ouverture du gap de l'oscillateur harmonique à $N = 70$. Si un tel gap existe, il sera peut-être particulièrement visible dans le ^{110}Zr, qui combine deux fermetures de couches d'oscillateur harmonique avec ses 40 protons et 70 neutrons. Une autre perspective, suggérée par d'autres travaux ont prédit l'apparition d'une symétrie tétraédrique dans ce noyau. Une symétrie tétraédrique, qui peut être imaginée comme une sorte de forme pyramidale, est une symétrie exotique prédite mais jamais confirmée. Les nombres 40 et 70 correspondent également à des fermetures de couche tétraédriques, et certains calculs montrent que le ^{110}Zr peut être tétraédrique dans son état fondamental avec une structure différente qu'attendu pour un noyaux pair-pair, notamment la présence d'un premier état excité 3^-, ce qui peut être examiné avec une mesure de spectroscopie.

Si le ^{110}Zr présente une certaine stabilité, en raison de l'émergence des fermetures de couche d'oscillateur harmoniques ou de symétries tétraédriques, cela peut avoir des conséquences sur notre compréhension du processus de capture rapide des neutrons, ou processus-r, qui serait responsable d'environ 50% des abondances des éléments plus lourds que le fer dans l'univers. Traditionnellement, les modèles ont eu du mal à reproduire les abondances entre les masses 110 et 120, et un ^{110}Zr stabilisé a été proposé comme solution potentielle.

Ces symétries exotiques ne représentent toutefois que les résultats d'une minorité de calculs, et la plupart des théoriciens s'accordent pour dire que ^{110}Zr devrait être bien déformé et présenter une certaine coexistence de formes, à l'instar des noyaux voisins. Mais l'intérêt dû aux scénarios exotiques a conduit à une multitude de calculs de ce noyau, faisant de sa structure, quelle qu'elle soit, une référence essentielle pour comprendre la structure nucléaire des noyaux très riches en neutrons.

F.1. Dispositif expérimental

La première spectroscopie de ^{110}Zr faisait partie de la deuxième campagne SEASTAR (acronyme anglais de *Shell Evolution And Search for Two-plus Energies At RIBF* signifiant en français : évolution de la structure en couche et recherche d'énergies deux-plus à RIBF).). Le noyau parent ^{111}Nb a été créé par fission en vol d'un faisceau primaire de ^{238}U sur une cible de production de béryllium de 3 mm d'épaisseur et sélectionné avec le spectromètre BigRIPS [152]. Le ^{110}Zr a été produit par arrachage d'un proton sur une cible d'hydrogène liquide de 10 cm d'épaisseur, faisant partie du système MINOS [4]. Les rayons gamma émis en vol ont été détectés par les scintillateurs de DALI2 et les protons émis pendant la réaction ont été détectés par la chambre de projection temporelle de MINOS qui a permis la reconstruction du vertex de la réaction. Les résidus de réaction ont été détectés dans le spectromètre ZeroDegree. Tous les noyaux ont été identifiés événement par événement dans les deux spectromètres.

F.2. Analyse et Interprétation

Les spectres gamma Doppler corrigés pour ^{110}Zr et ^{112}Mo sont présentés sur le Figure F.1 par les traces noires. Les deux spectres sont dominés par une composante importante de bruit du fond atomique à basse énergie dans la même région que les transitions d'intérêt. Cette composante a été extraite expérimentalement (traces bleues) en regardant les spectres gamma pour le faisceau direct

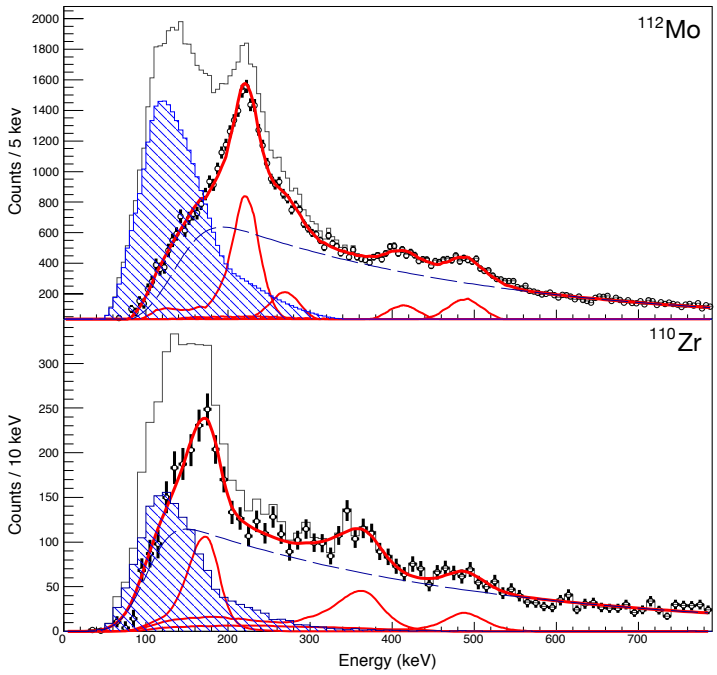

Figure F.1. Spectres gamma Doppler corrigés pour le ^{112}Mo et le ^{110}Zr (traces noires), la composante atomique normalisée (traces bleues), et les spectres avec la composante atomique soustraite (points noirs). Les fonctions de réponses simulées et le fit total sont en rouge.

(^{112}Mo $\rightarrow$ ^{112}Mo, par exemple), normalisés par le nombre d'ions incidents sur la cible d'hydrogène, et soustraits pour donner les spectres en points noirs. Les spectres soustraits ont été ajustés avec des fonctions de réponse DALI2 simulées avec GEANT4. Pour chaque pic visible dans les spectres, les fonctions de réponse ont été simulées avec des énergies et temps de vie différents, et les spectres soustraits ont été ajustés avec toutes les combinaisons des fonctions de réponse. Le χ^2 du fit a été transformé en probabilité sous l'ansatz que les données peuvent être décrit par une loi normale multidimensionnelle, et les régions de confiance dans le surface de probabilité utilisés pour déterminer l'incertitude en énergie des transitions. Une incertitude additionnelle systématique de 5 keV est ajoutée quadratiquement avec l'incertitude venant du fit pour déterminer les incertitudes finales. Les schémas de niveaux ont été construits en regardant les coïncidences gamma-gamma avec le pic principal, et l'évolution des pics avec des spectres de multiplicités différentes. Les schémas de niveaux finals sont présentés en Figure F.2.

En regardant les systématiques du N=70, les énergies des 2^+ mesurées ici montrent une diminution progressive allant vers la mi-couche sans signe d'effet de stabilisation à $N = 70$. La comparaison avec trois calculs au-delà du champ moyen confirme que ^{110}Zr est un noyau bien déformé, et les données suggèrent une déformation étonnamment plus forte encore que prévue par ces modèles. La meilleure reproduction du spectre expérimental est fournie par les prédictions du modèle en couches Monte Carlo, cependant, ces calculs ont été ajustés sur la chaîne isotopique du zirconium. Bien que les deux approches présentent un accord global satisfaisant avec le schéma de niveau mesuré, la principale différence entre les prédictions du modèle au-delà du champ moyen et du modèle en couches repose sur la nature des premier et second états 0+. Les prédictions des calculs au-delà du champ moyen indiquent un état fondamental triaxial et un deuxième 0^+ prolate, tandis que le modèle en couches prévoit un état fondamental prolate et un deuxième 0^+ triaxial. Une mesure de résolution supérieure

Figure F.2. Schémas de niveaux pour le ^{112}Mo et le ^{110}Zr obtenus dans ce travail.

avec la capacité de mesurer les électrons de conversion serait nécessaire pour différencier les deux scénarios proposés. Les résultats sont également incompatibles avec un état fondamental tétraédrique dans ^{110}Zr. Ces résultats ont été publiés à titre de suggestion de l'éditeur dans Physical Review Letters 118, 032501 (2017).

F.3. Étude de Sections Efficaces Inclusives

Une étude complémentaire explore les systématiques des sections efficaces inclusives pour l'arrachage d'un nucléon sur la cible d'hydrogène liquide MINOS. Les données proviennent des campagnes SEASTAR 2014 et 2015 et utilisent la même configuration que pour la mesure de spectroscopie de ^{110}Zr. Les détails de l'analyse et de la méthodologie se trouvent au chapitre 6. 55 sections efficaces d'arrachage d'un nucléon ont été extraites pour des masses comprises entre 66 et 114. Les données (p, 2p) montrent deux caractéristiques principales. La première est une tendance décroissante avec l'énergie de séparation des neutrons négative, vue précédemment dans la littérature, par exemple [155]. La seconde est une augmentation d'environ 50% de la section efficaces pour des projectiles avec un Z pair par rapport aux projectiles de Z-impairs avec la même énergie de séparation des neutrons. C'est la première fois que cet effet est noté dans la littérature pour ces réactions directes. Les sections efficaces (p,pn) ne montrent aucune systématique notable mais sont dispersés autour de 45 mb. Dans un première temps ces données ont été comparées au *Intranuclear Cascade Model of Liège* (INCL) [186]. Les calculs INCL reproduisent bien la tendance à la baisse des données (p, 2p) et la valeur moyenne des sections efficaces (p, pn). Les détails manquent cependant, car la division entre la séquence impaire-paire dans les données (p, 2p) n'est pas reproduite et les calculs INCL montrent un fort effet pair-impair dans les systématiques (p, pn) qui n'est pas vu dans les données. Ces divergences suggèrent que le désaccord a pour origine le manque de la densité de niveau microscopique dans INCL. Notamment, on s'attend à une densité de niveau réduite chez les noyaux fils pairs pair en raison d'effets d'appariement qui ne sont pas inclus dans le modèle.

Une modification phénoménologique a été apportée à l'énergie d'excitation INCL pour tenter de capturer ces effets, équivalent à la différence entre les énergies de séparation proton (neutron) fils et parent pour l'arrachage d'un proton (neutron). Ces calculs modifiés reproduisent la division pair-impaire dans les prédictions (p,2p) et réduisent celle-ci dans les prédictions (p,pn), étayant qualitativement notre compréhension de l'origine de ces effets. Ces résultats ont été soumis pour publication.

F.4. Optimisation de Cage de Champ pour la TPC de PUMA

La dernière partie de ma thèse portait sur l'optimisation électromécanique de la cage de champ pour une nouvelle chambre à projection temporelle pour la future expérience PUMA. PUMA, ou *antiProton Unstable Matter Annihilation*, est une future expérience au CERN qui cherche à sonder le rapport de densité proton sur neutron à la surface du noyau par l'annihilation de noyaux exotiques avec des antiprotons. Au cœur de PUMA se trouve une chambre de projection temporelle qui mesure les pions émis lors du processus d'annihilation. Bien que la taille de ce TPC soit très similaire à celle du dispositif MINOS, le projet PUMA présente un certain nombre de contraintes de conception supplémentaires. La TPC doit notamment tenir dans un solénoïde supraconducteur et ne peut pas être retirée facilement. Elle doit donc être stable électromécaniquement pendant des mois sans nécessiter de maintenance. De plus, l'ensemble de l'installation PUMA est portable et passe de l'anneau AD à ISOLDE. Le TPC doit donc être stable contre les vibrations, avec une conception aussi simple et robuste que possible. Enfin, pour distinguer les différents pions chargés du noyau de recul, le TPC doit disposer de la zone active la plus grande possible pour une reconstruction optimale des traces.

L'optimisation électrostatique de la cage de champ PUMA a été réalisée avec la suite logicielle multiphysique COMSOL. Trois régions d'intérêt ont été étudiées : 1) l'interface entre la première piste de la cage de champ et la cathode 2) l'interface entre la dernière piste de la cage de champ et l'anode 3) l'isolation par rapport à la cage de champ et la coquille extérieure de TPC. Une solution a été trouvée pour améliorer l'homogénéité du champ dans le coin de la cathode en allongeant la cathode derrière la cage de champ et en aval de la première piste tout en maintenant une distance mécanique de 4,5 mm entre la cathode et la première piste afin de réduire les risques d'étincelles. Une solution a été trouvée pour améliorer l'homogénéité du champ dans le coin de l'anode en réduisant les espacements mécaniques à 0,5 mm entre la dernière piste et l'anode et en déplacant l'anode contre le mur du TPC. Enfin, les courbes de Paschen et les lignes de champ ont été étudiées en fonction de la largeur de la région gazeuse isolante entre la cage de champ et la coque en aluminium mise à la terre. Une région isolante de 3 mm de large a été trouvée pour satisfaire les préoccupations d'étincelles et fournir une homogénéité de champ satisfaisante avec un budget minimum de matériaux. Les étapes suivantes sont un calcul de dérive des électrons réaliste avec le logiciel CERN Garfield++ en utilisant la géométrie optimisée avec COMSOL, et l'intégration éventuelle dans une simulation complète du détecteur en Geant4. Le travail, se prolongeant au-delà du cadre de la thèse, sera poursuivi par la collaboration PUMA.

Bibliography

[1] S. Aoki, "Nucleon-nucleon interactions via Lattice QCD: Methodology", *Eur. Phys. J. A* **49** (2013) 81.

[2] S. Weinberg, "Phenomenological Lagrangians", *Phys. A Stat. Mech. its Appl.* **96** (1979) 327–340.

[3] M. Warda, X. Viñas, X. Roca-Maza, and M. Centelles, "Neutron skin thickness in the droplet model with surface width dependence: Indications of softness of the nuclear symmetry energy", *Phys. Rev. C* **80** (2009) 024316.

[4] A. Obertelli, A. Delbart, S. Anvar, L. Audirac, G. Authelet, H. Baba, B. Bruyneel, D. Calvet, F. Château, A. Corsi, P. Doornenbal, J. M. Gheller, A. Giganon, C. Lahonde-Hamdoun, D. Leboeuf, D. Loiseau, A. Mohamed, J. P. Mols, H. Otsu, C. Péron, A. Peyaud, E. C. Pollacco, G. Prono, J. Y. Rousse, C. Santamaria, and T. Uesaka, "MINOS: A vertex tracker coupled to a thick liquid-hydrogen target for in-beam spectroscopy of exotic nuclei", *Eur. Phys. J. A* **50** (2014) 8.

[5] C. Santamaria, A. Obertelli, S. Ota, M. Sasano, E. Takada, L. Audirac, H. Baba, D. Calvet, F. Château, A. Corsi, A. Delbart, P. Doornenbal, A. Giganon, A. Gillibert, Y. Kondo, Y. Kubota, C. Lahonde-Hamdoun, V. Lapoux, D. Leboeuf, C. Lee, H. Liu, M. Matsushita, T. Motobayashi, M. Niikura, M. Kurata-Nishimura, H. Otsu, A. Peyaud, E. Pollacco, G. Prono, H. Tokieda, T. Uesaka, and J. Zenihiro, "Tracking with the MINOS Time Projection Chamber", *Nucl. Instruments Methods A* **905** (2018) 138–148.

[6] E. Gibney, "Physicists plan antimatter's first outing — in a van", *Nature* **554** (2018).

[7] M. G. Mayer, "On Closed Shells in Nuclei", *Phys. Rev.* **74** (1948) 235–239.

[8] W. Elsasser, "Sur le principe de Pauli dans les noyaux - III.", *J. Phys. le Radium* **5** (1934), no. 12, 635–639.

[9] K. Guggenheimer, "Remarques sur la constitution des noyaux atomiques - I.", *J. Phys. le Radium* **5** (1934) 253–256.

[10] E. Wigner, "On the Structure of Nuclei Beyond Oxygen", *Phys. Rev.* **51** (1937) 947–958.

[11] W. H. Barkas, "The Analysis of Nuclear Binding Energies", *Phys. Rev.* **55** (1939) 691–698.

[12] A. Chodos, E. Tretkoff, J. Ouellette, and N. Ramlagan, "Maria Goeppert Mayer and the Nuclear Shell Model", *APS News*, 2008.

[13] M. G. Mayer, "On Closed Shells in Nuclei. II", *Phys. Rev.* **75** (1949) 1969–1970.

[14] O. Haxel, J. H. D. Jensen, and H. E. Suess, "On the "Magic Numbers" in Nuclear Structure", *Phys. Rev.* **75** (1949) 1766–1766.

[15] S. Quaglioni, P. Navrátil, G. Hupin, J. Langhammer, C. Romero-Redondo, and R. Roth, "No-Core Shell Model Analysis of Light Nuclei", *Few-Body Syst.* **54** (2013) 877–884.

[16] E. Caurier, G. Martínez-Pinedo, F. Nowacki, A. Poves, and A. P. Zuker, "The shell model as a unified view of nuclear structure", *Rev. Mod. Phys.* **77** (2005) 427–488.

[17] Y. Utsuno, T. Otsuka, Y. Tsunoda, N. Shimizu, M. Honma, T. Togashi, and T. Mizusaki, "Recent Advances in Shell Evolution with Shell-Model Calculations", vol. 6. Journal of the Physical Society of Japan, 2015.

[18] N. Tsunoda, T. Otsuka, N. Shimizu, M. Hjorth-Jensen, K. Takayanagi, and T. Suzuki, "Exotic neutron-rich medium-mass nuclei with realistic nuclear forces", *Phys. Rev. C* **95** (2017) 021304.

[19] E. Gebrerufael, K. Vobig, H. Hergert, and R. Roth, "Ab Initio Description of Open-Shell Nuclei: Merging No-Core Shell Model and In-Medium Similarity Renormalization Group", *Phys. Rev. Lett.* **118** (2017) 152503.

[20] P. Ring and P. Schuck, "The nuclear many-body problem", Springer-Verlag, 1980.

[21] T. Skyrme, "The spin-orbit interaction in nuclei", *Nucl. Phys.* **9** (1958) 635–640.

[22] T. Skyrme, "The effective nuclear potential", *Nucl. Phys.* **9** (1958) 615–634.

[23] J. Dechargé and D. Gogny, "Hartree-Fock-Bogolyubov calculations with the D 1 effective interaction on spherical nuclei", *Phys. Rev. C* **21** (1980) 1568–1593.

[24] M. Bender and P.-H. Heenen, "Configuration mixing of angular-momentum and particle-number projected triaxial Hartree-Fock-Bogoliubov states using the Skyrme energy density functional", *Phys. Rev. C* **78** (2008) 024309.

[25] W. Pauli, "Zur Frage der theoretischen Deutung der Satelliten einiger Spektrallinien und ihrer Beeinflussung durch magnetische Felder", *Naturwissenschaften* **12** (1924) 741–743.

[26] H. Schuler and T. Schmidt, "ber die Abweichung des Cassiopeiumatomkerns von der Kugelsymmetrie", *Zeitschrift fur Phys.* **95** (1935) 265–273.

[27] T. Schmidt, "The Electric Quadrupole Moment of the Nucleus", *Nature* **138** (1936) 404–404.

[28] W. Nazarewicz, "Microscopic origin of nuclear deformations", *Nucl. Phys. A* **574** (1994), no. 1, 27–49.

[29] P.-G. Reinhard and E. Otten, "Transition to deformed shapes as a nuclear Jahn-Teller effect", *Nucl. Phys. A* **420** (1984) 173–192.

[30] S. G. Nilsson, "Binding States of Individual Nucleons in Strongly Deformed Nuclei", *Dan Mat Fys Medd* **29** (1955), no. 16,.

[31] T. S. Kuhn, "The structure of scientific revolutions", University of Chicago Press, 2nd ed., 1970.

[32] M. Freer, "The clustered nucleus—cluster structures in stable and unstable nuclei", *Reports Prog. Phys.* **70** (2007) 2149–2210.

[33] I. Talmi and I. Unna, "Order of Levels in the Shell Model and Spin of Be 11", *Phys. Rev. Lett.* **4** (1960) 469–470.

[34] T. Otsuka, A. Gade, O. Sorlin, T. Suzuki, and Y. Utsuno, "Evolution of nuclear structure in exotic nuclei and nuclear forces", *arXiv*, 2018 1805.06501.

[35] R. Casten, "Quantum phase transitions and structural evolution in nuclei", *Prog. Part. Nucl. Phys.* **62** (2009) 183–209.

[36] A. Bohr and B. R. Mottelson, "Nuclear structure", Benjamin, New York, 1998.

[37] N. Paul, A. Corsi, A. Obertelli, P. Doornenbal, G. Authelet, H. Baba, B. Bally, M. Bender, D. Calvet, F. Château, S. Chen, J.-P. Delaroche, A. Delbart, J.-M. Gheller, A. Giganon, A. Gillibert, M. Girod, P.-H. Heenen, V. Lapoux, J. Libert, T. Motobayashi, M. Niikura, T. Otsuka, T. Rodríguez, J.-Y. Roussé, H. Sakurai, C. Santamaria, N. Shimizu, D. Steppenbeck, R. Taniuchi, T. Togashi, Y. Tsunoda, T. Uesaka, T. Ando, T. Arici, A. Blazhev, F. Browne, A. Bruce, R. Carroll, L. Chung, M. Cortés, M. Dewald, B. Ding, F. Flavigny, S. Franchoo, M. Górska, A. Gottardo, A. Jungclaus, J. Lee, M. Lettmann, B. Linh, J. Liu, Z. Liu, C. Lizarazo, S. Momiyama, K. Moschner, S. Nagamine, N. Nakatsuka, C. Nita, C. Nobs, L. Olivier, Z. Patel, Z. Podolyák, M. Rudigier, T. Saito, C. Shand, P.-A. Söderström, I. Stefan, R. Orlandi, V. Vaquero, V. Werner, K. Wimmer, and Z. Xu, "Are There Signatures of Harmonic Oscillator Shells Far from Stability? First Spectroscopy of Zr 110", *Phys. Rev. Lett.* **118** (2017) 032501.

[38] J. Dobaczewski, N. Michel, W. Nazarewicz, M. Płoszajczak, and J. Rotureau, "Shell structure of exotic nuclei", *Prog. Part. Nucl. Phys.* **59** (2007) 432–445.

[39] J. Dobaczewski, I. Hamamoto, W. Nazarewicz, and J. Sheikh, "Nuclear shell structure at particle drip lines.", *Phys. Rev. Lett.* **72** (1994) 981–984.

[40] G. Lalazissis, D. Vretenar, W. Pöschl, and P. Ring, "Reduction of the spin-orbit potential in light drip-line nuclei", *Phys. Lett. B* **418** (1998) 7–12.

[41] W. Nazarewicz and R. Casten, "Physics at the Rare Isotope Accelerator (RIA): Exploring the nuclear landscape", *Nucl. Phys. A* **682** (2001) 295–309.

[42] R. F. Casten, "Nuclear Structure from a Simple Perspective", Oxford University Press, 2001.

[43] T. Otsuka, R. Fujimoto, Y. Utsuno, B. A. Brown, M. Honma, and T. Mizusaki, "Magic Numbers in Exotic Nuclei and Spin-Isospin Properties of the NN Interaction", *Phys. Rev. Lett.* **87** (2001) 082502.

[44] T. Otsuka, T. Suzuki, R. Fujimoto, H. Grawe, and Y. Akaishi, "Evolution of nuclear shells due to the tensor force.", *Phys. Rev. Lett.* **95** (2005) 232502.

[45] D. Steppenbeck, S. Takeuchi, N. Aoi, P. Doornenbal, M. Matsushita, H. Wang, H. Baba, N. Fukuda, S. Go, M. Honma, J. Lee, K. Matsui, S. Michimasa, T. Motobayashi, D. Nishimura, T. Otsuka, H. Sakurai, Y. Shiga, P.-A. Söderström, T. Sumikama, H. Suzuki, R. Taniuchi, Y. Utsuno, J. J. Valiente-Dobón, and K. Yoneda, "Evidence for a new nuclear 'magic number' from the level structure of 54Ca.", *Nature* **502** (2013) 207–10.

[46] B. Bastin, S. Grévy, D. Sohler, O. Sorlin, Z. Dombrádi, N. L. Achouri, J. C. Angélique, F. Azaiez, D. Baiborodin, R. Borcea, C. Bourgeois, A. Buta, A. Bürger, R. Chapman, J. C. Dalouzy, Z. Dlouhy, A. Drouard, Z. Elekes, S. Franchoo, S. Iacob, B. Laurent, M. Lazar, X. Liang, E. Liénard, J. Mrazek, L. Nalpas, F. Negoita, N. A. Orr, Y. Penionzhkevich, Z. Podolyák, F. Pougheon, P. Roussel-Chomaz, M. G. Saint-Laurent, M. Stanoiu, I. Stefan, F. Nowacki, and A. Poves, "Collapse of the N = 28 Shell Closure in 42Si", *Phys. Rev. Lett.* **99** (2007) 022503.

[47] C. Thibault, R. Klapisch, C. Rigaud, A. M. Poskanzer, R. Prieels, L. Lessard, and W. Reisdorf, "Direct measurement of the masses of Li 11 and Na 2 6 3 2 with an on-line mass spectrometer", *Phys. Rev. C* **12** (1975) 644–657.

[48] D. Guillemaud-Mueller, C. Detraz, M. Langevin, F. Naulin, M. de Saint-Simon, C. Thibault, F. Touchard, and M. Epherre, "β-Decay schemes of very neutron-rich sodium isotopes and their descendants", *Nucl. Phys. A* **426** (1984) 37–76.

[49] A. Navin, D. W. Anthony, T. Aumann, T. Baumann, D. Bazin, Y. Blumenfeld, B. A. Brown, T. Glasmacher, P. G. Hansen, R. W. Ibbotson, P. A. Lofy, V. Maddalena, K. Miller, T. Nakamura, B. V. Pritychenko, B. M. Sherrill, E. Spears, M. Steiner, J. A. Tostevin, J. Yurkon, and A. Wagner, "Direct Evidence for the Breakdown of the N = 8 Shell Closure in 12Be", *Phys. Rev. Lett.* **85** (2000) 266–269.

[50] A. Huck, G. Klotz, A. Knipper, C. Miehé, C. Richard-Serre, G. Walter, A. Poves, H. L. Ravn, and G. Marguier, "Beta decay of the new isotopes K 52 , Ca 52 , and Sc 52 ; a test of the shell model far from stability", *Phys. Rev. C* **31** (1985) 2226–2237.

[51] K. Tshoo, Y. Satou, H. Bhang, S. Choi, T. Nakamura, Y. Kondo, S. Deguchi, Y. Kawada, N. Kobayashi, Y. Nakayama, K. Tanaka, N. Tanaka, N. Aoi, M. Ishihara, T. Motobayashi, H. Otsu, H. Sakurai, S. Takeuchi, Y. Togano, K. Yoneda, Z. Li, F. Delaunay, J. Gibelin, F. Marqués, N. Orr, T. Honda, M. Matsushita, T. Kobayashi, Y. Miyashita, T. Sumikama, K. Yoshinaga, S. Shimoura, D. Sohler, T. Zheng, and Z. Cao, "N=16 Spherical Shell Closure in 24O", *Phys. Rev. Lett.* **109** (2012) 1–5.

[52] F. Wienholtz, D. Beck, K. Blaum, C. Borgmann, M. Breitenfeldt, R. B. Cakirli, S. George, F. Herfurth, J. D. Holt, M. Kowalska, S. Kreim, D. Lunney, V. Manea, J. Menéndez, D. Neidherr, M. Rosenbusch, L. Schweikhard, A. Schwenk, J. Simonis, J. Stanja, R. N. Wolf, and K. Zuber, "Masses of exotic calcium isotopes pin down nuclear forces", *Nature* **498** (2013) 346–349.

[53] T. Duguet, H. Hergert, J. D. Holt, and V. Somà, "Nonobservable nature of the nuclear shell structure: Meaning, illustrations, and consequences", *Phys. Rev. C* **92** (2015) 034313.

[54] R. B. Cakirli, R. F. Casten, and K. Blaum, "Correlations of experimental isotope shifts with spectroscopic and mass observables", *Phys. Rev. C* **82** (2010) 061306.

[55] P. Federman and S. Pittel, "Towards a unified microscopic description of nuclear deformation", *Phys. Lett. B* **69** (1977), no. 4, 385–388.

[56] B. Pfeiffer, K.-L. Kratz, J. Dobaczewski, and P. Moller, "Calculation of Decay Properties of Very Neutron-Rich Nuclei with a Modified Nilsson Potential", *Acta Pol. Phys. B* **27** (1996) 475.

[57] J. Dudek, A. Góźdź, and N. Schunck, "Atomic Nuclei with Tetrahedral and Octahedral Symmetries", *Acta Phys. Pol. B* **34** (2003).

[58] K. Zberecki, P.-H. Heenen, and P. Magierski, "Nuclear tetrahedral configurations at spin zero", *Phys. Rev. C* **79** (2009) 014319.

[59] N. Schunck, J. Dudek, A. Góźdź, and P. H. Regan, "Tetrahedral symmetry in ground and low-lying states of exotic A 110 nuclei", *Phys. Rev. C* **69** (2004) 061305.

[60] S. Tagami, Y. R. Shimizu, and J. Dudek, "Microscopic study of tetrahedrally symmetric nuclei by an angular-momentum and parity projection method", *Phys. Rev. C* **87** (2013) 054306.

[61] M. Kortelainen, T. Lesinski, J. Moré, W. Nazarewicz, J. Sarich, N. Schunck, M. V. Stoitsov, and S. Wild, "Nuclear energy density optimization", *Phys. Rev. C* **82** (2010) 024313.

[62] J. P. Delaroche, M. Girod, J. Libert, H. Goutte, S. Hilaire, S. Péru, N. Pillet, and G. F. Bertsch, "Structure of even-even nuclei using a mapped collective Hamiltonian and the D1S Gogny interaction", *Phys. Rev. C - Nucl. Phys.* **81** (2010), no. 1, 014303.

[63] J. Skalski, S. Mizutori, and W. Nazarewicz, "Equilibrium shapes and high-spin properties of the neutron-rich A 100 nuclei", *Nucl. Phys. A* **617** (1997) 282–315.

[64] F. R. Xu, P. M. Walker, and R. Wyss, "Oblate stability of A 110 nuclei near the r -process path", *Phys. Rev. C* **65** (2002) 021303.

[65] Y. Shi, P. M. Walker, and F. R. Xu, "High-K isomers in neutron-rich zirconium isotopes", *Phys. Rev. C - Nucl. Phys.* **85** (2012) 027307.

[66] A. Petrovici, K. W. Schmid, and A. Faessler, "Self-consistent description of shape coexistence in the A100 Zr nuclei", *J. Phys. Conf. Ser.* **312** (2011) 092051.

[67] B. P. Abbott and E. al., "GW170817: Observation of Gravitational Waves from a Binary Neutron Star Inspiral", *Phys. Rev. Lett.* **119** (2017) 161101.

[68] K.-L. Kratz, J.-P. Bitouzet, F.-K. Thielemann, P. Moeller, and B. Pfeiffer, "Isotopic r-process abundances and nuclear structure far from stability - Implications for the r-process mechanism", *Astrophys. J.* **403** (1993) 216.

[69] K. L. Kratz, B. Pfeiffer, O. Arndt, S. Hennrich, and a. Wöhr, "R-process isotopes in the 132Sn region", *Eur. Phys. J. A* **25** (2005), no. SUPPL. 1, 633–638.

[70] B. Pfeiffer, K.-L. Kratz, F.-K. Thielemann, and W. Walters, "Nuclear structure studies for the astrophysical r-process", *Nucl. Phys. A* **693** (2001) 282–324.

[71] I. Dillmann, K.-L. Kratz, A. Wöhr, O. Arndt, B. A. Brown, P. Hoff, M. Hjorth-Jensen, U. Köster, A. N. Ostrowski, B. Pfeiffer, D. Seweryniak, J. Shergur, and W. B. Walters, "N=82 shell quenching of the classical r-process "waiting-point" nucleus 130Cd", *Phys. Rev. Lett.* **91** (2003) 162503.

[72] A. Jungclaus, L. Cáceres, M. Górska, M. Pfützner, S. Pietri, E. Werner-Malento, H. Grawe, K. Langanke, G. Martínez-Pinedo, F. Nowacki, A. Poves, J. J. Cuenca-García, D. Rudolph, Z. Podolyak, P. H. Regan, P. Detistov, S. Lalkovski, V. Modamio, J. Walker, P. Bednarczyk, P. Doornenbal, H. Geissel, J. Gerl, J. Grebosz, I. Kojouharov, N. Kurz, W. Prokopowicz, H. Schaffner, H. J. Wollersheim, K. Andgren, J. Benlliure, G. Benzoni, A. M. Bruce, E. Casarejos, B. Cederwall, F. C. L. Crespi, B. Hadinia, M. Hellström, R. Hoischen, G. Ilie, J. Jolie, A. Khaplanov, M. Kmiecik, R. Kumar, A. Maj, S. Mandal, F. Montes, S. Myalski, G. S. Simpson, S. J. Steer, S. Tashenov, and O. Wieland, "Observation of Isomeric Decays in the r -Process Waiting-Point Nucleus Cd 82 130", *Phys. Rev. Lett.* **99** (2007) 132501.

[73] D. Atanasov, P. Ascher, K. Blaum, R. B. Cakirli, T. E. Cocolios, S. George, S. Goriely, F. Herfurth, H.-T. Janka, O. Just, M. Kowalska, S. Kreim, D. Kisler, Y. A. Litvinov, D. Lunney,

V. Manea, D. Neidherr, M. Rosenbusch, L. Schweikhard, A. Welker, F. Wienholtz, R. N. Wolf, and K. Zuber, "Precision Mass Measurements of (129-131)Cd and Their Impact on Stellar Nucleosynthesis via the Rapid Neutron Capture Process.", *Phys. Rev. Lett.* **115** (2015) 232501.

[74] G. Lorusso, S. Nishimura, Z. Y. Xu, A. Jungclaus, Y. Shimizu, G. S. Simpson, P. A. Soderstrom, H. Watanabe, and E. al., "Beta-Decay Half-Lives of 110 Neutron-Rich Nuclei across the N = 82 Shell Gap: Implications for the Mechanism and Universality of the Astrophysical r Process", *Phys. Rev. Lett.* **114** (2015) 192501.

[75] F. Browne, A. Bruce, T. Sumikama, I. Nishizuka, S. Nishimura, P. Doornenbal, G. Lorusso, P.-A. Söderström, H. Watanabe, R. Daido, Z. Patel, S. Rice, L. Sinclair, J. Wu, Z. Xu, A. Yagi, H. Baba, N. Chiga, R. Carroll, F. Didierjean, Y. Fang, N. Fukuda, G. Gey, E. Ideguchi, N. Inabe, T. Isobe, D. Kameda, I. Kojouharov, N. Kurz, T. Kubo, S. Lalkovski, Z. Li, R. Lozeva, H. Nishibata, A. Odahara, Z. Podolyák, P. Regan, O. Roberts, H. Sakurai, H. Schaffner, G. Simpson, H. Suzuki, H. Takeda, M. Tanaka, J. Taprogge, V. Werner, and O. Wieland, "Lifetime measurements of the first 2+ states in (104,106)Zr: Evolution of ground-state deformations", *Phys. Lett. B* **750** (2015) 448–452.

[76] T. Sumikama, K. Yoshinaga, H. Watanabe, S. Nishimura, Y. Miyashita, K. Yamaguchi, K. Sugimoto, J. Chiba, Z. Li, H. Baba, J. S. Berryman, N. Blasi, a. Bracco, F. Camera, P. Doornenbal, S. Go, T. Hashimoto, S. Hayakawa, C. Hinke, E. Ideguchi, T. Isobe, Y. Ito, D. G. Jenkins, Y. Kawada, N. Kobayashi, Y. Kondo, R. Krücken, S. Kubono, G. Lorusso, T. Nakano, M. Kurata-Nishimura, a. Odahara, H. J. Ong, S. Ota, Z. Podolyák, H. Sakurai, H. Scheit, K. Steiger, D. Steppenbeck, S. Takano, a. Takashima, K. Tajiri, T. Teranishi, Y. Wakabayashi, P. M. Walker, O. Wieland, and H. Yamaguchi, "Structural evolution in the neutron-rich Nuclei Zr106 and Zr108", *Phys. Rev. Lett.* **106** (2011) 202501.

[77] O. Tarasov and D. Bazin, "LISE++: Radioactive beam production with in-flight separators", *Nucl. Instruments Methods B.* **266** (2008) 4657–4664.

[78] O. Tarasov, "NSCL Rates Version 1.03", 2018. https://groups.nscl.msu.edu/frib/rates/nscl_pac35_rates.html.

[79] A. Obertelli and T. Uesaka, "Hydrogen targets for exotic-nuclei studies developed over the past 10 years", *Eur. Phys. J. A* **47** (2011) 105.

[80] Nishina Center for Accelerator Based Science, "RIBF : Introduction to RI Beam Factory and Users' Information". www.nishina.riken.jp/RIBF/.

[81] N. Fukuda, T. Kubo, T. Ohnishi, N. Inabe, H. Takeda, D. Kameda, and H. Suzuki, "Identification and separation of radioactive isotope beams by the BigRIPS separator at the RIKEN RI Beam Factory", *Nucl. Instruments Methods B* **317** (2013) 323–332.

[82] T. Kubo, "In-flight RI beam separator BigRIPS at RIKEN and elsewhere in Japan", *Nucl. Instruments Methods B* **204** (2003) 97–113.

[83] T. Ohnishi, T. Kubo, K. Kusaka, A. Yoshida, K. Yoshida, N. Fukuda, M. Ohtake, Y. Yanagisawa, H. Takeda, D. Kameda, Y. Yamaguchi, N. Aoi, K.-i. Yoneda, H. Otsu, S. Takeuchi, T. Sugimoto, Y. Kondo, H. Scheit, Y. Gono, H. Sakurai, T. Motobayashi, H. Suzuki, T. Nakao, H. Kimura, Y. Mizoi, M. Matsushita, K. Ieki, T. Kuboki, T. Yamaguchi, T. Suzuki, A. Ozawa, T. Moriguchi, Y. Yasuda, T. Nakamura, T. Nannichi, T. Shimamura,

Y. Nakayama, H. Geissel, H. Weick, J. A. Nolen, O. B. Tarasov, A. S. Nettleton, D. P. Bazin, B. M. Sherrill, D. J. Morrissey, and W. Mittig, "Identification of New Isotopes 125 Pd and 126 Pd Produced by In-Flight Fission of 345 MeV/nucleon 238 U: First Results from the RIKEN RI Beam Factory", *J. Phys. Soc. Japan* **77** (2008) 083201.

[84] H. Kumagai, T. Ohnishi, N. Fukuda, H. Takeda, D. Kameda, N. Inabe, K. Yoshida, and T. Kubo, "Development of Parallel Plate Avalanche Counter (PPAC) for BigRIPS fragment separator", *Nucl. Instruments Methods B* **317** (2013) 717.

[85] The SUNFLOWER Collaboration and Riken Nishina Center, "SUNFLOWER Collaboration website". http://www.nishina.riken.jp/collaboration/SUNFLOWER/.

[86] S. Takeuchi, T. Motobayashi, Y. Togano, M. Matsushita, N. Aoi, K. Demichi, H. Hasegawa, and H. Murakami, "DALI2: A NaI(Tl) detector array for measurements of γ rays from fast nuclei", *Nucl. Instruments Methods A* **763** (2014) 596–603.

[87] M. Deleplanque, I. Lee, K. Vetter, G. Schmid, F. Stephens, R. Clark, R. Diamond, P. Fallon, and A. Macchiavelli, "GRETA: utilizing new concepts in γ-ray detection", *Nucl. Instruments Methods A* **430** (1999), no. 2, 292–310.

[88] I.-Y. Lee, "The Gammasphere", *Nucl. Phys. A* **520** (1990) 641.

[89] W. Mueller, J. Church, T. Glasmacher, D. Gutknecht, G. Hackman, P. Hansen, Z. Hu, K. Miller, and P. Quirin, "Thirty-two-fold segmented germanium detectors to identify γ-rays from intermediate-energy exotic beams", *Nucl. Instruments Methods A* **466** (2001) 492–498.

[90] I. Lee, "Gamma-ray tracking detectors", *Nucl. Instruments Methods A* **422** (1999) 195–200.

[91] S. Agostinelli and E. al., "Geant4—a simulation toolkit", *Nucl. Instruments Methods A* **506** (2003), no. 3, 250–303.

[92] P. Doornenbal, "In-beam gamma-ray spectroscopy at the RIBF", *Prog. Theor. Exp. Phys.* **3C004-0** (2012).

[93] Y. Giomataris, P. Rebourgeard, J. Robert, and G. Charpak, "MICROMEGAS: a high-granularity position-sensitive gaseous detector for high particle-flux environments", *Nucl. Instruments Methods A* **376** (1996) 29–35.

[94] C. Santamaria, "Quest for new nuclear magic numbers with MINOS", PhD thesis, Université Paris-Sud, 2015.

[95] P. Baron, D. Calvet, F. Chateau, A. Corsi, E. Delagnes, A. Delbart, A. Obertelli, and N. Paul, "Operational experience with the readout system of the MINOS vertex tracker", in "2016 IEEE-NPSS Real Time Conf.", pp. 1–3. IEEE, 2016.

[96] H. Kumagai, A. Ozawa, N. Fukuda, K. Sümmerer, and I. Tanihata, "Delay-line PPAC for high-energy light ions", *Nucl. Instruments Methods A* **470** (2001), no. 3, 562–570.

[97] K. Kimura, T. Izumikawa, R. Koyama, T. Ohnishi, T. Ohtsubo, A. Ozawa, W. Shinozaki, T. Suzuki, M. Takahashi, I. Tanihata, T. Yamaguchi, and Y. Yamaguchi, "High-rate particle identification of high-energy heavy ions using a tilted electrode gas ionization chamber", *Nucl. Instruments Methods A* **538** (2005) 608–614.

[98] H. Baba, T. Ichihara, T. Ohnishi, S. Takeuchi, K. Yoshida, Y. Watanabe, S. Ota, and S. Shimoura, "Common trigger firmware for GTO", tech. rep., Riken Nishina Center, 2014.

[99] R. Grzywacz, R. Anne, G. Auger, D. Bazin, C. Borcea, V. Borrel, J. Corre, T. Dörfler, A. Fomichov, M. Gaelens, D. Guillemaud-Mueller, R. Hue, M. Huyse, Z. Janas, H. Keller, M. Lewitowicz, S. Lukyanov, A. Mueller, Y. Penionzhkevich, M. Pfützner, F. Pougheon, K. Rykaczewski, M. Saint-Laurent, K. Schmidt, W.-D. Schmidt-Ott, O. Sorlin, J. Szerypo, O. Tarasov, J. Wauters, and J. Żylicz, "Identification of μs-isomers produced in the fragmentation of a 112Sn beam", *Phys. Lett. B* **355** (1995) 439–446.

[100] G. F. Knoll, "Radiation Detection and Measurement, Second Edition", John Wiley and Sons, Hoboken, NJ, 3 ed., 2000.

[101] C. Santamaria, C. Louchart, A. Obertelli, V. Werner, P. Doornenbal, F. Nowacki, G. Authelet, H. Baba, D. Calvet, F. Château, A. Corsi, A. Delbart, J.-M. Gheller, A. Gillibert, T. Isobe, V. Lapoux, M. Matsushita, S. Momiyama, T. Motobayashi, M. Niikura, H. Otsu, C. Péron, A. Peyaud, E. C. Pollacco, J.-Y. Roussé, H. Sakurai, M. Sasano, Y. Shiga, S. Takeuchi, R. Taniuchi, T. Uesaka, H. Wang, K. Yoneda, F. Browne, L. X. Chung, Z. Dombradi, S. Franchoo, F. Giacoppo, A. Gottardo, K. Hadynska-Klek, Z. Korkulu, S. Koyama, Y. Kubota, J. Lee, M. Lettmann, R. Lozeva, K. Matsui, T. Miyazaki, S. Nishimura, L. Olivier, S. Ota, Z. Patel, N. Pietralla, E. Sahin, C. Shand, P.-A. Söderström, I. Stefan, D. Steppenbeck, T. Sumikama, D. Suzuki, Z. Vajta, J. Wu, and Z. Xu, "Extension of the N = 40 Island of Inversion towards N = 50 : Spectroscopy of Cr 66 , Fe 70 , 72", *Phys. Rev. Lett.* **115** (2015) 192501.

[102] R. Evans, "The Atomic Nucleus", McGraw-Hill, 1955.

[103] R. Anholt, C. Stoller, J. D. Molitoris, D. W. Spooner, E. Morenzoni, S. A. Andriamonje, W. E. Meyerhof, H. Bowman, J.-S. Xu, Z.-Z. Xu, J. O. Rasmussen, and D. H. H. Hoffmann, "Atomic collisions with relativistic heavy ions. VI. Radiative processes", *Phys. Rev. A* **33** (1986) 2270–2280.

[104] D. Kameda, T. Kubo, T. Ohnishi, K. Kusaka, A. Yoshida, K. Yoshida, M. Ohtake, N. Fukuda, H. Takeda, K. Tanaka, N. Inabe, Y. Yanagisawa, Y. Gono, H. Watanabe, H. Otsu, H. Baba, T. Ichihara, Y. Yamaguchi, M. Takechi, S. Nishimura, H. Ueno, A. Yoshimi, H. Sakurai, T. Motobayashi, T. Nakao, Y. Mizoi, M. Matsushita, K. Ieki, N. Kobayashi, K. Tanaka, Y. Kawada, N. Tanaka, S. Deguchi, Y. Satou, Y. Kondo, T. Nakamura, K. Yoshinaga, C. Ishii, H. Yoshii, Y. Miyashita, N. Uematsu, Y. Shiraki, T. Sumikama, J. Chiba, E. Ideguchi, A. Saito, T. Yamaguchi, I. Hachiuma, T. Suzuki, T. Moriguchi, A. Ozawa, T. Ohtsubo, M. A. Famiano, H. Geissel, A. S. Nettleton, O. B. Tarasov, D. Bazin, B. M. Sherrill, S. L. Manikonda, and J. A. Nolen, "Observation of new microsecond isomers among fission products from in-flight fission of 345 MeV/nucleon 238 U", *Phys. Rev. C* **86** (2012) 054319.

[105] P. Doornenbal, "Shogun Sim". http://ribf.riken.jp/ pieter/shogun/.

[106] Y. L. Tong, "The Multivariate Normal Distribution", Springer New York, New York, NY, 1990.

[107] "R: The R Project for Statistical Computing". https://www.r-project.org/.

[108] B. Bally, B. Avez, M. Bender, and P.-H. Heenen, "Beyond Mean-Field Calculations for Odd-Mass Nuclei", *Phys. Rev. Lett.* **113** (2014) 162501.

[109] J. Sadoudi, M. Bender, K. Bennaceur, D. Davesne, R. Jodon, and T. Duguet, "Skyrme pseudo-potential-based EDF parametrization for spuriousity-free MR EDF calculations", *Phys. Scr.* **T154** (2013) 014013.

[110] M. Borrajo, T. R. Rodríguez, and J. Luis Egido, "Symmetry conserving configuration mixing method with cranked states", *Phys. Lett. B* **746** (2015) 341–346.

[111] J. Libert, "Microscopic descriptions of superdeformed bands with the Gogny force: Configuration mixing calculations in the A190 mass region", *Phys. Rev. C* **60** (1999), no. 5, 1–26.

[112] K. Pomorski and J. Dudek, "Nuclear liquid-drop model and surface-curvature effects", *Phys. Rev. C* **67** (2003) 044316.

[113] S. Tagami, M. Shimada, Y. Fujioka, Y. R. Shimizu, and J. R. Dudek, "Nuclear tetrahedral states and high-spin states studied using the quantum number projection method", *Phys. Scr.* **89** (2014) 054013.

[114] N. Shimizu, T. Abe, Y. Tsunoda, Y. Utsuno, T. Yoshida, T. Mizusaki, M. Honma, and T. Otsuka, "New-generation Monte Carlo shell model for the K computer era", *Prog. Theor. Exp. Phys.* **2012** (2012) 01A205.

[115] F. Flavigny, P. Doornenbal, A. Obertelli, J.-P. Delaroche, M. Girod, J. Libert, T. Rodriguez, G. Authelet, H. Baba, D. Calvet, F. Château, S. Chen, A. Corsi, A. Delbart, J.-M. Gheller, A. Giganon, A. Gillibert, V. Lapoux, T. Motobayashi, M. Niikura, N. Paul, J.-Y. Roussé, H. Sakurai, C. Santamaria, D. Steppenbeck, R. Taniuchi, T. Uesaka, T. Ando, T. Arici, A. Blazhev, F. Browne, A. Bruce, R. Carroll, L. Chung, M. Cortés, M. Dewald, B. Ding, S. Franchoo, M. Górska, A. Gottardo, A. Jungclaus, J. Lee, M. Lettmann, B. Linh, J. Liu, Z. Liu, C. Lizarazo, S. Momiyama, K. Moschner, S. Nagamine, N. Nakatsuka, C. Nita, C. Nobs, L. Olivier, R. Orlandi, Z. Patel, Z. Podolyák, M. Rudigier, T. Saito, C. Shand, P. Söderström, I. Stefan, V. Vaquero, V. Werner, K. Wimmer, and Z. Xu, "Shape Evolution in Neutron-Rich Krypton Isotopes Beyond N = 60 : First Spectroscopy of Kr 98 , 100", *Phys. Rev. Lett.* **118** (2017) 242501.

[116] S. Chen, P. Doornenbal, A. Obertelli, T. R. Rodríguez, G. Authelet, H. Baba, D. Calvet, F. Château, A. Corsi, A. Delbart, J.-M. Gheller, A. Giganon, A. Gillibert, V. Lapoux, T. Motobayashi, M. Niikura, N. Paul, J.-Y. Roussé, H. Sakurai, C. Santamaria, D. Steppenbeck, R. Taniuchi, T. Uesaka, T. Ando, T. Arici, A. Blazhev, F. Browne, A. M. Bruce, R. Caroll, L. X. Chung, D. Linh, J. Liu, Z. Liu, C. Lizarazo, S. Momiyama, K. Moschner, M. Rudigier, T. Saito, C. Shand, P.-A. Söderström, I. Stefan, V. Vaquero, V. Werner, K. Wimmer, and Z. Xu, "Low-lying structure and shape evolution in neutron-rich Se isotopes", *Phys. Rev. C- Rapid Commun.* **95** (2017) 041302.

[117] N. Zamfir and R. Casten, "Signatures of γ softness or triaxiality in low energy nuclear spectra", *Phys. Lett. B* **260** (1991) 265–270.

[118] T. Togashi, Y. Tsunoda, T. Otsuka, and N. Shimizu, "Quantum Phase Transition in the Shape of Zr isotopes", *Phys. Rev. Lett.* **117** (2016) 172502.

[119] O. Chamberlain and E. Segrè, "Proton-Proton Collisions within Lithium Nuclei", *Phys. Rev.* **87** (1952) 81–83.

[120] R. Serber, "The Production of High Energy Neutrons by Stripping", *Phys. Rev.* **72** (1947) 1008–1016.

[121] M. L. Goldberger, "The Interaction of High Energy Neutrons and Heavy Nuclei", *Phys. Rev.* **74** (1948) 1269–1277.

[122] C. A. Bertulani and C. De Conti, "Pauli blocking and medium effects in nucleon knockout reactions", *Phys. Rev. C* **81** (2010) 064603.

[123] J. B. Cladis, W. N. Hess, and B. J. Moyer, "Nucleon Momentum Distributions in Deuterium and Carbon Inferred from Proton Scattering", *Phys. Rev.* **87** (1952) 425–433.

[124] G. Jacob and T. A. J. Maris, "Quasi-Free Scattering and Nuclear Structure", *Rev. Mod. Phys.* **38** (1966) 121–142.

[125] G. Jacob and T. A. J. Maris, "Quasi-Free Scattering and Nuclear Structure. II.", *Rev. Mod. Phys.* **45** (1973) 6–21.

[126] T. Wakasa, K. Ogata, and T. Noro, "Proton-induced knockout reactions with polarized and unpolarized beams", *Prog. Part. Nucl. Phys.* **96** (2017) 32–87.

[127] L. Lapikás, "Quasi-elastic electron scattering off nuclei", *Nucl. Phys. A* **553** (1993) 297–308.

[128] T. Aumann, C. A. Bertulani, and J. Ryckebusch, "Quasifree (p,2p) and (p,pn) reactions with unstable nuclei", *Phys. Rev. C* **88** (2013) 06461010.

[129] V. Panin, J. Taylor, S. Paschalis, F. Wamers, Y. Aksyutina, H. Alvarez-Pol, T. Aumann, C. Bertulani, K. Boretzky, C. Caesar, M. Chartier, L. Chulkov, D. Cortina-Gil, J. Enders, O. Ershova, H. Geissel, R. Gernhäuser, M. Heil, H. Johansson, B. Jonson, A. Kelić-Heil, C. Langer, T. Le Bleis, R. Lemmon, T. Nilsson, M. Petri, R. Plag, R. Reifarth, D. Rossi, H. Scheit, H. Simon, H. Weick, and C. Wimmer, "Exclusive measurements of quasi-free proton scattering reactions in inverse and complete kinematics", *Phys. Lett. B* **753** (2016) 204–210.

[130] I. Tanihata, H. Hamagaki, O. Hashimoto, Y. Shida, N. Yoshikawa, K. Sugimoto, O. Yamakawa, T. Kobayashi, N. Takahashi, B. C. Target Al, and L. Li, "Measurements of Interaction Cross Sections and Nuclear Radii in the Light p-Shell Region", *Phys. Rev. Lett.* **55** (1985), no. 24, 2676.

[131] P. G. Hansen and J. A. Tostevin, "Direct Reactions with Exotic Nuclei", *Annu. Rev. Nucl. Part. Sci* **53** (2003) 219–61.

[132] J. Tostevin, "Single-nucleon knockout reactions at fragmentation beam energies", *Nucl. Phys. A* **682** (2001) 320–331.

[133] J. A. Tostevin and A. Gade, "Systematics of intermediate-energy single-nucleon removal cross sections", *Phys. Rev. C* **90** (2014) 057602.

[134] F. Flavigny, A. Obertelli, A. Bonaccorso, G. F. Grinyer, C. Louchart, L. Nalpas, and A. Signoracci, "Nonsudden Limits of Heavy-Ion Induced Knockout Reactions", *Phys. Rev. Lett.* **108** (2012) 252501.

[135] J. Lee, M. B. Tsang, D. Bazin, D. Coupland, V. Henzl, D. Henzlova, M. Kilburn, W. G. Lynch, A. M. Rogers, A. Sanetullaev, A. Signoracci, Z. Y. Sun, M. Youngs, K. Y. Chae, R. J. Charity, H. K. Cheung, M. Famiano, S. Hudan, P. O'Malley, W. A. Peters, K. Schmitt, D. Shapira, and L. G. Sobotka, "Neutron-Proton Asymmetry Dependence of Spectroscopic Factors in Ar Isotopes", *Phys. Rev. Lett.* **104** (2010) 112701.

[136] F. M. Nunes, A. Deltuva, and J. Hong, "Improved description of Ar 34 , 36 , 46 (p , d) transfer reactions", *Phys. Rev. C* **83** (2011) 034610.

[137] F. Flavigny, A. Gillibert, L. Nalpas, A. Obertelli, N. Keeley, C. Barbieri, D. Beaumel, S. Boissinot, G. Burgunder, A. Cipollone, A. Corsi, J. Gibelin, S. Giron, J. Guillot, F. Hammache, V. Lapoux, A. Matta, E. C. Pollacco, R. Raabe, M. Rejmund, N. de Séreville, A. Shrivastava, A. Signoracci, and Y. Utsuno, "Limited Asymmetry Dependence of Correlations from Single Nucleon Transfer", *Phys. Rev. Lett.* **110** (2013) 122503.

[138] J. Hüfner, K. Schäfer, and B. Schürmann, "Abrasion-ablation in reactions between relativistic heavy ions", *Phys. Rev. C* **12** (1975) 1888–1898.

[139] C. A. Bertulani and P. Danielewicz, "Introduction to nuclear reactions", Institute of Physics, 2004.

[140] M. L. Miller, K. Reygers, S. J. Sanders, and P. Steinberg, "Glauber Modeling in High-Energy Nuclear Collisions", *Annu. Rev. Nucl. Part. Sci.* **57** (2007) 205–243.

[141] V. F. Weisskopf and D. H. Ewing, "On the Yield of Nuclear Reactions with Heavy Elements", *Phys. Rev.* **57** (1940) 472–485.

[142] E. Fermi, "Zur Quantelung des idealen einatomigen Gases", *Zeitschrift fr Phys.* **36** (1926) 902–912.

[143] A. Kelic, M. V. Ricciardi, and K.-H. Schmidt, "ABLA07 - towards a complete description of the decay channels of a nuclear system from spontaneous fission to multifragmentation", IAEA, Vienna, 2008.

[144] R. J. Glauber, "Theory of High Energy Hadron-Nucleus Collisions", in "High-Energy Phys. Nucl. Struct.", pp. 207–264. Springer US, Boston, MA, 1970.

[145] J. L. Rodríguez-Sánchez, J.-C. David, D. Mancusi, A. Boudard, J. Cugnon, and S. Leray, "Improvement of one-nucleon removal and total reaction cross sections in the Liège intranuclear-cascade model using Hartree-Fock-Bogoliubov calculations", *Phys. Rev. C* **96** (2017) 054602.

[146] C. Gelbke, C. Olmer, M. Buenerd, D. Hendrie, J. Mahoney, M. Mermaz, and D. Scott, "Energy dependence of peripheral reactions induced by heavy ions", *Phys. Rep.* **42** (1978) 311–358.

[147] A. Boudard, J. Cugnon, S. Leray, and C. Volant, "Intranuclear cascade model for a comprehensive description of spallation reaction data", *Phys. Rev. C* **66** (2002) 044615.

[148] D. Mancusi, A. Boudard, J. Carbonell, J. Cugnon, J.-C. David, and S. Leray, "Improving the description of proton-induced one-nucleon removal in intranuclear-cascade models", *Phys. Rev. C* **9140** (2015), no. 21, 034602.

[149] J. L. Rodríguez-Sánchez, J. Benlliure, C. A. Bertulani, J. Vargas, Y. Ayyad, H. Alvarez-Pol, J. Atkinson, T. Aumann, S. Beceiro-Novo, K. Boretzky, M. Caamaño, E. Casarejos, D. Cortina-Gil, J. Díaz-Cortes, P. Díaz Fernández, A. Estrade, H. Geissel, A. Keli-Heil, Y. A. Litvinov, M. Mostazo, C. Paradela, D. Pérez-Loureiro, S. Pietri, A. Prochazka, M. Takechi, H. Weick, and J. S. Winfield, "Knockout and fragmentation reactions using a broad range of tin isotopes", *Phys. Rev. C* **96** (2017) 034303.

[150] L. Atar, S. Paschalis, C. Barbieri, C. A. Bertulani, P. Díaz Fernández, M. Holl, M. A. Najafi, V. Panin, H. Alvarez-Pol, T. Aumann, V. Avdeichikov, S. Beceiro-Novo, D. Bemmerer, J. Benlliure, J. M. Boillos, K. Boretzky, M. J. G. Borge, M. Caamaño, C. Caesar, E. Casarejos, W. Catford, J. Cederkall, M. Chartier, L. Chulkov, D. Cortina-Gil, E. Cravo, R. Crespo, I. Dillmann, Z. Elekes, J. Enders, O. Ershova, A. Estrade, F. Farinon, L. M. Fraile, M. Freer, D. Galaviz Redondo, H. Geissel, R. Gernhäuser, P. Golubev, K. Göbel, J. Hagdahl, T. Heftrich, M. Heil, M. Heine, A. Heinz, A. Henriques, A. Hufnagel, A. Ignatov, H. T. Johansson, B. Jonson, J. Kahlbow, N. Kalantar-Nayestanaki, R. Kanungo, A. Kelic-Heil, A. Knyazev, T. Kröll, N. Kurz, M. Labiche, C. Langer, T. Le Bleis, R. Lemmon, S. Lindberg, J. Machado, J. Marganiec-Gałązka, A. Movsesyan, E. Nacher, E. Y. Nikolskii, T. Nilsson, C. Nociforo, A. Perea, M. Petri, S. Pietri, R. Plag, R. Reifarth, G. Ribeiro, C. Rigollet, D. M. Rossi, M. Röder, D. Savran, H. Scheit, H. Simon, O. Sorlin, I. Syndikus, J. T. Taylor, O. Tengblad, R. Thies, Y. Togano, M. Vandebrouck, P. Velho, V. Volkov, A. Wagner, F. Wamers, H. Weick, C. Wheldon, G. L. Wilson, J. S. Winfield, P. Woods, D. Yakorev, M. Zhukov, A. Zilges, and K. Zuber, "Quasifree (p,2p) Reactions on Oxygen Isotopes: Observation of Isospin Independence of the Reduced Single-Particle Strength", *Phys. Rev. Lett.* **120** (2018) 052501.

[151] S. Kawase, T. Uesaka, T. L. Tang, D. Beaumel, M. Dozono, T. Fukunaga, T. Fujii, N. Fukuda, A. Galindo-Uribarri, S. Hwang, N. Inabe, T. Kawabata, T. Kawahara, W. Kim, K. Kisamori, M. Kobayashi, T. Kubo, Y. Kubota, K. Kusaka, C. Lee, Y. Maeda, H. Matsubara, S. Michimasa, H. Miya, T. Noro, Y. Nozawa, A. Obertelli, K. Ogata, S. Ota, E. Padilla-Rodal, S. Sakaguchi, H. Sakai, M. Sasano, S. Shimoura, S. Stepanyan, H. Suzuki, T. Suzuki, M. Takaki, H. Takeda, A. Tamii, H. Tokieda, T. Wakasa, T. Wakui, K. Yako, J. Yasuda, Y. Yanagisawa, R. Yokoyama, K. Yoshida, K. Yoshida, and J. Zenihiro, "Exclusive quasi-free proton knockout from oxygen isotopes at intermediate energies", *Prog. Theor. Exp. Phys.* **2018** (2018) 021D01.

[152] T. Kubo, D. Kameda, H. Suzuki, N. Fukuda, H. Takeda, Y. Yanagisawa, M. Ohtake, K. Kusaka, K. Yoshida, N. Inabe, T. Ohnishi, A. Yoshida, K. Tanaka, and Y. Mizoi, "BigRIPS separator and ZeroDegree spectrometer at RIKEN RI Beam Factory", *Prog. Theor. Exp. Phys.* **2012** (2012) 3C003.

[153] P.-A. Söderström, S. Nishimura, P. Doornenbal, G. Lorusso, T. Sumikama, H. Watanabe, Z. Xu, H. Baba, F. Browne, S. Go, G. Gey, T. Isobe, H.-S. Jung, G. Kim, Y.-K. Kim, I. Kojouharov, N. Kurz, Y. Kwon, Z. Li, K. Moschner, T. Nakao, H. Nishibata, M. Nishimura, A. Odahara, H. Sakurai, H. Schaffner, T. Shimoda, J. Taprogge, Z. Vajta, V. Werner, J. Wu, A. Yagi, and K. Yoshinaga, "Installation and commissioning of EURICA – Euroball-RIKEN Cluster Array", *Nucl. Instruments Methods B.* **317** (2013) 649–652.

[154] P.-A. Söderström, "EURICA isomeric contamination", 2018. private communication.

[155] R. F. Schall and A. A. Caretto, "Nuclear Structure Effects in (p, 2 nucleon) Reactions on the Separated Isotopes of Tellurium at 300 Mev", *Phys. Rev. C* **2** (1970), no. 5, 1924.

[156] A. Bohr, "The Coupling of Nuclear Surface Oscillations to the Motion of Individual Nucleons.", Pp. 40. København, 1952.

[157] B. N. L. National Nuclear Data Center, "NNDC". www.nndc.bnl.gov.

[158] L. Audirac, A. Obertelli, P. Doornenbal, D. Mancusi, S. Takeuchi, N. Aoi, H. Baba, S. Boissinot, A. Boudard, A. Corsi, A. Gillibert, T. Isobe, A. Jungclaus, V. Lapoux, J. Lee, S. Leray, K. Matsui, M. Matsushita, T. Motobayashi, D. Nishimura, S. Ota, E. C. Pollacco, G. Potel, H. Sakurai, C. Santamaria, Y. Shiga, D. Sohler, D. Steppenbeck, R. Taniuchi, and H. Wang, "Evaporation-cost dependence in heavy-ion fragmentation", *RAPID Commun. Phys. Rev. C* **88** (2013) 041602.

[159] W. M. Bugg, G. T. Condo, E. L. Hart, H. O. Cohn, and R. D. McCulloch, "Evidence for a Neutron Halo in Heavy Nuclei from Antiproton Absorption", *Phys. Rev. Lett.* **31** (1973) 475–478.

[160] S. Wycech, J. Skalski, R. Smolańczuk, J. Dobaczewski, and J. R. Rook, "Antiprotonic studies of nuclear neutron halos", *Phys. Rev. C* **54** (1996) 1832.

[161] R. Schmidt, F. J. Hartmann, B. Ketzer, T. von Egidy, T. Czosnyka, J. Jastrzbski, M. Kisieliński, P. Lubiński, P. Napiorkowski, L. Pieńkowski, A. Trzcińska, B. Kłos, R. Smolańczuk, S. Wycech, W. Pöschl, K. Gulda, W. Kurcewicz, and E. Widmann, "Composition of the nuclear periphery from antiproton absorption using short-lived residual nuclei", *Phys. Rev. C* **60** (1999) 054309.

[162] B. Kłos, A. Trzcińska, J. Jastrzębski, T. Czosnyka, M. Kisieliński, P. Lubiński, P. Napiorkowski, L. Pieńkowski, F. J. Hartmann, B. Ketzer, P. Ring, R. Schmidt, T. von Egidy, R. Smolańczuk, S. Wycech, K. Gulda, W. Kurcewicz, E. Widmann, and B. A. Brown, "Neutron density distributions from antiprotonic Pb 208 and Bi 209 atoms", *Phys. Rev. C* **76** (2007) 014311.

[163] S. D. Schery, D. A. Lind, and H. Wieman, "Nuclear matter distribution in Sn 112 , Sn 116 , and Sn 124 from the (p,n) reaction", *Phys. Rev. C* **14** (1976) 1800–1807.

[164] P. G. Hansen and B. Jonson, "The Neutron Halo of Extremely Neutron-Rich Nuclei", *Europhys. Lett.* **4** (1987) 409–414.

[165] P. G. Hansen, A. S. Jensen, and B. Jonson, "Nuclear Halos", *Annu. Rev. Nucl. Part. Sci.* **45** (1995) 591–634.

[166] T. Nakamura, N. Kobayashi, Y. Kondo, Y. Satou, J. Tostevin, Y. Utsuno, N. Aoi, H. Baba, N. Fukuda, J. Gibelin, N. Inabe, M. Ishihara, D. Kameda, T. Kubo, T. Motobayashi, T. Ohnishi, N. Orr, H. Otsu, T. Otsuka, H. Sakurai, T. Sumikama, H. Takeda, E. Takeshita, M. Takechi, S. Takeuchi, Y. Togano, and K. Yoneda, "Deformation-Driven p -Wave Halos at the Drip Line: Ne 31", *Phys. Rev. Lett.* **112** (2014) 142501.

[167] N. Kobayashi, T. Nakamura, Y. Kondo, J. Tostevin, Y. Utsuno, N. Aoi, H. Baba, R. Barthelemy, M. Famiano, N. Fukuda, N. Inabe, M. Ishihara, R. Kanungo, S. Kim, T. Kubo, G. Lee, H. Lee, M. Matsushita, T. Motobayashi, T. Ohnishi, N. Orr, H. Otsu, T. Otsuka, T. Sako, H. Sakurai, Y. Satou, T. Sumikama, H. Takeda, S. Takeuchi, R. Tanaka, Y. Togano, and K. Yoneda, "Observation of a p -Wave One-Neutron Halo Configuration in Mg 37", *Phys. Rev. Lett.* **112** (2014) 242501.

[168] X. Roca-Maza, M. Centelles, X. Viñas, and M. Warda, "Neutron Skin of Pb 208 , Nuclear Symmetry Energy, and the Parity Radius Experiment", *Phys. Rev. Lett.* **106** (2011) 252501.

[169] F. Fattoyev, J. Piekarewicz, and C. Horowitz, "Neutron Skins and Neutron Stars in the Multimessenger Era", *Phys. Rev. Lett.* **120** (2018) 172702.

[170] S. Typel, H. H. Wolter, G. Röpke, and D. Blaschke, "Effects of the liquid-gas phase transition and cluster formation on the symmetry energy", *Regul. Artic. Phys. Eur. Phys. J. A* **50** (2014) 17.

[171] A. Trzcińska, J. Jastrzbski, P. Lubiński, F. J. Hartmann, R. Schmidt, T. von Egidy, and B. Kłos, "Neutron Density Distributions Deduced from Antiprotonic Atoms", *Phys. Rev. Lett.* **87** (2001) 082501.

[172] V. Rodin, "Neutron skin and giant resonances in nuclei", *Prog. Part. Nucl. Phys.* **59** (2007) 268–276.

[173] T. Aumann, C. A. Bertulani, F. Schindler, and S. Typel, "Peeling Off Neutron Skins from Neutron-Rich Nuclei: Constraints on the Symmetry Energy from Neutron-Removal Cross Sections", *Phys. Rev. Lett.* **119** (2017) 262501.

[174] J. S. Cohen, "Capture of antiprotons by some radioactive atoms and ions", *Phys. Rev. A* **69** (2004) 022501.

[175] T. Suda, T. Adachi, T. Amagai, A. Enokizono, M. Hara, T. Hori, S. Ichikawa, K. Kurita, T. Miyamoto, R. Ogawara, T. Ohnishi, Y. Shimakura, T. Tamae, M. Togasaki, M. Wakasugi, S. Wang, and K. Yanagi, "Nuclear physics at the SCRIT electron scattering facility", *Prog. Theor. Exp. Phys.* **2012** (2012) 03C008.

[176] T. Alexopoulos, J. Burnens, R. de Oliveira, G. Glonti, O. Pizzirusso, V. Polychronakos, G. Sekhniaidze, G. Tsipolitis, and J. Wotschack, "A spark-resistant bulk-micromegas chamber for high-rate applications", *Nucl. Instruments Methods A* **640** (2011) 110–118.

[177] "COMSOL Multiphysics® Modeling Software". https://www.comsol.com/.

[178] J. N. Reddy, "An introduction to the finite element method", McGraw-Hill, 2006.

[179] R. Veenhof, "Garfield++". https://garfieldpp.web.cern.ch.

[180] A. G. Ingalls, "The Amateur Scientist", *Sci. Am.* **192** (1955) 110–119.

[181] C. Brand, R. Cirio, H. Foeth, and M. Schluter, "Improvement of the wire gain near the frame of a time projection chamber", *Nucl. Instruments Methods A* **237** (1985) 501–504.

[182] J. M. Meek, "A Theory of Spark Discharge", *Phys. Rev.* **57** (1940) 722–728.

[183] M. A. M. A. Lieberman and A. J. Lichtenberg, "Principles of plasma discharges and materials processing", Wiley, 1994.

[184] E. Husain and R. S. Nema, "Analysis of Paschen Curves for air, N2 and SF6 Using the Townsend Breakdown Equation", *IEEE Trans. Electr. Insul.* **EI-17** (1982) 350–353.

[185] F. Bacon, "The Works of Francis Bacon", New York, 1896.

[186] A. Boudard, J. Cugnon, J.-C. David, S. Leray, and D. Mancusi, "New potentialities of theLì ege intranuclear cascade model for reactions induced by nucleons and light charged particles", *Phys. Rev. C* **87** (2013) 014606.

université PARIS-SACLAY | ÉCOLE DOCTORALE PHENIICS

Titre : Première Spectroscopie de ^{110}Zr avec MINOS

Mots-clés : physique nucléaire, spectroscopie gamma, noyaux exotiques, réactions nucléaires

Résumé : Une fermeture de sous-couche à N=70 dans le ^{110}Zr a longtemps été considérée comme une explication possible du désaccord entre la théorie et les abondances observées des éléments lourds près de la masse 130 résultant du processus de capture rapide des neutrons (processus r). Le processus r n'est pas bien compris en partie à cause des incertitudes relatives aux mécanismes d'évolution de la structure en couches des noyaux riches en neutrons. La fermeture de sous-couche dans le ^{110}Zr, bien qu'improbable, pourrait résulter d'une symétrie tétraédrique ou sphérique. Ces symétries laissent des indications distinctes sur la structure des niveaux de basse énergie et leur effet peut donc être détecté par une simple mesure de spectroscopie. Le système MINOS a été employé à l'installation de faisceaux d'isotopes radioactifs (RIBF) de RIKEN au Japon pour effectuer la première spectroscopie du ^{110}Zr. MINOS, développé au CEA-IRFU, combine une cible de protons épaisse avec un dispositif de reconstruction de vertex de réaction pour permettre une spectroscopie à haute résolution des noyaux rares. Les états de basse énergie dans le ^{110}Zr ont été peuplés par arrachage des protons de la cible MINOS, et les rayons gamma de désexcitation ont été détectés avec l'ensemble de scintillateurs DALI2. Les résultats sont compatibles avec un noyau bien déformé. Aucune preuve n'est obtenue pour une fermeture de sous-couche à N = 70 ni en faveur de la symétrie tétraédrique. Une étude complémentaire explore les sections efficaces inclusives pour les réactions (p,2p) et (p,pn) avec les noyaux riches en neutrons. Environ 60 sections efficaces inclusives ont été mesurés pour l'arrachage d'un nucléon sur la cible MINOS. La systématique (p,2p) montre une augmentation de la section efficace pour les noyaux fils de Z impair, ce qui révèle l'importance des corrélations d'appariement. Les sections (p,pn) sont plus grandes que les sections efficaces (p,2p), d'environ un facteur 10, distribuées aléatoirement autour de 45 mb. La comparaison avec les modèles semi-classiques suggère que ces deux systématiques peuvent être expliquées par le rôle important des corrélations d'appariement dans les réactions directes induites par les noyaux exotiques. Enfin, des simulations électrostatiques ont été menées pour optimiser la cage de champ électrique de la chambre de projection temporelle MINOS, en vue d'une future application pour un nouveau programme de physique au CERN appelé PUMA.

Title: First Spectroscopy of ^{110}Zr with MINOS

Keywords: nuclear physics, gamma spectroscopy, exotic nuclei, nuclear reactions

Abstract: A predicted N=70 subshell closure in ^{110}Zr has long been considered a potential explanation for the disagreement between theory and observed abundances of the heavy elements near mass 130 resulting from the rapid neutron capture process (r-process). The r-process is not well understood, due in part to the uncertainties of the neutron-rich structure evolution mechanisms. A subshell closure in ^{110}Zr, though unlikely, could result from either a tetrahedral or spherical symmetry. Each of these symmetries leaves distinct fingerprints on the low lying level structure, and thus can be discerned with a simple spectroscopy measurement. The MINOS system has been used at the Radioactive Isotope Beam Factory of RIKEN in Japan to perform the first spectroscopy of ^{110}Zr. MINOS, developed at CEA-IRFU, combines a thick proton target with a vertex tracker to allow high resolution spectroscopy of rare nuclei. Low lying states in ^{110}Zr were populated via proton removal on the MINOS target, and deexcitation gamma rays detected with the DALI2 scintillator array. Results are consistent with a well deformed nucleus. No evidence is found for a subshell closure at N=70 nor tetrahedral symmetry. A complementary study explores inclusive cross sections for (p,2p) and (p,pn) reactions with neutron rich nuclei. Approximately 60 inclusive cross sections have been measured for single nucleon removal on the MINOS target. The (p,2p) systematics reveal an enhanced cross section to odd-Z daughter nuclei, pointing to the importance of pairing correlations. The (p,pn) cross sections are approximately a factor of 10 larger than the (p,2p) cross sections, randomly distributed around 45 mb. Comparison with semi-classical models suggest that both these systematics can be explained by the important role of pairing correlations in direct reactions with exotic nuclei. Finally, the electric field cage of the MINOS time projection chamber is optimized with electrostatic simulations in view of a future application as a pion tracker for antiproton-nucleus collisions in a new physics program at CERN called PUMA.

Université Paris-Saclay
Espace Technologique / Immeuble Discovery
Route de l'Orme aux Merisiers RD 128 / 91190 Saint-Aubin, France